MEASUREMENT TECHNIQUES AND MODELLING OF MULTIPHASE SYSTEMS

A. Busciglio

Universitá degli Studi di Palermo
Dottorato di Ricerca in Ingegneria Chimica, XXII ciclo

Tutors

Prof. Alberto Brucato
Prof. Giorgio Micale

Submission to the experimental data
is the golden rule that dominates any scientific discipline

Maurice Allais
Nobel Memorial Prize in Economics

Abstract

Multiphase systems are often encountered in process industry. Widely diffused applications and operations involve the contact between different phases (gas-solid, gas-liquid, solid liquid, *etc.*) for different purposes, such as chemical reactions of physical operations (heat transfer, mass transfer). Multiphase flows are therefore one of the most frequent applied fields in chemical engineering.

The present thesis is aimed at the development of experimental techniques for the investigation of multiphase flow in general, with particular focus on the analysis of gas-solid and gas-liquid systems. Notably, the development of image analysis techniques is the central thread of the present contribution, and it will be shown that the knowledge so far accumulated allowed to obtain considerable results in both fields investigated.

The approach to multiphase systems here adopted is based on the development of novel reliable experimental techniques for the assessment of multiphase system properties and subsequent collection of new experimental information through application of the original techniques here developed. The techniques are mainly based on image analysis, they are non-intrusive, capable of securing several properties simultaneously and cost effective. In particular, the expertise in digital image processing was applied to the investigation of two different classes of multiphase systems, *i.e.* gas-liquid dispersions and dense gas-solid systems (fluidized beds).

With reference to gas liquid dispersions, an effective experimental technique for measuring local gas hold-up and interfacial area, as well as bubble size distribution, was developed and subsequently exploited for collecting experimental information. The technique, named Laser Induced Fluorescence with Shadow Analysis for Bubble Sizing (LIF-SABS) is based on laser sheet illumination of the gas-liquid dispersion and synchronized image acquisition, *i.e.* on equipment typically available within PIV set-ups.

With reference to fluidized beds, a digital image analysis technique was developed

to study the fluidization dynamics of a lab-scale two-dimensional bubbling bed. Several significant bubble properties were simultaneously measured, ranging from overall bed properties to bubble size and bubble velocity distributions. Moreover, since a lack of knowledge exists on the bubbling dynamics of mixed powders, a large experimental campaign was set up to investigate the fluidization behavior of such powder mixtures.

In the field of fluidized bed modeling, a novel linear stability criterion for the state of homogeneous fluidization regime was developed, based on a new mathematical model for gas-fluidized beds. A fully predictive criterion for the stability of homogeneous fluidization state was proposed and validated with literature data.

Publications

Some ideas and figures have appeared previously in the following publications:

ISI Publications

- Busciglio A., Vella G., Micale G, Rizzuti L. (2008)
  Analysis of the Bubbling Behaviour of 2-D Gas Fluidized Beds. Part I: Digital Image Analysis Technique
  Chemical Engineering Journal 140:398-413
  doi:10.1016/j.cej.2007.11.015

- Busciglio A., Vella G., Micale G., Rizzuti L., (2009)
  Analysis of the bubbling behaviour of 2-D gas solid fluidized beds part II: Comparison between experiments and numerical simulations via Digital Image Analysis Technique
  Chemical Engineering Journal, 148:145-163.
  doi:10.1016/j.cej.2008.11.010

- Scargiali F., Busciglio A., Grisafi F., Brucato A., (2010)
  Simplified Dynamic Pressure Method for $k_L a$ *measurement in aerated bioreactors*
  Biochemical Engineering Journal, 49:165-172
  doi: 10.1016/j.bej.2009.12.008

- Busciglio A., Micale G., Vella G., Rizzuti L. (2010)
  Linear stability analysis of gas-fluidized beds for the prediction of incipient bubbling conditions
  Chemical Engineering Journal 157:489-500
  doi: 10.1016/j.cej.2009.12.040

- Busciglio A., Grisafi F., Scargiali F., Brucato A. (2010)
  On the measurement bubble size distribution in gas-liquid contactors via light sheet and image analysis
  Chemical Engineering Science 65(8): 2558-2568
  doi: 10.1016/j.ces.2009.12.031

- Busciglio A., Grisafi F., Scargiali F., Brucato A. (2010)
  On the measurement of local gas hold-up and interfacial area in gas-liquid contactors via light sheet and image analysis
  Chemical Engineering Science, 65(12):3699-3708
  doi: 10.1016/j.ces.2010.03.004

- Busciglio A., Vella G., Micale G., Rizzuti L., (2010)
  Experimental Analysis of Bubble Size Distributions in 2D gas-fluidized beds
  Chemical Engineering Science 65(16):4782-4791
  doi: doi:10.1016/j.ces.2010.05.016

Non-ISI publications

- Busciglio A., Vella G., Micale G., Rizzuti L., (2009)
  CFD prediction of bubbles behaviour in 2-Dimensional gas fluidized beds
  Multiphase Science and Technology, 21(1):13-24
  doi: 10.1615/MultScienTechn.v21.i1-2.20

Inbook publications

- A. Busciglio, G. Micale, L. Rizzuti, G. Vella (2008)
  Study of bubbling fluidization dynamics via Digital Image Analysis Technique
  Advances in Fluid Mechanics VII, WIT Transaction on Engineering Science, Vol. 59
  editors M. Rahman and C.A. Brebbia, WIT press, ISBN: 978-1-84564-109-2.
  Acts of the Seventh International Conference on Advances in Fluid Mechanics (AFM2008), 21 - 23 May, 2008, The New Forest, UK.

Patents

- Brucato A., Grisafi F., Scargiali F., Busciglio A., Lino L. (2009)
  Reattore per la precipitazione di micro e nano-particelle
  number RM2009A679.

International congress presentations

- A. Busciglio, F. Scargiali, F. Grisafi, A. Brucato (2010)
  Local gas-liquid dispersion properties assessment via light sheet and image analysis
  12th Workshop on two-phase flow predictions, 22. - 25. March 2010, Halle-Wittenberg, Germany
  ISBN: 978-3-86829-222-0

- Brucato A., Busciglio A., Di Stefano F., Grisafi F., Micale G., Scargiali F., (2010)
  High temperature solid-catalized transesterification for biodiesel production
  Chemical Engineering Transaction , 19:31-36
  4th Int.l Conf. on Safety & Environment in Process Industry (CISAP4), 14 -17 March 2010 Florence, Italy
  DOI: 10.3003/CET1019006.

- Scargiali F., Busciglio A., Grisafi F., Brucato A., (2010) $k_L a$ *measurement in bioreactors*
  Chemical Engineering Transaction , 20:229-234
  Industrial Biotechnology 2nd Int. Conf. (IBIC 2010), 11- 14 April, 2010 - Padua, Italy
  DOI: 10.3303/CET1020039.

- Brucato A., Busciglio A., Grisafi F., Scargiali F. (2009)
  A novel technique for investigating gas-liquid contactors via light sheet and image analysis
  8th World Congress of Chemical Engineering (WCCE8), Montréal (Canada), August 23-27, 2009.

- Busciglio A., Micale G., Rizzuti L., Vella G., Lombardo A. (2009)
  Advanced statistical analysis of Local Bubble Size Distributions in 2D gas fluidized beds
  Chemical Engineering Transactions, 17: 513-518
  Ninth Int. Conf. on Chemical & Process Engineering (ICheaP-9), 10-13 May 2009, Rome, Italy
  DOI: 10.3303/CET0917086

- Busciglio A., Grisafi F., Scargiali F., Brucato A. (2009)
  Area-to-volume data translation in the measurement of bubble size distributions

via laser sheet and image analysis
Chemical Engineering Transactions, 17:603-608
Ninth Int. Conf. on Chemical & Process Engineering (ICheaP-9), 10-13 May 2009, Rome, Italy
DOI: 10.3303/CET0917101

- Scargiali F., Busciglio A., Grisafi F., Brucato A. (2009)
  On the performance of a narrow-gap Taylor-Couette reactor for nano-particle precipitation
  Chemical Engineering Transactions, 17: 969-974
  Ninth Int. Conf. on Chemical & Process Engineering (ICheaP-9), 10-13 May 2009, Rome, Italy
  DOI: 10.3303/CET0917101

- Busciglio A., Micale G., Rizzuti L., Vella G., Canalella F., Lombardo A. (2008)
  Study of bubble size distribution in bubbling fluidized beds via Digital Image Analysis Technique
  11th Int. Conf. on Multiphase Flow in Industrial Plant (MFIP 2008), 7 - 10 september, 2008, Palermo
  ISBN: 88-88198-13-X.

- Busciglio A., Micale G., Rizzuti L., Vella G. (2008)
  CFD prediction of bubbles local hold-up in 2-dimensional gas-solid fluidized beds
  11th Int. Conf. on Multiphase Flow in Industrial Plant (MFIP 2008), 7 - 10 september, 2008, Palermo
  ISBN: 88-88198-13-X.

- Brucato A., Busciglio A., Grisafi F., Pipitone F., Scargiali F. (2008)
  Particle Image Velocimetry in a gas-sparged stirred tank
  11th Int. Conf. on Multiphase Flow in Industrial Plant (MFIP 2008), 7 - 10 september, 2008, Palermo
  ISBN: 88-88198-13-X.

- Brucato A., Busciglio A., Grisafi F., Rizzuti L., Scargiali F. (2008)
  Bubble formation at single nozzles
  11th Int. Conf. on Multiphase Flow in Industrial Plant (MFIP 2008), 7 - 10 september, 2008, Palermo
  ISBN: 88-88198-13-X.

- Busciglio A., Micale G., Rizzuti L., Vella G. (2008)
  Experimental Analysis of bubbling dynamics in bidisperse gas-solid 2D fluidized beds
  18th Int. Congress of Chemical and Process Engineering (CHISA 2008), 24 - 28 August, Prague, Czech Republic
  ISBN:978-80-02-02047-9.

- Busciglio A., Vella G., Micale G., Rizzuti L. (2007)
  Digital Image Analysis Techniques for 2D Gas-Fluidized Beds
  Int. Conf. of Multiphase Flows (ICMF 2007), Liepzig, 9-13 July 2007
  ISBN: 978-3-86010-913-7, atti su CD-ROM

- Busciglio A., Micale G., Rizzuti L., Vella G. (2007)
  Numerical Simulations of Bubbling Fluidized Beds
  Chemical Engineering Transactions, 11:303-308
  Eight Int. Conf. on Chemical & Process Engineering (ICheaP-8), Ischia 24-27 June 2007
  ISBN: 978-88-95608-00-6

- Vella G., Busciglio A., Micale G., Rizzuti L. (2006)
  Analysis of Bubbling Fluidization Dynamics
  10th Int. Conf. on Multiphase Flow Industrial Plant (ANIMP-MFIP 2006), Tropea, 20-22 September 2006
  ISBN: 88-7458-049-5.

- Busciglio A., Vella G., Micale G., Rizzuti L. (2006)
  Mathematical Model and Stability analysis of Multiphase Flow in Fluidized Beds
  10th Int. Conf. on Multiphase Flow Industrial Plant (ANIMP-MFIP 2006), Tropea, 20-22 September 2006
  ISBN: 88-7458-049-5.

National Congress presentations

- Vella G., Busciglio A., Micale G., Rizzuti L. (2006)
  Experimental investigation of fluidization dynamics at various flow regimes
  8° Convegno Nazionale AIMAT, Palermo, 27 Giugno- 1 Luglio 2006, su CD-ROM.

- Busciglio A., Micale G., Rizzuti L., Vella G. (2008)
  Lagrangian simulation of bubbling behaviour in gas fluidized beds and validation with experimental data
  Convegno GRICU 2008, 14 - 17 settembre , 2008, Le Castella (KR).

Submitted Papers

- Busciglio A., Vella G., Micale G., Brandani S., Rizzuti L.
  Modeling of Magnetic Field Assisted Fluidization. I. Model development and Linear Stability Analysis
  Submitted to Chemical Engineering Science.

- Busciglio A., Vella G., Micale G., Brandani S., Rizzuti L.
  Modeling of Magnetic Field Assisted Fluidization. II. CFD simulation of magnetically stabilized fluidized beds
  Submitted to Chemical Engineering Science.

- Busciglio A., Vella G., Micale G., Rizzuti L.
  On the bubbling dynamics of binary mixtures of particles in 2D gas-solid fluidized beds
  Submitted to Chemical Engineering Science.

Contents

II Fluidization 89

III Fluidization Modeling 167

List of Figures

List of Tables

Acronyms and notation

A_b	bubble projected area $[m^2]$
a_i	actual specific interfacial area $[m^{-1}]$
$a_{i,a}$	apparent specific interfacial area $[m^{-1}]$
$cP(l\|r)$	cumulative conditional probability density $[-]$
D	impeller diameter $[m]$
D_b	bubble diameter $[m]$
$D_{i,j}$	average bubble diameter computed as ratio between $i-th$ and $j-th$ moment of relevant distribution $[m]$
d_p	particle diameter $[m]$
f_{a_i}	gas-phase volume fraction correction factor[-]
f_ϵ	gas-phase volume fraction correction factor[-]
F_d	drag force $[kg/m^2/s^2]$
g	acceleration due to gravity $[m/s^2]$
G_i	gamma distribution parameters for BSD [-]
H	elevation above the distributor $[m]$
H_0	settled bed height $[m]$
H_{bed}	bed surface elevation above the distributor $[m]$
H_{max}	maximum bed surface elevation above the distributor $[m]$
HU	bubble hold up in fluid bed $[-]$
K_b	bubble number density coalescence rate $[num/frame/m^2]$

k_b	specific bubble number density coalescence rate $[m^{-1}]$
L	bubble intercept diameter $[m]$
$L_{i,j}$	average bubble intercept diameter computed as ratio between $i-th$ and $j-th$ moment of relevant distribution $[m]$
L_i	lognormal distribution parameters for BSD [-]
l	bubble intercept radius $[m]$
$l_{i,j}$	average bubble intercept radius computed as ratio between $i-th$ and $j-th$ moment of relevant distribution $[m]$
$l(x,y)$	pixel luminance [-]
N	impeller rotational speed $[s^{-1}]$
N_{pi}	number of pixels along ith laser ray $[s^{-1}]$
N_b	bubble number density $[num/frame/s]$
N_0	bubble number density at distributor $[num/frame/m^2]$
N_s	bubble number density in slugging region $[num/frame/m^2]$
n	Richardson-Zaki exponent $[-]$
P	impeller power dissipation $[W]$
P	pressure $[Pa]$
P_g	impeller power dissipation under gassed conditions $[W]$
$P(l\|r)$	conditional probability density $[m^{-1}]$
$P_b(r)$	biased probability function $[-]$
Q	gas flow rate $[m^3/s]$
Q_{mf}	gas flow rate at minimum fluidization $[m^3/s]$
r_l	bubble visible radius intercept by left extreme of thick light sheet $[m]$
r_r	bubble visible radius intercept by right extreme of thick light sheet $[m]$
$r_{i,j}$	average bubble radius computed as ratio between $i-th$ and $j-th$ moment of relevant distribution $[m]$
S	gas-phase surface $[m^2]$
T	tank diameter $[m]$
U	inlet gas velocity $[m/s]$

U_{mf}	inlet gas velocity at minimum fluidization $[m/s]$
U_{mb}	inlet gas velocity at minimum bubbling $[m/s]$
u_t	terminal velocity $[m/s]$
u_p	particle phase velocity $[m/s]$
u_f	gas phase velocity $[m/s]$
u_K	kinematic wave velocity $[m/s]$
u_D	dynamic wave velocity $[m/s]$
V	liquid volume $[m^3]$
V_g	gas-phase volume $[m^3]$
v_s	gas superficial velocity $[m/s]$
V_b	bubble volume $[m^3]$
V_s	bubble shell volume $[m^3]$
w_{ls}	laser sheet thickness $[m]$
x_c, y_c	bubble centroid coordinates $[m]$
α	solid-phase volume fraction [-]
α_i	parameter of local BSD fitting function [-]
β_i	parameter of local BSD fitting function [-]
β	ratio between the thickness of the laser sheet and the bubble average radius [-]
χ_i	local BSD peak mode value $[m]$
δ	averaging length $[m]$
ϵ	actual gas-phase volume fraction [-]
ϵ_a	apparent gas-phase volume fraction [-]
ϵ_{mf}	gas-phase volume fraction at minimum fluidization [-]
ϵ_{mb}	gas-phase volume fraction at minimum bubbling [-]
ρ_l	liquid density $[kg/m^3]$
ρ_f	gas density $[kg/m^3]$
ρ_p	solid density $[kg/m^3]$

μ	liquid viscosity $[Pa\, s]$
μ_g	gas viscosity $[Pa\, s]$
μ_i	local BSD peak mean value $[m]$
σ	liquid surface tension $[N/m]$
σ_i	local BSD peak standard deviation value $[m]$
ζ_i	luminance function along $i-th$ laser ray $[N/m]$
Φ	local phase indicator [-]
ϕ	velocity coefficient in fluidized beds correlation for bubble velocity [-]
ATI	Anisotropically Transformed Image
BSD	Bubble Size Distribution
BZM	Brandani-Zhang Model
CCD	Charged Coupled Device
CSP	Capillary Suction Probe
cBSD	Cumulative Bubble Size Distribution
cVISD	Cumulative Visible Intercept Size Distribution
DIAT	Digital Images Analysis Technique
EBI	Enhanced Bubble Image
ESI	Enhanced Shadow Image
FEM	Finite Element Method
GKT	Granular Kinetic Theory
LDA	Laser Doppler Anemometry
LED	Light Emitting Diode
LVT	Lagrangian Velocimetry Technique
NMR	Nuclear Magnetic Resonance
MBV	Minimum Bubbling Voidage
PBM	Particle Bed Model
PDA	Partial Decoupling Approach

PIV	Particle Image Velocimetry
PTV	Particle Tracking Velocimetry
RGB	Red Green Blue image color encoding
TDA	Total Decoupling Approach
VISD	Visible Intercept Size Distribution

Part I

Mixing

1 Introduction to Gas-liquid stirred tanks

There are many processes in which gas liquid contacting is important. Gas must be effectively and efficiently contacted with liquid to provide mass transfer (absorption or desorption; absorption of gas into liquid to produce a chemical reaction). Sometimes the gas merely provides energy for mixing the liquid (via buoyancy, level rise, bubble wakes, bubble coalescence, or gas expansion). Different contexts bring different challenges. Fermentations and effluent treatment can be at very large scale but the product value and workup tend to be comparatively low, so mixer capital and energy are important. Gas liquid reactions in low viscosity liquids:

- Are often also at large scale
- they have reaction selectivity issues involving the dissolved gas concentration
- they have rapid reactions with large heat generation
- they involve subsequent processing producing comparatively valuable products

So for these, scale up, liquid mixedness, and mass and heat transfer are important while plant and energy costs are not. Chlorinations and sulfonations tend to be fast reactions involving quite soluble gases, so high transfer is efficient, even with short contact times. With oxidations the gas is less soluble, but selectivity is often critical. Hydrogenations involve longer contact times, often with gas recycling and solid particles to be kept in suspension.

The processes of liquid mixing, generation of interface area, and gas liquid mass transfer in turbulent systems are controlled primarily by the power dissipated in the fluids and the gas volume fraction ϵ. Power dissipation (together with fluid properties) affects bubble size. The gas is broken up into a dispersion of bubbles in high shear zones such as the discharge from the sparger holes in bubble columns or the impeller stream in agitated vessels, or the gas inlet and wall shear zones in static mixers. It is the power dissipated in such zones that controls bubble breakup processes. However, with agitated vessels the design correlations are commonly based on the average energy dissipation per unit mass in the vessel, P/V. Power in this expression is the sum of the shaft power and the (mainly potential) energy introduced as a result of injecting the gas at some depth. It may be noted that the ratio of local to average energy dissipation rates can be large and will differ between impeller types.

Bubbles may or may not subsequently coalesce, depending on the local fluid dynamics and the interfacial behavior. The lack of predictability of these phenomena makes *a priori* predictions of bubble size and interface area troublesome, so design via scale-up from experiments is often preferred. The gas fraction in an agitated vessel is determined by bubble size and the degree of bubble recirculation (which is in turn a function of agitation, bubble size, and scale). For a static mixer, ϵ is largely set by the ratio of the average gas flow to liquid flow, but with corrections for bubble *slip*, which depend on flow orientation and the bubble size.

Bulk circulation is the rate-determining step for liquid mixing (blending) in stirred vessels. Turbulence ensures that mixing at smaller scales (mesomixing and micromixing) is comparatively fast. Again, the gas presence affects liquid mixing intensity *via* its effects on impeller power and in turn on its pumping efficiency. In particular, at low gas rates the gas is entrained in the trailing vortexes behind impeller blades, with small effects on impeller pumping efficiency, while at larger gas flow rates and impeller speeds, large gas cavities may form behind impeller blades that considerably lower both pumping efficiency and required power.

Good mass transfer performance requires large interfacial areas between gas and liquid (hence small bubble size and high gas fraction) and a high mass transfer coefficient (associated with local levels of turbulence). A high gas fraction is not always desirable however since the profitability of a reactor is largely controlled by the quantity of liquid it contains. Excessive gas retention may also lead to overreaction.

The flow behavior of both gas and liquid phases can be important. When complex reaction schemes are involved the process selectivity may be variously affected. Even for simple gas liquid mass transfer, the gas flow pattern is critical unless a very small proportion of the dissolvable gas is absorbed per pass. For example, if 95% of the inlet dissolvable gas is absorbed, its mean concentration in the gas phase (and hence its mean transfer rate to the liquid) may be up to 5.17 times larger than that for an perfectly backmixed gas phase, depending on the closeness to plug flow conditions of the gas.

Here a conflict can arise in an agitated vessel. High power input per unit mass is required to enhance mass transfer area and heat transfer coefficient, but this will result in a high degree of gas recirculation, reducing the mean gas phase concentration driving force for mass transfer. Local shear rates will also increase with power input. The balance will vary with scale.

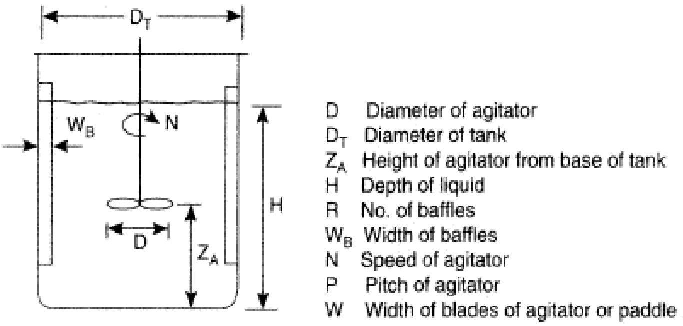

Figure 1.1: Typical stirred tank: $D_T = 3D$; $H = D_T$; $Z = D$; $W_B = D_T/10$.

A typical arrangement of the agitator and baffles in a standard stirred tank (whose geometry is shown in Fig.1.1), and the flow patterns generated, is shown in Fig.1.2. Mixing occurs through the bulk flow of the liquid and, on a microscopic scale, by the motion of the turbulent eddies created by the agitator. Bulk flow is the predominant mixing mechanism required for the blending of miscible liquids and for solids suspension. Turbulent mixing is important in operations involving mass and heat transfer; which can be considered as shear controlled processes.

The most suitable agitator for a particular application will depend on the type of mixing required, the capacity of the vessel, and the fluid properties, mainly the viscosity. The gas should be fed beneath the impeller such that the impeller will capture the rising gas plume. With radial or upward flow impellers it is sufficient to use a sparger that has a smaller diameter than the impeller itself. To provide the maximum gas contact time, the impeller should be near the base of the vessel but not so near as to inhibit its liquid pumping action. The bubble breakup mechanism relies on a high relative velocity between the blades and the liquid, so wall baffles are necessary to restrict the circumferential motion of the liquid. They also enhance the vertical motion of the liquid and hence the mixing of the liquid bulk and the recirculation of liquid and gas back to the impeller, increasing the gas hold-up. For any single impeller this

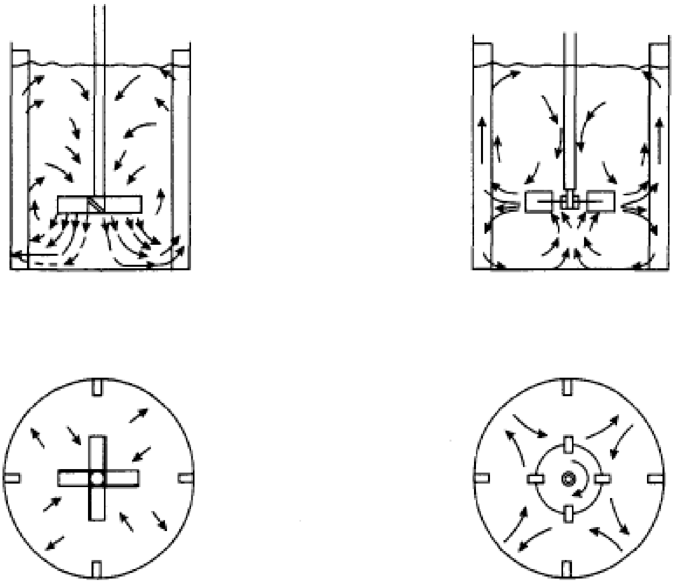

Figure 1.2: Bulk motion in buffled stirred tanks.

recirculation is favored by an aspect ratio liquid height/vessel diameter of about 1. All of these factors lead to a recommended geometry, which is illustrated in Fig.1.1.

Agitator tasks in gas-liquid systems are:

1. breaking the gas into smaller bubbles for high interfacial areas;
2. dispersing the bubbles throughout the liquid;
3. keeping the bubbles in the liquid for sufficient time;
4. mixing the liquid throughout the vessel;
5. providing turbulent eddies to feed liquid to and from the interfaces;

In general, high levels of turbulence are required for the first task, while high flow is required for all others. With turbines, high turbulence is created by the roll vortex field which forms behind impeller blades.

For all the gas to flow through this region, it must enter the vessel close to the disc, preferably underneath it. Once near the blade vortex, the centrifugal forces will draw the gas in. In general, to ensure that sufficient turbulence is created, a large power input (larger than $100\,W/m^3$) must be provided to the gas-liquid mixture by the agitator. Alternatively, criteria based on tip speed ($\pi ND > 1.5\,m/s$) or Froude number ($N^2D/g > 0.1$) are often quoted (Harnby et al., 1992). To maximize the gas handling capacity of the impeller, many blades should be used on the agitator, and they should preferably have concave shapes. For mechanical stability, an even number of blades not less than six, should be used. The nature of the gas inlet device is only of secondary importance, provided that the design is such that the gas is effectively captured and dispersed by the agitator. As an example, multiple orifice ring sparger with diameter equal to $0.75D$ is recommended for maximizing mass transfer coefficients, but it is only marginally different from the performances of the same reactor equipped with a simple open pipe placed beneath the disc.

An impeller that approximately maintains the ungassed power level when gas is introduced will give more stable operation and minimal scale-up difficulties. Recommended types (Fig.1.3) include, for radial flow, hollow blade designs such as the Scaba SRGT, Chemineer CD6 or BT6, Lightnin R130, or for axial flow, an upward pumping wide-blade hydrofoil such as the Lightnin A345 or A340 or the Prochem-Chemineer MaxfloW. Downflow hydrofoils or pitched blade turbines may be unstable during gas liquid operation. The liquid flow induced by a downpumping impeller is opposed to the natural tendency of buoyant gas to rise. With a single impeller this is evidenced in the transition between indirect and direct loading that occurs as the gas flow is increased. At certain impeller speeds there may be an accumulation of gas below the impeller plane which can become hydrodynamically unstable. These physical phenomena, which are independent of scale, have been found to lead to an unpredictable loading of the impeller and a source of mechanical problems. A single upflow hydrofoil may not be optimum in a vessel with $H = T$, if the D/T ratio is larger than say 0.5 (which may occur if high P/NV is required), since recirculation will be localized and zones of high local gas fraction will be formed.

Characterization of the flow pattern of either phase is often limited to the ideals of perfect plug flow or fully backmixed flow. In practice, it is necessary to consider degrees in between: many in-line mixers such as ejectors and static mixers in turbulent flow achieve a close approximation to plug flow for both phases, but in industrial agitated vessels a close approach to complete backmixing is rare for either phase. If gas liquid mass transfer is the process rate-controlling step, the flow behavior of the gas is important: typically, it has a large effect on the rate of mass transfer. If the limiting step is reaction in the bulk liquid phase, the liquid phase flow pattern

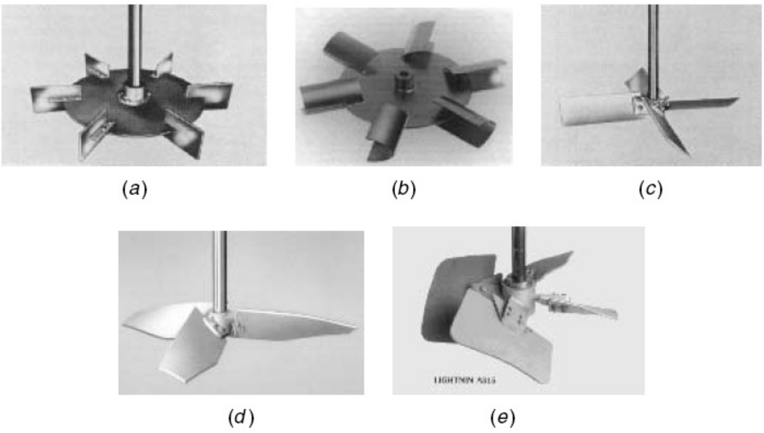

(*a*) (*b*) (*c*)

(*d*) (*e*)

Figure 1.3: Impeller design.

(residence time distribution in case of continuous flow) may be important. For batch systems a stirred vessel or loop reactor with an in-line mixer is used. Where plug flow is required, for long residence times a cascade of stirred vessels or loop reactors is commonly used, and for short residence times the choice will often be a static mixer. For continuous flow systems requiring an approach to backmixed flow, stirred vessels or loop reactors are indicated.

In the homogeneous regime in an agitated vessel, the superficial gas velocity, $v_S < 0.02 \div 0.03 m/s$, and the bubbles have a monomodal size distribution with a small mean size, generally between $0.5 \div 4mm$. Here, the impeller controls the flow pattern and bubble size. At higher gas superficial velocities, the heterogeneous regime occurs, in which the overall bubble size distribution is bimodal, with some large bubbles ($10mm$ or greater), and is controlled more by the gas velocity (possibly void fraction) than by the agitator. In this regime the influences of impeller speed and gas rate are different from those in the homogeneous regime. Gas flow pattern is important, since it controls the degree of recirculation and backmixing of the gas phase, which in turn determines the mean concentration driving force for mass transfer. It can also profoundly affect the liquid phase macrocirculation and homogenization (Paul et al., 2004).

The flow pattern of the gas depends on the regime of gas-impeller interaction. For six-blade disk-turbine impellers, three regimes of flow in the vessel can be defined, as shown in Fig.1.4:

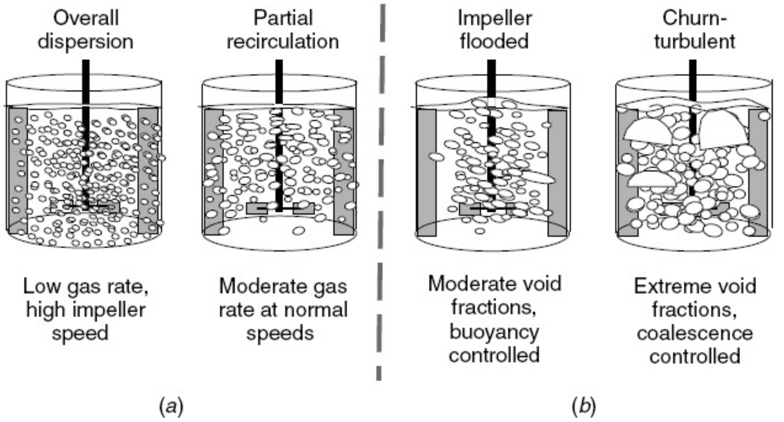

Figure 1.4: Typical void fraction distributions in vessels with a single impeller: (a) impeller controlled regimes; (b) void fraction controlled regime (Paul et al., 2004).

- Flooding in which the impeller is overwhelmed by gas and gas liquid contact; mixing, and so on, are very poor;
- Loading in which the impeller disperses the gas through the upper part of the vessel;
- Complete dispersion in which gas bubbles are distributed throughout the vessel and significant gas is recirculated back to the impeller.

These are closely related to the regimes of gas-impeller interaction: as more gas is fed to the impeller (or speed diminishes), there is more tendency for the gas to be accumulated in the low pressure regions behind the blades, forming ventilated cavities. When these are large they can cause a strong reduction of the impeller power number and hence of its performance for mixing, mass, and heat transfer. This is particularly important for flat blade turbines with four, six, or eight blades. For six-blade disk turbines the cavity regime is best obtained from the flow regime maps shown in Fig.1.5 since they are dimensionless and tested for several scales (Paul et al., 2004).

Given the complexity of phenomena occurring in gas-liquid dispersions, it is of fundamental importance the development of suitable measurement techniques able to reliably measure gas-liquid dispersion properties such as bubble size distribution, gas volume fraction and specific interfacial area. Accurate knowledge of these dispersion properties is in fact the basis for the setting up the reliable correlations needed for design as well as new process development purposes.

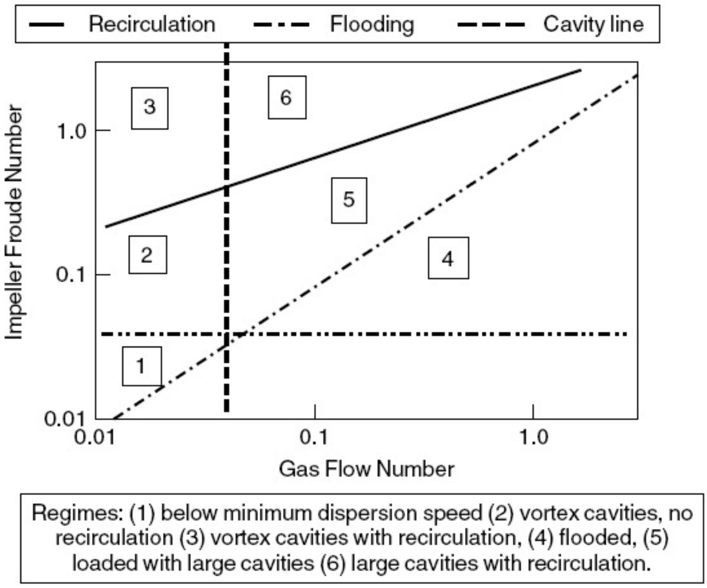

Figure 1.5: Flow map for single Rushton turbine (Paul et al., 2004).

2 Experimental assessment of gas-liquid dispersion properties

Gas-liquid contactors are widely employed as reactors and bio-reactors in the process industry. In most of these applications, gas liquid mass transfer is the main rate-determining step. Local mass transfer areas depend on bubble size and concentration, and was shown to vary notably even in small stirred tanks (Calderbank, 1958; Sridhar and Potter, 1980; Barigou and Greaves, 1992b, 1996; Laakkonen et al., 2005a). Mass transfer area is obtained most reliably from knowledge on the bubble size distribution (BSD) and gas hold-up. A comprehensive review of measuring techniques in gas liquid contactors can be found in Boyer et al. (2002).

Measurement techniques can be classified according to different ways. A first classification concerns time-averaged *versus* transient measurements as well as local *versus* global measurement (averaged either over one- two- or three-dimensional domains). Different types of non invasive techniques for the assessment of global and multiphase flow characteristics have been developed. These are based on different physical principles:

- **Conductimetry**: if the liquid in a gas-liquid or gas-liquid-solid reactor is electrically conductive and presents a constant ionic concentration, the conductivity between two points of the reactor is an increasing function of the liquid volume fraction. Unfortunately, the conductivity depends also on the spatial distribution of the phases. A number of mainly empirical relations have been proposed to correlate the dispersion properties with the conductivity in presence and in absence of gas. It is therefore advisable to calibrate this technique by means if independently measured data.

- **Radiation attenuation**: when crossing a two-phase mixture, all types of electromagnetic radiation are attenuated. Depending on the kind of radiation used, the attenuation is a function of the density along the radiation path or of the interfacial area. Gases, liquids and solids have for example quite different absorption coefficients of X-ray or γ-ray radiation or of neutron beams. By measuring the attenuation of a radiation beam between a source and a receptor on the other side of the reactor gives access to the integral average of the local mass density distribution along the beam path. There are no theoretical limits to time resolution; limits are, however, given by safety and/or price considerations. Space resolution is limited by the size of the available sensors ($10\,mm$ for γ-rays, $100\,\mu m$ for X-rays). These radiographic techniques are the basis of a number of tomographic techniques. In the case of a clean transparent liquid containing bubbles or drops, light attenuation is an increasing function of the dispersed-phase specific interfacial area. Early applications of this technique were limited to quite small interfacial areas and required that no multiple scattering of the light beam by the bubbles took place (Calderbank, 1958) and the optical density aL_O (*i.e.* the product aL_O, a being the interfacial area per unit volume and L_O the optical path length) was limited to quite small values. In any case, bubbles have to be approximately spherical and stringent measures have to be taken to avoid parasitic light sources, electronic noise, liquid turbidity, etc. Ultrasound-based measurement techniques can be also adopted, and the main advantage compared to visible radiation based techniques is that transparency of the liquid is not required.

- **Visualization techniques**: these techniques can be classified into photographic (including of course video) techniques and radiographic techniques, Particle Image Velocimetry techniques and NMR based techniques. The aspect of the flow as seen through the wall is an important feature, and taking pictures through the wall is very frequent in literature. The limitations of these technique are obvious: only the vicinity of the wall can be observed at high gassing rates, and a transparent wall and liquid are required. Quantitative image analysis can allow the assessment different bubble properties simultaneously. Using more energetic kinds of radiation (*e.g.* Flash X-ray Radiography) to observe bubble forms is an extension of the photographic technique. The advantage is that such techniques may yield results even in the presence of a non-transparent fluid; as with the photographic technique, only a single layer of bubbles can be observed reliably.

  Particle image velocimetry technique has become quite classical for the determination of velocity fields in single-phase flow. A laser sheet is used to illuminate a well defined slice of the fluid containing seeding particles; two or more pictures of the sheet are taken at short time intervals. The distances between the positions of seeding particles provides information on the instantaneous velocity field of the liquid. Different variants have been proposed: particle streak velocimetry (long exposure), particle tracking velocimetry (video recording of particle motion). In recent years, a number of authors have used PIV in gas-liquid flow to determine either the liquid velocity field or the bubble velocity and size, or both. Reviews on this subject may be found in Chaouki et al. (1997).

When trying to adopt PIV based techniques to velocity field measurement in multiphase flows, the problem arise of distinguish between the seeding particles used for flow field measurement and the dispersed phase. In order to discriminate the different phases, a number of possibilities have been proposed: using fluorescent seeding particles for the liquid and filtering the signals (Broder et al., 2000). The same technique combined with refractive index matching has been used by (Northrup et al., 1993) to determine interstitial velocity fields in a fixed bed. It is also possible to use numerical techniques to exploit images obtained with a single CDD camera as shown by Delnoij et al. (1999); the latter authors propose an original Ensemble correlation technique to extract the relevant signals from the results obtained with a CDD camera. Recently, PIV has been applied to confirm the predictions of velocity calculations in visco-elastic liquids around rising bubbles (Funfschilling and Li, 2001).

The possibility of isolating a well defined volume of the system, coupled with advanced digital image processing techniques, has the potential to allow the simultaneous measurement (in addition to flow quantities) of important dispersion properties such as local BSD, hold-up and interfacial area. Recent applications of PIV apparatuses also focused on the simultaneous measurement of gas and liquid flow-field quantities by means of back lighting and macro lenses (Sommerfeld and Broder, 2009), local BSD (Montante et al., 2007), BSD and interfacial area distributions through laser sheet and some statistical corrections (Laakkonen et al., 2005a), gas phase velocity in micro-reactors through fluorescent liquid and laser sheet (Chung et al., 2009). In many cases no well defined control volume could be assessed so that volume dependent quantities, such as specific interfacial area and gas hold-up, were only approximately assessed.

Nuclear magnetic resonance (NMR) imaging has been widely used in the field of medical imaging and is more and more frequently applied to chemical engineering problems. The theoretical background of these techniques is based on the determination voxel by voxel of the quantity of given nuclei (usually protons 1H); radio-frequency pulses and magnetic field gradient pulses interact with the spins of the nuclei positioned in a static magnetic field.

- **Laser Doppler Anemometry**: the principle and the main applications of LDA are well known and well described (Chaouki et al., 1997): if there is a relative motion between a wave source (laser) and a wave receiver (seeding particle of the liquid or bubble in the liquid), there is a shift of wave frequency; this phenomenon is called the Doppler effect; measuring this frequency shift by using interference fringes gives access to the velocity. This technique has been applied to the determination of local velocities for some time. LDA yields well-localized values of velocity; the measurements are very fast, so that velocity fluctuations can be assessed. The last years have seen the application of LDA to the determination of liquid velocities (average values and fluctuations) in bubble columns with quite high gas throughputs (Joshi, 2001). At higher gas velocities, it may happen that the smaller bubbles are not discriminated from the seeding particles. This can be overcome by using fluorescent seeding particles and by using a color filter, able to suppress the incident light wavelength, but transparent to the light emitted by fluorescence (Broder et al., 2000). Another pitfall may also be encountered: one of the basic assumptions of LDA is that the seeding particles move exactly with the liquid. However, the distribution of fine particles in the presence of bubbles may not necessarily be homogeneous in the whole of the liquid phase: over-concentrations of particles in the immediate vicinity of bubbles have been observed, therefore resulting into errors on liquid phase velocity measurements.

- **Radioactive tracking**: Liquid mixing in bubble columns was investigated by Chen et al. (1999a) using single neutrally buoyant spheres containing radionucleides emitting γ-rays. The use of radioactive emitting tracers is also the basis of the radioactive particle tracking (RPT or CARP) technique used by Chaouki et al. (1997) to investigate mixing of the solid in three-phase gas-solid-liquid dispersions. In the techniques proposed by both teams, the rays emitted by the tracer particle are followed by a number of detectors around the column. The reliable and rapid determination of the position of the particle from the signals obtained by all the detectors is a demanding task since a long and complicated calibration procedure is required, but it has been solved by both teams. The results of these techniques are trajectories of the particles. These trajectories can be used to validate CFD calculations or to determine axial dispersion coefficients of the solid; on the other hand, long-term averages of the velocity yields global circulation patterns.

- **Tomographic techniques**: the tomographic techniques have been fully developed during the last 20 years, first for medical applications and more recently for industrial process applications. These techniques are powerful since they give the opportunity of obtaining the phase fraction distribution inside a reactor or a column by a rigorously non-intrusive measurement. The general principle consists in measuring through the column a physical property that can be related to the phase fraction. Measurements are performed at different angular positions and deliver the average values of the property over the corresponding diameters. By using a reconstruction algorithm, the acquired signals are then analysed to provide the phase fraction image on a cross-section of the column. Depending on the kind of physical property used, time and space resolution may differ widely. For tomographic systems that need to have a complete rotation of sensors all around the column, the measurements are not simultaneous and the results are only time-averaged results. Different kinds of tomographic systems have been developed. Photon attenuation tomography system is based on the attenuation measurement of photon rays such as γ- or X-rays. As such attenuation is directly proportional to the material density for a given energy, the resulting image gives the density at each pixel and then the phase fraction map. The photon fluxes being very high with X-ray tube, the detector sensing area can be quite reduced and spatial resolution can be as small as $1\,mm^2$. However, such photon rays have generally a rather low energy level and their use is limited to low attenuating material or to small column diameter. With γ-rays, the photons are more penetrating since their energy can be as high as 1 MeV, the spatial resolution is rather lower (around $1\,cm^2$) but remains interesting for practical purposes.

  A lot of work has been done to develop tomographic systems based on impedance measurements at the wall of a column, a tank or pipe including multiphase flows These techniques are easy to implement with relatively low cost. Their characteristic response dynamics is very fast, and therefore they can reliably describe rapid evolutions of flows. Nevertheless, the measured signal is a non-linear function of the phase fractions and of the flow configuration: the electric capacity or resistance between two separate elements at the wall depends on the whole phase repartition in the column, not only on the phases present on a straight line between the two elements. The reconstruction calculations are not easy to perform and not yet totally satisfying; the spatial resolution remains very poor unless a priori knowledge is included in the reconstruction procedure. Nevertheless, these tomographic techniques give a good information on large inhomogeneities inside a vessel or a column and they are quite well adapted for flow configuration change detection.

2.1 Measurement of specific interfacial area

Average specific interfacial area has been investigated by means of chemical methods, such as those based on steady-state carbon dioxide absorption into sodium hydroxide solutions (Hassan and Robinson, 1980; Mandal et al., 2005; Mohanty et al., 2007), while local interfacial areas have been measured by means of light scattering probes (Calderbank, 1958), photographic techniques (Marrucci and Nicodemo, 1967; Kawecki et al., 1967), and light-sheet based imaging techniques (Laakkonen et al., 2005a).

Calderbank (1958) report the following equation for the estimation of specific interfacial area in vessels agitated by Rushton turbines:

$$a_i = 1.44 \left[\frac{(P_g/V)^{0.4} \rho_l^{0.2}}{\sigma^{0.6}} \right] \left(\frac{v_s}{u_t} \right)^{0.5} \tag{2.1}$$

where the original value adopted by the author for the bubble terminal velocity $u_t = 0.265 m/s$ should be used.

Bouaifi et al. (2001) reported the following equation as a fitting of indirect data on specific interfacial area (computed from the measurement of gas volumetric fraction and average bubble diameter as $a_i = 6\epsilon/d_{32}$) in a dual-impeller stirred vessel:

$$a_i \propto \left(\frac{P_g}{V} \right)^{0.44} v_s^{0.65} \tag{2.2}$$

Laakkonen et al. (2005a) measured local specific interfacial area values in agitated vessels by means of planar laser and image analysis and reported that local values measured correctly follow the functional dependencies of specific interfacial area on specific power input and superficial gas velocity, but strong differences exist between different regions of the vessel.

2.2 Measurement of gas volume fraction

The overall gas hold-up can be easily measured from increase of liquid level with respect to ungassed conditions by measuring the two phase pressure drop, though these methods are generally inaccurate in the case of low hold-up systems. Several methods have been used for *local* hold up measurement, such as pressure probes (Linek et al., 1996), light sheet coupled with image analysis (Laakkonen et al., 2005a), conductivity probes (Gao et al., 2001), hot-film anemometry (Lo and Ju, 1987), suction probes coupled with image analysis (Kamiwano et al., 2003), optical probes (Bouaifi et al., 2001), electrical probes (Takenaka and Takahashi, 1996; Bombac et al., 1997; Bombac and Zun, 2000; Paglianti, 2001), optical holography (Ilchenko et al., 2002), and several types of tomography, ranging from electrical to gamma ray (Williams et al., 1993; Wang et al., 2000; McKee et al., 1995; Toye et al., 2005; Ford et al., 2008; Boden et al., 2008; Chen et al., 1999b; Khopkar et al., 2005; Hampel et al., 2007). Suction probes can also be adopted Alves et al. (2002a) by sampling gas-liquid dispersion through a glass tube meter using a peristaltic pump: both phases are separated and the volume of each one is measured, though results are bound to be effected by uncertainities on the sampling efficiency of the two phases.

The general findings report a dependence of gas volume fraction on the specific power input and gas superficial velocity:

$$\epsilon \propto \left(\frac{P_g}{V}\right)^a v_s^b \tag{2.3}$$

with both exponents ranging from 0.2 to 0.7. Notably, a tendency is reported for the specific power input exponent to be larger for non-coalescing systems than for coalescing systems

Bouaifi and Roustan (1998) report values of $a = 0.24$ and $b = 0.65$ for multiple impeller systems. It is also observed that the overall gas volume fraction mainly depends on the choice of the lower impeller: this is well expected since gas hold up strongly depends on bubble size, which in turn depends on impeller type where all other conditions were fixed.

Calderbank (1958) developed the following equation to correlate data obtained in sparged stirred vessel by means of scattered light probes:

$$\epsilon = \left(\frac{v_s \epsilon}{u_t}\right)^{0.5} + 0.000216\left[\frac{(P_g/V)^{0.4}\rho_l^{0.2}}{\sigma^{0.6}}\right]\left(\frac{v_s}{u_t}\right)^{0.5} \tag{2.4}$$

where u_t is the bubble terminal velocity, which is set to $0.265 m/s$. Although the bubble rise velocities actually depend on bubble size, the original value suggested by Calderbank (1958) should be used, because this value was originally used for data fitting. Notably, in the absence of agitation, the proposed equation reduces to $\epsilon = v_s/u_t$.

In the work by Bombac et al. (1997); Bombac and Zun (2000), a micro-resistivity probe is used for phase detection in a stirred vessel agitated by a single Rushton turbine (Bombac et al., 1997) or dual-impeller turbine (Bombac and Zun, 2000). Frequency-domain analysis of the data obtained near the impeller allow the characterization of the fluid-dynamic regimes at the impeller from the vortex-clinging (VC) regime the different possible large cavities regimes (depending on the number and size of large cavities formed below the blades of a 6 blade Rushton turbine). The same authors developed a flow-map for the prediction of the fluid-dynamic regime an for some cases take accurately measurement of the gas volume fraction map, also putting in evidence the main characteristics of local hold up distribution as a function of the relevant regime, showing for example that the transition from vortex-clinging regime to S33 regime (in which 3 large cavities are formed and 3 vortex-clinging) and to L33 (three large cavities and 3 smaller cavities) results in a considerable decrease of the turbine pumping efficiency and therefore in a sudden decrease of the entrained gas in the recirculation loops, especially below the impeller.

2.3 Measurement of Bubble size distribution

Many small bubbles are required in a dispersion to give large gas-liquid interfacial area and therefore effective mass transfer. Moreover, small bubbles are more readily entrained in the recirculating liquid inside the vessel, so giving more gas backmixing than larger bubbles under similar hydrodynamic conditions.

Local BSD was largely investigated by means of Capillary Suction Probe techniques (Greaves and Kobbacy, 1984; Barigou and Greaves, 1992a,b; Alves et al., 2002b; Laakkonen et al., 2005b,c). This intrusive technique involves withdrawing, by means of a vacuum system, a continuous stream of gas-liquid dispersion through a short length calibrated capillary. Gas bubbles are transformed into elongated slugs inside the capillary, which are then detected by a pair of LED photo-transistors. The bubble diameter detection limit is determined by capillary diameter.

Optical imaging techniques (Calderbank, 1958; Aslan et al., 2006) or photographic techniques were also adopted in different cases (Takahashi et al., 1992; Takahashi and Nienow, 1993; Machon et al., 1997; Bouaifi and Roustan, 1998; Hebrard et al., 2001;

Mandal et al., 2005; Winterton and Munaweera, 2001; Horn et al., 2007; Montante et al., 2008).

Montante et al. (2008) used an LED background light source in a shadow imaging technique to determine bubble size in a bubble column and in a stirred vessel. Sommerfeld and Broder (2009) also applied a similar technique to study the hydrodynamics in the bubbly flow within a rectangular bubble column. They determined bubble size, shape and orientation within the focal plane, as well as the gas phase velocities using an in-house developed code. An array of 551 high performance LEDs provided background diffused illumination to project bubbles situated between the light source and camera as dark circles on the captured image. Planar measurements were achieved by adjusting the depth of the focal plane; for example, in-plane bubbles were recognized by their relatively thin edges whereas the contours of out-of-plane bubbles appeared smudged. However, even with a macro camera lens setup to provide a small depth of view, the thickness of the focal plane was only resolved down to 4 mm.

Measurements of bubble sizes in a closed stirred vessel with and without added solid particles by means of image analysis techniques was performed by Hu et al. (2005). A stereo microscope was linked to a digital camera with shutter frequency synchronized to a high-energy fiber optic strobe lightby which it is possible to produce sharp images of air bubbles. The bubble diameters were measured using image analysis.

Essadki et al. (1997) proposed an electrochemical probe as a way for measuring bubble sizes. The apparent local mass transfer coefficient on a spherical surface was measured in a bubble column with homogeneous bubbling regimes (bubbles of approximately equal size and uniformly distributed across the column). Thus, the characteristic average frequency of the fluctuations of the diffusion-limited current detected by the probe was postulated as being equal to the bubble frequency and led to a determination of an average bubble size in a homogeneous bubbling flow.

Comparison of different techniques for local bubble size measurement can be found in Hernandez-Aguilar et al. (2004) and Laakkonen et al. (2005c).

It was firstly show by Calderbank (1958) that the bubble size strongly depends on the measurement position. Bubble sizes near vessel wall at the same level as the impeller or above it were found to be more than four times larger than those in the impeller region. Calderbank (1958) obtained the following equation for the mean surface/volume diameter from measurement of interfacial area and gas volume fraction in pure liquids (*i.e.* coalescing systems):

$$d_{32} = 4.15 \left[\frac{\sigma^{0.6}}{(P_g/V)^{0.4} \rho_l^{0.2}} \right] \epsilon^{0.5} \left(\frac{\mu_g}{\mu} \right)^{0.25} + 0.0009 \tag{2.5}$$

However, it was found that small concentrations of electrolytes, surfactants, alcohols, oils (among others), in agitated vessels or bubble columns have a profound effect on the average bubble size and gas volume fraction (and therefore on specific interfacial area), changing the empirical constant of Eqn.2.5, with effects clearly different on agitation speed and inlet gas velocity. In general, in non-coalescing systems the average bubble diameter is found to be considerably lower. This effect is caused by solute concentration or temperature gradients near the gas-liquid interface, setting up local surface tension gradients that oppose the drainage and stretching of the liquid film between approaching bubbles and hence hinder coalescence (Lee and Meyrick, 1970). An equation is proposed by the same authors for average diameter correlation:

$$d_{32} = 4.25 \left[\frac{\sigma^{0.6}}{(P_g/V)^{0.4} \rho_l^{0.2}} \right] \epsilon^{0.5} \tag{2.6}$$

Notably, the dependence of $\sigma^{-0.6}$ can be theoretically obtained from the application of Kolmogoroff's theory of locally homogeneous isotropic turbulence. This model assumes that maximum stable drops/bubbles size is controlled by breakage only and exists when the disruptive stresses resulting from the turbulent flow of the continuous phase are equal to cohesive stresses resulting from the interfacial tension. Similar finding on the influence of electrolytes on dispersion properties in bubble columns were found by Marrucci and Nicodemo (1967). Bubble size reduction was found to occur even in weak solutions of electrolytes, which practically have the same interfacial tension as pure water, with bubbles much smaller and much higher hold-up than in pure water. To explain this anomaly, it has been postulated that the bubble size (and in turn hold-up) in gas/liquid dispersions may be controlled by coalescence phenomena instead of breakage, this latter being relatively unimportant. Conversely, Machon et al. (1997) report a systematic decrease of bubble size while increasing height above the vessel base in several coalescing and non-coalescing systems. This behavior was justified by the authors by assuming that whilst the turbulence level away from the impeller is relatively low, it could be still sufficient to disrupt the largest bubbles and therefore decrease average bubble diameter. The authors support their reasons reporting that the many hundreds of video frames inspected never revealed a coalescence event in any of them.

It was confirmed by Barigou and Greaves (1992b) that bubble size distribution varied widely from one region of the reactor to another, deviating considerably from a normal distribution. In the impeller region at low gas flow rate increasing the impeller speed caused a sharp drop of mean bubble size while, no effect was observed for high gas flow rates, owing to the increased role of bubble coalescence. The results obtained by Bouaifi et al. (2001) with photographic technique show that for dual-impeller systems the average Sauter diameter is affected by the power consumption but not by gas flow rate. The Sauter diameter decreases when the power consumption increases. This is the consequence of the simultaneous increase in shear characteristics and turbulence. For the various configurations and gas flow rates studied, the following relationship was proposed by the authors for predicting bubble Sauter diameter:

$$d_{32} = 10.1 \cdot 10^{-3} \left(\frac{P_g}{V} \right)^{-0.2} \tag{2.7}$$

Parthasarathy and Ahmed (1994) analyzed theoretically the evolution of bubble size distribution shape (typically a bimodal shape, made up of two log-normal distributions) while varying impeller speed. Alves et al. (2002a) report that the general trend in a multiple impeller systems is for bubble size to increase along the circulation path, which indicates that bubble coalescence prevails over breakage. Coalescence is usually observed by the same authors to be most intense in the turbine discharge stream, which may be explained by a larger collision frequency due to higher turbulence. The authors confirmed in their work previous findings on the dependence of average Sauter diameter on (P_g/V) by Barigou and Greaves (1992b)

The results obtained by Hu et al. (2005, 2006b) for a wide range of liquid phase characteristics (*i.e.* liquid viscosity and surface tension) in a closed stirred vessel in which the gas is entirely recirculated pointed out that for given fluid dynamic regime (transitional or turbulent) the We number $(\rho_l N^2 D^3/\sigma)$ can be reliably adopted for data correlation, though with an exponent quite different from the value of -0.6 predicted by applying Kolmogoroff's theory of locally homogeneous isotropic turbulence. Notably the results obtained are very different from those obtained with aqueous solutions of electrolytes and alcohols where We does not bring results for different surface tension fluids together (Machon et al., 1997).

Even if a number of works dealt with the measurement of the overall or local average bubble size in stirred vessels, few works are available in literature dealing with the complete bubble size distribution. The most extensive work was done by Barigou and Greaves (1992b), who measured local BSDs from dense dispersions in a $1m$ diameter Rushton turbine agitated vessel and observed a significant spatial spread of BSDs with the measurement position and agitation conditions. They also observed the expected decrease of Sauter mean bubble diameter with the increasing stirring speed only in the impeller discharge flow. It appears that due to higher gas hold-up the coalescence had an important role in controlling bubble size in regions far away from the impeller. Alves et al. (2002b) compared previous studies and concluded that stirred vessels can be divided roughly into impeller and bulk regions in terms of bubble size. They reported that coalescence was mostly completed as the flow of dispersion from the Rushton turbine reaches the wall, although some coalescence may still occur in the upward or downward flow near the wall.

Laakkonen et al. (2005b) analyzed local bubble size distributions in different agitated vessels and different gas-liquid systems with capillary suction probe (CSP) technique. For the air-water system, bubble size varied more with the Rushton turbine than with the flat-blade turbine (FBT) agitated vessel because of differences in flow fields. The addition of a small amount of $NaCl$ caused a sharp decrease of bubble size in the vicinity of liquid surface. In the impeller discharge flow, bubble size decreased less. The lower coalescence rates due to higher apparent viscosity likely explain the smaller bubbles in the air-aqueous starch system than in the air-water system. In the $CO_2 - n - butanol$ system, bubbles were notably smaller compared to other systems and bubble size decreased unexpectedly in the flow from the impeller discharge to the liquid surface. Local BSD were found in general positively skewed in air-water systems. The effect of stirring speed found by the authors is complicated: at low stirring speed, bubbles are found to be smaller in the central region of the vessel than close to the wall, while at higher stirring speed, the opposite is observed above the impeller. Below the impeller, dispersion becomes more homogeneous when stirring speed is increased. Bubble size decreases while increasing stirring speed in the impeller discharge flow, close to the wall and near the liquid surface. On the contrary, in the central region above the impeller and below the impeller, bubble size increases while increasing stirring speed. The better recirculation of bubbles and surface entrainment of gas are probable explanations according to the authors.

Laakkonen et al. (2005a) used a self developed image analysis technique based on laser sheet illumination of the gas liquid stirred tank to investigate local bubble size distributions in several gas-liquid systems. The overall Sauter mean diameter measured was in good agreement with the Calderbank (1958) correlation. Local BSD measured were all positively skewed.

Montante et al. (2008) simultaneously measured bubble size distributions and liquid-phase flow field in an agitated vessel. They found that about 50% of the measured bubbles are characterised by an equivalent diameter lower than $0.8mm$ and 90% of them are smaller than $2mm$. Similar results were obtained in the vessel upper part. A slight increase in the gas flow rate corresponds to a moderate increase in bubble size, that is reasonably due to coalescence. The bubble size is slightly decreased for higher rotational speed, as one would expect due to increased stress in the impeller region.

Each procedure is affected by drawbacks. It is well known that the adoption of the chemical method for interfacial area measurement affects system coalescence behavior and in turn dispersion properties. The use of probes has several disadvantages, *i.e.* the flow field is bound to be more or less affected by the probe presence and long experimental campaigns are needed to obtain data distribution over the entire system. If a stream of dispersion is continuously drawn from the vessel (Parthasarathy and Ahmed, 1994), care must be taken in order to avoid changing dispersion properties such as bubble size distribution or interfacial area, for example because of coalescence phenomena in the measurement circuit. Also sampling effects undermine the accuracy of results. Classical photographic techniques are generally unable to isolate a well defined volume of the system, even when advanced image analysis coupled with macro-lenses are adopted. The same problem is encountered when suction probes are adopted. Tomographic techniques are in general quite expensive and are often affected by poor spatial resolution.

It may be concluded that there still is a need for setting up novel measuring techniques, possibly able to overcome some of the above highlighted drawbacks. Part of the present thesis was actually devoted to this purpose, as described in the following chapters.

3 Novel imaging technique for gas-liquid stirred tanks

In this chapter, a novel experimental technique coupled with a self developed Digital Images Analysis Technique is presented and discussed. The experimental technique is based on the use of a fluorescent dye dissolved in the liquid phase, that allows to identify in plane bubbles by means of a novel set of imaging techniques. These techniques is able to provide with high reliability physical data on bubble cut by laser sheets.

This novel technique, hereafter referred-to as *Laser-Induced Fluorescence with Shadow Analysis for Bubble Sizing* (*LIF-SABS*), allows a clear identification of the bubble surface *immersed* within the laser sheet. This technique ties to overcome some of the limitation of other measurement techniques, being totally non-intrusive. Moreover, the use of images allows the simultaneous measurement of several dispersion properties in a wide region of the vessel, thus resulting in very simple experiments.

Nevertheless, some care must be adopted in data interpretation: in fact, only the larger intercept is in practice measured by image analysis. The technique is somewhat similar to that proposed by (Chung et al., 2009), but a quite different out-of-plane bubbles discarding algorithm is proposed. The ability of unambiguously identify and size in-plane bubbles gives *LIF-SABS* the potential for reliable measurements of local interfacial area, gas hold-up and BSD. Clearly, the intercept sizes are in general different from each other, so that a visible intercept size distribution, $VISD(l)$, can be experimentally assessed. This distribution is related to the actual bubble size distribution $BSD(r)$ but clearly does not coincide with it, as the laser sheet intercepts bubbles over non diametrical planes at random distances from bubble center. It may be expected that the $VISD(l)$ is bound to be skewed to smaller sizes with respect to the actual $BSD(r)$ to some extent. The way to tackle the problem of correct measurement of dispersion properties from planar intercept data will be widely discussed in the following chapters.

3.1 Experimental set-up

The experimental system here investigated was a fully baffled cylindrical vessel (diameter $T = 0.19m$) with a flat base, stirred by a standard six-blade Rushton turbine (diameter $D = T/3$) placed at $T/3$ from the vessel bottom. The liquid phase was deionized water at $25°C$ and the gas phase (air) was supplied through a $6mm_{ID}$ open ended pipe, placed $5mm$ under the turbine. In the liquid phase $0.48kg/m^3$ of a fluorescent dye (Rhodamine-B) were dissolved.

The cylindrical vessel was immersed in a water filled rectangular vessel in order to minimize optical distortions due to the vessel geometry. The rectangular vessel front wall was accurately placed perpendicularly to the camera.

The bubble measurements were conducted using directly the laser light re-emitted by the bubbles and the liquid phase. For the measurements, a PIV apparatus was conveniently employed. It consisted of a $Nd - YAG$ pulsed laser source ($50mW$ per pulse, New Wave Research *Solo III*, wavelength equal to $532nm$), coupled with a 1280×1024 pixel digital camera (Dantec 80C60 HiSense) and the control- synchronization unit Dantec FlowMap 1500. A band-pass filter centered on the wavelength of fluoresced light ($570nm$) was placed in front of the camera in order to allow only this light to reach the CCD. The laser plane was focused in order to obtain a thin light sheet inside the vessel, with thickness equal to $0.5mm$.

Preliminary tests were conducted in order to assess the optimal rhodamine concentration: in fact, higher concentrations give rise to excessive attenuation phenomena involving the laser sheet, and therefore higher non-uniformities in the tank illumination level. Lower concentrations give rise to poor illumination of the vessel.

In Fig.3.1, a schematic representation of the experimental set-up is shown. In the same figure, also the five regions of the vessel on which statistical data will be calculated are shown.

Several operative condition (reported in Table3.1) were investigated.

$Q\ (l/min)$	$N\ (rpm)$
0.3	300
0.3	400
0.4	300
0.4	400
0.5	300
0.5	400

Table 3.1: Experimental cases investigated for the analysis of gas-liquid stirred tank properties

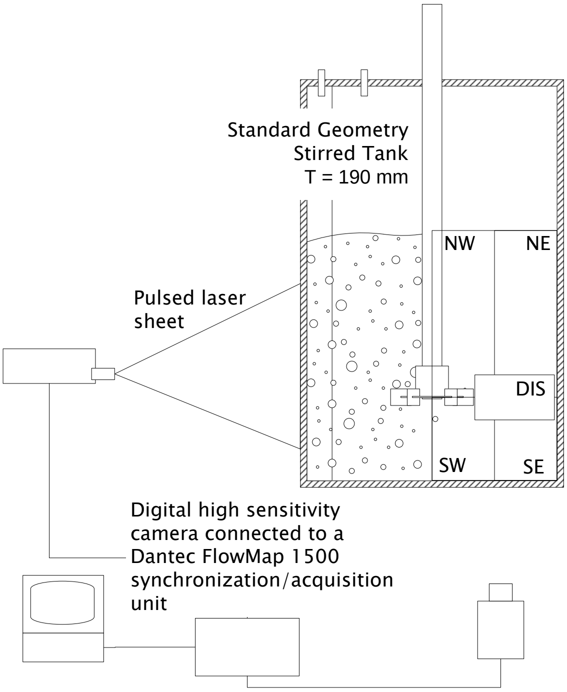

Figure 3.1: Gas-Liquid experimental Set-up.

3.2 Image Analysis Technique

A typical image of the vessel obtained by the above described apparatus is shown in Fig.3.2, where the right border coincides with the vessel axis and the impeller region is digitally shielded in order to avoid spurious results in the subsequent image analysis. The laser sheet entered from the left side of the image and traveled toward the right side on a vertical plane at $45°$ between subsequent baffles. All the light observable in Fig.3.2 is that re-emitted by the fluorescent dye, that practically turns the laser sheet into a planar (fluoresced) light source.

In this image gas bubbles can be clearly observed. As it can be seen there are *dark bordered* bubbles, clearly placed beyond the light sheet, and *white bordered* bubbles. These may be either in front of the light plane or right on the light plane. These last are however easily identified as they are the only ones that give rise to a neat straight *shadow* in the image, caused by the fact that the laser light intercepted is diverted in many directions and fails to excite the dye on the light path rear the bubble. It may be worth noting that the vertical dark and white lines in Fig.3.2 is are baffle borders.

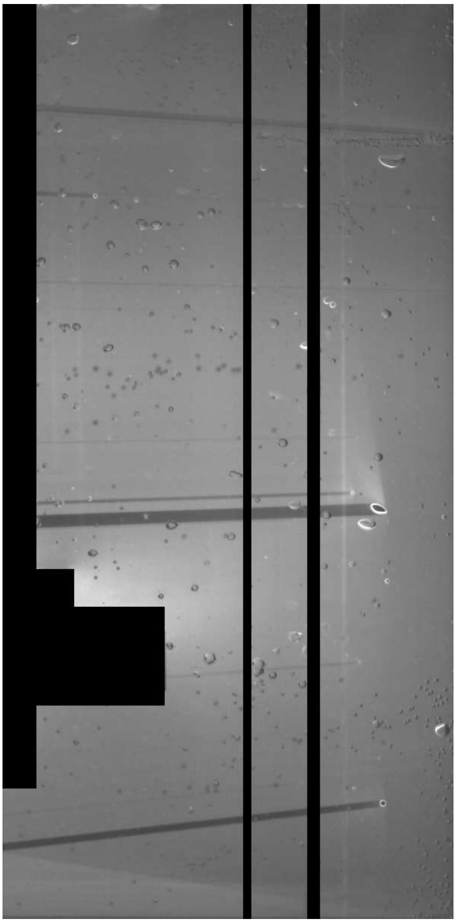

Figure 3.2: Raw Image.

The use of the experimental technique described in relevant section allows the visualization of:

- white bordered bubbles: they can be either in-plane bubbles or bubbles located rear the light plane

- dark bordered bubbles. These are out of plane bubbles, located in front of the light plane.

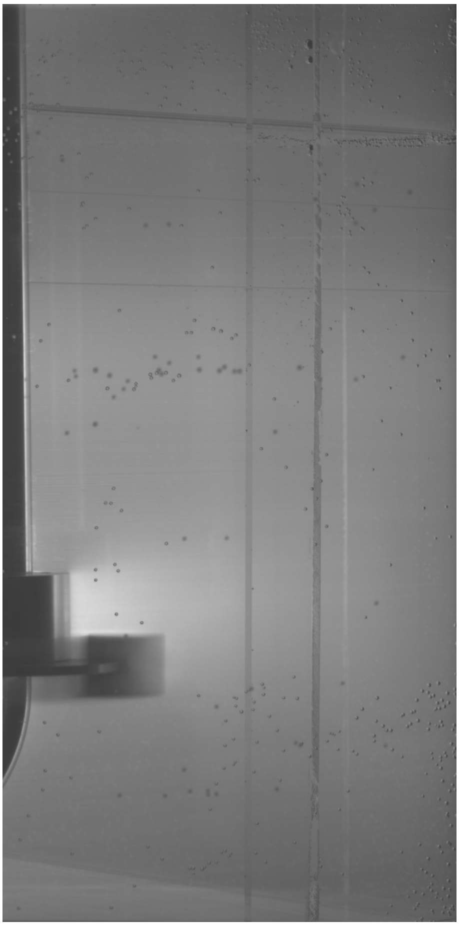

Figure 3.3: Background Image.

The main task of the imaging technique is the isolation of the in-plane bubbles, *i.e.* the white bordered bubbles associated with the straight shadows due to the lack of direct laser illumination of the fluorescent liquid phase rear the bubble. The first processing step adopted in this work was background subtraction from the original image. It is worth noting that the average background luminance in the presence of gas bubbles was found to be quite different from that obtained in absence of gas, and lead to rather noisy images if adopted. Better results were obtained using time-averaged images of the gassed system as the background image. In this way, given the quite low gas flow rates investigated and correspondingly low gas hold-up, the noise introduced in the background image is of the order of 1% of the image signal. A typical backgroung image is shown in Fig.3.3.

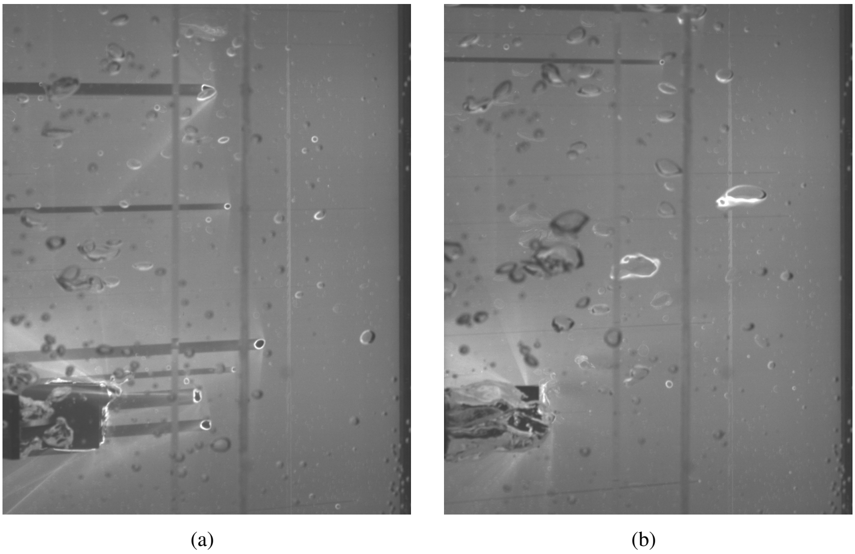
(a) (b)

Figure 3.4: Closeups of bubbles in gas-liquid dispersion

In order to unequivocally identify in-plane bubbles (those white-bordered and associated with the straight shadows) and discard all other bubbles from subsequent analysis (*i.e.* the assessment of dispersion properties as gas hold-up and bubble size distribution sharply pertaining to the investigated plane) some image processing aimed at enhancing white borders and bubble *shadows* was found to be advisable.

In particular once a background image had been obtained it was subtracted pixel by pixel from the raw image. The resulting image is different depending on how the pixels with a resulting negative luminance are treated: they may be set to zero (hereafter referred to as *simple difference*) or their absolute value may be considered (*absolute difference*). Notably:

- shadows have generally a luminance value smaller than the background image and the *absolute* difference, by exalting the darkest pixels, will make shadows very evident, as it can be seen in Fig.3.5(a). This last is therefore best suited for shadows identification;

- bubble white borders have a luminance value greater than the background image hence the simple difference between the raw image and the background will put them in evidence (Fig.3.5(b)). Simple difference images are therefore suited to exactly identify bubble size and position, once their in-plane position has been ascertained by the previous shadows elaboration.

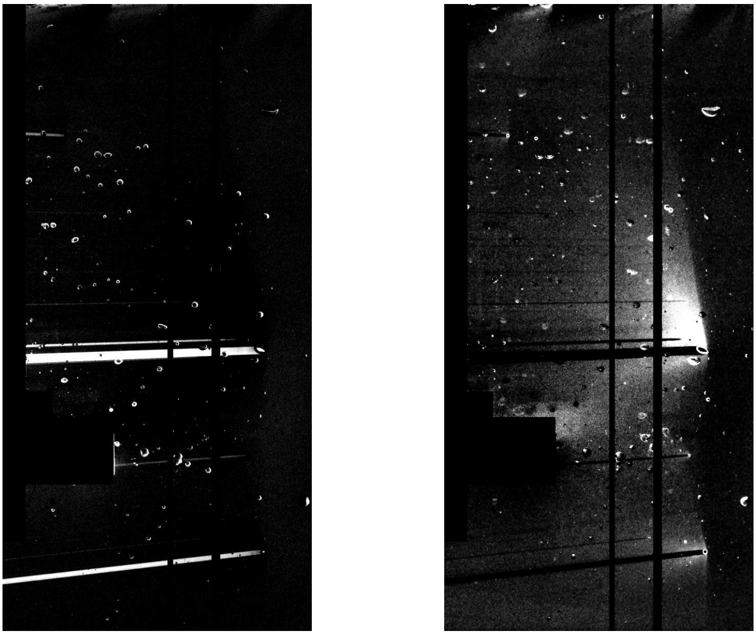

(a) Shadow difference.

(b) Bubble difference

Figure 3.5: Background elimination.

Though not strictly needed, after trial and error attempts, improvement in bubble automatic identification was obtained by further image processing. In particular images like Figs.3.5a-b underwent 2-dimensional Wiener filtering (a pixelwise adaptive method based on statistics estimated from a local neighborhood of each pixel, particularly suitable for noise reduction without edge blurring effects). After this transformation, different image processing routes were followed.

The first evidence from Fig.3.5(b) is that in some cases the laser light scattered by bubbles gives straight lines whose intensity is similar to that of bubbles. In this case, it would be impossible to correctly distinguish bubble border from scattered light. This phenomenon is more evident the thinner the laser plane used for the image acquisition. This is because the thicker the light plane, the more intense is the emitted light by the fluorescent dye inside the plane with respect to that emitted by out-of-plane dye excited by scattered light. Unfortunately, for best data analysis, a thin laser plane is preferable (for some aspects). On this basis, some image processing is needed to better recognize bubble borders and damp-out the scattered light effect.

To overcome this problem, two different anisotropic top hat transforms of the original image were performed with rectangular ($20x2$ and $2x20$ pixel) structuring element. This kind of transformation was shown to be suitable for enhancing out-of-background objects, under the case of respectively horizontal and vertical noise structure (*i.e.* respectively horizontal and vertical straight lines in original image). The result of this transformation is reported in Fig.3.6. The square root of the pixelwise product between these two images (hereafter referred to as Anisotropically Transformed Image, ATI), reported in Fig.3.7(b) can be adopted as the final Enhanced Bubble Image (hereafter EBI). It is possible to observe that white bordered bubbles are more clearly distinguished from scattered light.

On the other hand, the Enhanced Shadow Image (hereafter ESI) underwent a morphological transform by which most of the round objects (*i.e.* dark bordered bubbles in the raw image) were deleted, in order to isolate the long straight shadows. This was achieved through the creation of suitably binarized versions of both ESI and EBI; the threshold value was chosen in such a way as to highlight the bubbles still present in both images (in particular white bordered bubbles visible in EBI and black bordered bubbles that are evident in ESI). EBI underwent binarization and subsequent object filling. The same processing was done on ESI, but two further steps were performed (binary image dilation followed by erosion). The merging of these two binary images, and the elimination of high aspect ratio objects (*i.e.* the binarized shadows clearly visible in the binarized ESI) resulted in a suitable mask that was applied to the filtered ESI to retain only shadows, aresulting in the image shown in Fig.3.7(a).

To better appreciate the results so obtained, in Figs.3.8-3.9, the transformation from original to final binarized version of ATI is shown. As it can be clearly observed, any artefact linked to light scattering has practically disappeared.

In Fig.3.10, the summary of the entire image processing route set-up for ESI and EBI is reported.

For shadows automatic recognition in Fig.3.7(a) no standard algorithms for straight lines (for instance based on image Fourier transforms or Hough transforms) could

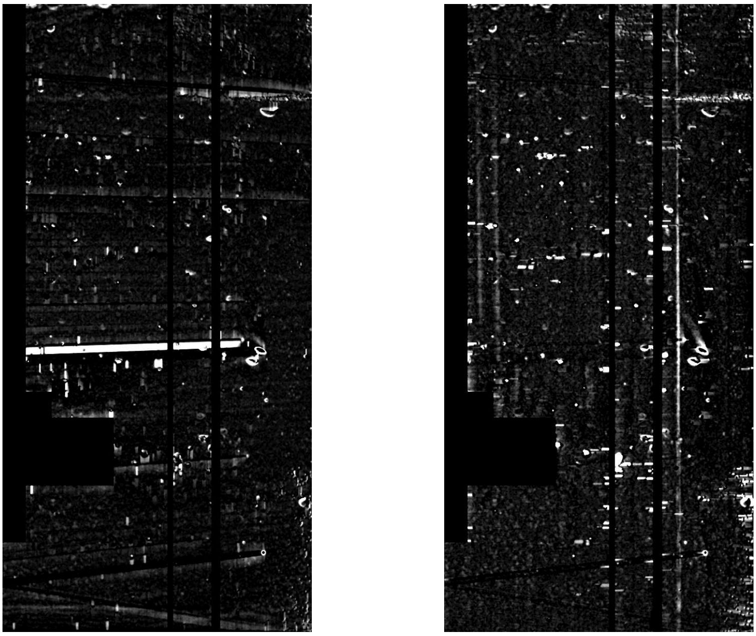

(a) Vertically filtered image. (b) Horizontally filtered image.

Figure 3.6: Components of Anisotropically transformed image.

be employed, because of: i) the diffuse border of the shadows, ii) the non-uniform intensity of the shadows and iii) the fact that the shadows are not exactly parallel to each other. However, as the laser behaves as a pointwise source, bubble shadows concur to the same point, covering a certain angle range with respect to the horizontal direction. Hence the shadow recognition algorithm employed was based on the only invariant property of the shadows themselves, *i.e.* the common passage through the laser emission point.

In particular, since the emission point and the range of angles (with respect to the horizontal plane) included in the image are known, it is possible to isolate only the pixel sequences lying on each possible laser ray. Each of these pixel sequences behaves differently whether it includes a shadow or not. Namely, the average value of pixel luminance will be larger when a bright shadow is involved, while a smaller mean value will be observed in the other case. Moreover, some care must be taken to recog-

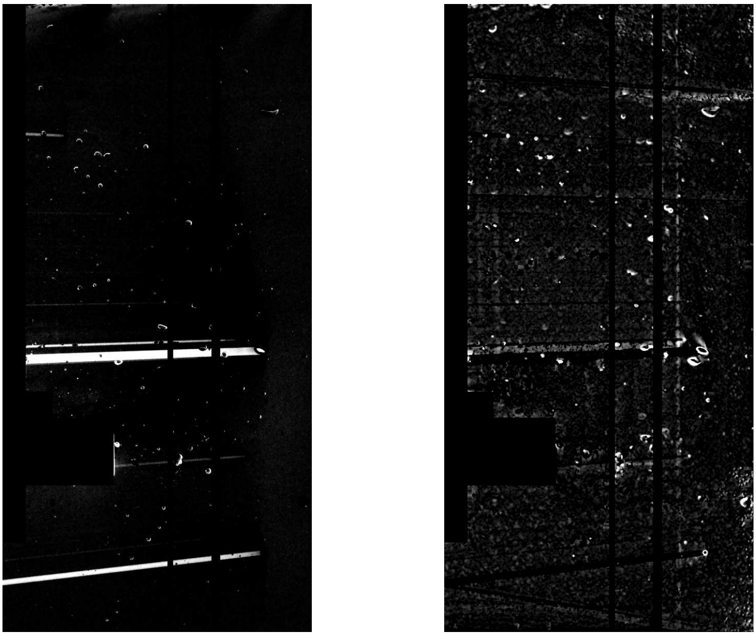

(a) Enhanced Shadows. (b) Enhanced bubbles

Figure 3.7: Final results of image processing.

nize long (projected by near wall bubbles) and short shadows (projected by near center bubbles), and in preparing sufficiently robust algorithms to avoid influence of image noise on shadow recognition.

In this work, a suitable vertical coordinate is used instead of the relevant angle: in particular, each laser ray is computed by finding all pixel lying on the same line that contains the coordinate of the center (in pixel units) and each of the pixel of the right border of the image. By finding the pixels luminance along the line (j coordinate), it is possible to characterize the different behavior in the case of presence or absence of the shadow. In particular, In Fig.3.11 the pixel luminance values of final ESI are reported in the case of a shadow along the line (Fig.3.11(a)) and in another case (Fig.3.11(b)). It is possible to observe the noisy signal. To equally consider both long and short shadows, a suitable integral function of luminance along $i-th$ laser ray is computed, defined as:

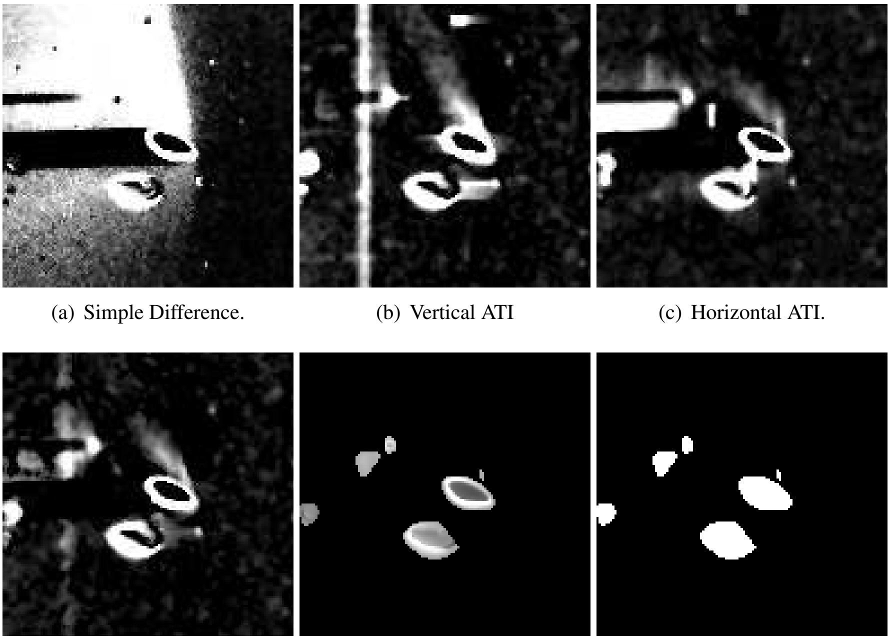

(a) Simple Difference. (b) Vertical ATI (c) Horizontal ATI.

(d) ATI (e) Isolated ATI. (f) Binarized image

Figure 3.8: Background elimination.

$$\zeta_i(j) = \sum_{k=j}^{N_{pi}} \frac{lum_i(k)}{N_{pi} - k} \tag{3.1}$$

where j is the pixel coordinate along the $i-th$ laser ray and N_{pi} is the total number of pixel along the $i-th$ laser ray.

With such definition, the closer is taken j to the entrance of the laser ray, the less weight is assigned to the point; at the same time, noise is damped out because of the cumulative sum, end-of-ray pixels (whose luminance is surely higher on average if a shadow is included) have the maximum weight. In Fig.3.11, the relevant ζ_i functions are plotted in the cases of encountered and not encountered shadow.

A simple local maxima and minima searcher was used in this work (a point is considered a peak if it is larger than its two neighbors) for first identification of all peaks in the output function when reported as a function of the ray index. This allows the simultaneous identification of both effective and noise peaks. To discard the latter, a peak-area based threshold algorithm was developed. For each local maxima, the adja-

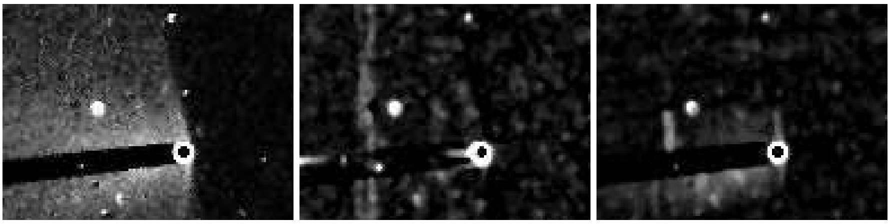

(a) Simple Difference. (b) Vertical ATI (c) Horizontal ATI.

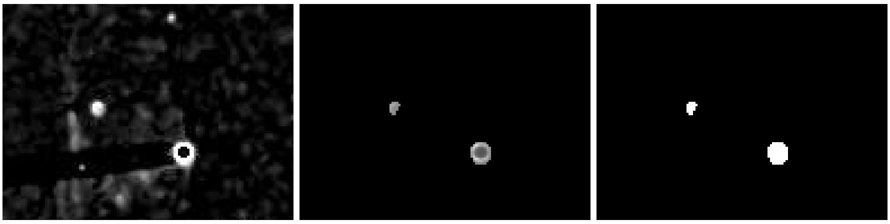

(d) ATI (e) Isolated ATI. (f) Binarized image

Figure 3.9: Background elimination.

cent local minima were found. This defines a single peak. Its net area (total area of the peak minus the area subtended to the baseline) can therefore be computed. Notably, noise peaks are generally larger in number than actual peaks, and have an area quite smaller. On this basis, it was found mean peak area is quite effective as a threshold value for peak identification. The peaks whose height is larger than the above presented threshold value were considered as *actual* peaks. Despite of the easiness of the peak recognition algorithm, all peaks have been correctly considered, even if some doubt exist for few peaks, as can be clearly seen in Fig.3.12. Therefore, the peaks whose area is more than 3 times the average peak area were considered as *confirmed* peaks, while all other *actual* peaks were considered as *unconfirmed* peaks.

The peaks, *i.e.* shadows (and in turn in-plane bubbles) could therefore be automatically recognized along the selected laser ray. The identification algorithm is based on some simple evidences: i) along each selected ray a neat change of luminance must be found where the in-plane bubble is encountered; ii) a bubble must be present where the change in luminance is found. By combining this information, in-plane bubbles could be correctly identified in most of the cases, as reported in Fig.3.13, where in-plane bubbles are identified. Clearly, the technique can further be improved by means of more advanced image analysis technique for noise suppression or more efficient algorithms for peak isolation in the average ζ function or for in plane bubbles identi-

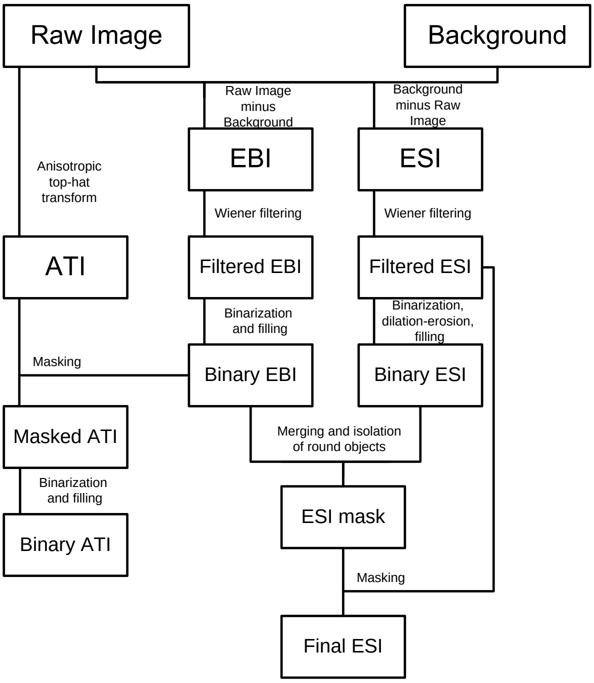

Figure 3.10: Summary of image processing procedure.

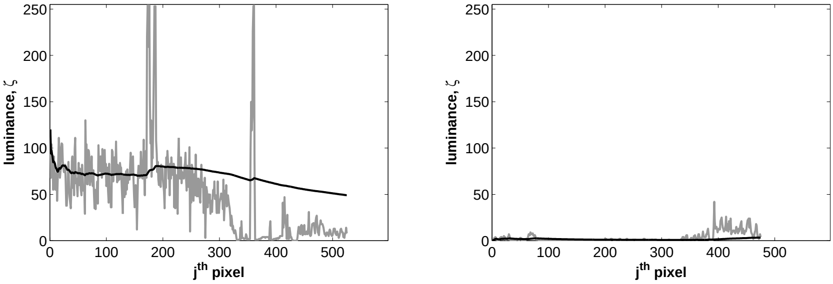

(a) Shadow on-ray luminance.

(b) Non-shadow on-ray luminance

Figure 3.11: Shadow recognition.

fication.

Remarkably, the final output of the technique here proposed is a binarized phase matrix $\Phi(x, y)$, in which pixels belonging to in-plane gas phase are set to one and all

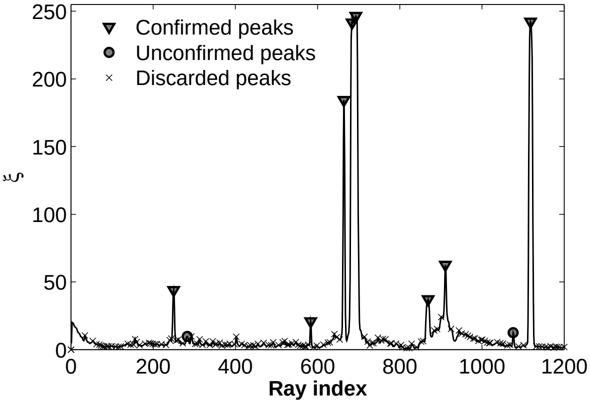

Figure 3.12: Peak detection.

other pixels are set to zero. For each bubble present in the image, its area, equivalent diameter and centroid coordinates can be computed and stored. As it will be clearer in the following, this kind of information can be used for the assessment of typical gas-liquid dispersion properties such as local bubble size distribution, local specific interfacial area and local gas hold up, provided that some data elaboration is performed to transform planar data into relevant volumetric data.

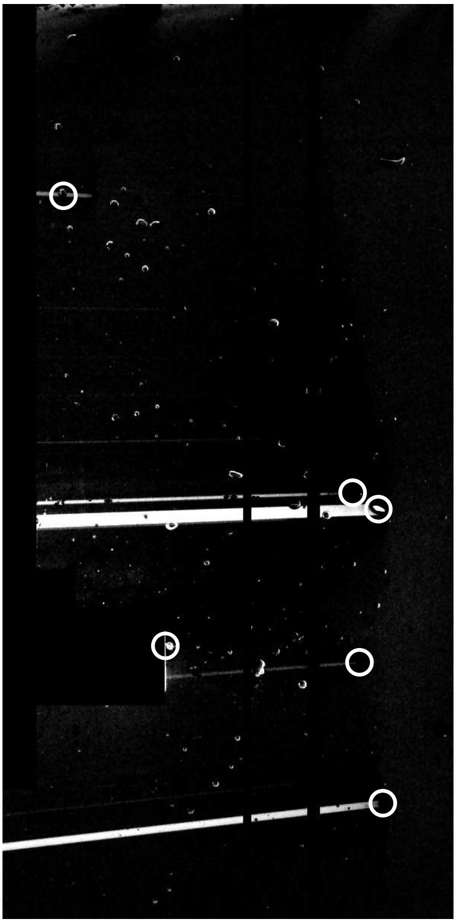

Figure 3.13: Final image with in-plane bubbles identified.

4 Assessment of dispersion properties

As shown in Chapter 3, light sheet based techniques seem to have the potential for the development of reliable measurements of local interfacial area, gas hold-up and BSD. One of the problems encountered when using these techniques is that, in the images obtained, laser plane bubble intercepts are visible. The intercept sizes are in general different from each other, so that a *visible intercept size distribution*, $VISD(l)$, can be experimentally assessed. This distribution is related to the actual bubble size distribution $BSD(r)$ but clearly does not coincide with it, as the laser sheet intercepts bubbles over non diametrical planes at random distances from bubble center. It may be expected that the $VISD(l)$ is bound to be skewed to the left with respect to the actual $BSD(r)$ to some extent.

The above defined $VISD(l)$ quantifies the likelihood of finding intercepts of size l among the whole set of intercept chords, and is determined by the following factors:

- the actual bubble size distribution $BSD(r)$;
- the conditional probability function $P(l|r)$ of intercepting a chord of length l from a particular bubble having a radius equal to r;
- the *biased probability* $P_B(r)$, that describes the probability of an r sized bubble of being sampled when bubbles are uniformly distributed in the system. Such probability is known as the *biased probability* and accounts for the circumstance that the sampling device is more likely to sample larger bubbles than smaller ones.

These three probability density functions are strictly independent of each other.

The relationship between BSDs and relevant chord distributions ($VISD$s) has been widely investigated in the past because of its relevance to multiphase dispersed flow measurements. Such relationships are in fact needed when needle probes are used to investigate bubble properties such as size or velocity in both gas-solid flows (Gunn and Al-Doori, 1985; Clark and Turton, 1988; Liu and Clark, 1995; Clark et al., 1996; Liu et al., 1996, 1998) and gas-liquid flows (Herringe and Davis, 1976; Hobbel et al., 1991). A number of works can be also found on the techniques needed to infer the bubble (particle or droplet) size distribution from chord length distributions as directly obtained by specific instruments, based on fixed or rotating laser beams, such as the Lasentec Par-Tec 300 (Simmons et al., 1999; Langston et al., 2001) or the Lasentec FBRM (Ruf et al., 2000; Wynn, 2003; Worlitschek et al., 2005; Li and Wilkinson, 2005; Li et al., 2005) .

In general, the probability that the sampling device intercepts a bubble at a distance interval $[x, x + dx]$ from bubble center can be modelled, once probe geometry and bubble shape are known:

$$Prob(x, x + dx) = P(x|r)dx \tag{4.1}$$

Once the bubble and sampling device are geometrically defined, a function relating the chord intercept length l to the position of the sampling device with respect to bubble center can be obtained:

$$L = f(x, r); \tag{4.2}$$

It is self evident that the probability of finding the sampling device in the interval $[x, x + dx]$ coincides with the probability of measuring an intercept length $[l, l - dl]$ (l typically decreases as x increases). This latter probability density is the conditional probability that a bubble of size r has to give rise to a measured intercept l:

$$P(x|r)dx = -P(l|r)dl; \tag{4.3}$$

The equality above can be rearranged as follows:

$$P(l|r) = P(x|r) \left| \frac{dx}{dl} \right| \tag{4.4}$$

With such definitions, the $VISD(l)$ can be obtained as:

$$VISD(l) = \int_0^\infty P(l|r)P_B(r)BSD(r)dr \tag{4.5}$$

It may be worth noting that the lower integration bound could have been set to L rather than 0 considering that an intercept having length l can only derive from bubbles having diameters greater than l itself. However no error is incurred with

Eqn.4.5 as for $r < l$, $P(l|r)$ is identically nil. When the $VISD(l)$ is measured, in theory the relevant $BSD(r)$ can be analytically inferred through Eqn.4.5, provided that closed forms are available for $P(l|r)$ $P_B(r)$ and $VISD(l)$. The analytical form of conditional probability $P(l|r)$ has been derived for different bubble shapes when pierced by a needle probe (Clark and Turton, 1988) or obtained by means of Focused Beam Reflectance Measurement (Ruf et al., 2000; Li and Wilkinson, 2005). Some works focused on the derivation of non-analytical $VISD(l)$ in the case of complex shapes such as two spheres aggregates (Gruy and Jacquier, 2008) or on the basis of detailed optical models of a specific laser-beam instrument (Kail et al., 2009)

The dependence of the biased probability $P_B(r)$ on R^2 in the case of punctual probes was firstly addressed on the basis of bubble geometrical properties by Herringe and Davis (1976), and subsequently formalized by Liu and Clark (1995).

In practice, two basic strategies can be adopted to tackle the problem of inferring the $BSD(r)$ once a measured $VISD(l)$ is obtained from experiment: (i) direct manipulation of conditional probability functions, and (ii) Eqn.4.5 discretization.

The first strategy, proposed by Herringe and Davis (1976), involves the manipulation of Eqn.4.5, in order to obtain the inferred $BSD(r)$ as a closed function of the $VISD(l)$ and its derivative for the case of gas bubbles ascending in a liquid medium and pierced by a needle probe. Such technique, even if the biased probability was not accounted for in the original paper, was subsequently adopted by Liu and Clark (1995) who applied the $BSD(r)$ inferring technique to Rayleygh and Gamma distributed $VISD(l)$ while accounting for the biased probability. Clark et al. (1996) directly transformed timing measurements (as obtained from point probes) into the relevant $BSD(r)$ under the hypothesis of a strict relation between bubble size and bubble rise velocity, once again in the cases of Rayleygh and Gamma distributed $VISD(l)$. In Liu et al. (1998), a similar procedure was employed to infer the $BSD(r)$ in the case of heterogeneously bubbling fluidized beds, *i.e.* systems with $BSD(r)$ dependent on the position of the probe, under the hypothesis of known $BSD(r)$ variation law.

The second strategy, firstly proposed by Clark and Turton (1988), is based on the possibility of discretizing the integral in Eqn.4.5 by defining a discretized vector r_j and relevant vector l_i of intercept sizes:

$$\begin{aligned}
V_i &= \int_{l_i}^{l_{i+1}} VISD(l)dl \\
&= \int_{l_i}^{l_{i+1}} \int_0^{R_{max}} P(l|r)P_B(r)BSD(r)drdl \\
&\approx \int_{l_i}^{l_{i+1}} \sum_{j=1}^{N-1} P(l|r_j)P_B(r_j)BSD(r_j)dl\Delta r \\
&= \sum_{j=1}^{N-1} \int_{l_i}^{l_{i+1}} P(l|r_j)P_B(r_j)BSD(r_j)dl\Delta r \\
&= \sum_{j=1}^{N-1} C_{i,j}BSD(r_j)\Delta r \qquad (4.6)
\end{aligned}$$

where V_i is the probability of measuring an intercept size in the range $[l_i, l_{i+1}]$, $BSD(r_j)$ is the bubble size distribution evaluated at r_j and $\mathbf{C}_{i,j}$ is a square matrix defined by:

$$C_{i,j} = \int_{l_i}^{l_{i+1}} P(l|r_j)P_B(r_j)dl \qquad (4.7)$$

in which $P(l|r_j)$ is the chord length distribution associated with the r_j sized bubbles. Notably the $\mathbf{C}_{i,j}$ matrix is upper triangular, as a consequence of the fact that the probability of measuring an intercept greater that bubble diameter is zero, *i.e.* the terms $\mathbf{C}_{i,j}$ with $i < j$ are zero. The discretized form of Eqn.4.5 can therefore be written as a linear systems:

$$\mathbf{C}_{i,j} \cdot \mathbf{BSD}_i = \mathbf{V}_i \qquad (4.8)$$

where the dot operator indicates the usual row-by-column matrix product. Eqn.4.8 solution may follow a simple *peeling* algorithm (Hobbel et al., 1991).

The solution of the above linear system is guaranteed by the invertibility of the $\mathbf{C}_{i,j}$ matrix and the non-catastrophic noise propagation during matrix inversion, as pointed out by Wynn (2003). This approach was also adopted for ellipsoidal bubbles by Liu et al. (1998) who compared it with other BSD reconstruction techniques. It is worth noting however that this class of inferring techniques is known to be affected by instability and noise problems, especially in the range of the largest diameters. On this basis, several additional techniques were subsequently developed in order to increase stability: the Single Value Decomposition algorithm for non-square matrix pseudo-inversion, that allows minimizing noise effects in the measured $VISD$, or the application of smoothing equations during the matrix inversion (Hu et al., 2006a), the use of constrained least squares algorithms (Li and Wilkinson, 2005), the adoption of the Parzen window estimator in order to maximize the statistical reliability of the measured $VISD$ (Liu et al., 1996), the adoption of non-equispaced intervals for minimizing errors in $VISD(l)$ calculation (Wynn, 2003) and the adoption od a purposely developed POCS solution technique (Projection Onto Convex Sets) directly based on n-dimensional space theory (Worlitschek et al., 2005).

Apart from these, it is worth quoting the Finite Element Method proposed by Simmons et al. (1999), an ensemble reconstruction method based on functional minimization similar to that adopted in Galerkin approximation for differential equations solution, and the Probability Apportioning Method, introduced by Simmons et al. (1999) and reviewed in Langston et al. (2001), based on an elementwise reconstruction of the probability that each intercept chord has to derive from each of the possible radius classes in the system and the cumulation of such probabilities in order to reconstruct the original $BSD(r)$.

It is worth noting that all of the above mentioned works tackled the problem of inferring $BSD(r)$ from unidimensional data sources, such as needle probes or laser beams. The authors are aware of only one paper (Laakkonen et al., 2005a) dealing with the problem of reconstructing $BSD(r)$ from laser sheet intercepted bubble areas. The algorithm there adopted is akin to that proposed by Clark and Turton (1988), adapted to the special sampling device. The analysis took into account different light sheet thicknesses, but apparently did not consider the biased probability of bubble interception.

As discussed in chapter 2, the conditional probability density function represents the probability that a bubble of size r randomly cut by a laser sheet gives rise to an intercept chord length in the interval $[l, l + dl]$. In this section the $P(l|r)$ for spherical bubbles is derived first in the case of zero-thickness (*thin*) light sheet and then in the case of *thick* light sheets. The biased probability function is finally discussed for both thin and thick light sheets.

4.1 Conditional probabilities in the case of single-sized spherical bubbles

The $P(l|r)$, *i.e.* the distribution of visible intercept sizes in the simplest case of univariate $BSD(r)$ (single-sized bubbles of radius r) and zero thickness light sheet (thin light sheet), can be estimated by stochastic methods or statistical geometry methods. The cut plane is simply characterized by its distance x_i from bubble centre, as depicted in Fig.4.1. Once a given cut plane has been specified, this results into a visible intercept only if the distance between the cut plane and bubble centre is smaller than bubble radius:

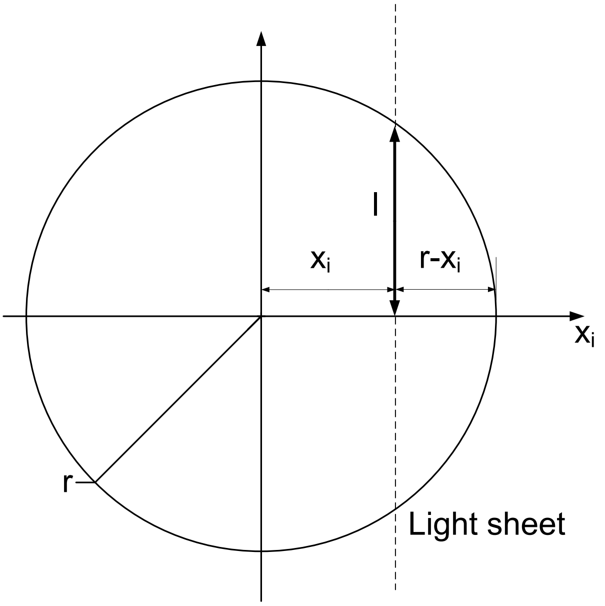

Figure 4.1: Schematic representation of a spherical bubble cut by zero thickness light sheet.

$$l = \sqrt{r^2 - x_i^2} \tag{4.9}$$

The analytical form of such distributions can be directly obtained from geometrical considerations, based on the hypothesis of cut planes randomly equidistributed over bubble radius:

$$P(x_i|r)dx_i = -\frac{1}{r}dx_i \tag{4.10}$$

By combining Eqns.4.4, 4.9 and 4.10, conditional probability density and relevant cumulative density can be simply obtained:

$$P(l|r) = \frac{1}{r}\left|\frac{d}{dl}\sqrt{r^2 - l^2}\right| \tag{4.11}$$

That finally results into:

$$P(l|r) = \begin{cases} \frac{l}{r^2\sqrt{1-\left(\frac{l}{r}\right)^2}} & \text{if } l < r \\ 0 & \text{if } l \geq r \end{cases} \tag{4.12}$$

$$cP(l|r) = \begin{cases} 1 - \sqrt{1 - \left(\frac{l}{r}\right)^2} & \text{if } l < r \\ 1 & \text{if } l \geq r \end{cases} \tag{4.13}$$

To give an idea of the shape of the two distribution functions (Eqns.4.12 and 4.13), these are plotted in Fig.4.2 for the case of $r = 10mm$. As it can be seen, the conditional probability density function diverges when l approaches r, a feature from which numerical difficulties may stem.

The typical thickness of laser sheets in PIV apparatuses is of the order of few millimeters and is therefore comparable with the size of bubbles in most gas-liquid systems. Therefore the effect of laser sheet thickness on bubble properties measurement must be properly accounted for.

In the more complex case of finite-thickness light sheet (thick light sheets), the ratio between bubble radius and light-sheet thickness may be included as a new variable when assessing the statistical distributions of apparent radii. Light sheet thickness is typically known in PIV apparatuses. It will also be assumed that the camera depth of field is larger than light sheet thickness, so that the contours of all bubbles intersected by the laser sheet are not blurred.

Clearly a thick light sheet intersecting gas bubbles may give rise to one or two detectable intercept radii, as depicted in Fig.4.3. The light sheet can be unambiguously positioned with respect to the bubble by giving the distance x_i of its median plane from bubble center.

The light sheet will result into detectable intercept(s) if the distance between the light median plane and bubble center is smaller or equal to the sum of the bubble radius r and half of the light sheet thickness w_{ls}, as can be seen in Fig.4.3, case A.

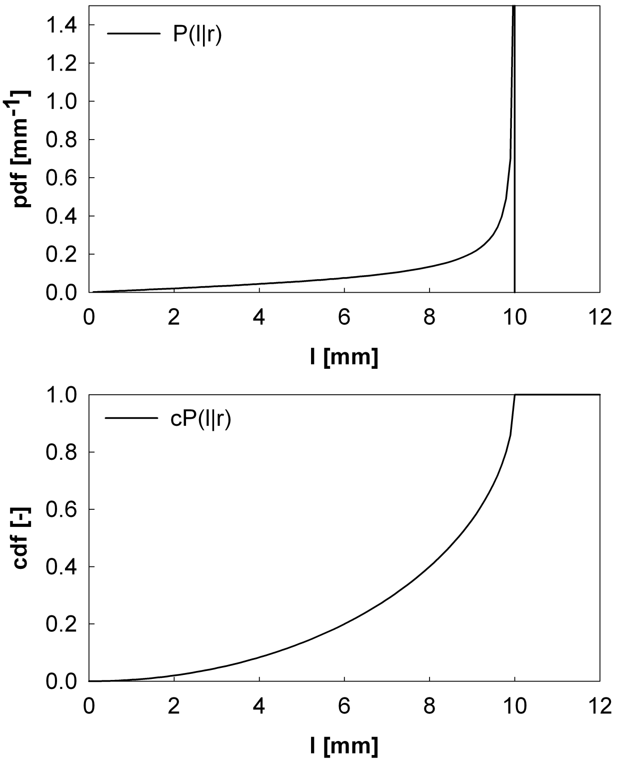

Figure 4.2: Probability density function and relevant cumulative density of intercept sizes for single sized bubbles ($r = 10mm$) and thin light sheet.

In Chapter 3 a novel experimental technique for measuring intercept bubble sizes and position in a gas liquid contactor was presented. With this technique, only the largest intercept is neatly measured by image analysis.

With this detection technique, the way in which the light sheet cuts gas bubbles gives rise to different apparent radii: if only one of the light sheet boundaries intersects the bubble, only one intercept radius is detectable and no ambiguity is incurred (case D in Fig.4.3); when both light sheet boundaries intersect the bubble in such a way that intercepts lie on the same side with respect to the bubble diametrical plane, two intercept radii may be detected (case B in Fig.4.3); experimental experience shows that under such circumstances the external boundary is easier to detect than the internal one and gives rise to smaller sensitivity to image processing parameters, such as binarization thresholding; the former is therefore adopted as the nominal intercept ra-

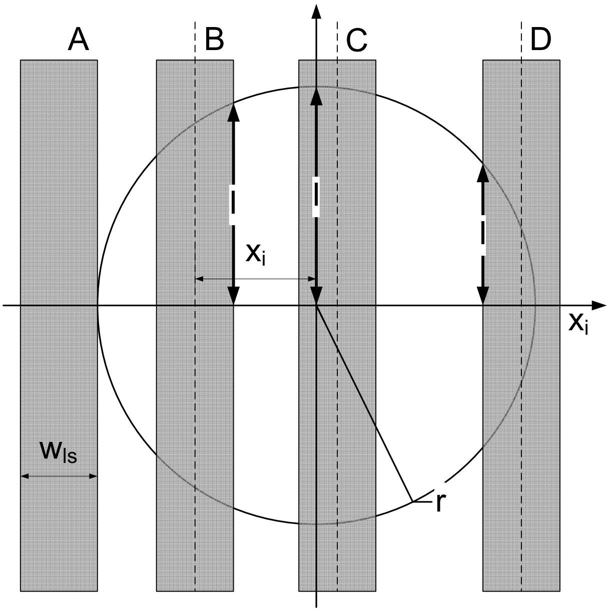

Figure 4.3: Schematic representation of a spherical bubble cut by thick light sheet.

dius in such cases. Finally, when both light sheet boundaries intersect the bubble in such a way that intercepts lie on different sides of bubble center (case C in Fig.4.3) then the visible bubble boundary coincides with the diametrical plane.

To evaluate the $P(l|r)$, the procedure is repeated with a statistically significant number of randomly distributed cut planes, resulting in a simulated sample of intercept radii. Each of the light planes randomly generated is then used for the computation of the two intercept radii corresponding to the two light sheet boundary planes:

$$l_l = \sqrt{r^2 - \left(x_i + \frac{w_{ls}}{2}\right)^2} \tag{4.14}$$

$$l_r = \sqrt{r^2 - \left(x_i - \frac{w_{ls}}{2}\right)^2}$$

The nominal intercept size is then determined on the basis of the relative position of the light sheet median plane and the bubble diametrical plane:

$$l = \begin{cases} max\left(l_l, l_r\right) & \Leftrightarrow |x_i| > w_{ls}/2 \\ r & \Leftrightarrow |x_i| \leq w_{ls}/2 \end{cases} \tag{4.15}$$

This can be easily visualized in Fig.4.4, where the radii detected by left and right light sheet sides are shown in the case of different values (respectively equal to 0.01, 0.1, 1, 10) of the ratio β between the thickness of the laser sheet and bubble radius.

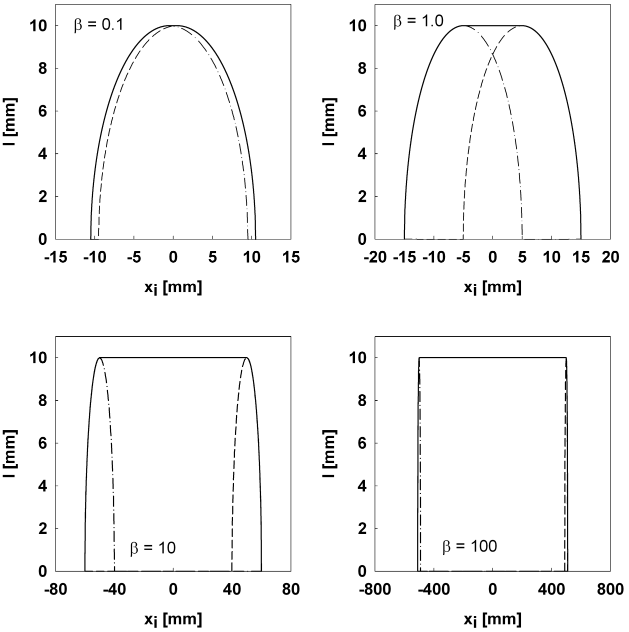

Figure 4.4: Bubble size detection by light sheet right boundary plane (dashed line), left boundary plane (dash-dot line) and output intercept size (solid line) as a function of light sheet median plane position, for different values of β.

$$\beta = \frac{w_{ls}}{r} \tag{4.16}$$

For thick light sheets, it is clear that the probability of finding apparent radii equal to the effective bubble radius increases with β, since the probability of finding the diametrical plane of the bubble inside the light sheet increases in turn. The analytical expression for $cP(l|r)$ in the case of thick light sheet can be obtained with a procedure similar to that used for Eq.4.13, with the only exception that part of the planes adopted for the bubble cut give rise to an intercept radius exactly equal to r. In particular, all cut planes at a distance from bubble center lower than half of the light sheet thickness will result in an intercept radius equal to r. On this basis, the fraction of intercept planes giving rise to visible intercept radii equal to r, *i.e.* the probability P_d of the light sheet to include the diametrical plane is given by:

$$P_d = \frac{w_{ls}}{2r + w_{ls}} \tag{4.17}$$

Conversely, all others cut planes will give rise to a statistical distribution of visible intercept radii identical to that for thin light sheet (Eqn.4.13) multiplied by the relevant fraction of planes $P_{nd} = (1 - P_d)$, thus resulting into the following equation:

$$cP(l|r) = \begin{cases} \frac{2r}{2r+w_{ls}} \left[1 - \sqrt{1 - \left(\frac{l}{r}\right)^2}\right] & \text{if } l < r \\ 1 & \text{if } l \geq r \end{cases} \tag{4.18}$$

where

The discontinuity at $l = r$ in Eqn.4.18 derives from the above mentioned considerations on the probability of including the bubble diametrical plane into the light sheet.

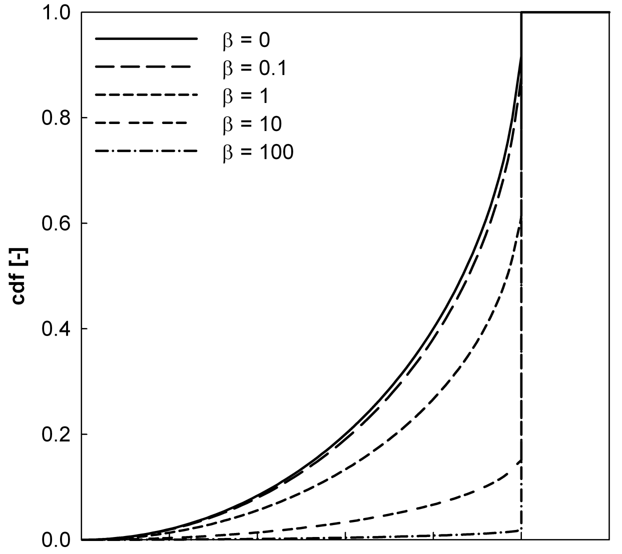

Figure 4.5: Cumulative intercept probability density functions $cP(l|r)$ for single sized bubbles ($r = 10mm$)and thick light sheets.

In Fig.4.5 the $cP(l|r)$ obtained with β values ranging from 0, to 100 are reported. As it could have been expected, for small values of β ($\beta = 0.1$) the $cP(l|r)$ practically coincides with that obtained for an ideally thin laser sheet (β=0.0), while at the highest values of β almost only the actual bubble radius appears, since most of the light-bubble interaction events result into the actual bubble radius to be output.

In addition to the analytical form of conditional probabilities, attention has to be paid to the fact that when multisized bubbles dispersed in a physical space are considered, the biased probability for the light sheet to intercept each bubble depends on bubble size. In particular, if an r sized bubble is considered in a physical space having length equal to λ, and is cut by a light sheet having thickness equal to w_{ls}, with positions equidistributed over the length λ, the probability of the light sheet to intercept the bubble is equal to:

$$P_B(r) = \frac{2r + w_{ls}}{\lambda} \tag{4.19}$$

In the followings the biased probability defined by Eqn.4.19 will be employed; this will introduce a common proportionality factor in all subsequent calculations. This will however be wiped out at the end, when the reconstructed BSD is normalized to make it consistent with a probability density function (*i.e.* to insure that the relevant cumulative curve tends to unity when r diverges).

4.2 From BSD to VISD and back

Once the $P(l|r)$ is known, it is possible to tackle the problem of reconstructing the actual $BSD(r)$ from the relevant $VISD(l)$. To this end, the probability density function of actual bubble sizes is discretized by suitably defining N equispaced discrete bubble-radius classes and associating weights BSD_j to each class, proportional to the number n_j of bubbles in each class.

$$\begin{align} W_j &= \int_{r_j-\Delta r/2}^{r_j+\Delta r/2} BSD(r)dr \tag{4.20} \\ &= \frac{n_j}{n_{TOT}} \tag{4.21} \end{align}$$

It is self evident that, if each bubble size class gives its $P(l|r_j)$ independently of all other size classes, the overall $VISD(l)$ can be computed as the sum of all $P(l|r_j)$s associated to each bubble size class, weighted on the basis of the product between BSD_j and the relevant biased probability $P_B(r_j)$:

$$VISD(L) = \sum_{j=1}^{N} W_j \cdot P_B(r_j) \cdot P(l|r_j) \tag{4.22}$$

This is the same approach as that behind Eqn.4.6 (Clark and Turton, 1988). In order to increase numerical stability, it is suggested here to consider the cumulative (integral) density functions instead of the relevant probability densities:

$$\begin{aligned} \int_0^{l_i} VISD(l)dl &\approx \int_0^{l_i} \sum_{j=1}^{N} W_j \cdot P_B(r_j) \cdot P(l|r_j)dl && (4.23)\\ cVISD_i &= \sum_{j=1}^{N} W_j \cdot \int_0^{l_i} P_B(r_j) \cdot P(l|r_j)dl && (4.24)\\ cVISD_i &= \sum_{j=1}^{N} W_j \cdot P_B(r_j) \cdot cP(l_i|r_j) && (4.25) \end{aligned}$$

Since the cumulative density function of intercepts ($cVISD_i$) and the values of $cP(l|r)$ and $P_B(r)$ are known, the problem becomes that of finding the W_j values that satisfy Eqn.4.25. Since N equations of the same type can be written (one for each bubble class r_j), Eqn.4.25 results in a closed linear system, that, by adopting for i and j the meaning of row and column indexes respectively, can be rewritten in compact form as:

$$\mathbf{B}_{i,j} \cdot \mathbf{W}_i = \mathbf{cVISD}_i \tag{4.26}$$

where the dot operator indicates the usual row by column matrix product, and:

$$B_{i,j} = P_B(r_j) \cdot cP(l_i|r_j) \tag{4.27}$$

Eqn.4.26 can be solved by any standard linear system solution algorithm, therefore resulting into the probability vector $\mathbf{W}_i$, that may be translated into the relevant discretized probability density $\mathbf{BSD}_i$ by simple division of its element by the relevant sum. The common factor $1/\lambda$ is clearly wiped out by the division.

$$BSD(r_i) = \frac{W_i}{\sum W_i} \tag{4.28}$$

Eqn.4.26 is akin to Eqn.4.8 from which it differs only for the use of cumulative distribution functions in the coefficient matrix and the right hand side vector. It can be solved by any standard linear system solution procedure, so resulting in the $BSD(r_i)$ discrete values of the actual $BSD(r)$. It is worth noting that in this case none of the elements of the coefficient matrix is equal to zero, because the $cP(l_i|r_j)$ are identically equal to one when $l_i \geq r_j$. Therefore, the use of cumulative condititional probabilities instead of probability densities has positive drawbacks on the numerical stability. Moreover, the use of a bounded (in the interval $0-1$) cumulative function, whose values do not depend on the bin size adopted for the function discretization (Δr), also adds to the algorithm robustness.

This procedure requires as an input the intercept size data set and the depth of the laser sheet, together with analytical or numerical (discretized) expressions for the individual $cP(L_i|r_j)$. The number N of size classes used to solve the problem should be large enough for accurately describing the investigated bubble system.

Notably different bubble shapes can be employed for the various size classes, so allowing to consider spherical shape for small enough bubbles (up to about $1mm$ for air water-systems), ellipsoidal shapes for intermediate sizes and even spherical cap shape for the largest bubbles. All is to be done is computing the $\mathbf{B}_{i,j}$ elements accordingly.

4.3 Hold up and interfacial area measurement

The overall gas hold-up in gas liquid dispersions is simply defined as the ratio between gas phase volume and overall volume (Eqn.4.29):

$$\epsilon = \frac{\int_V \mathrm{d}V_{gas}}{\int_V \mathrm{d}V_{gas} + \int_V \mathrm{d}V_{liq}} \tag{4.29}$$

Conversely, a local gas hold-up is more difficult to define: in fact, when infinitesimal volumes dV are considered, the instantaneous local hold-up is either 0 or 1 depending on the fact that the point considered is occupied by the liquid or the gas phase respectively. Therefore the instantaneous local hold up can be expressed by defining an instantaneous phase indicator (Eqn.4.30):

$$\Phi(x,y) = \begin{cases} 1 & \Leftrightarrow \Phi \in V_{gas} \\ 0 & \Leftrightarrow \Phi \notin V_{gas} \end{cases} \tag{4.30}$$

The average instantaneous hold-up over volume V may be written as:

$$\epsilon_{av} = \frac{\int_V \Phi \mathrm{d}V}{\int_V \mathrm{d}V} \tag{4.31}$$

By averaging over time:

$$\overline{\epsilon_{av}} = \frac{\iint_{T,V} \Phi \mathrm{d}V \mathrm{d}t}{T \int_V \mathrm{d}V} \tag{4.32}$$

$$= \frac{1}{V} \int_V \left(\frac{1}{T} \int_T \Phi \mathrm{d}T \right) \mathrm{d}V \tag{4.33}$$

and by defining the time averaged local hold-up as:

$$\overline{\epsilon_{loc}} = \frac{1}{T} \int_T \Phi \mathrm{d}T \tag{4.34}$$

This last clearly abides by the property that:

$$\overline{\epsilon_{av}} = \frac{1}{V} \int_V \overline{\epsilon_{loc}} \mathrm{d}V \tag{4.35}$$

Equation 4.34 is therefore a perfectly consistent local hold-up definition. In discretized form, if N time-equispaced images of the system are taken, the above defined local hold-up can be simply computed in each image pixel:

$$\overline{\epsilon_{loc}} (i,j) = \frac{\sum_N \Phi (i,j)}{N} \tag{4.36}$$

In practice, upon suitable treatment of the images obtained from a light sheet cutting the gas liquid dispersion (see Chapter 3), it is possible to discriminate the regions of the image occupied by gas phase from those occupied by liquid phase. By assigning to gas-phase occupied pixels a unitary luminance value, and zero luminance value to liquid phase pixels, luminance values do exactly coincide with the gas phase indicator defined in Eqn.4.30.

It is now possible to compute time-averaged local gas hold-ups by simply averaging, pixel by pixel, a number of phase matrices. The simple procedure proposed is therefore able to measure (with high reliability) local hold-up values in gas liquid systems. The procedure is absolutely independent of bubble shape and size distribution, and only depends on the robustness of the image processing techniques adopted to perform phase discrimination.

If an image area larger than a pixel is considered, *e.g.* a square with a λ side corresponding to m pixels, then the time and area averaged hold-up will simply be given by:

$$\overline{\epsilon_{av}}\left(i,j\right)=\frac{\sum\overline{\epsilon_{loc}\left(i,j\right)}}{m^2} \tag{4.37}$$

Notably, this procedures directly applies to phase matrix procedure as obtained from experiment, regardless of the effects due to the use of a thick laser sheet. Once the raw (uncorrected) data are available, the above described procedure may be employed to infer the actual gas hold-up. This proof is somewhat similar to the well known Delesse's principle in the field of stereology (Delesse, 1847), which states that the volumetric fraction of a phase in a mixture statistically equals the area fraction of the same phase in a random slice of the sample.

Given the ease and reliability by which locally averaged gas hold-up may be extracted from gas-liquid dispersion images, one may wish to see whether information on interfacial area may be easily obtained from the same images. In particular, provided that efficient bubble identification algorithms have been set up in order for in-plane gas-phase-occupied pixels to be identified, then extracting information on the gas-liquid interface perimeter observable in a λ by λ square is fairly straightforward. This information may be summed over N images to get a time averaged perimeter in the same area and by dividing it by λ^2 a quantity akin to specific interfacial area is obtained. Let us call it *apparent interfacial area*:

$$a_{i,a}=\frac{\frac{1}{N}\sum_N p_i}{\lambda^2} \tag{4.38}$$

where p_i is the gas-liquid perimeter found in each image in the above defined region. Equation 4.38 defines in practice the quantity that would be experimentally accessed from LIF-SABS technique.

However , the relation with actual (volumetric) specific interfacial area is not as plain as in the case of gas hold-up, in which volumetric and apparent phase fraction coincide if an infinitesimally thin slice is considered. The fundamentals of this problem were stated in the Buffon's needle problem (Buffon, 1777), whose solution was the start of modern statistical geometry and stereology (Mandarim De Lacerda, 2003; Stroeven and Hu, 2006). It is universally accepted that the following relation exists between apparent and actual specific interfacial area, when bubbles of any shape intercepted by infinitesimally thin light sheets are considered (see for instance Russ and Dehoff (1999)):

$$a_{i,a} = \frac{\pi}{4} a_i \tag{4.39}$$

In addition to these difficulties, the laser sheet thickness (that in PIV apparatuses is generally *thick*, *i.e.* comparable with bubble size) must be accounted for. In fact, the thicker the laser sheet, the greater the probability of including the diametrical plane into the light sheet. Moreover, knowledge of the gas-to-dispersion volume ratio depends on the way in which bubbles are cut. As discussed above, only the largest of the two plane intercepts can be reliably recorded from image analysis by means of LIF-SABS technique. In this way, the gas-to-dispersion volume ratio can be approximated by considering cylindrical intercepts having radius equal to the recorded intercept size and height equal to the laser sheet thickness. This identification clearly introduces an overestimation of both gas hold up and specific interfacial area. In the following paragraphs, a more consistent theoretical correction will be developed and validated by comparison with Monte Carlo simulation results.

4.3.1 Hold-up and interfacial area correction

The local hold up in gas-liquid contactors via digital image analysis and *thin* light sheet can be easily obtained by local time averaging of the phase indicator, as discussed earlier. Unfortunately, in the case of *thick* light sheet, application of the same procedure would result in a general overestimation of the local hold up. It is worth noting that even if both intercept diameters were known, and bubbles were spherical, problems would be encountered. For instance, in all cases when bubbles are intercepted by only one of the two light sheet boundaries there would be no way of knowing which portion of the bubble volume is inside the light sheet.

It is therefore impossible to exactly measure local hold up by means of *thick* light sheets. It is however possible to correct such measurements by means of statistical analysis under the hypothesis of spherical bubbles.

In fact, the actual average interfacial area per unit volume of the dispersed gas can be written as:

$$\frac{S}{V_g} = \frac{\sum 4\pi r^2}{\sum 4\pi r^3/3} = 3\frac{\sum r^2}{\sum r^3} = \frac{3}{r_{32}} \tag{4.40}$$

As mentioned earlier, the apparent interfacial area per unit volume can be expressed by approximating the bubble volume and area inside the light sheet with the relevant volume and area of a cylinder with base radius equal to the measured intercept length l and height equal to the laser sheet thickness w_{ls}:

$$\frac{S_a}{V_a} = \frac{\sum 2 w_{ls} \pi l}{\sum w_{ls} \pi l^2} = 2 \frac{\sum l}{\sum l^2} = \frac{2}{l_{21}} \tag{4.41}$$

On the basis of the same approximation and the above definitions (Eqn.4.40 and 4.41) it is possible to compute the actual and apparent specific interfacial area:

$$a_i = \frac{S}{V} = \frac{S}{V_g} \frac{V_g}{V} = 3 \frac{\epsilon}{r_{32}} \tag{4.42}$$

$$a_{i,a} = \frac{S_a}{V_{Sheet}} = \frac{S_a}{V_a} \frac{V_a}{V_{Sheet}} = 2 \frac{\epsilon_a}{l_{21}} \tag{4.43}$$

Since it is possible to directly measure, by means of digital image analysis and PIV apparatuses, both ϵ_a (by means of the pixel-wise time averaging discussed in Section 4.3) and $a_{i,a}$ (as the ratio between bubble intercept perimeter and image size), it is necessary to suitably correct the measured apparent values in order to infer the actual quantities.

In order to do this, it is necessary to model the problem by relating the actual bubble size distributions $BSD(r)$ to the relevant visible intercept size distributions $VISD(l)$. In general, it has been already shown in previous sections of the present Chapter that the $VISD(l)$ can be expressed in integral form as:

$$VISD(l) = \int_0^\infty P_B(r) P(l|r) BSD(r) dr \tag{4.44}$$

where the biased probability and the cumulative conditional intercept probability density are respectively given by:

$$P_B(r) = \frac{2r + w_{ls}}{\lambda} \tag{4.45}$$

$$cP(l|r) = \begin{cases} \frac{2r}{2r+w_{ls}} \left(1 - \sqrt{1 - \frac{l^2}{r^2}}\right) & \Leftrightarrow \quad l < r \\ 1 & \Leftrightarrow \quad l = r \end{cases} \tag{4.46}$$

where λ is the characteristic size of the investigated system area and an arbitrary $BSD(r)$ is considered. In the followings, the primitive function of the probability density function (*i.e.* the cumulative density function) will be conveniently employed.

The correction factors needed to infer actual quantities from light sheet intercept data can be simply defined as follows:

$$f_\epsilon = \frac{\epsilon}{\epsilon_a} \tag{4.47}$$

$$f_{a_i} = \frac{a_{i,a}}{a_i} = \frac{3}{2}\frac{\epsilon_a}{\epsilon}\frac{l_{21}}{r_{32}} = \frac{2}{3} f_\epsilon \frac{l_{21}}{r_{32}} \tag{4.48}$$

4.3.2 Estimation of the hold-up correction factor

The definition of the hold-up correction factor can be immediately expressed as a function of the actual radii data set and the intercept data set.

$$\frac{\epsilon}{\epsilon_a} = \frac{\sum 4\pi r^3/3}{\lambda^3}\frac{w_{ls}\lambda^2}{\sum w_{ls}\pi l^2} = \frac{4}{3\lambda}\frac{\sum r^3}{\sum l^2} \tag{4.49}$$

It is possible to substitute the sums in Eqn.4.49 with the relevant distribution moments (in the followings, all integrals are meant as definite integrals between 0 and ∞, unless otherwise indicated):

$$\begin{aligned} \frac{\epsilon}{\epsilon_a} &= \frac{4}{3\lambda}\frac{\int r^3 BSD(r)\mathrm{d}r}{\int l^2 VISD(l)\mathrm{d}l} \\ &= \frac{4}{3\lambda}\frac{\int r^3 BSD(r)\mathrm{d}r}{\iint l^2 P_B(r)P(l|r)BSD(r)\mathrm{d}r\mathrm{d}l} \end{aligned} \tag{4.50}$$

and by introducing Eqns. 4.19 and 4.18, by simple manipulation the following result is obtained:

$$\begin{aligned} \frac{\epsilon}{\epsilon_a} &= \frac{4}{3\lambda}\frac{\int r^3 BSD(r)\mathrm{d}r}{\frac{1}{\lambda}\iint l^2(2r+w_{ls})P(l|r)BSD(r)\mathrm{d}r\mathrm{d}l} \\ &= \frac{4}{3}\frac{\int r^3 BSD(r)\mathrm{d}r}{\int (2r+w_{ls})BSD(r)\left[\int l^2 P(l|r)\mathrm{d}l\right]\mathrm{d}r} \\ &= \frac{4}{3}\frac{\int r^3 BSD(r)\mathrm{d}r}{\int (2r+w_{ls})BSD(r)\left[\frac{r^2(4r+w_{ls})}{3(2r+w_{ls})}\right]\mathrm{d}r} \\ &= \frac{4}{3}\frac{\int r^3 BSD(r)\mathrm{d}r}{\frac{4}{3}\int r^3 BSD(r)\mathrm{d}r + w_{ls}\int r^2 BSD(r)\mathrm{d}r} \\ &= \frac{4}{3}\frac{1}{\frac{4}{3}+\frac{w_{ls}}{r_{32}}} \end{aligned} \tag{4.51}$$

$$\frac{\epsilon}{\epsilon_a} = \frac{1}{1 + \frac{3w_{ls}}{4r_{32}}} \tag{4.52}$$

It is worth noting that is not possible to obtain a correction factor completely independent of actual bubble size distribution. Nevertheless, it has been shown that the correction factor only depends on the ratio between the known laser sheet thickness and the average bubble radius r_{32}, independently of BSD shape. If one could infer the BSD from $VISD$, for example with the procedure presented in previous section of the present Chapter, the problem would be solved.

Notably, when w_ls is made smaller and smaller, Eqn.4.52 correctly converges to 1::

$$\lim_{w_{ls} \to 0} \frac{\epsilon_a}{\epsilon} = 1 \tag{4.53}$$

i.e. there is no need to correct the measured bubble hold-up provided that the laser sheet thickness is negligibly thin with respect to average bubble radius r_{32}, as implied in Eqn.4.36.

4.3.3 Calculation of VISD-to-BSD moment ratios

Once the correction factor f_ϵ has been derived, only the value of the ratio l_{21}/r_{32} is needed in order to compute f_{a_i}, as shown by Eqn.4.48. Again, it is necessary to compute the average intercepts as the ratio between relevant distribution moments:

$$l_{21} = \frac{\int l^2 VISD(l)\mathrm{d}l}{\int l VISD(l)\mathrm{d}l} \tag{4.54}$$

All detailed integral calculation are reported, for the sake of clarity. It is worth noting that, by similar calculations, it is finally possible to compute the following equalities, correlating the statistical moments of $VISD$ and BSD:

$$\begin{aligned}
l_{21} &= \frac{\int l^2 VISD(l)\mathrm{d}l}{\int l VISD(l)\mathrm{d}l} \\
&= \frac{\iint l^2 P_B(r) P(l|r) BSD(r)\mathrm{d}r\mathrm{d}l}{\iint l P_B(r) P(l|r) BSD(r)\mathrm{d}r\mathrm{d}l} \\
&= \frac{\frac{1}{\lambda}\iint l^2(2r+w_{ls}) P(l|r) BSD(r)\mathrm{d}r\mathrm{d}l}{\frac{1}{\lambda}\iint l(2r+w_{ls}) P(l|r) BSD(r)\mathrm{d}r\mathrm{d}l} \\
&= \frac{\int (2r+w_{ls}) BSD(r)\left[\int l^2 P(l|r)\mathrm{d}l\right]\mathrm{d}r}{\int (2r+w_{ls}) BSD(r)\left[\int l P(l|r)\mathrm{d}l\right]\mathrm{d}r} \\
&= \frac{\int (2r+w_{ls}) BSD(r)\left[\frac{r^2(4r+w_{ls})}{3(2r+w_{ls})}\right]\mathrm{d}r}{\int (2r+w_{ls}) BSD(r)\left[\frac{r(\pi r+w_{ls})}{2(2r+w_{ls})}\right]\mathrm{d}r} \\
&= \frac{\frac{4}{3}\int r^3 BSD(r)\mathrm{d}r + w_{ls}\int r^3 BSD(r)\mathrm{d}r}{\frac{\pi}{2}\int r^2 BSD(r)\mathrm{d}r + w_{ls}\int r BSD(r)\mathrm{d}r}
\end{aligned} \tag{4.55}$$

These expressions can be directly used for obtaining the l_{21}/r_{32} as a function of $BSD(r)$ moments only:

$$\frac{l_{21}}{r_{32}} = \frac{\frac{\frac{4}{3}\int r^3 BSD(r)\mathrm{d}r + w_{ls}\int r^3 BSD(r)\mathrm{d}r}{\frac{\pi}{2}\int r^2 BSD(r)\mathrm{d}r + w_{ls}\int r BSD(r)\mathrm{d}R}}{\frac{\int r^3 BSD(r)\mathrm{d}r}{\int r^2 BSD(r)\mathrm{d}r}} \tag{4.56}$$

$$\frac{l_{10}}{r_{21}} = \frac{\frac{\pi}{2} + \frac{w_{ls}}{r_{21}}}{2 + \frac{w_{ls}}{r_{10}}} \tag{4.57}$$

$$\frac{l_{21}}{r_{32}} = \frac{\frac{4}{3} + \frac{w_{ls}}{r_{32}}}{\frac{\pi}{2} + \frac{w_{ls}}{r_{21}}} \tag{4.58}$$

$$\frac{l_{32}}{r_{43}} = \frac{\frac{3\pi}{8} + \frac{w_{ls}}{r_{43}}}{\frac{4}{3} + \frac{w_{ls}}{r_{32}}} \tag{4.59}$$

4.3.4 Calculation of interfacial area correction factor

On the basis of Eqns.4.48, 4.52 and 4.58, the following expression can be derived for the correction factor f_{a_i}:

$$f_{a_i} = \frac{3}{2}\frac{1}{1+\frac{3w_{ls}}{4r_{32}}}\frac{\frac{4}{3} + \frac{w_{ls}}{r_{32}}}{\frac{\pi}{2} + \frac{w_{ls}}{r_{21}}} \tag{4.60}$$

By simple manipulation, a simpler form can be derived:

$$f_{a_i} = \frac{2}{\frac{\pi}{2} + \frac{w_{ls}}{r_{21}}} \tag{4.61}$$

Equation 4.61 shows that once again it is not possible to obtain a correction factor completely independent of bubble size distribution. Nevertheless, it has been shown that the correction factor only depends on the ratio between the known laser sheet thickness and average bubble radius r_{21}, (instead of r_{32}). Again, if one could infer the BSD from $VISD$ the problem would be solved. It is worth noting that:

$$\lim_{w_{ls} \to 0} \frac{a_{i,a}}{a_i} = \frac{4}{\pi} \tag{4.62}$$

i.e. in the case of negligibly thick laser sheets, and spherical bubbles of any size distribution, the apparent interfacial area is about 1.27 times the actual area, as expected from classical stereology formulas.

4.4 Pseudo-experimental VISD(I) data sets

In order to validate the method, Monte Carlo simulations providing pseudo- experimental $VISD$ information were run in relation to several well defined input BSDs. The pseudo-experimental $VISD$ information so obtained was then processed by the procedure here proposed, so resulting in computed BSDs that could be compared with the known input BSDs.

The Monte Carlo approach employed involved a number of data sufficiently high to guarantee statistical reliability. Monte Carlo fundamentals are well known [Hammersley and Handscomb (1983)]. With this statistical approach, it is possible to simulate the random cut of an actual bubble with a laser sheet and the relevant apparent radius. The apparent radius clearly depends on the probability of the light sheet to cut the bubble at a certain distance from the center of the bubble itself, as seen in section 4.1.

In order to simulate the behavior of the bubble sample when randomly cut by a light sheet, a large sample (10^7 bubbles) obeying a given distribution was preliminarily created by means of simple pseudo-random number generators. A random position in the range $x_i = [-\lambda/2, \lambda/2]$ is associated to each bubble, where the maximum domain depth λ was assumed to be ten times the maximum between laser sheet thickness and maximum bubble size. This ensured that the bubble cutting events had the right biased probability dependence on bubble size. The laser sheet was assumed to be centered at $x_i = 0$. When a bubble was intercepted by the laser sheet the relevant measured intercept radius (computed as discussed in section 4.1) was obtained.

By repeating this calculation for all bubbles a set of apparent radii (and relevant $VISD(l)$ distributions) akin to data that could have been derived from experiment, was obtained. The set of pseudo-experimental intercept radii so obtained was subsequently processed by the reconstruction procedure described in section 4.2, so resulting in a reconstructed BSD that could be compared with the input $BSD(r)$ originally imposed to the sample.

A quite more complex Monte Carlo simulation was set-up for validation of bubble hold-up and specific interfacial area procedure validation. In practice, a realistic bubble sample (2000 bubbles) obeying a given distribution was preliminarily created by means of simple pseudo-random number generators. A set of uniformly random bubble positions in 3-dimensional space was then created. In order to realistically simulate an image-analysis based bubble sampling, the analysis was subsequently restricted to an inner cubic control volume (to insure uniform conditions inside the measurement control volume and avoid border effects). The volume and surface of bubbles inside the control volume was accurately computed.

In Figs.4.6 and 4.7, an example of bubbles obeying normal BSD (with $r_{10} = 5mm$ and $1.5mm$ standard deviation) represented in a simulated 3D space are reported for the case of 5% and 10% overall hold up respectively.

Is is worth noting that after a first random bubble placement in the simulated 3D space, overlapping bubbles were detected and randomly re-displaced, until no overlapped bubbles were left. The bubbles intercepted by the laser sheet were identified and the relevant measured intercept radii were obtained. On the basis of intercept radii and the knowledge of simulated laser sheet, the apparent hold-up and specific interfacial area could be computed and compared with actual (volumetric) relevant data.

4.5 Corrections viability

In order to test the viability, effectiveness and robustness of the procedure several BSDs were used to generate the intercept data sets, namely normal, beta, gamma, exponential, uniform and perfectly bivariate distributions, among others.

From each bubble data sample, several pseudo experimental $VISD(l)$ were obtained, using different values of laser sheet thickness, characterized by the dimensionless parameter β, defined as the ratio between laser sheet thickness and bubble (arithmetic) average radius r_{10}:

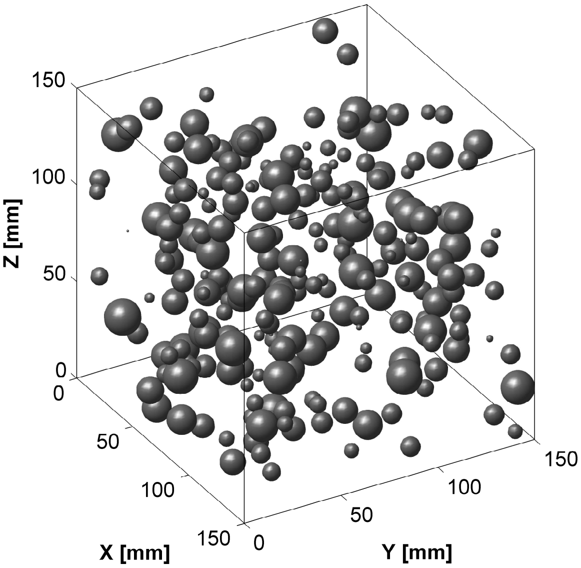

Figure 4.6: Simulated dispersion with $\epsilon = 5\%$.

$$\beta = \frac{w_{ls}}{r_{10}} \tag{4.63}$$

BSD	cpdf
Beta(1)	$\frac{1}{B(1.5,2.5)}\int_0^x t^{0.5}(1-t)^{1.5}dt$
Beta(2)	$\frac{1}{B(1.5,1.0)}\int_0^x t^{0.5}dt$
Biv.	0.6 if $6 \leq x < 10$; 1 if $x \geq 10$
Close-Biv.	0.7 if $10 \leq x < 10.5$; 1 if $x \geq 10.5$
Ext. Value	$1 - e^{-e^{\left(\frac{x-8}{0.5}\right)}}$
Gamma	$\frac{1}{0.5^6\Gamma(6)}\int_0^x t^{5.5}e^{-t/0.5}dt$
Normal	$\frac{1}{1.5\sqrt{2\pi}}\int_0^x e^{-(t-5)^2/4.5}dt$
Uniform	$\frac{x-0.01}{9.99}$ if $0.01 \geq x \leq 10$

Table 4.1: Pseudo-experimental cases simulated

For the sake of brevity, the results obtained for normal BSD (average radius of $5mm$), perfectly bivariate BSD (70% and 30% of the sample having radii of $6mm$ and $10mm$ respectively) and perfectly close-bivariate (70% and 30% of the sample

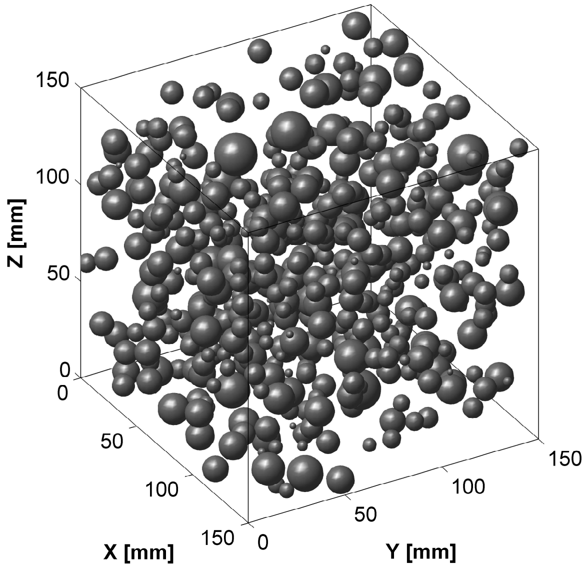

Figure 4.7: Simulated dispersion with $\epsilon = 10\%$.

having radii of $10mm$ and $11.5mm$ respectively) are reported to assess the viability and robustness of BSD inversion procedure. In all cases, a sample with 10^6 intercept chords was simulated and subsequently processed.

A quite realistic bubble numerousness (1000 simulated images, each with 2000 bubbles into the control volume, at a volumetric gas hold-up value of 5%) was employed to test the results of hold up and specific interfacial area correction factors. Intercept data relevant to all test distributions adopted (listed in Table 4.1) were computed and processed.

4.5.1 BSD reconstruction test

In Fig.4.8 the BSD and $cBSD$ of the original bubble sample are reported as solid lines, for the case of normally distributed sizes. The simulated $VISD$s and $cVISD$ obtained with several β values are reported as well (symbols) for comparison purposes.

As it can be seen, all $VISD$s underestimate the actual bubble size, as expected, with larger $VISD$ deviations the smaller the value of β. In particular, the $VISD$

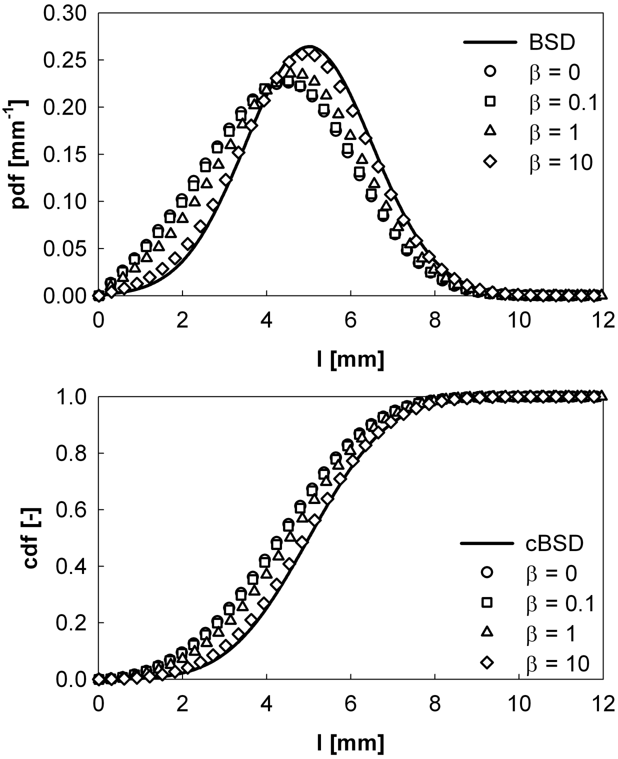

Figure 4.8: Monte Carlo simulated $VISD$ and $cVISD$ (symbols) obtained with different values of β from normal BSD and $cBSD$ (solid line)

obtained for thin light sheet and the actual BSD are the limiting distribution shapes that $VISD$ curves can assume. In fact, as thicker light sheets increase the probability of having intercept sizes coinciding with the actual bubble size, the relevant $VISD$s tend to coincide with the actual BSDs. It can also be observed that a light sheet thickness of 0.1 times the mean bubble radius is practically sufficient to consider the light sheet thickness as being negligible. It is worth noting however that this is not the case of real gas-liquid contactors, where often bubble sizes are comparable with laser sheet thickness.

Each of the simulated data sets appearing in Fig.4.8 was processed with the algorithm proposed in Section 4.2, and compared with the original BSD. Results are reported in Fig.4.9 where it can be observed that all reconstructed BSDs agree almost perfectly with the original BSD, thus validating the procedure employed. Not

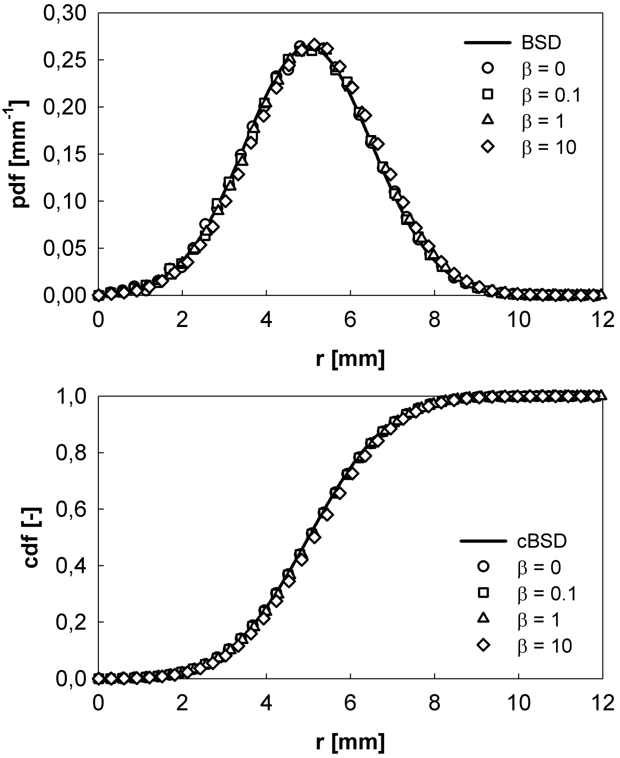

Figure 4.9: Comparison between reconstructed BSDs and $cBSD$s (symbols) and actual BSD and $cBSD$ (solid lines).

surprisingly the small scattering observable in the reconstructed BSDs (upper part of Fig.4.9) is almost completely dumped out when the reconstructed $cBSD$s are considered (lower part of Fig.4.9).

In order to test the procedure effectiveness and robustness with harsher distributions, Monte Carlo simulation results from a perfectly bivariate BSD (Fig.4.10(a)) and the reconstructed distributions (Fig.4.10(b)) are reported. Results are shown in the form of both probability density functions and cumulative probability functions. As it can be seen, even with this mathematically severe (though physically unlikely) distribution, the proposed procedure gives rise to a fully satisfactory agreement with the original distributions, independently of the β value adopted.

Finally, in order to stress the resolution capabilities of the procedure, several close-bivariate BSD, such as the one reported in Fig.4.11(a) were tested. Results were

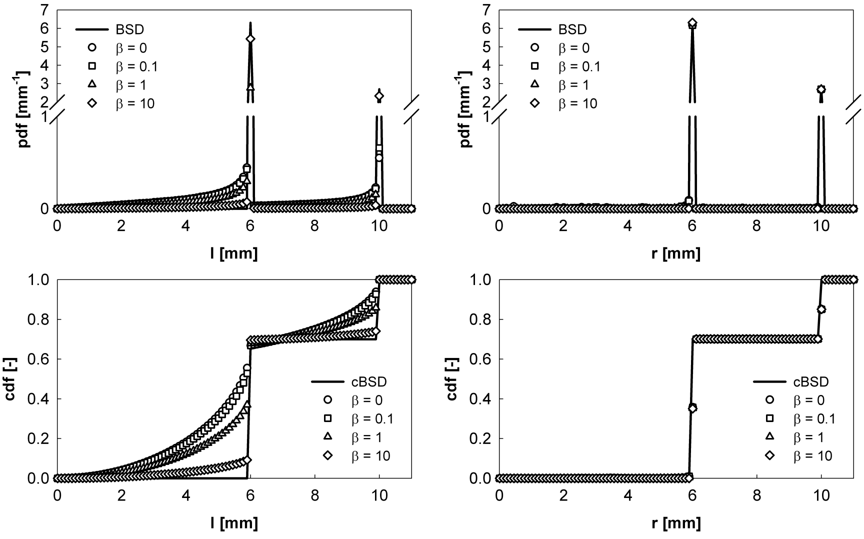

(a) $VISD$ (b) Reconstructed BSD

Figure 4.10: Monte Carlo simulated $VISD$ and $cVISD$ (symbols) obtained with different values of β from perfectly bivariate BSD and $cBSD$ (solid line) and relevant BSD reconstruction results.

always satisfactory (Fig.4.11(b)) with a closer adherence to the original distributions the smaller the bin size. In practice, it was found that peaks separated by only 3-4 bins are satisfactory resolved by the procedure.

As it can be seen in all the above cases the agreement between actual and reconstructed $cBSD$ is very good. Similar results were obtained with all the other distributions tested. As a consequence, the mathematical soundness of the procedure was considered as being fully ascertained.

4.5.2 Sensitivity analysis of BSD reconstruction method

So far a large number of bubble intercepts (10^6) was employed, hence a quite high sizes resolution (100 bins) could be afforded, so allowing the procedure precision to be properly evaluated. It is however quite difficult to collect such large samples from real experiments, and the question arises whether a satisfactory resolution can be obtained with more realistic sample numbers.

To estimate the number of bubble intercepts that can be obtained from usual equipment, one may consider that common PIV apparatuses have an image acquisition

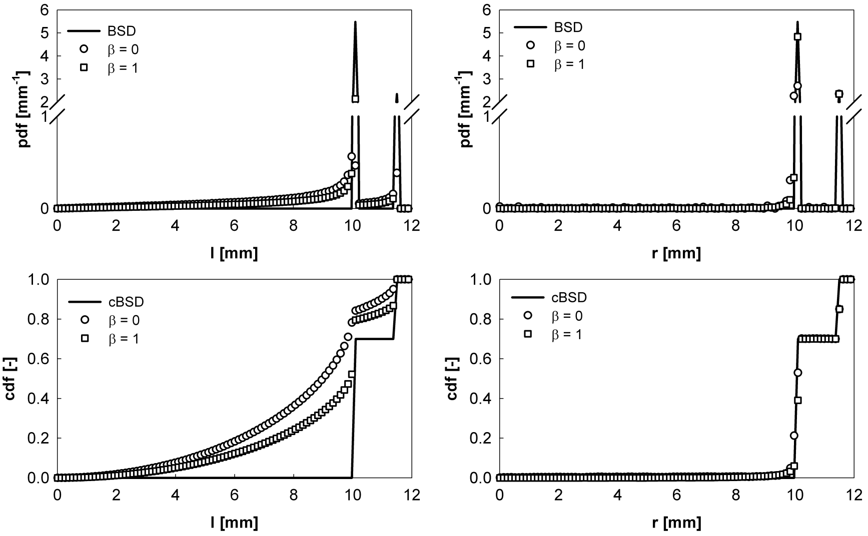

(a) $VISD$ (b) Reconstructed BSD

Figure 4.11: Monte Carlo simulated $VISD$ and $cVISD$ (symbols) obtained with different values of β from perfectly close-bivariate BSD and $cBSD$ (solid line) and relevant BSD reconstruction results.

frequency of the order of tens of Hertz. Hence, in a few minutes, thousands of images can be collected. If one assumes that in each image 10 bubbles are intercepted, it is possible to estimate a realistic sample numerousness in the order of tens of thousands. In this subsection, the sensitivity of the procedure developed to both sample numerousness and distribution resolution (bins number) is analyzed. In all tests, a value of $\beta = 0.1$ was adopted. This results in a particularly stringent test of the procedure. In fact, as previously pointed out, larger beta values give rise to more straightforward reconstruction, since less differences exist between $VISD$ and BSD.

In Fig.4.12(a), the BSD reconstruction results for the same BSD case of Fig.4.9 but with a reduced number of samples of $5 * 10^4$ are reported. In order to show the effects on reconstructed BSD resolution several bin numbers (20, 40 and 60 bins) are shown. It can be observed that larger bin numbers increase the reconstructed BSD noise, but the distribution shape is maintained. Also, the reconstructed $cBSD$ is only marginally affected by noise, with all bin numbers tested.

Often knowledge on one or more of BSD moments, or their ratios, is what is really needed rather than full distribution details. For instance in gas-liquid applications a

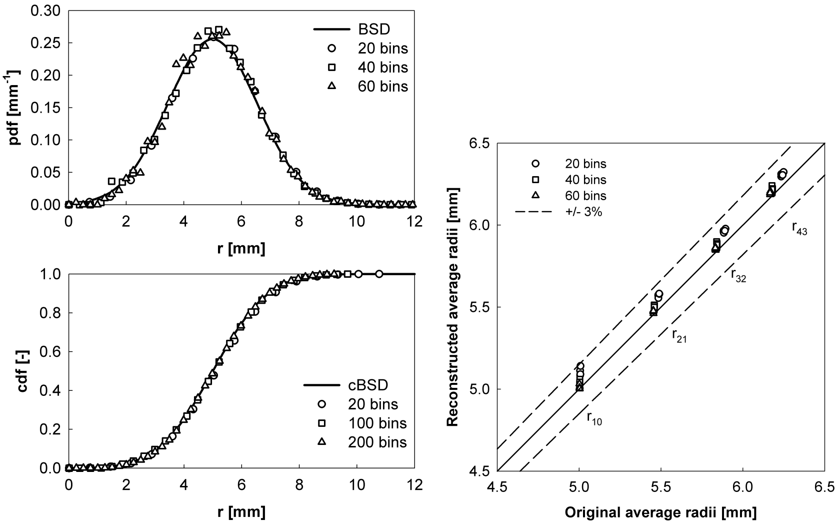

(a) (b)

Figure 4.12: Sensitivity of reconstructed BSD and $cBSD$ (symbols) to bins number ($5 * 10^4$ intercepts, $\beta = 0.1$) and relevant analysis of reconstructed versus actual average radii

particularly important role is played by the ratio between the third and the second moments r_{32} as this is immediately related to gas-liquid specific interfacial area. In Fig.4.12(b) the main statistical average radii obtained from BSD moments (r_{10}, r_{21}, r_{32}, r_{43}) are plotted *versus* the relevant values as obtained from the reconstructed BSD. As it can be seen, in all cases the reconstructed average radii agree well within 3% with the relevant actual values.

In Fig.4.13(a), the BSD reconstruction results for normal samples with 10^4, $5*10^4$ and 10^5 bubbles respectively, computed with 50 bins and $\beta = 0.1$ is reported. It can be observed that with 10^4 samples and 50 bins, although the distribution shape is maintained, the reconstructed BSD noise is unacceptably high, especially for the smallest bubble sizes. Notably, even then the reconstructed $cBSD$ remains practically free from noise.

As concerns average bubble sizes, these are reported in Fig.4.13(b) where it is possible to observe that 10^4 intercepts are practically sufficient to obtain fully converged results.

Finally, the procedure robustness with respect to experimental errors in measured chord lengths was investigated. In particular, to the simulated chord lengths obtained

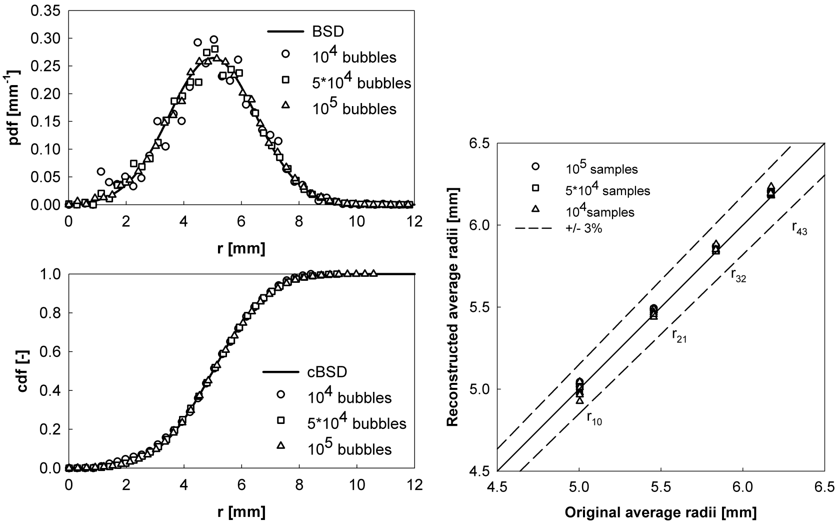

(a) (b)

Figure 4.13: Sensitivity of reconstructed BSD and $cBSD$ (symbols) to sample numerousness (50 bins, $\beta = 0.1$) and relevant analysis of reconstructed versus actual average radii

via Monte Carlo simulation, a 5% or 10% normally distributed noise was added. By applying the present procedure to these noisy data sets, the results reported in Fig. 4.14(a) were obtained. As it can be seen, a significant noise affetcs the reconstructed BSDs only for the case of 10% experimental error, while the relevant $cBSD$s practically coincide with the original curves, with negligible noise superposition.

The relevant inferred average sizes, are reported in Fig.4.14(b). In this case an increasing deviation of reconstructed average sizes as compared with the actual values is found the larger the moments involved. This is likely to depend on the fact that a symmetrically distributed noise becomes positively skewed to the right when higher moments are considered. Nevertheless, even in the worst case of r_{43} and 10% experimental error, final deviations from the actual value are practically within 3%.

Altogether, it may be concluded that the procedure here proposed, when applied to realistic data samples (in terms of number and experimental noise), is viable and effective as well as robust.

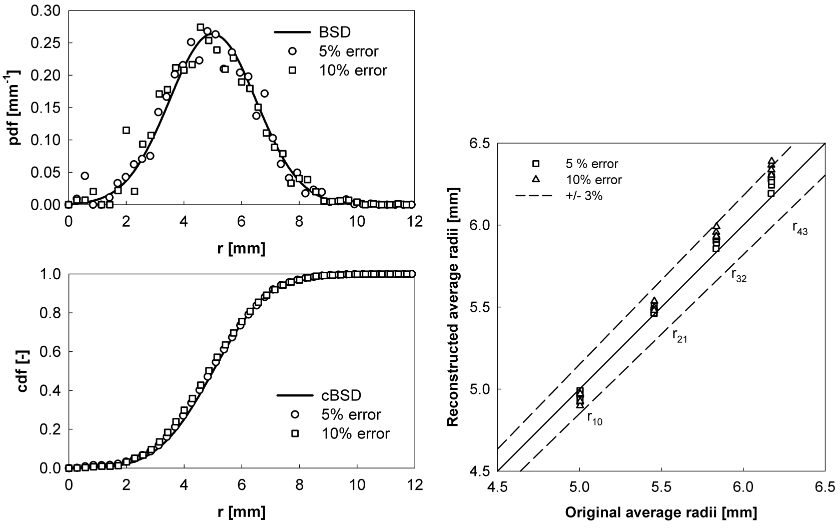

(a)

(b)

Figure 4.14: Sensitivity of reconstructed BSD and $cBSD$ (symbols) to experimental noise ($5{*}10^4$ intercepts, 50 bins, $\beta = 0.1$) and relevant analysis of reconstructed versus actual average radii

4.5.3 Specific dispersion properties correction viability

The ratios ϵ/ϵ_a obtained by Monte Carlo simulations are reported in Fig.4.15. As it can be seen, even in the case of particularly harsh BSDs, the agreement with the theoretical curve reported in the same figure is perfect. The soundness of both Eqn.4.52 and the Monte Carlo procedure set-up is therefore assessed.

The specific interfacial area correction as a function of the ratio w_{th}/r_{21} is reported in Fig.4.16. Again, the theoretical correction curve is reported, and an excellent agreement observed, regardless of the distribution adopted, so validating Eqn.4.61 as well the whole numerical procedure.

It must be emphasized that the laser sheet thickness is typically known from experiment, but the same does not hold true for the r_{32} and r_{21} values needed for computing the correction factors, because only intercept sizes are directly available from image analysis. On the other hand, Eqns.4.57 and 4.58 link r_{32} and r_{21} to l_{21} and l_{10} respectively. These results can be used to approximate the correction factors by only using functions of experimentally available quantities. In particular, it is possible to observe that limits of Eqns.4.57 and 4.58 can be computed for w_{ls} approaching zero and infinite. This will result in two *limiting* (though not bounding) values for the pro-

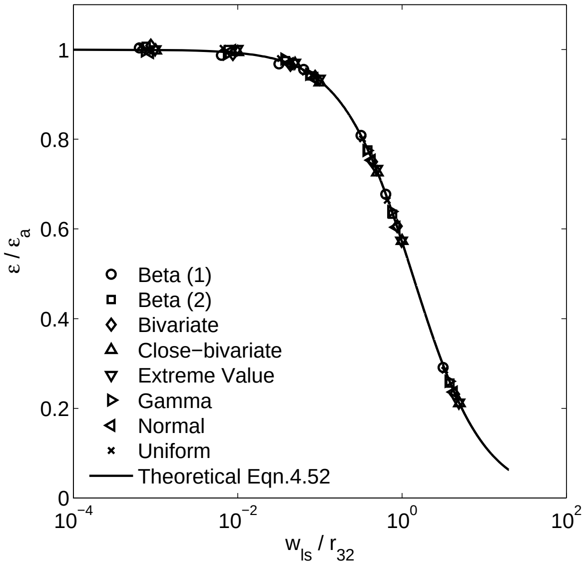

Figure 4.15: Hold up correction factor as a function of w_{ls}/r_{32} for different BSDs and theoretical prediction.

portionality between r_{32} and l_{21} (Eqn.4.65), and for the proportionality between r_{21} and l_{10} (Eqn.4.64).

$$l_{10} = \left(\frac{\pi}{4} \div \frac{r_{10}}{r_{21}} \right) r_{21} \tag{4.64}$$

$$l_{21} = \left(\frac{8}{3\pi} \div \frac{r_{21}}{r_{32}} \right) r_{32} \tag{4.65}$$

It is worth noting that the above quoted limiting values depend on the distribution shape. This is perfectly expected, since if an infinitely thick laser sheet is considered, only the actual bubble sizes are recorded, and therefore $l_{10} \equiv r_{10}$. For the case of Eqn.4.64 relevant to l_{10}, the limits above discussed can be fully assessed in Fig.4.18(a). Similar results are obtained analyzing the dependencies of Eqn.4.65, as reported in Fig.4.18(b).

As a simple (but reasonably realistic) case, by substituting the lower bounding values of Eqns.4.65 and 4.64, the theoretical correction factors can be computed as follows:

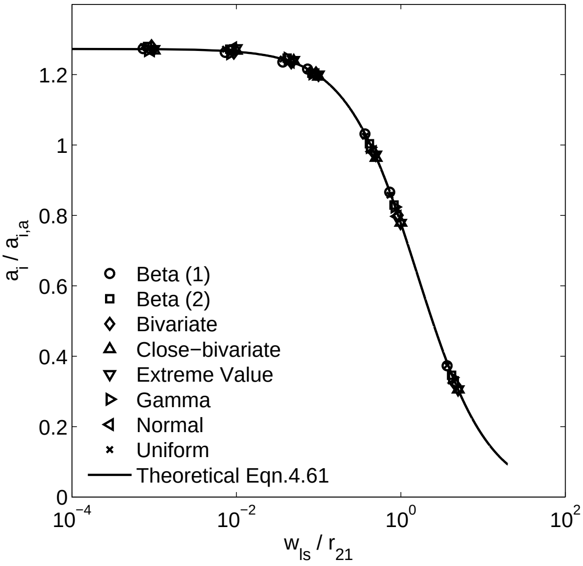

Figure 4.16: Specific interfacial area correction factor as a function of w_{th}/r_{21} for different BSDs and theoretical prediction.

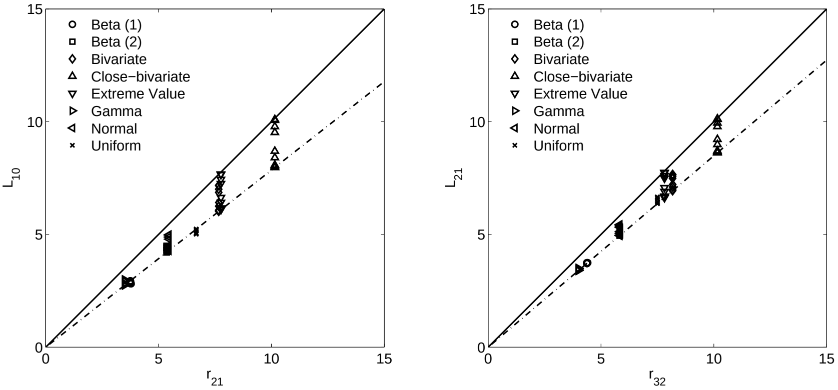

(a) (b)

Figure 4.17: l_{10} *versus* r_{21} (right) and l_{21} *versus* r_{32} (left).

$$f_\epsilon \cong \frac{1}{1+0.849\frac{3w_{ls}}{4l_{21}}} \tag{4.66}$$

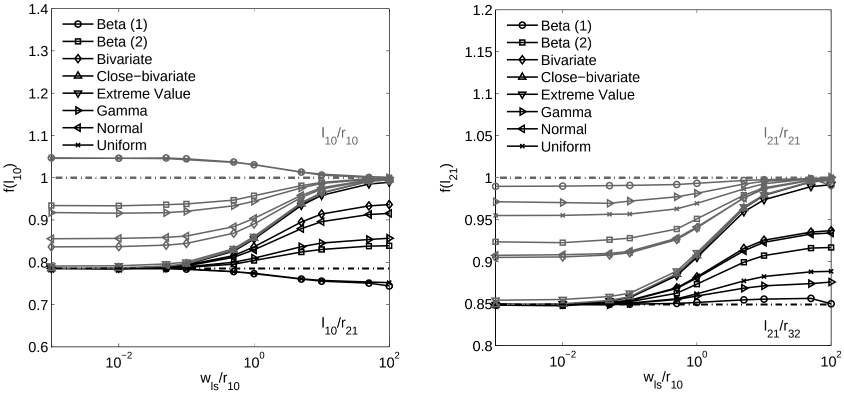

(a) (b)

Figure 4.18: l_{10} (right) and l_{21} (left): comparison with theoretical limits with w_{ls}

$$f_{a_i} \cong \frac{2}{\frac{\pi}{2} + 0.785\frac{w_{ls}}{l_{10}}} \tag{4.67}$$

In Fig.4.19 and 4.20 the comparison of pseudo-experimental data and the simplified theoretical correction curve are reported.

With these simple (yet effective) corrections, the l_{32} and the relevant correction factors for hold-up and interfacial area can be calculated for each region of the vessel image, and used for direct measurement of local gas hold-up and interfacial area from PIV images.

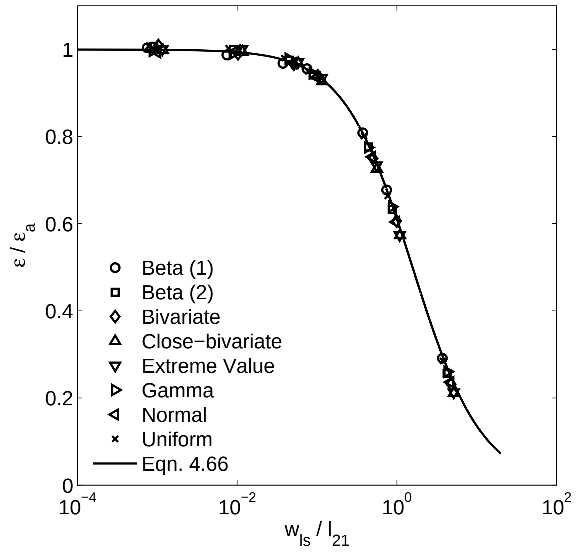

Figure 4.19: Approximated hold up correction factor as a function of w_{ls}/l_{21} for different BSDs.

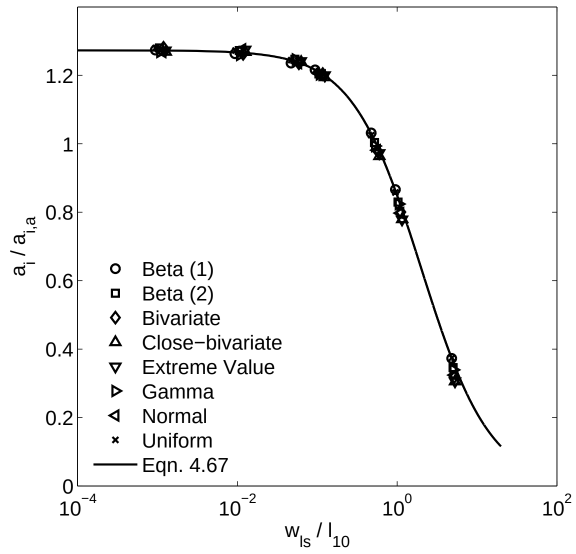

Figure 4.20: Approximated specific interfacial are correction factor as a function of w_{ls}/l_{10} for different BSDs.

5 Results

The procedure viability was checked by processing 1600 images obtained with the previously described experimental apparatus. It may be worth noting that collecting the 1600 images involved only few minutes of experimentation while much longer times were needed for the subsequent image processing The possibility of taking all images needed for each case in a few minutes allows to minimize the risk of fluid contamination, temperature changes, *etc.*, therefore increasing the accuracy of the results obtained. The image processing took about 6 CPU hours for each experiment on a Core 2 duo running at 2.33 GHz. It may be worth noting that for this type of computation parallelization is very easily accomplished by simply subdividing the total number of images to be processed among different jobs running on each available CPU.

In particular by merging results obtained over about $50x50$ pixel areas, the relevant local dispersion properties can be computed and reported in form of contour maps. The merging procedure is of course needed to obtain a sufficient bubble numerousness to guarantee statistical reliability of the reported datum. In particular, the vessel image was subdivided into non-overlapping regions that did not include any portion of masked zones (*e.g.* zones in which baffles or impeller were visible). For this last reason, the pixel extension of each region was somewhat different here and there from the above mentioned size of $50x50$ pixel. In such a way, any disturbance to measurements was virtually eliminated.

In Fig.5.1 data on local average intercept sizes L_{10} and L_{32} are reported for the same gas flow rate and impeller speed of 300 and $400rpm$ respectively.

A large average bubble diameter near the impeller region is clearly visible in the data distribution here reported. This is mainly due to the fact that the automated procedure can measure as a very large bubble the cavity formed in the rear-face of the impeller. along the impeller stream it is possible to observe a bubble plume following the up-flowing recirculation pattern towards the liquid surface and a second stream following the liquid recirculation loop below the impeller. The first plume is slightly skewed toward vessel center probably due to centrifugal field effects. It is worth noting

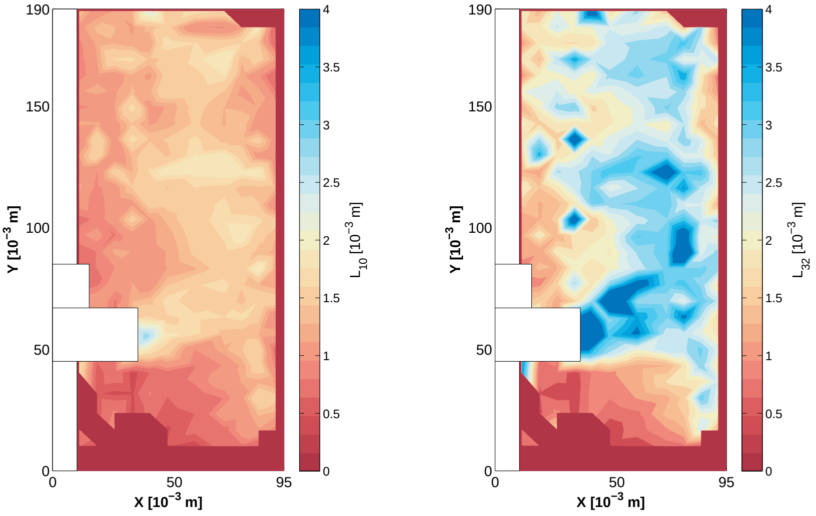

(a) $L_{10}, 300rpm$ (b) $L_{32}, 300rpm$

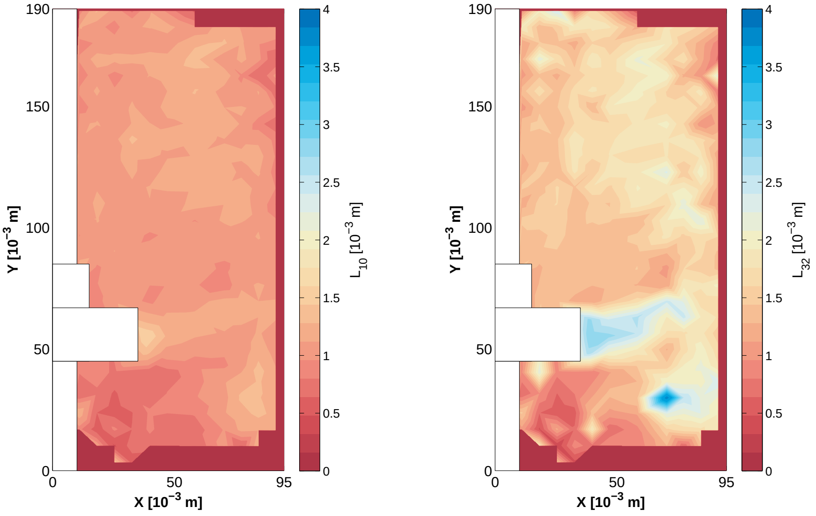

(c) $L_{10}, 400rpm$ (d) $L_{32}, 400rpm$

Figure 5.1: Average intercept radii maps in the case $Q = 0.3l/min$

that no appreciable bubble enlargement occurs along the up-flowing bubble path. Near the impeller shaft, a decrease in bubble average diameter is found, due to the fact that in this region only relatively small bubbles are successfully drawn in the down-flowing section of the upper recirculation path. By analyzing the average bubble intercepts for the case at $Q = 0.3l/min$, $N = 400rpm$, it is possible to observe a decrease of average bubble intercept in the whole vessel, as expected if a break-up driven mechanism for bubble size evolution is assumed. At this impeller speed is also possible to observe a slight bubble size increase in the recirculation loop region below the impeller height, that is likely to be due to some coalescence due to relatively high bubble concentration in this region linked to centrifugal field directing bubbles towards the center of the recirculation loop. It is moreover possible to observe a bubble size decrease along the high turbulent discharge region of the impeller.

By means of the numerical procedures discussed in Chapter 4 is also possible to infer bubble size distributions from the known VISDs. Notably, the analysis can be applied only to macro areas of the vessel, as indicated in Fig.3.1, to have sufficient intercept numerousness to reconstruct data.

Notably, both at 300 and $400rpm$, about half of the sample has dimension lower the $1mm$, while most of the difference in bubble size distributions is in bubbles having size larger than $2mm$, as can be seen in Fig.5.2. The analysis of relevant average sizes in the same figure confirms the previous discussion on Figs.5.1. In all cases analyzed positively skewed distributions are found.

As it concerns gas hold-up, although in principle an extremely detailed information can be collected (an average hold-up datum in each of the 1280*1024 pixel locations) once again the 1600 images analyzed were insufficient for getting statistically stable results and some data merging was needed to obtain meaningful results. In particular by merging results obtained over $\approx 50x50$ pixel areas the local gas hold-map map shown in Fig.5.4(a) was obtained. Notably, the local correction factor reported in Eqn.4.66 must be applied pointwise to the map reported in Fig.5.4(a), to infer the actual volumetric hold-up map. This latter is reported in Fig.5.4(b). Two examples of local hold up correction factors calculated for the investigated cases at $0.3l/min$ are reported in Fig.5.3. As it can be seen, the correction applied modifies substantially the relevant raw data

As it is possible to observe, the technique here proposed allows fairly detailed information on gas hold-up to be obtained, despite the suitable data binning needed to increase statistical reliability. It is possible to observe the gas plume in the upper section of the vessel slightly directed towards impeller shaft because of the centrifugal

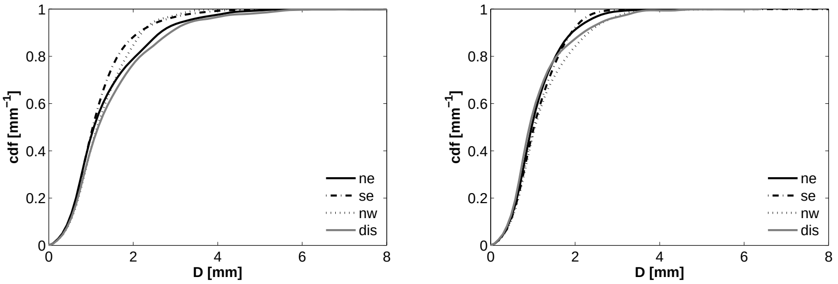

(a) $300rpm$ (b) $400rpm$

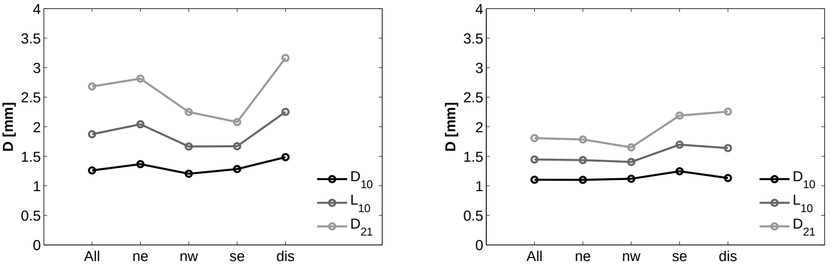

(c) $300rpm$, averages (d) $400rpm$, averages

Figure 5.2: Bubble size distributions in different region of the vessel in the case $Q = 0.3l/min$

field, and the hold up increase in the recirculation loop below the impeller plane. The gas leaving the impeller is not parallel to vessel bottom, but upward oriented. This is expected when a large cavity regime occurs because of the decreased pumping efficiency of the turbine. Notably, an increase of impeller velocity leads to more bubble being recirculated in both recirculation paths placed above and below the impeller plane. This is fully consistent with the increase of average liquid velocities in the vessel.

The apparent local interfacial area map reported in Fig.5.5(a) was produced by applying the previously described averaging procedure to local interfacial area raw data. After application of the relevant correction factor (Eqn.4.67) the final result reported in Fig.5.5(b) was obtained. The same observations reported for relevant hold up maps still applies in term of overall flux behavior. It is worth noting that when impeller speed is increased, a more uniform distribution of specific interfacial era is achieved. The value of interfacial era associated with bubbles in the near-impeller recirculation

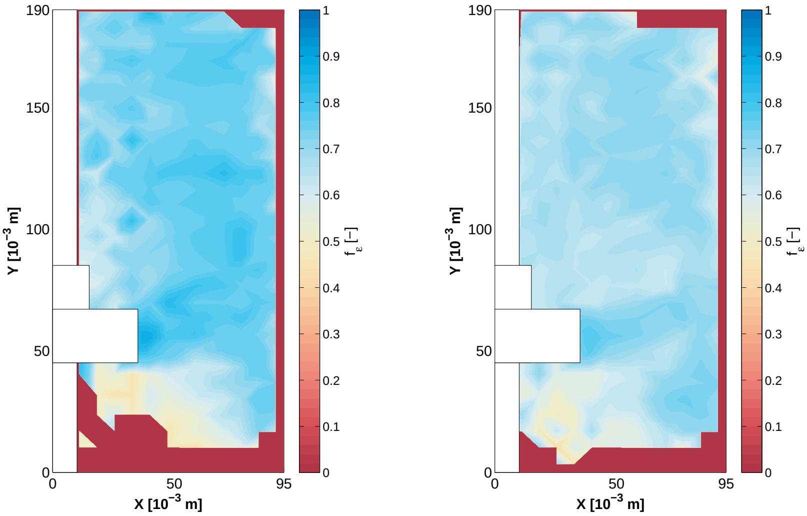

(a) f_ϵ, $300rpm$ (b) f_ϵ, $400rpm$

Figure 5.3: Apparent and actual hold up correction factors map in the case of $Q = 0.3l/min$

loop is also increased.

For the sake of a more concise comparison that can be obtained with the proposed technique, in Figs.5.6-5.9 the overall volume averaged data about the measured dispersion properties are reported together with relevant literature correlations. Notably, these results can only be qualitatively compared with the available correlations on average dispersion properties in agitated vessels, in particular with those proposed by Calderbank (1958). In fact, even if the in-plane data could be translated to relevant volumetric data, it should be expected that quite different distributions of gas volume fraction or average bubble diameter exist over different diametrical planes other that the one here analyzed. In particular, only a qualitative comparison with existing correlations can be proposed, since some well known gas accumulation regions are not considered in this analysis, *e.g.* the baffle regions. As the overall data reported in the following figures were computed by assuming a perfect axial symmetry, a condition that is actually far different from the real one.

In Fig.5.6, the average bubble diameter d_{32} are reported as a function of a suitable group derived from the equation proposed by Calderbank (1958).

A fitting on experimental data show a dependence on specific power input with

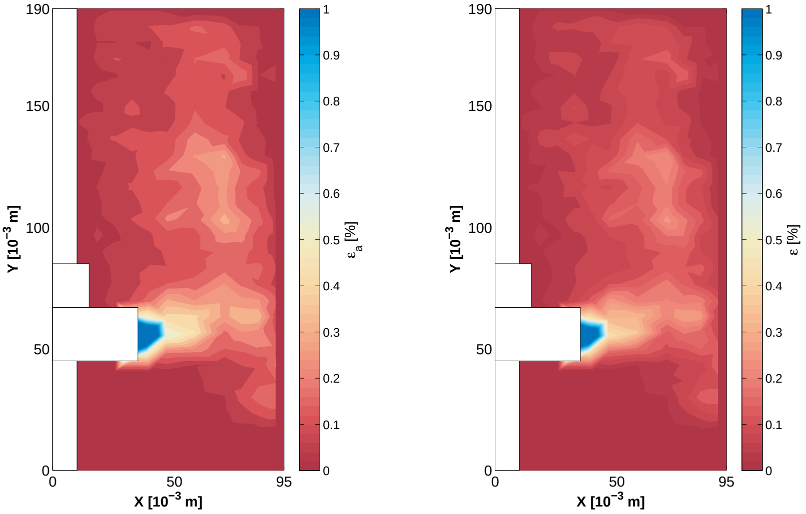

(a) Intercept ϵ, $300rpm$ (b) Actual ϵ, $300rpm$

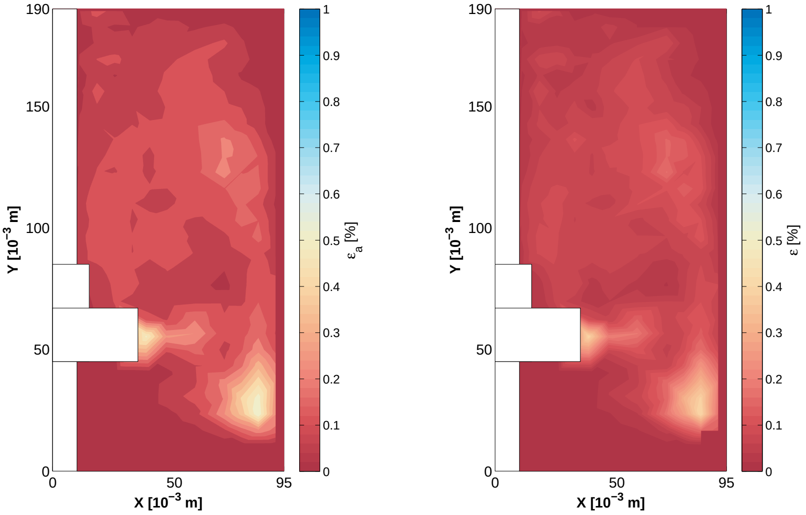

(c) Intercept ϵ, $400rpm$ (d) Actual ϵ, $400rpmp$

Figure 5.4: Apparent and actual hold up map measured in the case $Q = 0.3l/min$

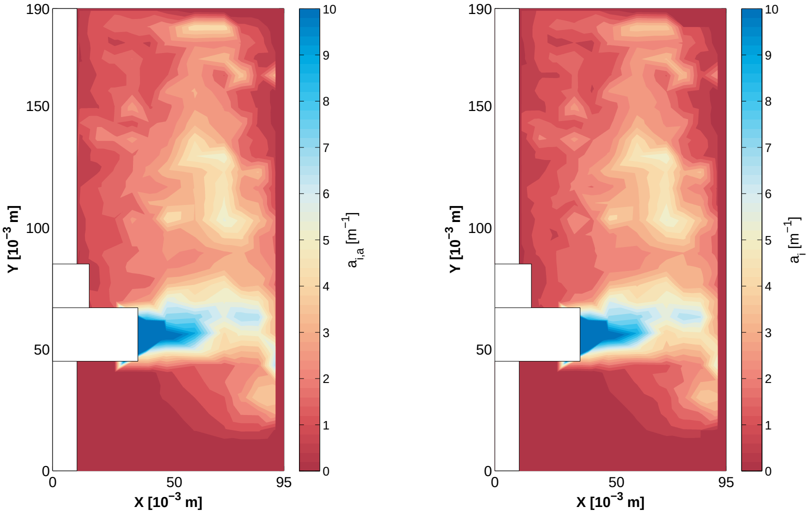

(a) Apparent a_i, $300rpm$ (b) Actual a_i, $300rpm$

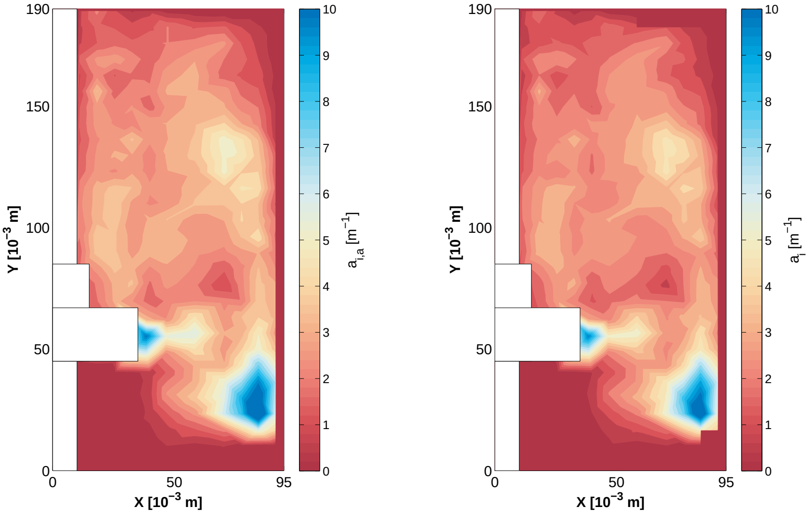

(c) Apparent a_i, $400rpm$ (d) Actual a_i, $400rpm$

Figure 5.5: Apparent and actual interfacial area maps measured in the case $Q = 0.3l/min$

exponent -0.44, that is in fair agreement with the exponent -0.4 obtained by Calderbank (1958), and somewhat different from that obtained by Bouaifi et al. (2001), equal to -0.2. It is worth noting that a negligibly low exponent is found for the superficial gas velocity (equal to 0.02).

$$d_{32} \propto \left(\frac{P_g}{V}\right)^{-0.44} v_s^{0.02} \tag{5.1}$$

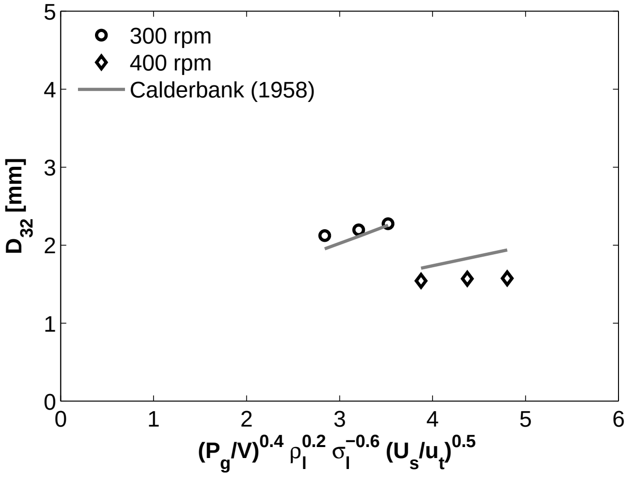

Figure 5.6: Comparison of average dispersion data: average Sauter diameter.

The average bubble diameter measured in different regions of the vessel is reported in Fig.5.7. The average diameter in the NE region (upper part of the vessel near lateral wall) shows a small dependence on gas superficial velocity (the average diameters remains practically unchanged at fixed impeller speed), while a strong dependence on impeller speed is clearly visible. In the NW region (near the shaft), the average bubble diameter appears to increase while increasing gas superficial velocity and decrease when increasing impeller speed. This latter phenomenon in particular depends on the decrease of average bubble diameter in the whole vessel already discussed. Notably, the average bubble diameter in the SE region (below the impeller plane and near the vessel wall) decreases with superficial gas velocity and increases with impeller speed. This can be explained by assuming that at fixed impeller speed an increase of gas flow tends to increase the cavities size, therefore lowering the average liquid velocity, and in turn the average size of entrained bubbles in the relevant recirculation loop. Conversely, an increase of impeller speed leads to an increase of average liquid velocity

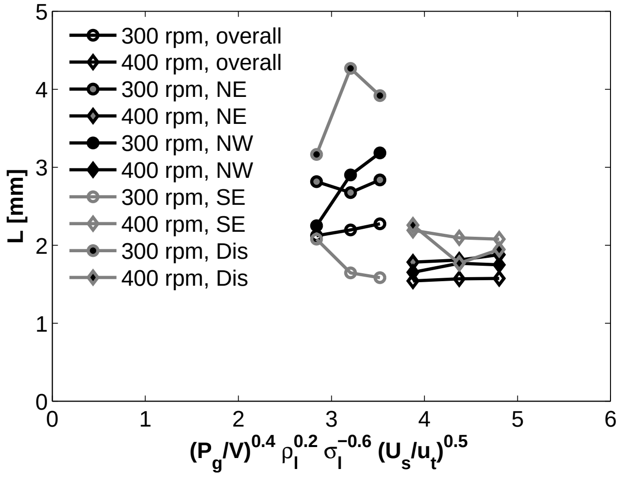

Figure 5.7: Comparison of average dispersion data: average Sauter diameter in different vessel locations.

and in turn an increase of entrained bubble sizes. The analysis of average sizes in the discharge regions is somewhat affected by the measurement of cavities already discussed, but a decrease of average bubble size in this region when increasing impeller speed is clearly observable.

In Fig.5.8, the measured average specific interfacial area is reported as a function of a suitable group derived by Calderbank (1958). By fitting the experimental data here obtained with a power law the following dependencies on specific power input and gas superficial velocity are obtained:

$$a_i \propto \left(\frac{P_g}{V}\right)^{0.28} v_s^{0.78} \tag{5.2}$$

Notably, these exponents are different from those obtained by Calderbank (1958), respectively equal to 0.4 for specific power input and 0.5 for superficial gas velocity.

The analysis of volume averaged gas volume fraction pointed out an unexpected trend, i.e. a decrease of ϵ whit the specific power input, that is in contrast with previous literature findings discussed in the relevant chapter.

Notably, this effect should be analyzed more in depth, since it possibly depends on the procedure and hypotheses used for average value calculation: in practice, as already mentioned, some zones of gas accumulation were not considered in this preliminary test of the LIF-SABS technique.

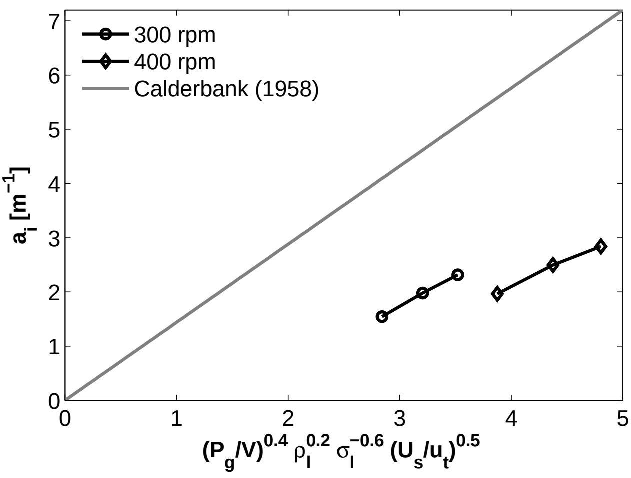

Figure 5.8: Comparison of average dispersion data: specific interfacial area

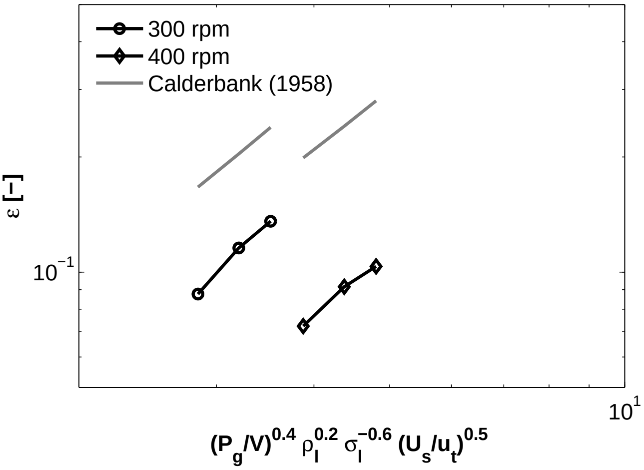

Figure 5.9: Comparison of average dispersion data: gas volume fraction

6 Concluding remarks

Concluding, a novel technique has been developed for measuring local bubble properties in gas liquid dispersions. The technique is based on the use of a fluorescent liquid phase coupled with a laser sheet and a purposely developed digital image analysis routine. It may be regarded as being particularly reliable thanks to its ability to discard from the analysis visible, yet out-of-plane, bubbles. It can be conveniently employed for measuring local features of gas liquid dispersions, such as bubble size, gas hold-up and interfacial area, provided that sufficiently dilute dispersions are investigated.

A novel reconstruction procedure has been developed for inferring actual Bubble Size Distributions in gas-liquid contactors from images obtained by illuminating the dispersion with laser sheets of arbitrary thickness. The procedure implies the solution of a simple linear system and has been found to be viable, effective and robust. Notably, the use of thick laser sheets was found to improve the reconstruction quality. The procedure has been tested with a number of Bubble Size Distributions, including quite demanding cases such as perfectly bivariate distributions. A thorough sensitivity analysis was also conducted, for highlighting bubble numerousness and resolution requirements for stable reconstruction results. The effects of adding a gaussian noise on the experimental measurements was also successfully tested.

Moreover, a theoretical method for translating information in light sheet images of gas-liquid dispersion into maps of local bubble hold-up and specific interfacial area was set up. To this end, assuming that images had already been suitably analyzed in order to recognize gas- and liquid-occupied pixels, it was shown how information on apparent local gas hold up and interfacial area could be derived. It was also shown that this does not coincide in general with the relevant physical properties. Theoretical correction equations to convert the above mentioned apparent values into the relevant physical values were obtained. The method fully accounts for light sheet thickness and is independent of Bubble Size Distribution shape.

The whole technique viability was tested in the case of a gas-liquid stirred tank. The preliminary results obtained were found to be in good agreement with expectations.

Part II

Fluidization

7 Introduction to fluidized beds

Gas-solid flows are often encountered in industrial processes. Discharge from hoppers, pneumatic transport of large quantities of powder are some of the industrial applications, where gas-solid flows are involved. In the area of chemical processes, fluidization is actually a widely employed technology for continuous operation of chemical reactors.

The first large-scaled, commercially significant use of fluidized beds was for the gasification of powdered coal, invented in 1922. The early use of fluidized beds for catalytic cracking processes expanded to applications outside of the petroleum industry in the 1940s, at which point the use and development of the fluidization technology was limited by a lack of understanding of the processes actually taking place inside the bed. In hope of finding a combustion system suitable for low grade coal and oil fuels that could not be burnt in conventional furnaces, fluidized bed combustion was developed in the early 1960s, but it was not commercialized until the early 1980s. At present, fluidization technology is widely used in a broad range of applications, *e.g.* chemical and catalytic reactors, combustion and gasification of solid fuel, and the drying of granular solids; it is now of interest to extend its operational ranges and areas of application.

The success of fluidized bed processes in chemical, petrochemical, food and pharmaceutical industries is due to the fact that a fluidized system enables high transport rates between the solid phase and the gas phase with respect to fixed bed operating at the same pressure loss, giving at the same time the possibility of easy handling of the particulates solids involved.

Fluidization may be defined as *the operation by which solid particles are transformed into a fluid-like state through suspension in a gas or a liquid.*

The industrial adoption of fluidized beds in the process industry is mainly related to to the following advantages:

- The smooth, liquid-like flow of particles allows continuous automatically controlled operations with easy handling.

- The rapid mixing of solids leads to close-to-isothermal conditions thought the reactor; hence the operation can be controlled simply and reliably.
- In addition, the whole vessel of well-mixed solids represents a large thermal flywheel that resists rapid temperature changes, responds slowly to abrupt changes in operating conditions, and gives a large margin of safety in avoiding temperature runaways for highly exothermic reactions.
- The circulation of solids between two fluidized beds makes it possible to remove (or add) the vast quantities of heat produced (or needed) in large reactors.
- It is suitable for large-scale operations.
- Heat and mass transfer rates between gas and particles are high when compared with other modes of contacting.
- The rate of heat transfer between a fluidized bed and an immersed object is high; hence heat exchangers within fluidized beds require relatively small surface areas.

Its disadvantages are:

- For bubbling beds of fine particles, the difficult to describe flow of gas, with its large deviations from plug flow represents inefficient contacting. This becomes especially serious when high conversion of gaseous reactant or high selectivity of a reaction intermediate is required.
- The rapid mixing of solids in the bed leads to no uniform residence times of solids in the reactor. For continuous treatment of solids, this gives a no uniform product and poorer performance, especially at high conversion levels. For catalytic reactions, the movement of porous catalyst particles, which continually captures and release reactant gas molecules, contributes to the back mixing of gaseous reactant, thereby reducing yield and performance.
- Friable solids are pulverized and entrained by the gas, and must be replaced.
- Erosion of pipes and vessels from abrasion by particles can be serious.
- For no catalytic operations at high temperature the agglomeration and sintering of fine particles can require a lowering in temperature of operations, thereby reducing the reaction rate.

When a fluid at low superficial gas velocities passes through a bed of solid particles placed on a porous distributor plate from the bottom, the particles lay on each other and they are not moved by the fluid; they are said to be in fixed bed state. The height of the bed remains constant and pressure drop over the bed linearly increases as the inlet gas velocity increases. Fluidization occurs when the forces exerted by the fluid to the particles counteract the particle weight. The gas superficial velocity at which the solid particles are just individually suspended is called minimum fluidization or incipient fluidization velocity U_{mf} and is defined as the ratio of the fluid volumetric flow rate Q_{mf} divided by the cross sectional area of the fluidization column. At this stage, the bed on the whole is just supported by the flowing gas and acquires fluid-like properties, free to flow and deform, keeping a horizontal level when tilted and allowing low-density objects to float on the bed surface. The pressure drop over the fluid-bed remains constant as the gas velocity is increased and its value equals the weight of all particles in the bed.

Fluidization of solid particles in liquids and gases leads to a variety of different behaviors (Fig.7.1). For liquid-solid fluidization, as the liquid velocity increases beyond the incipient fluidization point, the solid bed continues to expand as if it were an elastic continuum stretching under the dynamic forces of augmented flow, until, near the terminal velocity of the particles, the solid particles are suspended sparsely. Throughout this process of liquid velocity increase, the solid particles are dispersed quite uniformly, fully exhibiting their discrete behavior, essentially independent of one another. Therefore, liquid-solid fluidization was named particulate (Kwauk and Li, 1996).

Similar particulate fluidization behavior is encountered also for gas-solid systems in the case of relatively fine or light particles at inlet gas velocities close to the incipient fluidization velocity. More often, especially when relatively coarse particles with close size distribution are used, fluid velocity increment beyond incipient fluidization (or, for the above mentioned aeratable gas-solid systems exhibiting smooth expansion, incipient bubbling), is accompanied by the formation of bubbles, or cavities with hardly any solid particles in them. In general, gas flow beyond incipient incipient fluidization or incipient bubbling mostly reports to bubble flow, thus implying that gas velocity through the surrounding dense gas-solid bed remains essentially at the value for incipient fluidization or bubbling. Aggregation of solid particles into a dense continuous phase, making room for the passage of most of the gas in excess of incipient fluidization or bubbling through a bubbling discontinuous phase, bespeaks the two phase nature of gas-solid fluidization. Such a phenomenon of gas-solid systems was designated aggregative.

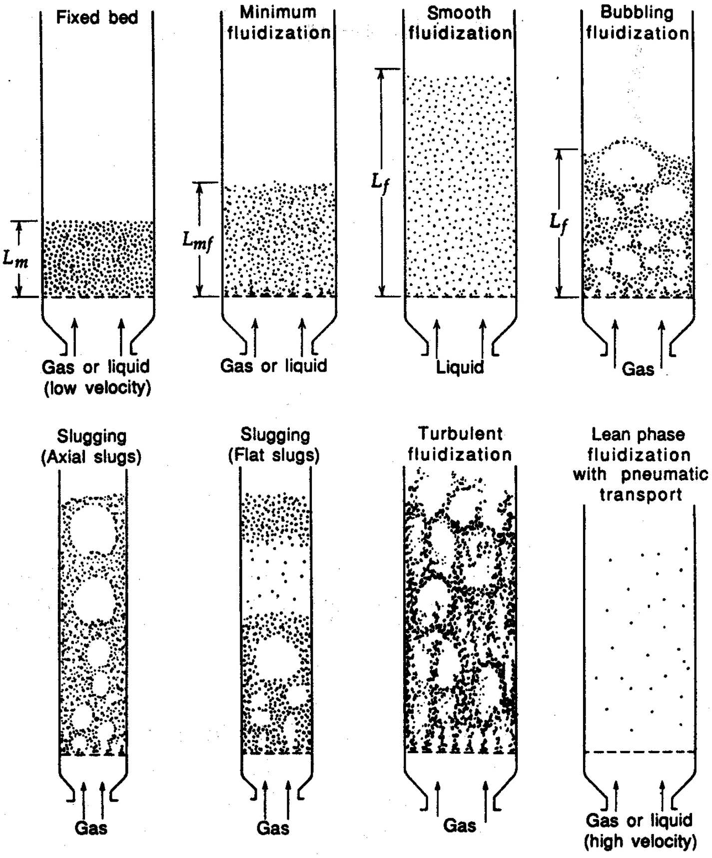

Figure 7.1: Fluidized Bed Regimes.

Referring in particular to gas-solid fluidization, gas voids, conveniently termed bubbles, may have different shapes from almost spherical to wide slugs depending on the material being fluidized, on the inlet superficial gas velocity and on the geometry of the bed (mainly on the ratio of height to width of the vessel containing the bed). The superficial gas velocity at which the first bubble appears is called minimum bubbling velocity, U_{mb} and the comparison between its value and the value of U_{mf} is used to distinguish between aeratable and non-aeratable particles.

For aeratable particles, the value of the U_{mb} is greater than that of U_{mf}, and the fluidization proceeds as an homogeneous suspension from the minimum fluidization velocity to the minimum bubbling velocity with the height of the bed as a function of the gas superficial velocity (also a typical of liquid fluidized beds). In the case of non-aeratable particles, the fluidized bed is quite unstable (typical of gas fluidized beds with particle size in the range of 100 to $500 \mu m$) and the bubbling regime starts as soon as the bed is fluidized, *i.e.* $U_{mb} = U_{mf}$. In analyzing the behavior of bubbling fluidized beds, one may distinguish between the bubble phase, *i.e.* the gas voids containing virtually no bed particles, and the emulsion phase, consisting of particles fluidized by interstitial gas. A bubbling bed may be conveniently defined as a bed in which the bubble phase occupies discontinuous regions within the emulsion phase. When the superficial gas velocity is further increased or in fluidizing a tall, narrow bed of solids, bubbles formed at the distributor may grow to the bed diameter to form slugs.

For beds of fine particles, particles will rain at the bed walls around the slugs. These are called axial slugs. At higher gas velocity and with either angular particles or rough vessel wall, the rising slugs tend to adhere to and slide up the wall. These are called wall slugs. With large particles (like Geldart group D powders), another mode of slugging is seen. Here the bed separates into slices of emulsion phase separated by gas. These slices of gas and emulsion phases rise up the bed, matched by a continuous rainfall of solids from slice to slice. These are called flat slugs.

A further increase of the inlet gas velocity would cause the volume occupied by the bubble phase to become higher and higher until the emulsion phase no longer forms a continuous medium between discrete bubbles. At this point the fluid-bed is at turbulent conditions, which are typical for risers in circulating gas fluidized beds. This phenomenon, also referred as phase inversion, leads in practice to the formation of a new two phase structure, with strands or clusters of solids, as a discontinuous phase dispersed in a dilute continuous phase of a population of sparse solid particles (Kwauk and Li, 1996).

For fine particles, the increase in gas velocity causes the bubbling action to become increasingly vigorous and is accompanied by increasing pressure fluctuations, as measured just above the distributor. These fluctuations peak decrease sharply and level off and this progression correspond to the transition from bubbling to turbulent fluidization.

At higher superficial gas velocities, the solid particles start to be conveyed out of the column and this is known as hydraulic or pneumatic transport. The superficial gas velocity, at which the pneumatic transport starts, is the so called terminal settling velocity of one unhindered particle in that gas, *i.e.* u_t (Bird et al., 2002). This velocity represents the velocity at which a single particle would fall in a stagnant fluidizing medium when no net force is applied to the particle (*i.e.* the sum of buoyancy and drag counteracts the particle weight). The unhindered conditions refer to the presence of one particle only, completely submerged in the fluid and well far from any another solid surface, like the walls of the vessel containing the fluid. Of course, the equilibrium condition experienced by a particle falling at velocity u_t in a stationary gas is equivalent to that of a motionless particle suspended in a upwardly flowing gas with velocity u_t. The operative range of inlet gas superficial velocity for fluidizing a bed of solids may be then defined by the value of the minimum fluidization velocity, which represents the lower limit, and by the terminal fall velocity that is the upper one.

The geometry and the size of the unit are other key points for the operation of fluidized beds. The relation between the fluidization behavior and the particle system properties were investigated and classified by Geldart (1973), who proposed an empirical classification in the form of a plot of density difference $\rho_p - \rho_f$ against particle diameter d_p for air at ambient conditions. Geldart identified four typical groups of materials fluidized with air at ambient conditions that he termed as A, B, C and D, as shown in Fig.7.2.

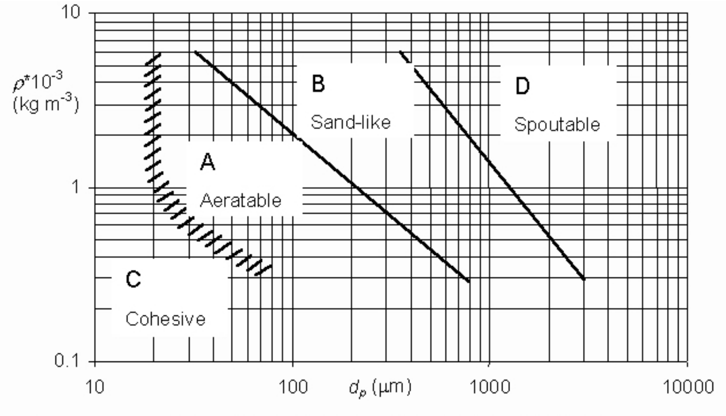

Courtesy: http://www.fi.uib.no/~hoffmann/papershtml/npt00/npt99.html

Figure 7.2: Geldart classification of powders fluidized by air at ambient conditions.

C : particles, which are cohesive in any way, belong to this group. Their fluidization is extremely difficult. Instead of fluidize, the powder tends to lift as a plug or forms channels, *i.e.* the gas passes through interconnected cracks extending from the distributor to the bed surface. The gas cannot really separate the particles and mechanical stirring or vibrations, which break up the stable channels, are sometimes employed in order to allow their fluidization.

A : (aeratable) ordinary cracking catalyst is a typical example of powders of this group ($d_p < 70 \mu m$, $\rho_p < 1500 Kg/m^3$). They show a net range of homogeneous fluidization behavior between U_{mf} and U_{mb}. At gas velocity above U_{mb} bubbling starts to occur. A maximum bubble size dependent on the particle diameter does appear to exist ad most bubble rise more rapidly than the interstitial gas.

B : (bubbling) this group contains most of the materials of the medium-range size and density ($d_p = 150 \div 500 \mu m$ $\rho_p = 1500 \div 4000 Kg/m^3$), being sand a typical example. Their main feature is to have $U_{mf} = U_{mb}$ and therefore to start bubbling just after being fluidized. There is no evidence of a maximum bubble size and most bubbles rise more quickly than the interstitial gas.

D : (spoutable) is made up of large or very dense particles ($d_p > 500 \mu m$, $\rho_p > 4000 Kg/m^3$). When bubbling all but the largest bubbles rise more slowly than the interstitial gas so providing a by pass way for the fluidizing gas. Segregation by size is likely when the size distribution is broad, even at high gas velocities.

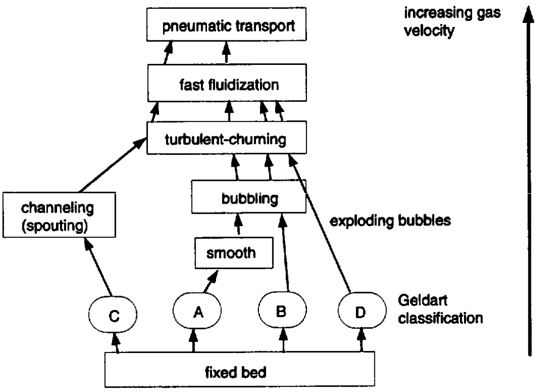

Figure 7.3: Kunii and Levenspiel classification of gas-solid fluidization regimes (Kunii and Levenspiel, 1991).

The operative range of inlet gas superficial velocity for fluidizing a bed of solids may be then defined by the value of the minimum fluidization velocity, which represents the lower limit, and the terminal fall velocity that is the upper limit. A classification of gas-solid fluidization regimes based on particles properties and inlet gas velocity was proposed by Kunii and Levenspiel (1991) and reported in Fig7.3

8 Literature review on bubbling fluidized beds

Industrial applications of fluidized beds utilize the high density of particle surface area that exist in the bed for operations such as drying, heat transfer, combustion, and chemical reaction between the gas and the particles. The high degree of mixing between the particle and the gas flowing through them can improve significantly the efficiency of a process. Mixing within the bed is driven by the particle-free voids of bubbles that form when the gas flow rate exceeds the superficial velocity of minimum bubbling. The bubbles ensure that the particles are circulated throughout the bed so that properties and process condition may be considered as uniform. They have a considerable importance in the fluidized solid-gas systems because they govern hydrodynamics and efficiency of the operation for which the bed is used, as well as providing good heat transfer (Bokkers et al., 2004). The fluidization quality of a bed is, therefore, highly dependent on bubble distribution and bubble physical properties in a bed. Ideally, for there to be good quality fluidization the population of bubbles in a bed should be large, but the bubbles should be small in size, and homogeneously occupy the bed (Lim et al., 2007).

8.1 Measurement techniques

The gas contained within the bubbles only partially satisfy its prime purpose of interacting with the materials in the bed. As a matter of fact the gas flow in excess of that required to maintain the dense phase at minimum fluidization conditions flows through the bed in the forms of bubbles and through flow (Johnsson et al., 1991).

Much has been written about bubbling phenomena in fluidized beds over the last years. In fact a good understanding of the bubble hydrodynamics is necessary to understand bubble-related phenomena such as solid mixing and segregation, reaction conversion, heat transfer tubes and particle entrainment in beds operated in the bubbling regime. Bubble size velocity, velocity, shapes and flow patterns are of key interest in bubbling hydrodynamics. These properties have been extensively measured experimentally by various methods. The experimental methods and finding have been summarized in several review articles (Davidson et al., 1985; Cheremisinoff, 1986; Yates and Simons, 1994):

- **Photographic Techniques**: Cineographic and still photography are among the most widely used techniques for studying bubble behavior. Photographic methods are generally limited to studies in two-dimensional cold models. Although semi-cylindrical columns are a closer approximation to actual systems, photography only provides information on wall-controlled phenomenon. Despite shortcomings in obtaining meaningful statistical properties on the bubble shape, effective size and volume, and rise velocity that can be related to actual reactor systems, many investigators have adopted these methods. Two key assumptions are needed in order to evaluate an effective bubble size, namely, the shape of any bubble observed is assumed to represent the central section, of a cylindrical bubble, and an equivalent size must be based on the diameter of a sphere which possesses the same volume as the bubble. These assumptions, along with wall distortion effects, impose some limitations to data accuracy.

- **X-rays techniques**: In commercial reactors where photographic methods generally cannot be implemented, direct observation of bubble characteristics can be made by using X-rays. Rowe and Partridge (1965) have employed X-rays for measuring bubbles. The principle difficulties in extending these techniques to measurements in commercial units are transmission limitations through thick-walled vessels and poor resolution of superimposed bubbles over the plane of focus. By this last point, it is meant that there are difficulties in resolving individual bubble sizes due to the superposition of bubbles at various depths of field. Photographs obtained from beds under profuse bubbling conditions are often distorted by this fact, preventing the determination of a statistically representative bubble size.

- **Light Transmission**: Light-scattering and fiber optical methods have been successfully applied in laboratory-scale testing. With both methods, the local bubble size distribution is perceived as a probability density function of a characteristic size such as the bubble radius that can be related to Maxwell-Boltzmann statistics, assumed to be valid for the distribution of the bubble energy taken proportional to its surface area. A weight fraction could be introduced to reckon with the geometrical configuration of the light probe. Again, the assumption of spherical bubbles is applied to the calculation of size. The experimental detection of the bubble size is based on the interaction between a horizontal light beam and the fluidized solids. When the fluidized solids are present within the beam, light is scattered and attenuation occurs; however, if only gas is present, there is no attenuation of the focused light. The technique has the disadvantage that its signal resolution is effected by bubble passage through the line of light transmission and, hence, is subject to providing a gross measurement when the detector and transmitter are far apart. In contrast, fiber optics, in the form of miniaturized light probes, provide in situ localized measurements. One disadvantage with the above optical techniques is that they are in situ measurements, whereby the probe distorts the flow phenomenon at the measuring point. This may be overcome by the use of laser beams transmitted through a transparent window of the test vessel.

- **Pressure Fluctuations**: Pressure fluctuations obtained from sensitive transducers located along the height of a fluid bed can provide information on the dense bed behavior as well as give information on bed expansion. A pressure transducer provides an electrical signal that is proportional to the pressure at the tip of the sensor. The two most important statistical properties of pressure fluctuations are the power spectrum and the mean amplitude of pressure fluctuations. The power spectrum shows the distribution of energy with the frequency and can be described by the power density function in terms of the autocorrelation function for the time lag of the signal. The accuracy of data and proper interpretation of pressure fluctuations largely depends on the transducer sensitivity and the sampling time interval selected for conversion of the voltage analog signals to the digital form. The sampling interval must be specified so as to ensure a good quality and undistorted character of the measured-bed frequencies. Both criteria must be calibrated to the specific system under investigation.

- **Electromagnetic and Acoustical Wave Transmission**. There are several techniques based on the transmission/attenuation of low level/short wavelength forms of radiation. The first of these is gamma rays which are electromagnetic waves characterized by short wavelengths and high frequencies. They are measured in units by radiation intensity in air. The basis of this detection technique involves an interaction of the radiation with the detection device to produce an ionizing reaction. The degree of ionization can be measured by using an appropriate electronic scheme. Two forms of detection are employed, namely, (i) a measurement of the number of interactions of radiation with the detector and (ii) measurement of the total effect of the radiation. The former is a counting process in which the energy level of the radiation is ignored and, hence, is best-suited for detecting the bubble frequency. The latter is characterized by a mean-radiation level, which can be related to bed voidage.

- **Electroresistivity Measurements**: Measurable differences between air and a packed bed of solid granulates form the basis for this technique, where point measurements of conductivity, capacitance, resistance/impedance, or inductance relate to the local state of fluidization. As an example, a closely packed volume of coke particles has a measurable resistance that can be on the order of several hundred ohms, whereas, the resistance of air is practically infinite. Unfortunately, the resistance of impedance of the volume of solids is a function of the packing arrangement of the particles. Thus, the response of an appropriately designed sensor located in situ to the bed will be comprised of a signal that contains information on both the bubble- phase and local porosity fluctuations of the solid particles.

- **Thermal Techniques**: Thermal and constant-temperature anemometry techniques have also been applied to indirectly detect bubbles in fluid beds. The measurement principle is based on the fact that the probe's heat-transfer coefficient in the emulsion phase is significantly greater than in the bubble phase. Consequently, when the probe is in the emulsion phase, its temperature decreases, resulting in an increase in the resistivity of the probe.

Experimental techniques are therefore applied to the study of the bubble behavior and particulate mixing throughout the bed. Investigations of bubble properties and dynamics are generally aimed at obtaining information on the following:

1. the onset of fluidization and the minimum bubbling state;

2. distributor dynamics, *i.e.* gas jet penetration and the formation of bubbles;

3. bubble interaction, *i.e.* bubble breakup and coalescence, its effect on mean bubble residence time within the bed, and the radial and axial distributions of bubble flow; and

4. bubble characteristics, *i.e.* bubble shape, bubble size distribution, and the attainment of mean and maximum stable sizes. This information relates not only

to the overall quality of fluidization and controls gas to solid exchange coefficients but establishes limits of bed expansion. Bubble characteristics depend on the physical properties of the particulates, namely particle size distribution, particle shape and bulk densities. Of interest within the bed are the dynamics of particle-particle and particle-bubble interactions. Specific information to gain understanding on are as follows:

- particle entrainment and circulation within the bubbles, this property contributes to bubble breakup and particle carryover into the freeboard region;
- particle segregation-in some commercial scale reactors (*e.g.*, coal gasifiers and fluid bed shale retorts) wide size distribution particles may be used; segregation within the bed can occur resulting in unfluidized regions which could adversely affect reaction kinetics and create localized-bed temperature maldistributions;
- particle-particle interaction, this often results in attrition which can cause the fluidization regime to change, as well as contribute to higher entrainment in the freeboard; the reaction kinetics of a process may not attain steady state in a bed undergoing transient flow behavior;
- particle mixing - *i.e.* the movement of particles and the overall turnover rate of solids defines their degree of mixedness which in turn provides surface renewal for transport processes between phases;
- residence time distribution, also an indication of the degree of mixing of solids; in particular, residence time distribution characterizes the tendency to back-mix the flow of solids and hence affects overall reaction kinetics.

Nevertheless, there is still room in bubbling dynamics analysis: in practice, the principal difficulty in analyzing fluidization quality and bubble dynamic is concerned with the possibility of measuring the physical and geometrical properties of gas bubbles rising in a solid granular medium. In general, the use of intrusive techniques implies an intrinsic source of error due to the presence of the measuring tool that creates some level of interference. On the contrary non-intrusive techniques can provide good visual observation without interfering with the fluidization process.

In recent years, thanks to the continuous development of digital imaging systems and digital image processing, a great number of researchers have chosen digital visual methods to be applied in the field of experimental fluid dynamics (Lim and Agarwal, 1990; Mudde et al., 1994; Gera and Gautam, 1995; Boemer et al., 1998; Hull et al., 1999). These kinds of techniques play a fundamental role in analysis and data acquisition for multiphase flows such as gas-solid, gas-liquid, solid-liquid flows, where the observation of inter-phase boundaries is relatively simple. Digital visual methods are limited of course to the case of bidimensional fluidized beds, as in this case bubbles can be easily observed. Lim and Agarwal (1990) developed a novel method based upon digital image analysis to automate the measurement of bubble properties in gas-fluidized beds. In order to identify the bubbles, the gray-level image is segmented by applying a global threshold. The distributions of various bubble properties (size, velocity distribution and bubble holdup distribution of bubbles) as a function of bed position and fluidizing velocity are presented. Results are compared with theoretical predictions using a population balance model. Mudde et al. (1994) reported experiments in a two-dimensional bubbling gas fluidized bed. The behavior of the bubbling bed is monitored using standard video techniques. The recorded video tapes have been analyzed using image analysis techniques. It has been shown that these techniques offer the possibility to quantify local hold-up and all kind of bubble properties, such as size, shape and velocity, as a function of the bubble height in the bed. The accuracy of the technique is good and the results are in agreement with those reported in the literature. Special attention is paid to determining shape properties of spherical-cap bubbles. The contour of these bubbles is decomposed into two circles, so that determination of the wake angle and wake area is possible. Both parameters are investigated as function of the bubble height in the bed. Hull et al. (1999) reported an experimental data on bubble characteristics averaged size and rise velocity were obtained using digital image analysis method from two-dimensional (thin) bubbling fluidized beds with and without simulated horizontal tube bundles. These data were used to develop semi empirical correlations for bubble size and rise velocity. Caicedo et al. (2003) reported an experimental study of bubbling behavior of gas-fluidized beds using digital image analysis. These authors investigated important parameters of bubbling dynamics such as bubble shape factor and aspect ratio. The results show that the investigated parameters obey to normal distribution across the operating fluid bed, and that statistical analysis must be performed when treating fluidized beds. Goldschmidt et al. (2003) developed an experimental technique based on digital analysis to measure bed expansion and segregation dynamics in dense gas-fluidized beds, in order to validate CFD simulation of mono-disperse and binary mixtures fluid beds. This technique allowed the authors to measure, through the use of differently colored particles and RGB images decomposition, the extent of mixing and segregation. Extensive data on several systems investigated have been reported. Shen et al. (2004) developed a new method based on image analysis to study the hydrodynamics of two-dimensional bubbling fluidized beds by means of a digital video camera. Simultaneous measurements of size and velocity of gas bubbles were performed, as well as axial and radial distribution of bubble voidage. Lim et al. (2007) used digital image analysis to investigate bubble distribution and behavior in planar gas-solid fluidized beds.

Bokkers et al. (2004) studied the extent of mixing and segregation in a bidispersed gas-solid fluidized bed induced by a single bubble injected in a monodispersed and bidispersed fluidized bed at incipient fluidization and in freely bubbling fluidized beds with both experiments and numerical simulation performed with the Discrete Particle Model. Experiments were run with a pseudo-2D fluidized bed, front-illuminated by halogen lamps. Fluid bed images were taken by means of a high-speed digital camera. The Particle Image Velocimetry (PIV) technique was applied for obtaining particles velocity fields of the experimental runs. The PIV technique adopted is the same widely used for single phase fluid flows, with the only exception that fluid seeding is substituted by direct particle tracking. Cheng et al. (2005) used various PIV techniques to investigate the bubbles velocity field in a bidimensional gas-liquid column operated at high bubble density. The authors used the bubbles images of the column recorded by a CCD camera. The images were then post processed off line applying different PIV and PTV (Particle Tracking Velocimetry) cross correlation without any seeding of the fluid, but using bubbles as particles to track. They showed that recursive cross correlation leads to the best measurements results because of the robustness with respect to optical and dynamic characteristic of bubbles. Zhu et al. (2005) reported a study on the characterization of agglomerates in nano-particle fluidization. This study performed size distribution of agglomerates at the bed surface by the use of imaging techniques. Images were recorded by a CCD camera and post processed off line by computer software in order to obtain detailed agglomerates size distribution charts. Wang et al. (2006) used laser-based images to evaluate the size and dimension of aggregates in nano-particles fluidized bed at different inlet gas velocities. To avoid distortion of the aggregate images due to curved surfaces, the authors used a square based fluid bed, instead of circular. The light coming from a pulsed laser was shaped as a sheet and used to illuminate a plane on the fluidized bed, while images were acquired by high resolution CCD camera. The commercial image processing software used allowed the authors to count and measure all aggregates present in each image. Accurate size distribution of aggregates at bed surface were obtained at various operating conditions.

8.2 Overall bed behavior

The average bed expansion in an aggregative fluidized bed can be simply calculated once the average bed voidage at incipient fluidization and during the operation (including bubbles) is known. The values that can be calculated are averaged since bed surface oscillates because of bubble breaking at the bed surface and bubbles formation at the distributor plate:

$$\frac{H_{bed}}{H_{mf}} = \frac{1-\epsilon_{mf}}{1-\epsilon} \tag{8.1}$$

If a constant bubble size is assumed through the bed, the bed height oscillation can be calculated once absolute bubble velocity U_a is known, and therefore the time it requires for traveling through the bed:

$$t = \frac{H_{max}}{U_a} = \frac{H_{max}}{(U-U_{mf})+U_b} \tag{8.2}$$

The bed expands from the minimum height H_{mf} to the maximum value, with a total bubble flow per unit cross-surface of the bed equal to $(U - U_{mf})$ if the two phase theory holds, thus leading to the following expression:

$$(U-U_{mf})t = H_{max} - H_{mf} \tag{8.3}$$

Combining the above equations, bed expansion can be readily obtained:

$$\frac{H_{max}-H_{mf}}{H_{mf}} = \frac{U-U_{mf}}{U_b} \tag{8.4}$$

If a model for bubble growth through the is assumed like that proposed by Darton et al. (1977), more complex expressions are obtained for bed expansion (Xavier et al., 1978; Geldart, 1975), in which the main parameter for bed expansion characterization is (again) the excess gas velocity with respect to incipient fluidization conditions. The experiments conduced by Geldart (1967) firstly reported a power-law dependence of bed expansion on excess gas velocity, mainly due to gas throughflow, that leads to visible bubble flow being less than the relevant excess gas velocity.

Abrahamsen and Geldart (1980) have examined the effect of powder properties on the dense phase expansion in vigorously bubbling beds of different solids with air. In particular the collapse rate technique has been used to evaluate the average dense phase properties in vigorously bubbling beds of fine powders. The results of experiments were used to correlate the average dense phase voidage, ϵ_d, with the physical properties of the gas and powder. In particular ϵ_d increased as the particle density and mean particle size was decrease, and as the fraction of fines $< 45\,\mu m$, gas viscosity and gas density was increased. The gas velocity through the dense phase of a bubbling fluidized bed was calculated from the relevant gas volume fraction assuming Darcy's law. Since it is less than the minimum bubbling velocity, the improved performance of fluidized bed reactors when the gas/solid properties are changed so as the increase of dense phase voidage can be attributed more to a smaller bubbles splitting and coalescing frequently rather than to the small amount of extra gas passing through the dense phase.

Werther and Molerus (1973b) measured the bubble spatial distribution in cylindrical vessels using capacitance probes developed by the same authors (Werther and Molerus, 1973a). They investigated the bubble spatial distribution in three-dimensional beds under various operating conditions, containing different solids and with different bed dimensions. It was found that close to the distributor an annulus structure with the bubbles concentrated toward the walls of the vessel was formed. As the bubbles rose through the bed, the diameter of this ring decreased until a single peak was formed at the center of a bed, if it was tall enough, which can then lead to slugging. When the bed was not sufficiently tall for a single peak to form, then solids returned to the bottom of the bed not only passing near the walls, but also through the center of the bed, indicating that the final stage of bubble distribution development was not achieved.

The authors claimed that bubble formation was favored near the walls leading to the annular concentration of bubbles, because the packing geometry of the particle layers near the wall was altered. The authors also proposed that the different conditions of friction between the particles and the wall surface and within the fluidized particles in the fluidized bed might favor bubble formation in the vicinity of the walls. A similar analysis on bed overall behavior was reported by Lim et al. (2007) who used digital image analysis to investigate bubble spatial distribution and relevant time-series characteristics in planar gas-solid fluidized bed. In addition, frequency domain and statistical analyses of the bed bubble void fraction were used for the description of bed dynamics. The authors measured a pair of narrow bands of high bubble concentration along either sides of the bed close to the walls near the distributor, which gradually migrated inwards, spreading over the center of the bed higher up in it. This created an area of bubble deprivation in the bed center near the bottom. The tapering of bubble distribution also left the regions close to the wall in the upper part of the bed deprived of bubbles. Although the bubble distribution profile was observed to change with the amount of gas flow into the bed, its overall characteristics (two narrow bands

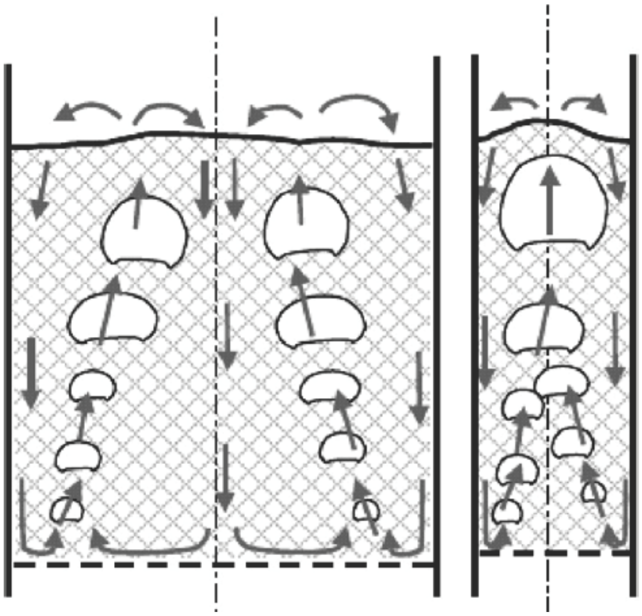

Figure 8.1: Preferential bubble paths in low aspect ratio (left) and high aspect ratio (right) fluidized beds

near the bottom and a single, wide band at the upper part of the bed, of high bubble concentration regions) were preserved. When the gas supply was increased, the high concentration bands became larger, though the position of the point of merging of the bands appeared to be constant. The height at which the narrow bands merged was considered by the authors as an indication of completion of development of the bubble spatial distribution. The increase in the overall number of bubbles in the bed with flow rate was because of the greater excess flow. The authors claimed that the onset of these characteristic preferential path was mainly due to wall-constrained motion of bubbles: in practice, when two bubbles in a fluidized bed are considered, one of which is located near the wall and the other in the middle of the bed, the one near the wall will either move inwards or maintain its distance from the wall, but the one away from the wall can move inwards, not at all, or also outwards. The wall is a physical constraint not encountered by the bubble in the middle; therefore, there is a net effect where there is a greater probability for a trailing bubble near the wall to either maintain its lateral position or move inwards if it were to be involved in an interaction or coalesce with a leading bubble placed somewhere closer to the middle to the bed. On the other hand, the bubble in the middle has equal tendency to laterally move to either sides of the bed depending on their interaction with a leading bubble.

The same authors (Lim et al., 2009) described the dynamic behavior of the bubbles in a planar gas-solid fluidized bed, reporting that the bubble void fractions measured and shown to relate consistently to the amount of gas supply above quiescent fluidization. Similar results are obtained by Shen et al. (2004) that measured the increases of overall bubble volumetric fraction in 2-dimensional bed with particle size. The authors report a characteristic dependence of bubble overall content on excess gas velocity.

8.3 Particle phase behavior

A good understanding of particle behavior is important in the design of physical and chemical processes in bubbling fluidized beds. Particle mixing studies, combined with gas flow analysis and the reaction mechanism provide the basis for designing commercial fluidized bed reactors. Mixing of particles within a fluidized bed is caused mainly by the movement of bubbles, as reported in Fig.8.2. A bubble rises, solids close enough to the bubble enter into its cloud and are eventually drawn into its wake and complete mixing of solids occurs in the wake where movement is generated. This contributes only partially to the lateral mixing of particles. In addition, a bubble causes a drift of particles to be drawn up as a spout below it. In a freely bubbling fluidized bed, wake fragments are periodically shed and replenished as the bubbles rise through the bed and there is a vertical displacement of the particles exclusive of the wake. At the bed surface, the bubble eruption induces lateral dispersion of part of the wake's particles over a large area, and the remainder of these particles is ejected into the freeboard.

The existence of bubble wake, the phenomenon of drift, and wake shedding have been discussed in detail by Davidson and Harrison (1971). According to the authors, the amount of solids induced upward by a single bubble is equal to about 0.6 times the bubble volume, of which about 60% is due to drift action. The lateral mixing of particles in gas-solid fluidized beds is induced by bubble movement through the bed, bubble bursting at the bed surface, and gross particle circulation inside the bed. Through the random walk theory, Kunii and Levenspiel (1991) derived an equation for the lateral dispersion coefficient for lateral mixing of solids in gas-solid fluidized beds depending on average bubble content of the bed and bubble diameter. The convective solids transport and mixing can be estimated based on the bubble properties, as suggested by Geldart (1986). The particle circulation flux in a fluidized bed can be calculated by suitable correlation based on a corrected form of the original two-phase

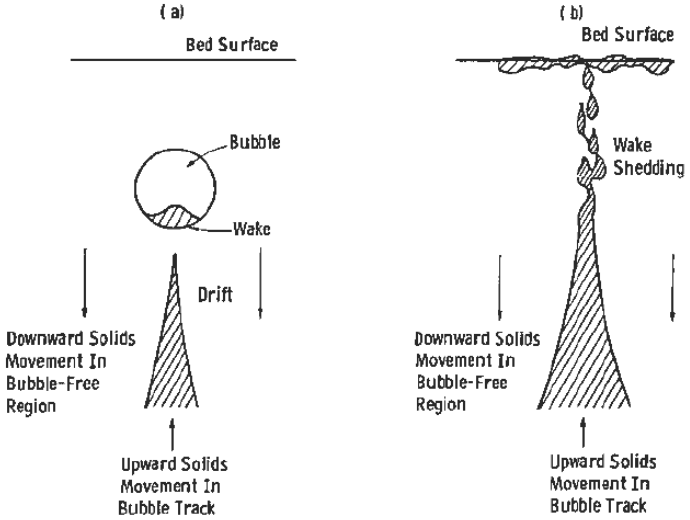

Figure 8.2: Particle mixing mechanism: wake mechanism and drift mechanism

theory of fluidization, including terms accounting for solids transported by bubbles by means of the above presented mechanisms of wake and drift transport. Solids mixing have been reviewed by many authors (Kunii and Levenspiel, 1991; Potter, 1971; van Deemter, 1985; Fan et al., 1990).

In general, the combined effects of gross circulation caused by drift and wake transport and small scale local mixing in bubble wakes leads to favorable axial mixing. The extent of lateral solids mixing is much less favorable, particularly in shallow fluid beds (height to diameter ratio $H_0/D_c < 0.25$) where the influence of axial wake transport is weakest. It is well known that vertical mixing in fluidized beds is many time faster than lateral mixing. Indeed it seems likely that solids move in a net horizontal direction largely by being (a) carried-up to surface where they are dispersed sideways by bursting bubbles and (b) carried down to, and across, the distributor by bubble-free flows of dense phase material.

The axial and radial transports of particles within the bed can influence:

- gas-solid contact,
- thermal gradients between a reaction zone and zone in which heat transfer sur-

face are located,

- heat transfer coefficients,
- the position and number of solids feed and withdrawal points,
- the presence and extent of dead zones at distributor level.

Mixing problems in fluid beds fall into four categories:

1. particles have uniform size and density,
2. particles have uniform size but variable density,
3. particles are all of same density but vary in size,
4. particles vary in both size and density.

In category (1) the main problem is to ensure that the overall solids transport or circulation flux is high enough to eliminate temperature gradients; in categories (2), (3) and (4) an additional concern is whether the local composition of the powder is everywhere equal to the overall average. The amount of solids circulation and degree of local mixing or segregation is primarily determined by the gas velocity, but particle shape, size, density, stickiness, and size distribution all play a part. Although mechanisms of mixing are now better understood, there is still much to be learn and experimentation is essential.

A variety of techniques have been used to study the vertical movement of the solids, for example:

- following the paths of individual tagged particles for long periods of time as they move about the bed,
- measuring the extent of intermixing of two kinds of solids, originally located one above the other in the bed;
- measuring the vertical spread of a thin horizontal slice of tracer solid;
- finding the residence time distribution of the flowing stream in a bed with a throughflow of solids, using a variety of a tracer techniques;
- measuring the axial heat flow in a bed with a heated top section and cooled bottom section. This technique assumes that heat transport is caused solely by the movement of solids. The results are most often reported in terms of the vertical dispersion DSV.

Valenzuela (1985) reported an experimental study of solids mixing in a freely bubbling two-dimensional bed using particle image analysis. Vertical and horizontal particle mixing were studied using heated particles as tracers. The steady-state temperature patterns around a heated wire and the transient response to an injected pulse of heated particles were measured. The bubbling behavior of the bed was recorded with a high-speed video camera and an optical bubble probe. Particle motion was found to be closely related to the random bubble motion in the bed. Mixing experiments must, therefore, be repeated numerous times to achieve meaningful results. Vertical particle transport is asymmetrical. Upward displacement is characterized by a mixing length of the order of the bubble diameter, whereas downward displacement is more uniform, and at a much lower velocity level. Horizontal solids mixing is partially due to mixing in the bubble wakes. In a freely bubbling bed, horizontal mixing is considerably augmented by the lateral motion of bubbles.

Lim et al. (1993) overcame some of the above mentioned limitations by a digital image analysis technique which determined tracer concentrations continuously in a two dimensional bubbling fluid bed. Yates and Simons (1994) reports a detailed review of some experimental techniques using tracer particles. Shen and Zhang (1995) and Shen and Zhang (1998) reports a study on the dynamics of solids mixing in a two-dimensional fluidized bed taking into account both radial and vertical mixing. Abanades and Grasa (2001) modeled both the axial and the lateral mixing of solids in fluidized beds. Mixing experiments using coal and PVC (as a tracer) were carried out to obtain experimental concentration maps for model validation. The experimental investigation of solid mixing was based on the application of an image-analysis technique to mixing experiments in a 2D fluidized bed. Coal was used as the main solid in the bed, and PVC powder was used as the optical tracer. This technique was pioneered with other colored solids by Lim et al. (1993) who reviewed a number of alternatives and highlighted the benefits of this technique for mixing experiments.

Bokkers et al. (2004) studied mixing and segregation induced by a single bubble injected in a fluidized bed at incipient fluidization conditions and in freely bubbling fluidized beds. PIV was applied to obtain the ensemble averaged particle velocity profile in the vicinity of a bubble in dense gas- solid fluidized systems. Pallares and F. (2006) presented a novel technique for particle tracking in 2-dimensional fluidized beds operated under ambient conditions. The method was applied to study the mixing mechanisms in fluidized beds and is based on tracking a phosphorescent tracer particle by means of video recording with subsequent digital image analysis. From this, concentration, velocity and dispersion fields of the tracer particle could be obtained with high accuracy. The characteristic found in all runs was that the mixing pattern of the tracer solids was structured in horizontally aligned vortexes induced by the bubble flow. The main bubble paths always gave low concentration of tracer solids and with the tracer moving upwards, while the downflow of tracer particles in the dense bottom bed was found to take place in zones with low bubble density and at the sidewalls. The amount of bed material had a strong influence on the bottom bed dynamics development and coalescence of bubbles and, consequently, on the solids mixing process. Local dispersion coefficients reached maximum values around the locations of bubble eruptions, while, in the presence of a dense bottom bed, an increase in fluidization velocity or amount of bed material enhanced the dispersion. Dispersion was found to be larger in the vertical than in the horizontal direction, confirming the critical character of lateral fuel dispersion in fluidized-bed combustors of large cross section. Winaya and Shimizu (2007) proposed a different method to evaluate horizontal dispersion of solids in bubbling fluidized beds based on a carbon-loaded bed material prepared using the capacitance effect (volatile matter captured by porous particles) as a tracer. The extent of solid dispersion is evaluated by measuring the horizontal concentration profile of CO, which was formed by the reaction of carbon in the tracers with CO_2 in the fluidizing gas. Transient change in the horizontal CO concentration profile was also measured in the freeboard and the experimental results were compared with the theoretically calculated results of one dimensional diffusion of solids. Thereby, the horizontal dispersion coefficient was determined.

Laverman et al. (2008) studied the hydrodynamics of an experimental freely bubbling, pseudo 2-D fluidized bed for different bed aspect ratios at different superficial gas velocities by means of Particle Image Velocimetry (PIV) combined with Digital Image Analysis (DIA). Coupling of both non-invasive measuring techniques allowed the authors to obtain the instantaneous emulsion phase velocity profiles (in a pseudo-2-D bed because of the required visual accessibility) together with detailed information on the bubble phase (local bubble size and velocity distribution and bubble fraction). This in turn allowed the authors to investigate the mutual interaction between the bubble and emulsion phase in detail. The measured time-averaged emulsion phase velocity profiles were measured as a function of the fluidization velocity, bed width, and bed height. The time-averaged emulsion phase velocity profiles showed two symmetric vortices with their centers located at the top half of the bed, that became more pronounced at higher fluidization velocities. Two additional smaller vortices were observed close to the bottom of the bed at lower velocities, which disappeared at higher fluidization velocities when the down-flow region extended completely to the bottom the bed. It was found that the time-averaged emulsion phase velocity profiles did not depend on the bed height, when compared at the same distance from the distributor at the same fluidization velocity.

8.4 Bubble motion

Bubble formation mechanics in fluidized bed was found experimentally to be very similar to that in an inviscid liquid. At a very low gas flow rate, the frequency and size of the bubbles formed are primarily governed by a balance between the surface tension of the liquid and the buoyancy force of the bubble. The inertia of the liquid moved by the rising bubbles becomes more important than the surface tension at higher gas rates. It is in this regime that the similarity between the formation of bubbles in a fluidized bed and that in an inviscid liquid is most applicable, because the surface tension in a fluidized bed is zero. Using the analogy of bubble formation in an inviscid liquid, Davidson and Harrison (1963) derived equations for both the bubble frequency and the bubble size (volume), assuming there is no gas leakage from the bubble to the emulsion phase. It was found that at high gas flow rates, where the bubble sizes are independent of the bed viscosity, the inviscid liquid theory can predict the bubble sizes satisfactorily, while some underestimation of bubble size was found at higher gas flow rates. Huttenhuis et al. (1996) reported an experimental and theoretical study on the effect of gas-phase density on the process of bubble formation at a single orifice in a two-dimensional gas-fluidized bed. A detailed comparison between experimentally observed and theoretically calculated bubble growth curves was made in the cases where the density of the gas injected through the orifice differed significantly from the density of the main fluidizing agent (air). The measured bubble sizes showed a satisfactory degree of agreement with predictions made using a hydrodynamic model based on the two fluid concept. In particular, the effect of gas-phase density on measured bubble sizes could fully be explained in terms of its effect on momentum transfer to the particulate phase. These models typically assume circular (two-dimensional) or spherical (three-dimensional) bubbles and a uniform leakage velocity through the bubble surface, assumptions which are critical at, respectively, the final and the initial stage of bubble formation. Nevertheless, the approximate models clearly have their utility due to their ability to predict the correct order of magnitude of bubble sizes.

From computer-enhanced video images of rising bubbles in fluidized beds, Yates et al. (1994) observed that the bubbles are surrounded by a region of emulsion phase in which the solids concentration is lower than that in the emulsion phase far from the bubbles. This region of increasing voidage was called the *shell.* The volumetric gas in the bubble and in the shell could be correlated as:

$$V_{shell} = 16V_b^{0.42} \tag{8.5}$$

Based on this equation, the volume of void following coalescence of two bubbles should be about 28% larger than the volumes of the two constituent voids, because of the incorporation of gas from the shells.

In 1961, Davidson developed a simple theory that was capable of explaining a lot of phenomena relating to bubbles in fluidized beds observed experimentally. His development (Davidson and Harrison, 1963) involved the following assumptions:

- The particulate phase is an incompressible fluid with a bulk density similar to that of a fluidized bed at minimum fluidization.
- The relative velocity between the particles and the fluidizing medium is assumed to be proportional to the pressure gradient within the fluid, and therefore D'Arcy's law is applicable.
- Fluidizing fluid is assumed to be incompressible.
- The pressure throughout the bubble is constant.
- The particulate phase behaves as an inviscid liquid.
- The bubble has a circular cross section.

Davidson solved the model equations in terms of particle motion, pressure distribution within the fluidizing fluid, absolute velocities of the fluidizing fluid, and the exchange between the bubble and the particulate phase, finding that the geometry of the stream function is crucially affected depending whether the bubble velocity U_b is larger or smaller than interstitial minimum fluidization velocity, U_{mf}/ϵ_{mf}. In particular, isolated bubbles could be characterized by two different regimes, graphically shown in Fig.8.3:

- Fast Bubbles Regime: in this case the fluidizing fluid moves downward relative to the bubble motion. The bubbles in the fluidized bed are accompanied by a *cloud* while rising through the bed. For fast bubbles where the bubble velocity is large, or for fluidized beds of fine powders when the minimum fluidization velocity is small, the cloud is usually very thin. In most of the fluidized beds of practical interests, this is the case.

- Fast Bubbles Regime: in this case, the fluidizing fluid moves upward relative to the bubble motion. This case is usual for beds of large particles and small bubbles. The majority of the fluidizing fluid enters the void at the base and leaves from the roof. The fluidizing fluid, in essence, uses the bubble void as the shortcut. The fluidizing fluid penetrates the particulate phase freely from the bubble except for a small fraction of fluid.

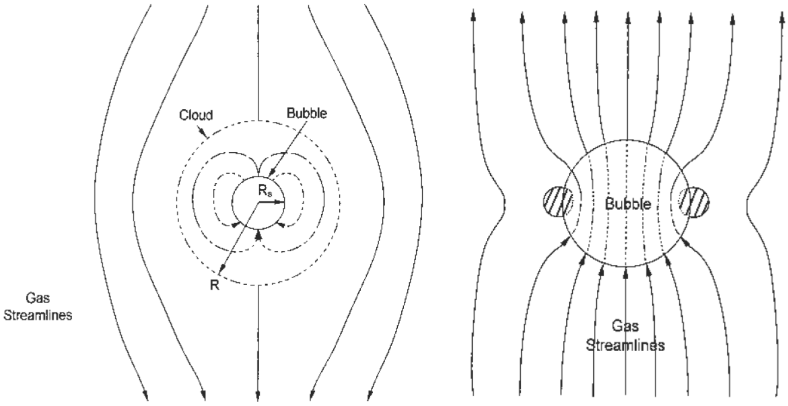

Figure 8.3: Fluid phase streamlines as described by Davidson model in the case of fast-bubble regime and slow bubble regime

A dense cloud region exists nearby the bubble responsible for particles motion through the bed and gas exchange between the emulsion phase and the bubble, as can be seen in Fig.8.4 (Kunii and Levenspiel, 1991).

Bubbles in gas-solid fluidized beds usually are spherical-capped (3 dimensional beds) of mushroom shaped (2-dimensional beds). The rising velocity of a single bubble in a quiescent bed has been found experimentally to be related to bubble volume (and then to bubble equivalent diameter):

$$U_b = 0.71 g^{0.5} V_b^{1/6} = \phi g^{0.5} D_b^{0.5} \tag{8.6}$$

The equation experimentally found is quite similar to that obtained for large bubbles in liquids of small viscosity, in which the rate of rise of large bubbles depends

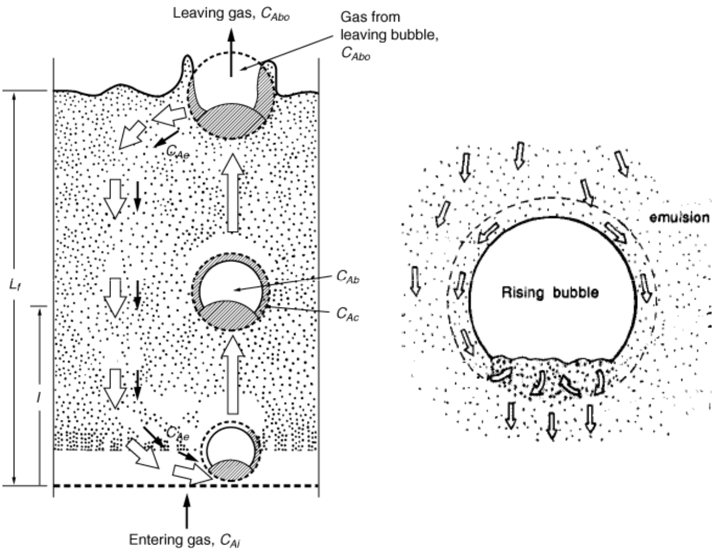

Figure 8.4: Bubble-emulsion interactions in the case of Geldart group A and B particles.

primarily on inertial forces and surface tension. The viscous effect is negligible in comparison.

$$U_b = 0.35 \div 0.71\sqrt{dD_b} \tag{8.7}$$

The value for ϕ was also measured by Rowe and Everett (1972) and found equal to 0.71 for bot 2 dimensional and 3 dimensional fluidized beds. A similar analysis on velocity coefficient is reported in Rowe and Yacono (1976), but a value in the range $0.7div1.0$ is reported for fine particles.

Gera and Gautam (1995) report a theoretical study on the bubble rise velocity in two-dimensional fluidized beds. In particular they proposed a simple model incorporating wake effect to derive the velocity of a two-dimensional gas bubble rising in a fluidized bed. It is inferred that the bubble rise velocity is a strong function of wake angle. In general, the bubble rise velocity can be related to its radius of curvature (a) for circular bubble by the equation and dependent on the wake angle θ:

$$U_b = K\sqrt{da} \tag{8.8}$$

with $K(\theta)$ in the range $0.5 \div 0.85$. The bubble rise velocity measured by Shen et al.

(2004) via Digital Image Analysis are well correlated if a velocity coefficient ϕ in the range $0.8 \div 1$, provided that unconstrained bubble growth occurs. Also, the bubble velocity was found to be constant beyond the height critical height at with constrained bubble growth starts to occur.

8.5 Bubble size evolution

The most evident phenomena in bubbling fluidized beds is the enlargement that each bubbles exhibit along their path through the bed. The bubble growth is mainly due to the following factors:

- The effective hydrostatic pressure decreases toward the top of the fluidized bed.
- Bubbles coalesce in the vertical direction with the trailing bubble catching up the leading bubble, and
- bubbles coalesce in the horizontal direction with the neighboring bubbles.

The effect of the hydrostatic pressure is usually small, and the bubbles grow in size owing largely to coalescence. This leads in turn to a subsequent decrease of bubble number with increasing the distance above the distributor plate.

Rowe and Everett (1972) reported a study on the transition from two to three dimensions of undisturbed bubbles, using X-rays. In this work the average size and the number of bubbles in a given volume were measured at a series of heights and flow-rates in beds all $30\,cm$ wide and increasing thickness from 1.4 to $30\,cm$. In all cases the average bubble size resulted to be a simple linear function of the height and flow-rate although the two factors interact in the thicker beds. The coefficients on the equation changed with thickness, but achieved steady values in the thicker ones. This transition from two-to-three dimensional behavior occurred in beds between about $5 \div 15\,cm$ thick. It was found that bubble size was thickness dependent in the two dimensional regime. Bubble number and size way obeyed at least the conditions of continuity although volume increases with diameter at a slower rate than the square (2-D) or (3D) law. This was because bubbles flatten as they grow in size. The rate of change of bubble number with height followed a simple growth law reported below:

$$N\left(H+h_0\right)^r = kf\left(U\right) \tag{8.9}$$

where N is the number of bubbles in observed volume, H is height above distributor, h_0 is a constant that appears equal to zero for a porous plate distributor, r is an empirical exponent equal to 1 in the limiting 2-D case 2 in the 3D case), U is the superficial gas velocity.

With respect to bubble diameter evolution, Geldart (1972) reported a study on the effect of particle size and size distribution on the behavior of gas-fluidized beds. The author showed the fluidization behavior of many powders to be independent both of mean particle size and particle size distribution. In particular, mean bubble size was found to depend only upon the gas distributor, the distance above the distributor and the excess gas velocity $U - U_{mf}$. An equation relating these variables giving good agreement with experimental data from beds using industrial type distributors was found:

$$D_b = \frac{1.43\left(U - U_{mf}\right)^{0.4}}{N^{0.4} g^{-0.2}} + 0.0027H\left(U - U_{mf}\right)^{0.94} \tag{8.10}$$

where $N[cm^{-2}]$ is the number of holes per unit area of gas distributor, $H[cm]$ is the distance above the distributor. The author reported also that the principal effect of adding fines to a bed of powder was that of reducing the mean particle size and therefore the relevant incipient fluidization velocity. Hence, at equal values of $U - U_{mf}$ an increased bed expansion and solid circulation rates was found, without decrease in mean bubble size. Similar results were obtained in term of functional dependencies by Rowe and Yacono (1976). In this contribution, it was shown that existing data on bubble size (when this were not restricted by the vessel dimensions) could be described by

$$D_b = \frac{\left(U - U_{mf}\right)^{0.5}\left(H - h_0\right)^{0.75}}{g^{0.25}} \tag{8.11}$$

where h_0 is a measure of the initial bubble size that characterizes the distributor (notably, h_0 is effectively zero for a porous plate but may be more than a meter for larger nozzles). In Agarwal (1985), the following expression was found to suitably fit experimental data on bubble diameter evolution:

$$D_b = d_{b,0} + 0.74 d_{b,0}^{0.5}\left(H - h_0\right)^{0.4} + 0.15\left(H - h_0\right)^{0.8} \tag{8.12}$$

in which the dependence of bubble diameter on excess gas velocity is implicit in the $d_{b,0}$ parameter.

Darton et al. (1977) reported a study on bubble growth due to coalescence in fluidized beds. A growth model based on two-phase theory by Davidson and Harrison (1963) was developed, where the fluidized bed was described in terms of two-continua: the emulsion phase, which was made up of the solid particles with gas at the minimum fluidization conditions, and the bubble phase gas, which took up the gas in excess of the minimum fluidization. The coalescence of bubbles in fluidized beds leaded to growth of bubble size with distance above the distributor. In particular, it was assumed that bubbles in a fluidized bed are lined up as close as possible, as reported in Fig.8.5, and coalescence occured between bubbles of neighboring streams by means of considerable lateral movement. The distance traveled by bubbles before coalescence should be therefore proportional to their lateral separation. This model was based on the well accepted observation that the mechanism of coalescence involves the capture of one bubble in the wake of another, but with the exception of the distributor region (in which vertically aligned bubbles may be formed within the range of coalescence), the capture motion always involved a lateral movement, that could be therefore the process determining the overall coalescence rate.

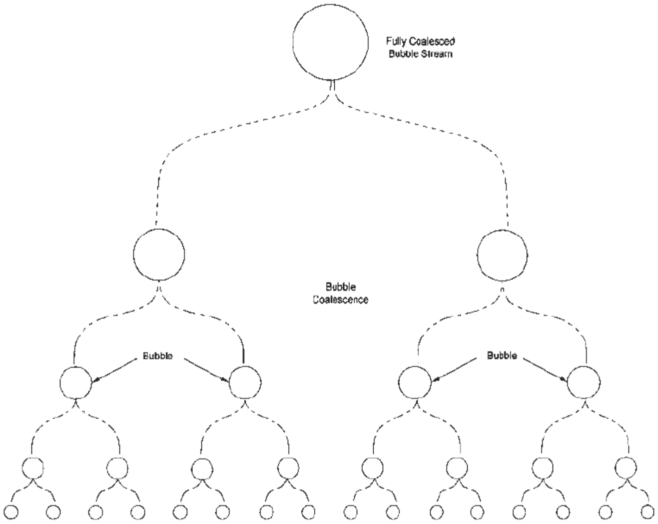

Figure 8.5: Bubble preferential path according to Darton

By assuming that coalescence occures in stages, as reported in Fig.8.5, and that bubble rise velocity only depends on bubble diameter, the following equation was found describing the bubble diameter evolution with height above the distributor:

$$D_b = 0.54\,(U - U_{mf})^{0.4}\left(H + 4\sqrt{A_0}\right)^{0.8} g^{-0.2} \tag{8.13}$$

where A_0 is the catchment area for the bubble stream at the distributor plate, which characterizes different distributors, and is usually the area of the plate per orifice. The above equation described quite quell with most of literature data on bubble size, provided bubble growth was not limited by the presence of fine particles. For beds containing appreciable proportions of fine particles, the above formula may not apply because the bubbles may reach a limiting size, nor does it apply for slug flow, which occurs when $(U - U_{mf}) > 0.2 * 0.35\sqrt{gD_b}$.

The Darton bubble growth model was adapted by Shen et al. (2004) to describe data relevant to a 2-D fluidized bed. The measured bubble size and diameter, obtained by means of digital image analysis technique where well correlated by means of

$$D_b = 0.89\left[(U - U_{mf})\left(H + 3\frac{A_0}{t}\right)\right]^{\frac{2}{3}} g^{-}\frac{1}{3} \tag{8.14}$$

where t is the thickness of the two-dimensional bed. Moreover, for group B particle and a given gas velocity U, if the bed height was sufficient, bubble diameter D_b could be able to reach a maximum value at a certain height $h*$, beyond which bubbles did not grow further and became unstable and break up. The height $h*$ could be correlated by:

$$h^* = \left[A + 3^{\left(-\frac{U}{U_{mf}}\right)}\right] D_t \tag{8.15}$$

where A = 0.45 and D_t is the bed diameter.

Horio and Nonaka (1987) developed generalized model for gas-fluidized beds accounting for bubble coalescence and splitting frequencies, in order to obtain a suitable diameter correlation that was simultaneously applicable to coarse particles (in which bubble size does not exhibit a limit value, provided the absence of geometrical size constraint) and aeratable particles (that conversely exhibit an upper limit in bubble size only dependent on particle size). The model was based on some fundamental postulates:

- Coalescence process obeys the dynamics of an ideal fluid and is completely determined by the diameters of interacting bubbles and relevant mutual positions, similarly to the assumptions of Darton et al. (1977);
- bubble coalescence models for Geldart group B and D (in which the bubble

splitting frequency is negligible) still hold true for group A particles;

- bubble splitting frequency only depends on particle diameter.

On this basis, the authors develop a diameter correlation for the prediction of diameter evolution along bed height and limit bubble size for Geldart group A particles. The correlation developed gives the Mori and Wen (1975) correlation for group B particles. This last model is in practice derived on the same postulates of the Horio and Nonaka (1987) model with the exception of that regarding bubble splitting.

9 Image Analysis Technique

It is the aim of the present chapter to present the technique used for the analysis of bubbling fluidization on the basis of digital image processing. This techniques in fact may well perform a rigorous and highly detailed assessment of experimental data and may even be adopted for the analysis of computational results conveniently expressed into image graphics. Of course, the stringent comparison between model and experimental results is the basis to further develop and strengthen modeling works.

As already discussed, the principal difficulty in analyzing fluidization quality and bubble dynamic is concerned with the possibility of measuring the physical and geometrical properties of the gas bubbles rising in a solid granular medium. In this chapter, the focus is on the development of a digital image analysis technique with the specific task of creating a fully automated and robust procedure to purposely measure the most significant bubble properties of two-dimensional bubbling fluidized beds. By in-house development of a suitable software, it is possible to get a total control over every single step of the procedure and every single parameter involved in the calculations, thus achieving a higher level of reliability of the data so far obtained. Thanks to the high level of automation of the purposely developed procedure it is possible to simultaneously compute a large number of bubble properties, allowing at the same time a meaningful statistical analysis that is intrinsically necessary given the nature of the source data.

9.1 Experimental set-up

Two different fluid-bed reactors were adopted for the present investigation. The first one is entirely made of Perspex with dimensions equal to $800(h)\,\times\,180(width)$ $\times\,15(depth)\,mm$. Front wall is made of glass in order to avoid wall opacization due to attrition. The second reactor is made of aluminium and equipped with glass walls at front and back with dimensions equal to $1200(height)\,\times\,240(width)\,\times$ $10(depth)\,mm$. Both reactors are therefore almost two-dimensional, and allows visual observation of bubble dynamics within the bed. Sintered plastic porous distributor (average particle diameter $150\mu m$, average porosity equal to 0.35 determined by SEM analysis), with thickness equal to $10\,mm$, is placed at the bottom of the particle bed. The measured pressure drop along the distributor is in accordance with the well accepted Ergun equation for porous media Bird et al. (2002). Below the distributor a wind box filled with large glass particles ($2-5mm$) allows to fully equalize the gas flow. The hydraulic general scheme of the experimental set-up is reported in Fig.9.1.

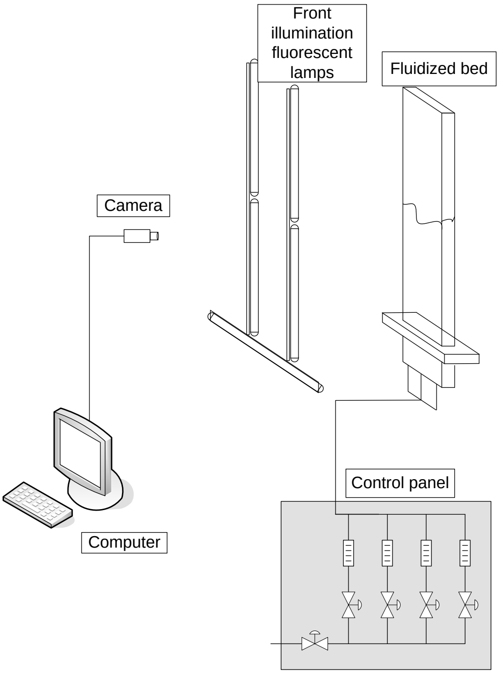

Figure 9.1: Fluid bed experimental set-up: hydraulic scheme.

Air was used as fluidizing gas, whose flow rate was accurately measured through a set of four flow-meters, covering the range $0-140\,lt/min$. Different kind of particulates were used for the experimental runs: silica particles with density equal to $2500\,kg/m^3$ and size range of $212-250\,\mu m$ (i) and $500-600\,\mu m$ (ii), and corundum particles with size range of $212-250\,\mu m$ (iii) and $500-600\,\mu m$ (iv) and density equal to $4000\,kg/m^3$. Moreover, the bubbling behavior of some corundum mixtures were investigated. The particles were filled up to a bed height of twice the bed width. For particle mixtures, the initial filling of the bed is made by two separate (unmixed) layers of particles.

The values of U_{mf} were experimentally determined for pure components, and found equal to $5.24\,cm/s$, $28.7\,cm/s$, $9.5 cm/s$ and $40.1\,cm/s$ respectively. The $U_{mf,mix}$ value was found by means of literature correlation (Yang, 2003):

$$\bar{d_p} = \frac{x}{d_{p,flot}} + \frac{1-x}{d_{p,jet}} \tag{9.1}$$

$$Ar = \frac{g\bar{d_p}^3 \left(\rho_p - \rho_f\right)\rho_f}{\mu_f^2} \tag{9.2}$$

$$Re_{mf,mix} = \frac{\rho_f \bar{d_p} u_{mf,mix}}{\mu_f} = 0.0054 Ar^{0.78} \tag{9.3}$$

Five corundum mixtures were fluidized having composition of 20%, 40%, 50%, 60%, 80% and (w/w) in the flotsam component. The investigated cases have been summarized in Table 9.1.

Experimental data were acquired after full steady state was achieved, in order to avoid measuring bubble behavior during the initial mixing of powders. In this thesis, the observation was focused on the whole bed, without selecting any particular region of interest, to allow a full field analysis of the bubbling fluidization dynamics.

Material	Flotsam $\%$	Bed Width	$U(m/s)$	Fps
Corundum	0.0	$0.24\,m$	0.56, 0.64, 0.72	1, 60
Corundum	0.2	$0.24\,m$	0.56, 0.64, 0.72	1, 60
Corundum	0.4	$0.24\,m$	0.56, 0.64, 0.72	1, 60
Corundum	0.5	$0.24\,m$	0.56, 0.64, 0.72	1, 60
Corundum	0.6	$0.24\,m$	0.56, 0.64, 0.72	1, 60
Corundum	0.8	$0.24\,m$	0.56, 0.64, 0.72	1, 60
Corundum	1.0	$0.24\,m$	0.56, 0.64, 0.72	1, 60
Glass	0.0	$0.18\,m$	0.09, 0.18, 0.27, 0.36	25
Glass	1.0	$0.18\,m$	0.33, 0.38, 0.44	25

Table 9.1: Experimental cases investigated for the analysis of bubbling fluidization dynamics

The bubble-related flow structures were visualized with the aid of a back-lighting device and recorded by a digital camcorder (mvBlueFox 121c), placed opposite to the bed at a distance of $270\,cm$. Continuous high intensity uniform illumination was obtained by placing six fluorescent lamps at the back side of the bed, at approximately $10\,cm$. A suitable ac system of fluorescent lamps was found to be best suited for bubble measurement, to avoid non-uniform illumination when high image acquisition rates are used (up to 50 fps). The digital visual acquisition system allowed to collect images of the bed at different frequencies, ranging from $1\,Hz$ to $60\,Hz$. Each experimental acquisition provides at least 500 frames. As can be seen in Fig.9.2, the experimental system was also equipped for high intensity front-lighting of the bed, but this last mode of operation was not used for the assessment of bubble properties.

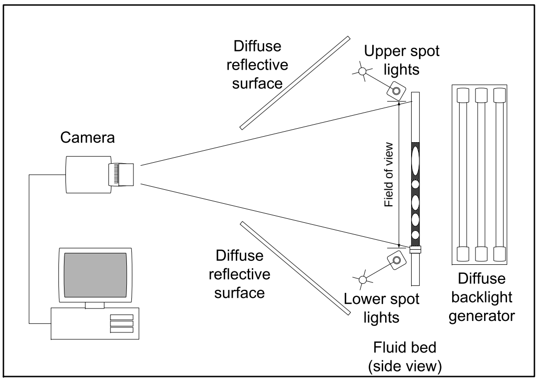

Figure 9.2: Fluid bed experimental set-up: optical scheme.

9.2 Image processing

The image processing routine was developed on Matlab 7.3 (The MathWorks inc.), using the Image Processing Toolbox. Thanks to the flexibility of the Matlab environment almost all steps in image processing, data acquisition and processing could be easily automated. The technique here adopted is based on the analysis of snapshots of the fluidized bed. Snapshots are appropriately obtained with high intensity backlighting of the bed, in order to enhancing the contrast between the emulsion phase and the bubble phase. Bubbles in the bed could be detected because they create transparent areas in the flat cross-sectional plane of the bed, through which light, emitted at the back of the bed, can pass through and reach the camera, as can be clearly seen in Fig.9.3.

Once recalled the image to analyze, the routine works through some simple steps:

- Image cropping: the image is cropped to allow the analysis of the fluid bed only, excluding all surroundings from the area of interest;
- Thresholding of the original RGB image to obtain a binary image of the bed.

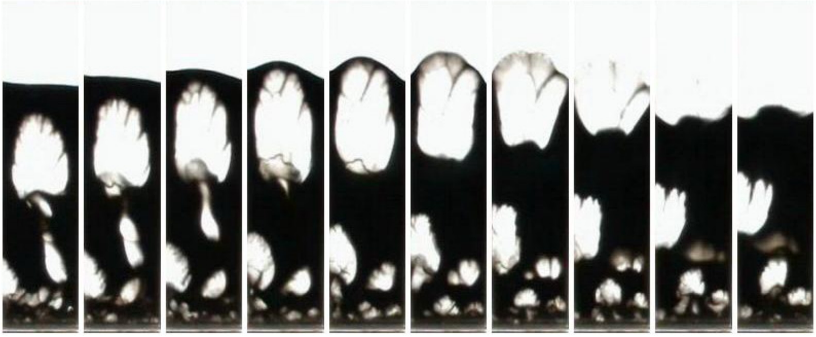

Figure 9.3: Typical snapshot sequence obtained by bed back-lighting.

This allows the discrimination of the bubble phase from the dense phase of the bed;

- Indexing of all individual regions inside the area of interest;
- Filtering of false bubbles and peripheral voids;
- Property recording of each region inside the area of interest.

Each one of these steps, except the first, requires further discussion.

The thresholding procedure is used to transform a greyscale image (in which any pixel assumes values ranging from 0 to 1) into a binary one, suitable for object identification. This can be accomplished by the following expression, relating the pixel luminance $l(x, y)$ of the original greyscale image to the pixel luminance of the binary image $\Phi(x, y)$:

$$\Phi\left(x,y\right)=\left\{\begin{array}{lcll}1 & \Leftrightarrow & l\left(x,y\right)\leq & Th\\ 0 & \Leftrightarrow & l\left(x,y\right)\leq & Th\end{array}\right. \tag{9.4}$$

All pixels whose luminance value equals 1 are identified as bubble phase pixels, while the others are identified as emulsion or dense phase. One of the crucial steps in image analysis is to choose a proper thresholding value. The problem is thus converted in finding a correlation between pixel luminance, ranging from 0.0 to 1.0 and voidage, ranging from 0.4 to 1.0. In fact the conventional distinction between the emulsion phase and the bubble phase is set at a voidage value of 0.80 Yates et al. (1994). If the relation between luminance and voidage were assumed linear, a luminance threshold value of about 0.67 would be used. However a linear correlation does not hold true in describing the phenomenon of light transmission across a fluid bed, where typically a Beer-Lambert law applies Yates et al. (1994); Rizzuti and Yue (1983); Yue et al. (1986); Brucato and Rizzuti (1997a,b); Boemer et al. (1998). On the other hand, the very wide and flat valley between the peaks in the bimodal distribution of gray-level, shown in Fig.9.4, ensures that the choice of any arbitrary value of luminance threshold in the range of $0.4 \div 0.8$ influences in a marginal way the bubble property measurements. This is equivalent to use the so called entropy method Kapur et al. (1985). The entropy method for thresholding an image is preferable when the two peaks of the gray-level distribution are separated by a wide and flat valley. For the images used in this PhD thesis, this condition holds true, and the threshold value can be chosen using different considerations. In the left part of Fig.9.4 a typical gray-scale bed image is shown, while a typical gray level distribution is shown in the center of the same figure (it must be noticed that different frames of the same run or different experimental runs give similar histograms). The threshold value, in this case can be chosen at any point in the range of $0.3 - 0.8$, resulting in negligible influence of threshold value on bubble size measurement.

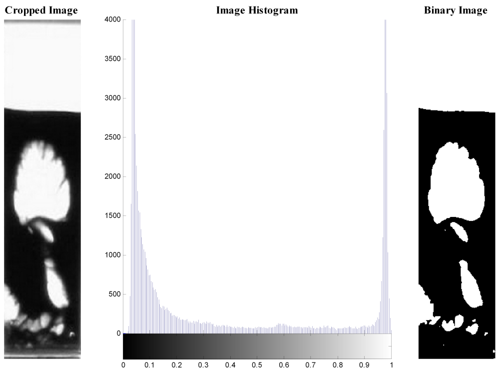

Figure 9.4: Original image (left), gray level histogram (center) and threshold image (right).

The binary image thus obtained is then subdivided (labeled) into different components, based upon connectivity analysis. For each bubble present in the image, its relevant area, equivalent diameter, and centroids coordinates are computed as reported in Eqns.9.5 and 9.6. These are recorded in a particular bubble data matrix. Distances and areas expressed in pixels can be easily converted in metric distances and areas by multiplying with scale factors. For each frame, the freeboard is the first region analyzed by the routine. The data relevant to the freeboard region, *i.e.* the freeboard area, are stored in a different matrix from that of bubbles. Preliminarily, the measurement device was accurately calibrated by means of a purposely generated set of still images.

$$A_b = \sum b\left(x, y\right) \tag{9.5}$$

Bubble centroid coordinates can be computed as follow

$$\begin{aligned} x_c &= \int\int xb\left(x, y\right) dxdy \\ y_c &= \int\int yb\left(x, y\right) dxdy \end{aligned} \tag{9.6}$$

where the integrals are extended to the area occupied by the analyzed bubble. Equivalent diameter is then calculated from the knowledge of bubble area.

Filtering of false bubbles is necessary because of the recirculation of solid particles inside each bubble rising through the bed. In high contrast images, this phenomenon appears in the form of high solid concentration zones at the bottom of the bubble. In the thresholding step this can lead to the appearance of a bubble followed by a constellation of small bubbles following the first one at the same velocity. The presence of the above mentioned false bubbles and peripheral voids, *i.e.* rising voids adherent to the lateral walls and bubbles bursting at the top of the bed, have been carefully excluded from the statistical analysis of bubble properties.

Once bubble in each frame were analyzed, it is possible to compute bubble velocity. This was accomplished by means of a in-house developed velocimetry technique (Busciglio et al., 2008). The Lagrangian velocimetry technique (LVT) here adopted uses a very simple tracking algorithm to follow the displacement of each bubble in two (or more) subsequent frames. This procedure is able to assign to each bubble a unique number, and thus it is able to follow each bubble in different frames. With this technique, it is possible to follow each bubble in its evolution from the formation to coalescence with another bubble or bursting at the freeboard. The algorithm consists of the following steps:

- All bubbles present in the first frame are sequentially numbered. This is automatically done by the processing routine. All bubbles present in the second frame are initially not numbered.

- For a given bubble in the first frame the procedure will locate the bubble present in the subsequent frame exhibiting a displacement physically consistent. This is done by finding in the subsequent frame all bubbles with a rise velocity greater than zero but lower than the maximum expected velocity, and a lateral velocity with absolute value lower than the maximum expected lateral velocity. To this bubble the same number of the bubble present in the first frame is assigned. If more than one bubble, present in the second frame, exhibits a physically consistent displacement with respect to the bubble considered in the first frame, then the same number of the bubble present in the first frame is assigned to the bubble of the second frame having minimum distance from bubble of the first frame.
- Repeat step 2 for all bubbles in frame 1;
- Assign, to all bubbles in frame 2 still not having a number, a new unique number: this is equivalent to consider these bubbles as new ones;
- Repeat the procedure for all frames.

Once all bubbles have been indexed, the data processing starts with the filtering of bubbles that appear for less than a threshold number of frames, typically set to 3. This allows the exclusion of not statistically significant tracked bubbles. For each bubble, accurate velocity measurement is possible, by simply evaluating the displacement of its centroid between subsequent frames. For a generic bubble, indexed with subscript i, that appears in two subsequent frames, labeled with subscript n and $n+1$ respectively, the displacement is computed as the difference of the bubble centroid coordinates in two subsequent frames.

By adopting the LVT procedure it is finally possible to obtain:

- Distribution (cloud) of bubble rise velocities and average velocity as function of equivalent diameter;
- Distribution (cloud) of bubble lateral velocities as function of equivalent diameter;
- Distribution of bubble rise angle (probability plot);
- Statistical distribution of velocity coefficients ϕ for each bubble, where the bubble velocity is given by $U_b = \phi(gD_b)^{0.5}$.

Once the bubbles rising up through the bed are indexed as above described, it is possible to measure other bubble local properties and follow the time evolution of each property for each bubble through its path along the bed.

10 Results

As discussed in the previous chapter, the image analysis technique here developed is able to obtain a very large amount of raw data about bubble properties inside the bed. Notably, few kind of data are directly obtained by the image processing routine, *i.e.* bubble centroid position, bubble projected area (and therefore its equivalent diameter), bubble velocity and average bed height. This quantities alone can not be directly used for bubbling regime characterization, but a further step of data post-processing is needed to assess fluidized bed behavior.

In this chapter, the data obtained will be discussed in detail, together with the numerical and statistical methods adopted for translation of large amount of raw data into information useful for fluidization quality characterization. In particular, the overall bed characteristics will be firstly analyzed such as bed height and overall bubble volume inside the bed. The main focus shall be the analysis of the relation between the variation with time of these quantities and well accepted operative parameters used for bubbling characterization such as the excess gas velocity with respect to the minimum fluidization velocity.

As a part of overall bed characterization, the time averaged bubble phase maps will be subsequently analyzed. Even if these maps report local time-averaged data, the main focus will be the link between the way in which the bubble phase is dispersed through the bed and the relevant fluid dynamic regime exhibited by the fluid bed.

Once analyzed all the available overall features, the bubble characteristics will be shown and firstly assessed. Thanks to the highly automated procedure developed, large amount of data were obtained. The first evidence is the highly dispersed cloudy aspect of raw data on bubble evolution diameter with the elevation above the distributor. Notably, this finding is miles away from the simple evolution curves described by the literature correlation presented in the previous chapters. Most of this chapter is therefore devoted at finding suitable statistical treatment able to put some order in the apparently topsy-turvy experimental data. This will be accomplished in different ways, starting from the analysis of average diameter curves, going through the analysis of overall bubble size distribution in the bed and evolution of average bubble number with the elevation above the distributor and finally leading to a detailed description of local bubble size distributions on the basis of simultaneous existence of both coalescence and break-up phenomena at all elevation of the bed. Notably, this last result could not be achieved if a very large amount of data would not be easily obtained by means of image analysis technique.

10.1 Bed expansion and bubble hold up measurements

In this section, bed height and overall bubble hold up data are shown for some of the experimental cases investigated. In particular, in Fig.10.1 data relevant to glass ballotini fluidized at two different inlet gas velocities are reported, and in Fig.10.2 data relevant to different corundum particle mixtures fluidized at the same inlet gas velocity. The data show the characteristic saw-tooth shaped fluctuations of the free surface of the bed, due to the eruption of bubbles.

Bubble hold up data are computed by dividing the sum of bubble projected areas in each frame by the total area occupied by the bed (this last being computed as the overall image area minus the freeboard projected area). It must be observed that the bed expansion dynamic and the relevant bubble hold-up dynamic, even if similar, represent rather different phenomena. In fact, overall bed expansion depends on both the extent of the bubble phase content and the average expansion of the emulsion phase (including, for example small non-visible bubbles, and the expanded cloud region), while bubble hold-up measures just bubbles overall content in the bed.

The mean value of bed expansion (*i.e.* the ratio between the mean bed height $\mu(H_{bed})$ and the settled bed height H_0) and the relevant normalized standard deviation (*i.e.* the ratio between standard deviation of bed height $\sigma(H_{bed})$ and relevant mean value $\mu(H_{bed})$) were computed for each case, the latter being a statistical measure of bed height fluctuations. All available data were reported in Fig.10.3 as a function of excess gas velocity. A power law dependence on excess gas velocity is generally adopted in literature (Geldart, 1967) for the average bed expansion.

The analysis of standard deviations can be very helpful in assessing the amplitude of bed height fluctuations. In fact such fluctuations are mainly due to the bubble eruption phenomenon, *i.e.* bubbling intensity, which in turn depends upon bubble eruption frequency and bubble size. In this respect the standard deviations plotted in are a qualitative measure of the bubbling intensity.

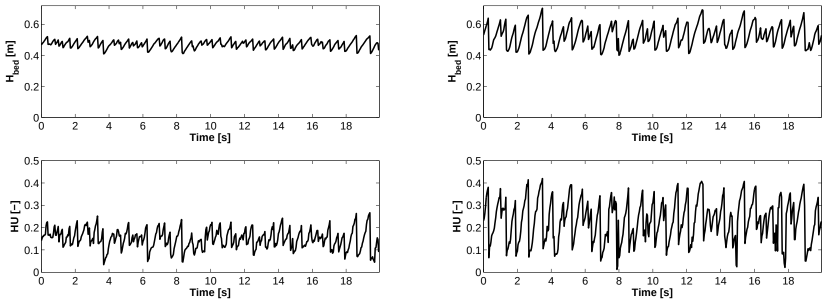

(a) $U = 0.18\,m/s$ (b) $U = 0.36\,m/s$

Figure 10.1: Experimental bed expansion and bubble hold up fluctuations at two different inlet gas velocities (Glass, $d_p = 212 - 250\,\mu m$)

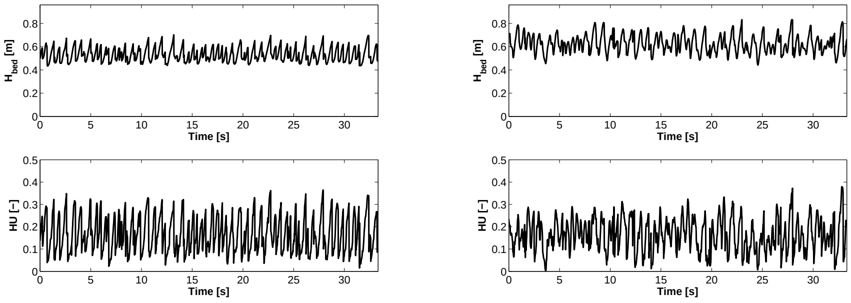

(a) $X = 0.20$ (b) $X = 0.80$

Figure 10.2: Experimental bed expansion and bubble hold up fluctuations at two different powder composition (Corundum, $U = 0.56\,m/s$)

The analysis of data reported in Fig.10.3 show that for each data serie (same particles and geometry, different inlet gas velocity), both mean expansion and relevant standard deviation increase linearly. Notably, the mean expansion variation with excess gas velocity appears to be grouped in three different trends: (i) glass expansion, show the larger increment of bed expansion with excess gas velocity; (ii) pure corundum particles, show a considerably smaller increase of bed expansion with excess gas velocity than glass particles because of larger particle density; (iii) corundum mixes, that show an average expansion even lower than pure corundum particles. This last evidence is probably due to the fact that the initial filling of the bed was performed with separate particle layers of flotsam and jetsam particles. This lead to a larger

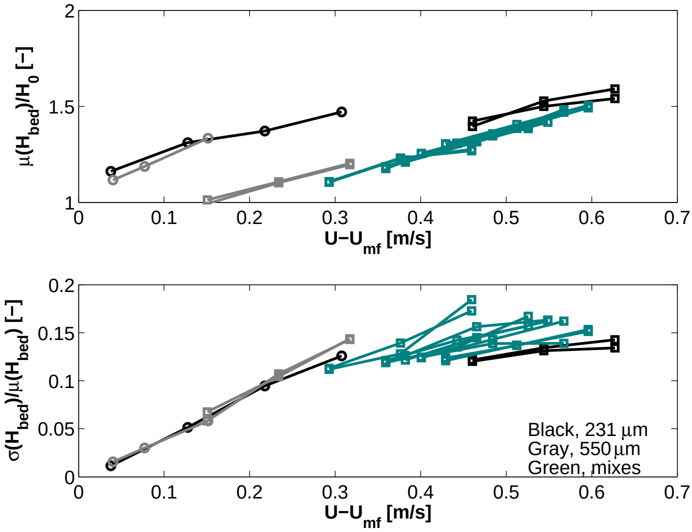

Figure 10.3: Bed expansion overall characterization: circles, glass particles; squares, corundum particles

mean value of bed voidage with respect of perfectly mixed condition of differently sized particles. The analysis of standard deviations puts in evidence a slightly different behavior: at the lowest excess gas velocities (below $0.3 m/s$) all data are aligned regardless of particle type. At higher excess gas velocities, it is possible to observe that for each composition (from pure jetsam to pure flotsam) a less steep dependence is found on excess gas velocity: this is counterintuitive, because a stronger bubbling would be expected, *i.e.* the eruption of larger bubbles. It will be shown in subsequent sections that this behavior is perfectly expected if a regime transition starts to occur.

The analysis of bubble hold up average data and relevant standard deviations, reported in Fig.10.4 show that for excess gas velocities smaller than $0.3 m/s$, the average bubble hold up increases linearly with excess gas velocity with slope dependent only on particle diameter. For higher excess gas velocities, increasing linear trends are observed again with inlet gas velocity, with decreasing slope when passing from pure jetsam to pure jetsam particles. The standard deviation values, on the other hand, follow the same (qualitative) trend of bed height normalized standard deviation.

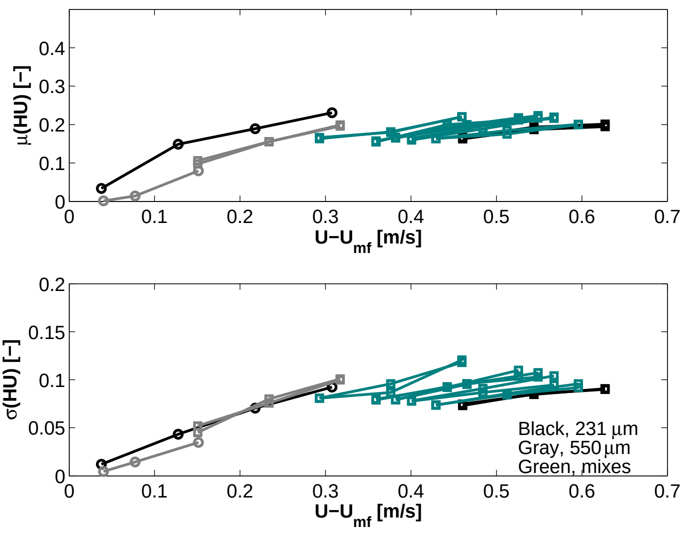

Figure 10.4: Bubble holdup overall characterization: circles, glass particles; squares, corundum particles

10.2 Local bubble hold-up distribution

Once the boundary between emulsion phase and bubble phase has been chosen, as already discussed in relevant chapter, the bubble hold up ϵ_b (or HU) can be simply defined as:

$$\epsilon_b = \frac{\int_V V_{bubble} dV}{\int_V V_{bubble} dV + \int_V V_{emulsion} dV} \tag{10.1}$$

To define the local gas hold-up, it is sufficient to define a proper control volume inside the whole system, and computing the limit for control volume towards zero.

$$\epsilon_{b,loc} = \lim_{V \to 0} \frac{\int_V V_{bubble} dV}{V} \tag{10.2}$$

To compute the time averaged local gas hold-up:

$$\epsilon_{b,av,loc} = \frac{1}{T} \int_0^T \lim_{V \to 0} \frac{\int_V V_{bubble} dV}{V} \tag{10.3}$$

If the control volume is infinitesimal, it can not admit the contemporary presence of both phases, thus the local hold up can be replaced with an instantaneous phase indicator:

$$\Phi\left(x,y\right)=\begin{cases}1 & \Leftrightarrow g\in V_{bubble}\\ 0 & \Leftrightarrow g\notin V_{bubble}\end{cases} \tag{10.4}$$

$$\epsilon_{av,loc}\left(x,y\right)=\frac{1}{T}\int_{0}^{T}g\left(x,y\right)dt \tag{10.5}$$

This definition of phase indicator is immediately applicable to compute local time averaged maps of gas hold-up by the means of digital image analysis techniques. We have to consider the images that can be obtained by the image analysis based on binarized images of the back-lighted fluidized bed already described. If we assume to assign to gas-phase occupied pixels a unitary luminance value, and zero luminance value otherwise, it is simple to observe that luminance value exactly coincides with the gas phase indicator above defined.

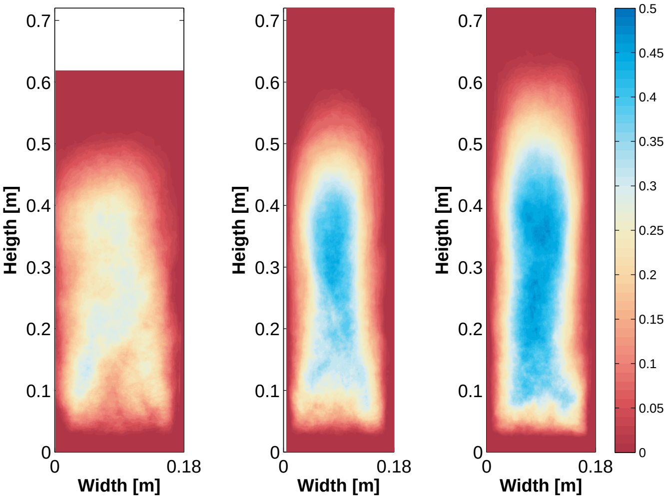

(a) $0.18\,m/s$ (b) $0.27\,m/s$ (c) $0.36\,m/s$

Figure 10.5: Local bubble hold-up maps at different inlet gas velocities (Glass, $d_p = 231\,\mu m$).

The analysis of experimental time averaged bubble phase hold-up, shown in Fig.10.5 for the cases of glass particles, allows the visual observation of preferential bubble paths along the bed, with a typical reverse-Y shaped pattern starting near the bottom of the bed and developing in the upper regions of the bed. The reverse-Y shaped pattern is due to the coalescence-driven bubble dynamics prevailing after bubble nucleation in the proximity of the distributor in the intermediate region of the bed. In particular, the analysis of the maps allows the observation and quantification of systematic trends in bubbles path characteristics. At low inlet gas velocity, bubbles appear to almost uniformly rise through the bed. Increasing inlet gas velocity, the tendency for bubbles to follow the reverse-Y path in the lower region of the bed increases, while the void distribution in the proximity of the bed surface appear to be less sharp, due to more intense eruption of bubbles. This is likely to be due to the influence of lateral walls on bubble dynamics.

The average holdup maps reported in Figs.10.6 - 10.8 show results that qualitatively agree with those by Lim et al. (2007), *i.e.* a pair of narrow bands of high bubble concentration along either sides of the bed close to the walls near the distributor, which gradually migrate inwards, spreading over the center of the bed higher up in it. The tapering of bubble distribution also leaves the regions close to the wall in the upper part of the bed deprived of bubbles. It is worth noting that the bed height at witch the lateral bands reach the bed centerline gives indication of a fully developed bubbling regime.

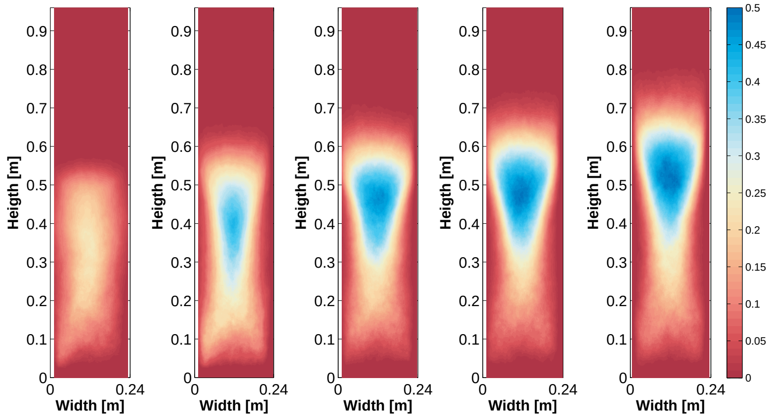

(a) $x = 0.0$ (b) $x = 0.2$ (c) $x = 0.5$ (d) $x = 0.8$ (e) $x = 1.0$

Figure 10.6: Local bubble hold-up maps at fixed inlet gas velocity ($0.56 m/s$) and different flotsam compositions.

A somehow different behavior is observed when analyzing bubble hold-up maps obtained for corundum mixtures. Increasing inlet gas velocity, the tendency for bub-

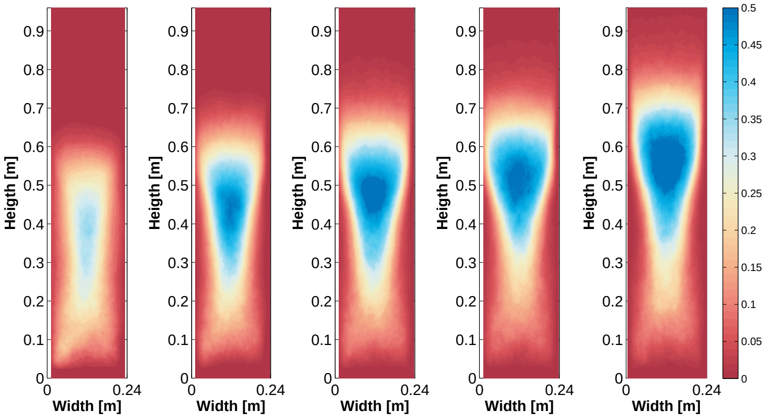

(a) $x = 0.0$ (b) $x = 0.2$ (c) $x = 0.5$ (d) $x = 0.8$ (e) $x = 1.0$

Figure 10.7: Local bubble hold-up maps at fixed inlet gas velocity $(0.64m/s)$ and different flotsam compositions.

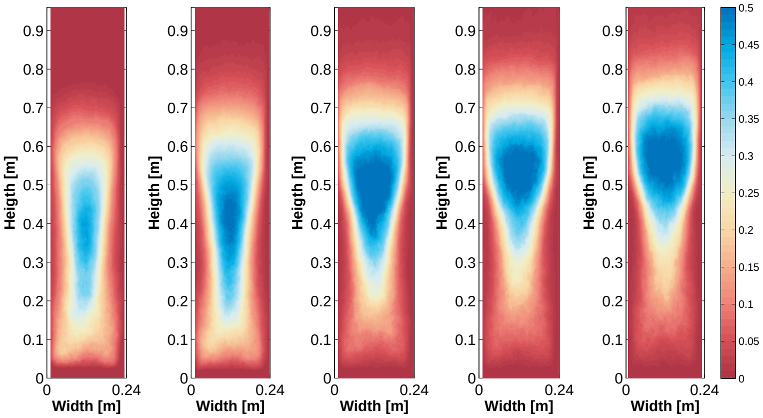

(a) $x = 0.0$ (b) $x = 0.2$ (c) $x = 0.5$ (d) $x = 0.8$ (e) $x = 1.0$

Figure 10.8: Local bubble hold-up maps at fixed inlet gas velocity $(0.72m/s)$ and different flotsam compositions.

bles to follow the reverse-Y path in the lower region of the bed increases, while the void distribution in the proximity of the bed surface appear to be less sharp, due to more intense eruption of bubbles, as it can be seen, for example in figure from 10.6.a to 10.6.e. When pure jetsam bed is considered (Figs.10.6.a, 10.7.a, 10.8.a), the lateral band appear to reach the bed center very close to the distributor, below $0.2m$. In agreement with Lim et al. (2007) findings, near-wall zones near the bed surface are almost bubble free. Conversely, when increasing flotsam content, a rather different behavior is observed, *i.e.* the lateral bands of bubbles formed at the distributor reach the bed center at higher elevations, and a wide zone of high bubble content is formed on the whole bubble width. This kind of behavior can be likely to be due to the onset of constrained bubble growth.

Notably, the region having average bubble hold-up larger than to 0.5 seems to be suitable for bubbling type characterization. Its shape strongly depends on both composition and inlet gas velocity. It changes from an almost uniform shape at lowest velocity and composition (related to a relatively weak bubbling regime, see Fig.10.6.a) to a straight I-shape at intermediate compositions and velocities (typical of partially slugging regimes, see for example figures from 10.8.b to 10.8.d) and eventually to a deep-U shape at the highest velocity and composition (due to the onset of a fast fluidization regime at least in the highest section of the bed, see for instance Fig.10.8.e). It is worth noting that the straight-vertical path in the upper sections of the bed appear to be straighter and thinner with increasing gas velocity at fixed composition (Figs.10.6.a, 10.7.a and 10.8.a), as a consequence of the formation of greater bubbles, rising up undisturbed through the bed because of a less significant presence of coalescence phenomena, as well as increasing flotsam composition at fixed inlet gas velocity (figures from 10.6.a to 10.6.e)

The analysis of time averaged hold-up maps is of course fully consistent with the bed height and bubble hold-up results previously presented in Fig.10.4

10.3 Bubble size evolution

Some of the available experimental distributions of bubble equivalent diameters are reported as function of bubble distance from distributor. The full set of data are presented in Fig.10.9 in raw cloudy form, in order to highlight the complex bubble behavior along bed height. The adoption of an average curve with indication of its variance would not account for the richness of the raw data. Conversely, the cloudy data presented allow the visualization of the small bubbles that are inside the bed even at the highest elevations, while an average curve, even if with variance, could not show such characteristic and complexity.

On the whole the experimental data show a characteristic increase in bubble diameter, with an upper envelope of data approximately following a power law, in accor-

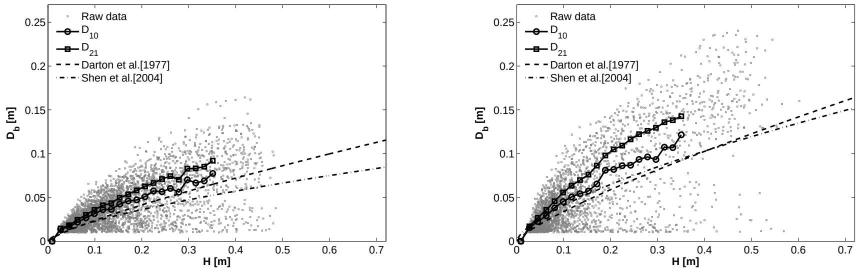

(a) $U = 0.18\,m/s$ (b) $U = 0.36\,m/s$

Figure 10.9: Bubble diameter evolution at two different inlet gas velocities (Glass, $d_p = 212 - 250\,\mu m$)

dance with the analysis by Darton et al. (1977). However, the presence of a wide distribution of bubble sizes is evident at all elevations of the bed, as a result of the splitting and/or nucleation phenomena. At increasing gas velocities, the increase in bubble diameter is more pronounced, as physically expected. Moreover, the presence of small bubbles in upper regions of the bed appear to be less pronounced with increasing velocity, due to the onset of slugs in such regions. This results are in agreement with the finding of Hulme and Kantzas (2004), in which large data scattering on bubble diameter *vs.* distance above the distributor was shown.

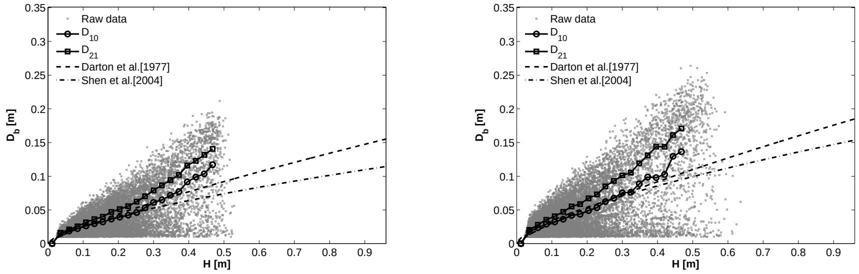

(a) $U = 0.56m/s$ (b) $U = 0.64m/s$

Figure 10.10: Bubble diameter evolution at two inlet gas velocities (Corundum, $d_p = 550\,\mu m$)

Similar data trend is shown in Fig.10.10 in which the raw data on bubble diameter as a function of elevation above the distributor are reported for the case of coarse corundum particles fluidized at two different velocities. When corundum particles are adopted, a considerably larger amount of small bubbles is evident at all elevations, but the average bubble size tends to increase with the excess gas velocity and elevation above the distributor.

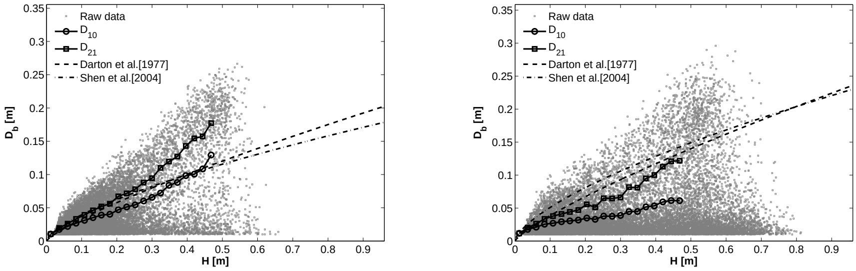

(a) $X = 0.20$

(b) $X = 0.80$

Figure 10.11: Bubble diameter evolution at two different powder composition (Corundum, $U = 0.56\,m/s$)

A rather different behavior can be observed in Fig.10.11, in which two raw data set obtained for two different corundum mixtures fluidized at the same inlet gas velocities are reported. Again, the data assume the form of a wide cloud, but the number of small bubbles is much larger at all elevations with respect to the data reported in Fig.10.9 and 10.10. This fact is due to the high inlet gas velocities adopted for these experiments (the inlet gas velocity must overcome the final fluidization velocity of the mixture U_{ff} to guarantee the homogeneous composition of the bed), that leads to very strong bubbling condition in the upper section of the bed. This regime leads to the strong presence of small shrank bubbles at all elevations, as also reported by Hulme and Kantzas (2004). This in turn leads to a slight decrease of the average diameter curve slope when increasing the inlet gas velocity.

This first analysis points out that the adoption of an average curve can not fully account for the richness of the raw data. Conversely, when raw data are presented, it is possible to observe small bubbles that are inside the bed even at the highest elevations. A good compromise between easiness of calculation, physical meaning and ability in describing bubble diameter evolution dynamics along bed height is in most of the cases given by the local value of D_{21}, *i.e.* the ratio between the second and the first moment of the local bubble size distribution Busciglio et al. (2010). An example of bubble D_{21} variation along bed height at fixed inlet gas velocity and different compositions is reported in Figs.10.12 and 10.13:

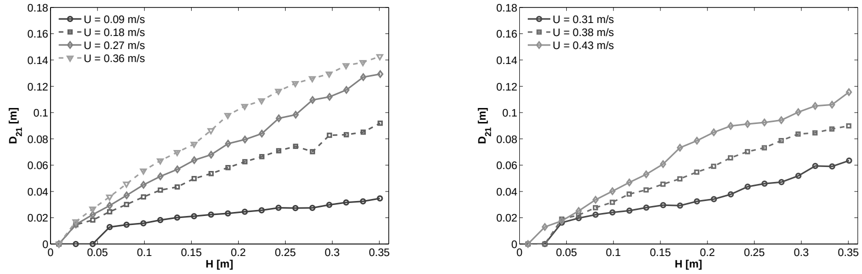

(a) $d_p = 212 - 250\,\mu m$ (b) $d_p = 500 - 600\,\mu m$

Figure 10.12: D_{21} evolution with the elevation above the distributor for glass ballotini varying the inlet gas velocity

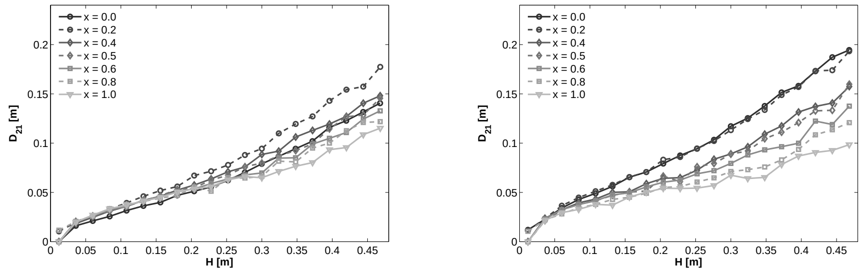

(a) $U = 0.56\,m/s$ (b) $U = 0.72\,m/s$

Figure 10.13: D_{21} evolution with the elevation above the distributor for corundum particle mixtures varying the powder composition

As expected, it is possible to observe in 10.12 a characteristic increase in bubble average diameter with elevation at each velocity investigated, and a steeper increase of bubble diameter increasing the inlet gas velocity. This is well expected and in qualitative agreement with literature correlations already discussed Darton et al. (1977); Shen et al. (2004). Nevertheless, unexpected trend appears when corundum mixtures are fluidized, as shown in Fig.10.13: in fact, it would be expected that larger bubbles will form when highest compositions are fluidized, once fixed the inlet gas velocity. In fact, an increase of the flotsam content generally leads a decrease of the minimum fluidization velocity, and would lead to a strongest bubbling regime or slugging, if the inlet gas velocity is fixed. This can be easily explained analyzing Fig.10.11: an increase of flotsam content of the fluidized powder in fact lead to an increase in number of small bubbles at the highest elevations instead of an increase of bubble diameter (that is eventually limited by fluid bed width). On this basis, more sophisticated statistical instruments could be applied to fully asses this complex behavior, *i.e.* showing the relevant standard deviation of local average values, see Figs.10.14 and 10.15

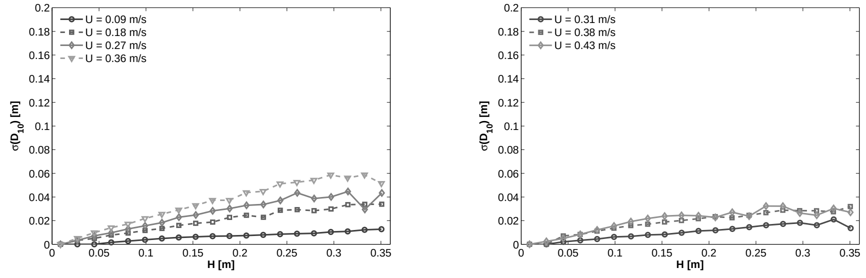

(a) $d_p = 212 - 250\,\mu m$ (b) $d_p = 500 - 600\,\mu m$

Figure 10.14: $\sigma(D_b)$ evolution with the elevation above the distributor for glass ballotini varying the inlet gas velocity

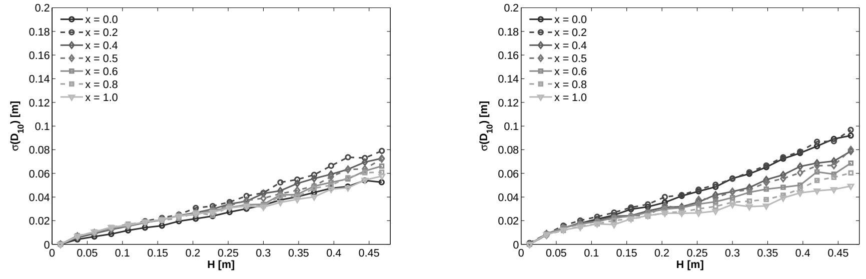

(a) $U = 0.56\,m/s$ (b) $U = 0.72\,m/s$

Figure 10.15: $\sigma(D_b)$ evolution with the elevation above the distributor for corundum particle mixtures varying the powder composition

The unexpected effect is again clearly visible in this last figure: in particular, an increase of standard deviation would be expected when mixtures richer in the flotsam component are considered. Conversely, it is possible to observe that an increase of the flotsam fraction leads to smaller-valued $\sigma(D_b)$ curves, with a smooth transition from pure jetsam to pure flotsam. This can be explained by a thorough observation of Fig10.11: in practice, in the case of pure jetsam component data, for any given inlet gas velocity, it is possible to observe that small bubbles are present at all elevations in the bed, but their number tends to decrease with elevations due to the coalescence with other bubbles, as will be further discussed in subsequent sections analyzing bubble density evolution. Different trends are observed if the ratio D_{21}/D_{10} is plotted as a function of bubble elevation above the distributor:

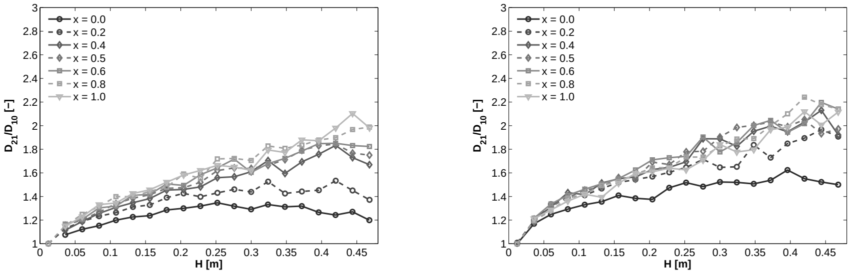

(a) $U = 0.56\,m/s$ (b) $U = 0.72\,m/s$

Figure 10.16: D_{21}/D_{10} evolution with the elevation above the distributor for corundum particle mixtures varying the powder composition

This index acts as an indicator of polydispersity of the analyzed sample of bubble diameters. Figure 10.16 highlight that the width of local bubble size distribution increase with elevation above the distributor and with the inlet gas velocity. Notably, this difference between the local standard deviation analysis and the local D_{21}/D_{10} values puts in evidence that local bubble size distribution must have a strong positive skewness. It was already observed that the mode of bubble diameters is quite different from the mean bubble diameter on the overall bed (Agarwal, 1985), because of the characteristic skewness of BSDs in fluidized beds. It was also proposed a suitable correlation for the prediction of average bubble diameters. Horio and Nonaka (1987) considered the bubble diameter evolution in steady-state condition as the results of a dynamic equilibrium between coalescence and break-up frequencies. In particular, the latter phenomenon is found to be related to particulate dimension instead of bubble diameter. The equation that results from the model was an extension of the equation proposed by Mori and Wen (1975). Nevertheless, a more in-depth data analysis and processing is actually needed for better understanding of the phenomena involved.

10.4 Bubble density evolution

A first more in depth understanding of bubbling behaviors, in which a wide range of operative conditions is analyzed can be performed through the analysis of bubble numerousness as a function of the elevation above the distributor.

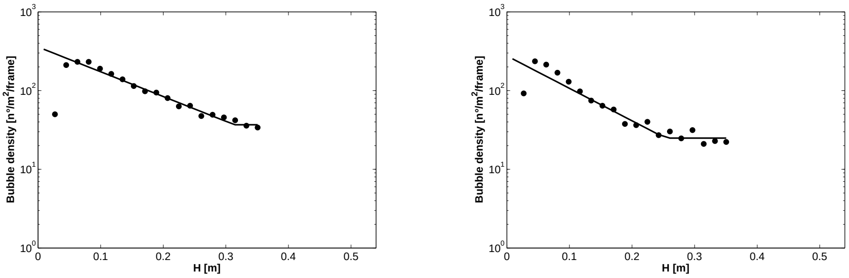

(a) $U = 0.18\,m/s$ (b) $U = 0.36\,m/s$

Figure 10.17: Bubble density evolution at two inlet gas velocities (Glass, $d_p = 212 - 250\,\mu m$)

Figure 10.17 shows the average bubble density along the bed height for two different glass particle systems fluidized at different inlet gas velocities. The bubble density is computed by discretizing the whole bed height in a certain number of slices, 20 here, and calculating the number of bubble centroids falling into each slice. This procedure is repeated for each individual frame and the results are averaged over all the frames analyzed.

A linear decay of bubble density can be easily observed in the semi-logarithmic chart of Fig.10.17. Such a behavior for a bubbling bed can be explained by performing a simple bubble density balance over an infinitesimal section of the bed, which gives:

$$N_b|_{z+dz} = N_b|_z + k_b dz \tag{10.6}$$

where k_b is the bubble density rate of change per unit volume of bed. Rearranging:

$$\frac{dN_b}{dz} = k_b \tag{10.7}$$

Assuming that the bubble density rate of change per unit volume of bed is proportional to bubble density itself (first order decay rate):

$$\frac{dN_b}{dz} = K_b N_b \tag{10.8}$$

and integrating between the bottom of the bed and the general elevation H:

$$ln\left(\frac{N_b}{N_0}\right) = K_b\, H \tag{10.9}$$

one finally gets

$$ln\,(N_b) = K_b\, H + ln\,(N_0) \tag{10.10}$$

which is in fact a first order bubble net coalescence rate. The experimental data reported in Fig.10.17 show an almost similar behavior at all inlet gas velocities, with a linear decay trend for all investigated cases. It is worth pointing out that the slope of the linear tend appears to reach an almost constant value at the highest velocities. A constant value of bubble density would be expected in the case of fully developed slug flows, or, more in general, in the case of fully developed bubbly flows resulting into a dynamic equilibrium condition between bubble coalescence and breakup. As a final statement, this behavior can be summarized as follows:

$$ln\,(N_b) = \left\{ \begin{array}{cll} = & k_b\, H + ln\,(N_0) & bubbling \\ = & ln\,(N_s) & slugging \end{array} \right. \tag{10.11}$$

where N_0 is the bubble number density at the distributor, N_s the slug number density and k_b is the specific rate of coalescence.

In Fig.10.18 all fitting data obtained are reported as a function of excess gas velocity. As it is possible to observe in Fig.10.18(a), the bubble density at the distributor N_0 slightly decreases with the excess gas velocity, while the slug number N_s increase. On overall, the bubble net coalescence rate decreases with inlet gas velocity.

The data previously discussed on bubbling characterization can be now discussed a little more in depth: in fact, the more important characteristic of high velocity bubbling regimes is the very small difference between N_0 and N_s. This in turn lead to fully developed bubbly flow (in which a dynamic equilibrium between bubble coalescence and breakup) is realized with higher bubble numbers. This leads to small k_b values

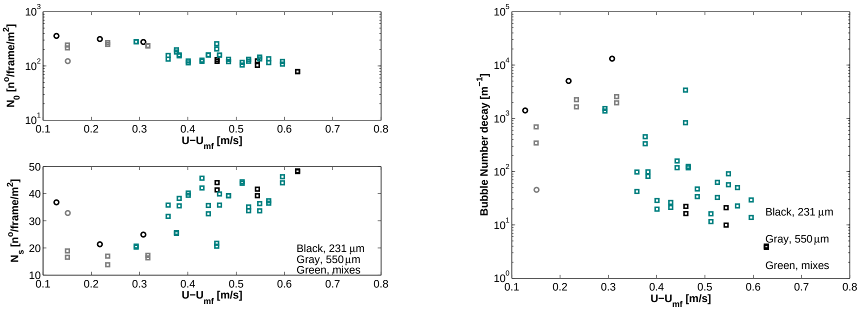

(a) Slug and Distributor densities

(b) Decay rate

Figure 10.18: Bubble decay rate fitting parameter as function of excess gas velocity: circles, glass particles; squares, corundum particles

and large N_s values (see also Fig.10.11), with large number of small bubbles at all elevations. This evidence can be clearly seen in Fig.10.19, where the data relevant to corundum mixtures are reported for two different inlet gas velocities. In fact it is possible to observe that for the pure jetsam particles a steep decrease of bubble density is observed, at both inlet gas velocities. When passing from pure jetsam to pure flotsam (this in turn leads to a decrease of the incipient fluidization velocity and therefore an increase of the excess gas velocity) the bubble density decrease appears to be less steep, and the regime bubble density N_s subsequently increase.

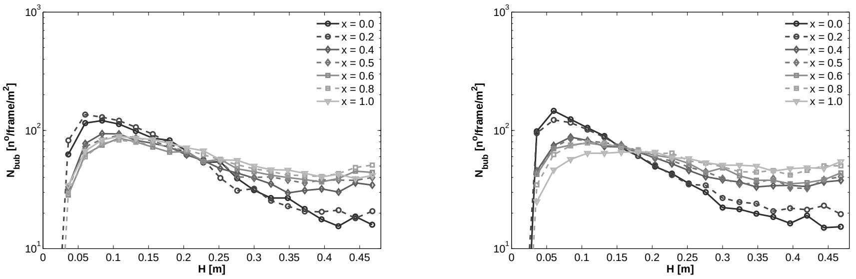

(a) $U = 0.56\,m/s$

(b) $U = 0.56\,m/s$

Figure 10.19: Bubble decay rate fitting parameter a s function of excess gas velocity

10.5 Bubble size distributions

A different way for bubbling characterization passes through the analysis of the overall bubble size distribution (BSD). Some experimental distributions of bubble equivalent size distribution on the whole bed are reported in Fig10.20. The experimental distributions show a characteristic positive skewness of the distributions at all inlet gas velocities, in accordance with relevant literature data (Argyriou et al., 1971; Morooka et al., 1972; Werther, 1974a,b; Rowe and Yacono, 1975; Lim and Agarwal, 1990; Liu and Clark, 1995; van Lare et al., 1997).

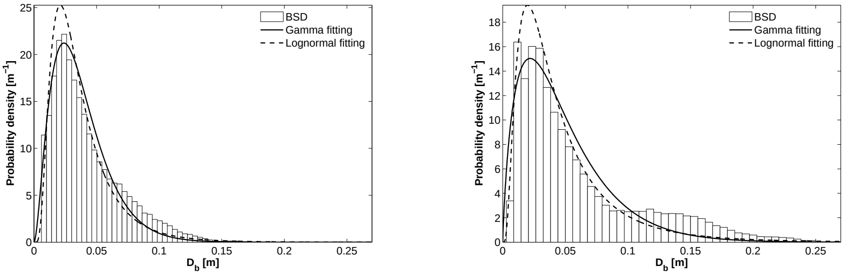

(a) $U = 0.18\,m/s$ (b) $U = 0.36\,m/s$

Figure 10.20: Overall BSD and relevant fitting curves at two inlet gas velocities (Glass, $d_p = 212 - 250\,\mu m$)

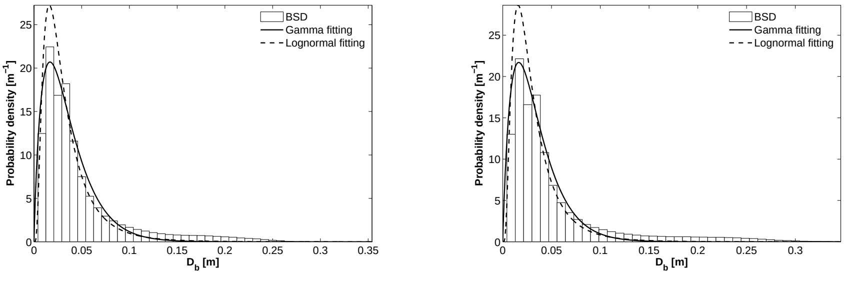

(a) $U = 0.56\,m/s$ (b) $U = 0.64\,m/s$

Figure 10.21: Overall BSD and relevant fitting curves at two inlet gas velocities (Corundum, $d_p = 212 - 250\,\mu m$)

Two kind of fitting were adopted, as suggested in several literature works , *i.e.* the Gamma distribution (Argyriou et al., 1971; Morooka et al., 1972; Rowe and Yacono, 1975; Liu and Clark, 1995) and the Log-normal (Werther, 1974a; van Lare et al., 1997) distributions can be seen in Fig.10.20 and Fig.10.20.

$$BSD_{gamma} = f\left(D_b|G_1, G_2\right) = \frac{1}{G_2^{G_1}\Gamma(G_1)} D_b^{G_1-1} e^{-\frac{D_b}{G_2}} \tag{10.12}$$

$$BSD_{logn} = f\left(D_b|L_1, L_2\right) = \frac{1}{D_b L_2 \sqrt{2\pi}} e^{-\frac{(lnx-L_1)^2}{2L_2^2}} \tag{10.13}$$

It is worth noting that in general both distribution types acceptably describe experimental data, with the exception of the right hand tail of the distribution. This is likely to be due to the simultaneous presence of small bubbles (at all elevation above the distributor) and large bubbles (formed by coalescence of smaller bubbles). Notably, it is well expected that the number of small bubbles largely exceeds that of large bubbles: this in practice gives rise to the disagreement in BSD fitting shown in Fig.10.20 and 10.21. Notably, this phenomenon results less evident in Fig.10.21: in fact, as discussed in previous section, for the case of corundum particles a considerably larger amount of small bubbles is always present at all elevation, therefore partially hiding the large-bubble-related tail.

The parameters of Gamma distribution that best fit experimental data were plotted in Fig.10.22 as a function of excess gas velocity, while the relevant parameters of Lognormal distributions are reported in Fig.10.23:

It is worth reminding that, in general, the Gamma distribution is a two parameter distribution in which the first parameter G_1 acts as a shape parameter, while the second parameter G_2 act as the scale parameter. Notably, the analysis of all data reported in Fig.10.22 points out that the smaller the excess gas velocity, the larger is the distribution shape parameter, and therefore, the distribution results more similar to a Gaussian (non-skewed) distribution. Conversely, at higher inlet gas velocities, an almost constant value of the shape parameter $G_1 \approx 2$ is found. A quite different dependence on excess gas velocity is found analyzing the second distribution parameter, *i.e.* the scale parameter G_2: for each data serie (constant composition and type of particles, varying inlet gas velocity), an increase of G_2 with excess gas flow is found, with a steeper dependence at the lowest excess gas velocities and almost constant values at the highest inlet gas velocities. This fact highlights that a wide range of bubbling behaviors is found in the experiments, ranging from normal bubbling to highly bubbling- fast bubbling regimes. Moreover, the evidences point out the need for different measure-

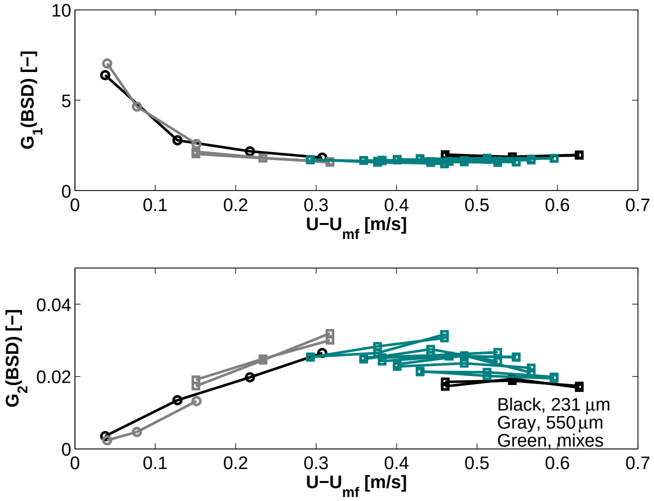

Figure 10.22: Gamma distribution parameters: circles, glass particles; squares, corundum particles

ment approaches in order to fully characterize bubbling behaviors in a wide range of conditions.

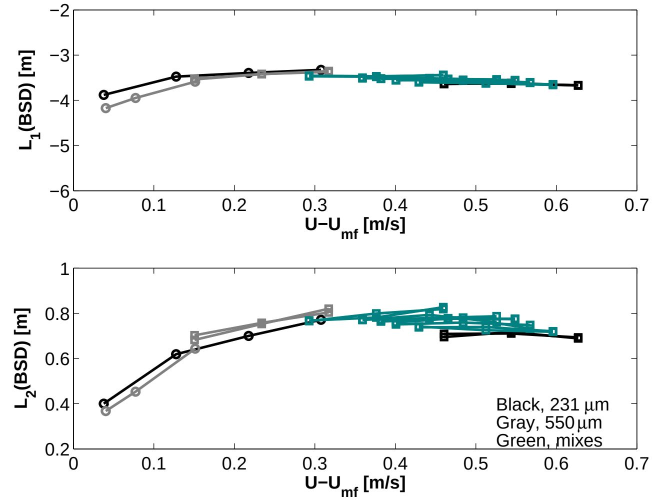

Figure 10.23: Lognormal distribution parameters: circles, glass particles; squares, corundum particles

A quite similar discussion applies to Fig.10.23: the first parameter represent the mean value of the logarithm of the bubble diameter sample under analysis, while the second parameter represent its relevant standard deviation. Notably, is the bed would exhibit a weak bubbling regime, the L_1 value will increase as well as the relevant L_2. This is shown in Fig.10.23 at the lowest inlet gas velocity, while again, at the highest inlet gas velocities, almost constant values of L_1 and weakly dependent L_2 values on excess gas flow are reported.

This is of course justified if it is assumed that at the highest inlet gas velocities a re-arrangement of bubbly flow occurs in which bubble break-up due to highly turbulent bubble motion and interactions lead to the formation of a population of smaller bubbles at all elevations, as already seen in previous sections.

10.6 Local Bubble Size Distribution

The characterization of bubble evolution through a simple average curve, even with indication of its variance would not account for the richness of the raw data, as shown in previous sections. In order to better characterize the bubbles behavior the Bubble Size Distributions over the bed have been extensively studied. In particular, for each experiment, the local non-parametric Bubble Size Distributions (BSD) can be computed. The non-parametric BSD of the bubbles whose centroid was inside each of the ROI (Region of Interest) investigated have been computed. Each BSD is computed by the discretization of the whole diameter range investigated in discrete diameter classes D_i and counting for each diameter class the fraction of bubbles having diameter lower or equal to each D_i value. The curve thus obtained coincides with the cumulative diameter distribution weighed on bubbles number. The BSD is then computed by numerically differentiating the cumulative distribution thus obtained.

The local non-parametric distribution functions are reported in Fig.10.24 and 10.25, for two different cases. Remarkably, the analysis of such BSDs points out a characteristic bimodality at all elevations.

This shape of BSDs is likely due to the coalescence and/or break-up phenomena occurring in the fluidized bed. It is well known that bubbles tend to grow mainly because of coalescence phenomena along bed height. If this phenomenon only is taken into account, a monomodal local BSD would be measured, with the mean diameter value changing with elevation. Nevertheless, our data show that in each of the analyzed ROI, a well defined fraction of bubbles having lower diameter range is found. This feature is likely to be related to nucleation and break-up phenomena, that lead to the presence of small bubbles at all elevations above the distributor. The separation between the secondary peak (*i.e.* the distribution peak having the larger mode) and the primary peak (*i.e.* the distribution peak having the lower mode) appears to be more pronounced with the elevation above the distributor.

The primary peak (small diameter range) is related to locally nucleated and split bubbles, that generally give rise to split bubbles having approximately the same size. Therefore the related peak would show mean and mode values that do not appreciably change with elevation above the distributor. Conversely, the secondary peak is related to the presence of coalescing bubbles. If these bubbles coalesce following (for the sake of simplicity) the pattern proposed by Darton et al. (1977), then the mode or the mean value of this peak would change with the elevation, following a power law Darton et al. (1977); Shen et al. (2004).

To verify these hypotheses, the experimental local BSDs have been fitted with weighted sums of Gamma distribution:

$$BSD(D_b) = \sum_{i=1,2} \phi_i \frac{D_b^{\alpha_i - 1}}{\beta_i^{\alpha_i} \Gamma(\alpha_i)} e^{-\frac{D_b}{\beta_i}} \tag{10.14}$$

$$\sum_{i=1,2} \phi_i = 1 \tag{10.15}$$

where α_i and β_i are the Gamma distribution parameters for the i^{th} peak, and the ϕ parameter accounts for the fraction of bubbles in the primary peak, therefore coinciding with the area of the primary deconvoluted peak. The so obtained distribution parameters will be further analyzed in the following sections.

A detailed analysis was separately carried out on each of the component of BSD fitting function reported in Eqn.10.14 (subsequently referred as component 1, the primary peak at lower diameter range, and component 2, the secondary peak at higher diameter range). For each experimental case investigated, the following set of parameters were finally obtained:

- μ_i: mean value of the i^{th} distribution component, computed as $\alpha_i \cdot \beta_i$;
- χ_i: mode value of the i^{th} distribution component, computed as $(\alpha_i - 1) \cdot \beta_i$;
- σ_i: standard deviation value of the i^{th} distribution component, computed as $\alpha_i \cdot \beta_i^2$;
- Ψ_i: skewness value of the i^{th} distribution component, computed as $2/\sqrt{\alpha_i}$;

- ϕ: small bubbles fraction (*i.e.* fraction of bubbles included in the primary peak).

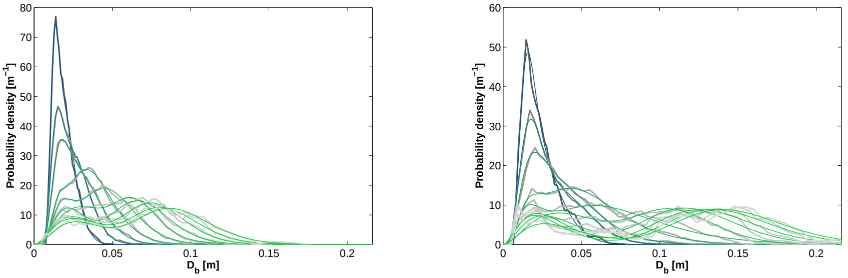

(a) $U = 0.18\,m/s$ (b) $U = 0.36\,m/s$

Figure 10.24: Local bubbble size distributions at two inlet gas velocities (Glass, $d_p = 212 - 250\,\mu m$)

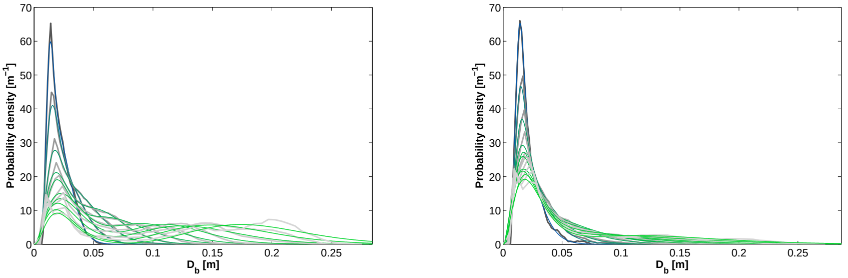

(a) $X = 0.20$ (b) $X = 0.80$

Figure 10.25: Local bubble size distributions at two powder compositions (Corundum, $U = 0.56\,m/s$)

It can be easily observed that, for the case of lower elevations the experimental data show a skewed distribution with one visible mode. This finding may be explained by taking into account that at all elevations near the distributor the prevalent phenomenon is the growth of almost mono-sized bubbles, with negligible break-up and coalescence. At higher elevations the dynamic behavior of bubbles is more complex, since there is the simultaneous presence of bubble growth and nucleation, bubble break-up and coalescence phenomena. The effects of the latter phenomena increase with elevation, resulting into the data distribution to change progressively from a skewed monomodal distribution into a skewed bimodal distribution.

The bimodal pattern evolution of BSD with elevation above the distributor can be explained in the following way. The primary peak (small diameter range) is related to locally nucleated and split bubbles: since it can be assumed that splitting phenomena will give rise to split bubbles of approximately the same size, the related peak would show mean and mode values not changing appreciably with elevation above the distributor. This assumption is justified if we consider that the analysis of BSD accounts for the bubble number and that the bubble-shrinking splitting phenomenon is the principal responsible for the bubbles of the primary peak. Conversely, the secondary peak is related to coalescing bubbles: since this bubbles will coalesce following the mechanism hypotized by Darton Darton et al. (1977), it is expected that the mode or the mean value of this peak would change with elevation above the distribution following a power law somewhat similar to those proposed by Darton et al. (1977) or Shen et al. (2004). The bimodal pattern of local BSD is a substantially new finding with respect of the previous works regarding fluidized beds BSD, that can be easily analyzed via Digital Image Analysis techniques because of the ability to acquire large amount of full-field data, therefore allowing the collection of a sufficient number of bubble data to perform such a detailed analysis.

The fitted mean values and relevant squared variances for different systems investigated are reported in Fis.10.26-10.28

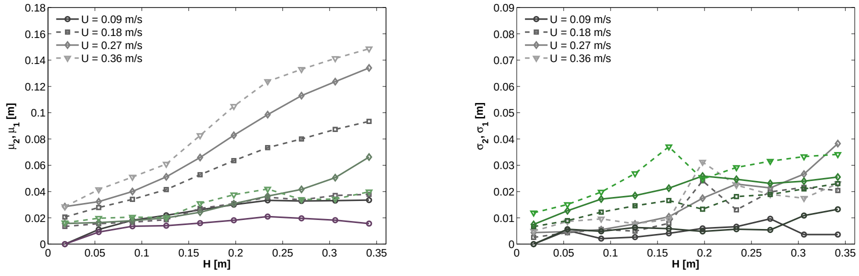

(a) Mean values (b) Squared variance

Figure 10.26: Local Bubble Size distribution parameters (Glass, $d_p = 212 - 250\,\mu m$)

The statistical approach developed in this work allows a separate description of bubbles belonging to the primary and secondary peak. Of course the link between the

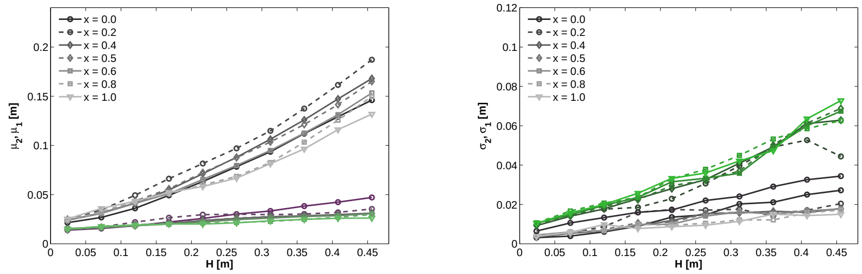

(a) Mean values (b) Squared variance

Figure 10.27: Local Bubble Size distribution parameters (Corundum, $U = 0.56\,m/s$)

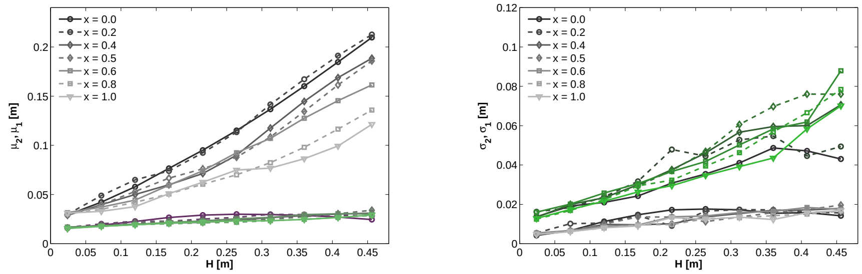

(a) Mean values (b) Squared variance

Figure 10.28: Local Bubble Size distribution parameters (Corundum, $U = 0.72\,m/s$)

primary and secondary peak is still to be assessed. To this aim, mean (μ_1) and mode (χ_1) values of the primary peak together with the relevant χ_2 have been plotted *versus* the mean value of the secondary peak μ_2, as reported in Fig.10.29. It is worth noting that in general, both the mode and the mean value of the primary peak slightly changes with the relevant μ_2 value, but for all cases investigated a very simple dependence was found.

Remarkably, the average value of the primary peak as a function of the relevant μ_2 value was fitted with a simple power law, finally leading to:

$$\mu_1 = 0.065\mu_2^{0.4} \qquad (10.16)$$

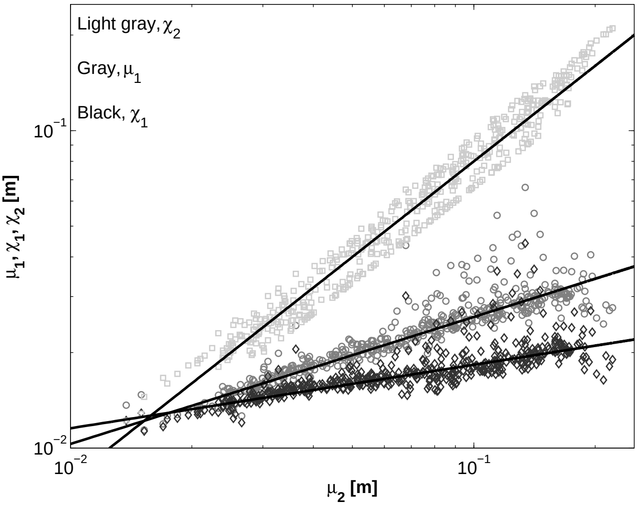

Figure 10.29: Local distribution parameters as a function of μ_2

$$\chi_1 = 0.029\mu_2^{0.2} \tag{10.17}$$

The different dependence shown by χ_1 and μ_1 as a function of μ_2 puts in evidence that the larger μ_2, the larger the skewness of the primary peak. Conversely the secondary peak mode value χ_2 is a linear function of μ_2, therefore highlighting a constant skewness of the secondary peak. A similar operation can be done for describing the relation between the standard deviations of both component peaks, i.e. σ_2 and σ_1, and the mean value of the secondary peak μ_2, ans can be seen in Fig.10.30:

$$\sigma_2 = 0.48\mu_2 \tag{10.18}$$

$$\sigma_1 = 0.15\mu_2 \tag{10.19}$$

It is worth noting that a simple relation exists between the μ_2 value and the relevant D_{21} value, as reported in Fig.10.31, this latter being approximately 0.8 times the μ_2 value.

By describing distribution parameters as an exclusive function of the μ_2 value, it would be therefore possible to estimate with sufficient reliability all the relevant dimensionless standard deviations, including implicitly the influence of the operating

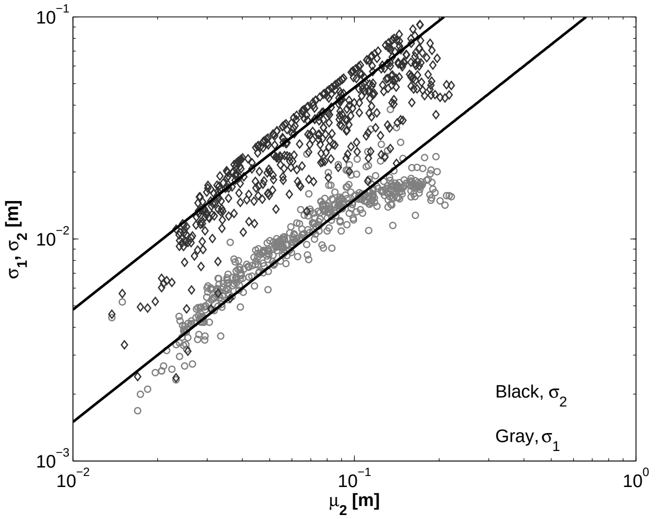

Figure 10.30: Local distribution width as a function of μ_2

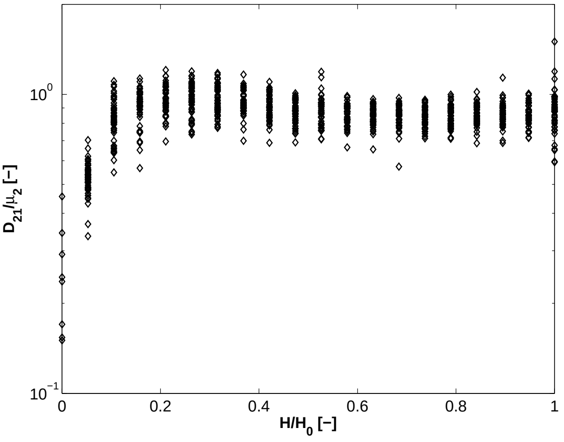

Figure 10.31: Comparison between D_{21} and relevant μ_2 values.

conditions (*e.g.* type of particulate and inlet gas velocity) and the elevation above the distributor.

This latter point has been addressed with a highly empirical method, given the lack of experimental relations covering so wide ranges of bubbling regimes. In particular, two different dependencies were analyzed of μ_2 on the elevation above the distributor and excess gas velocity, below and beyond the ecess gas velocity value of 0.3 m/s, that was found in several results previously shown a good limit for weak bubbling regime.

On this basis, the following equation was found to best fit the data ($R^2 = 0.89$):

$$\mu_2 = \begin{cases} 0.86H^{0.98}\left(U - U_{mf}\right)^{0.60} & \rightarrow \quad (U - U_{mf}) < 0.3m/s \\ 0.23H^{0.96}\left(U - U_{mf}\right)^{-0.47} & \rightarrow \quad (U - U_{mf}) > 0.3m/s \end{cases} \tag{10.20}$$

The results of the above presented fitted equation is reported in Fig.10.32, in which the μ_2 values computed by means of Eqn.10.20 are reported as a function of relevant experimental values.

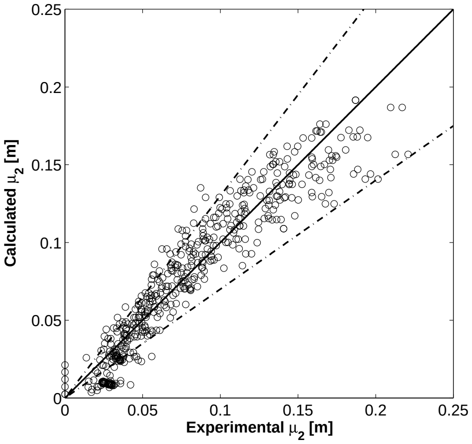

Figure 10.32: Comparison between calculated and experimental μ_2 values.

As it is possible to observe, almost all value are correctly predicted in the interval $\pm 30\%$.

10.7 Bubble velocity distribution

In Fig.10.33 and 10.34, the distribution of velocity coefficient for the bubbles in the bed in different experimental cases is reported. The velocity coefficient is defined on the basis of a generalization of the well known empirical equation for determining bubble rise velocity u_b:

$$U_b = \phi\sqrt{g\,Db} \tag{10.21}$$

Davidson and Harrison (1963) proposed a value for the velocity coefficient $\phi = 0.71$, whereas Shen et al. (2004) proposed $\phi = 0.8 \div 1.0$, specifically measured for 2-D fluidized beds.

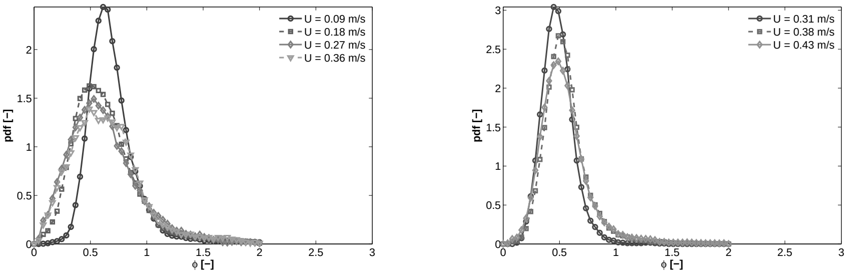

(a) $d_p = 212 - 250\,\mu m$ (b) $d_p = 500 - 600\,\mu m$

Figure 10.33: Velocity coefficient distribution parameters (Glass)

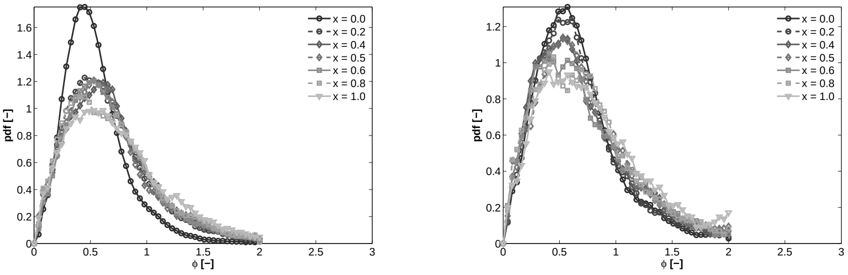

(a) $U = 0.56\,m/s$ (b) $U = 0.72\,m/s$

Figure 10.34: Velocity coefficient distribution parameters (Corundum)

Comparisons between the experimental distributions of the bubble velocity coefficient as computed by using the LVT bubble tracking data show that the velocity coefficient distribution has a characteristic positively skewness, probably linked to the relevant bubble size distribution. The measured skewed distributions appear to be larger with increasing gas velocity, therefore confirming that stronger bubble interactions occur. On the contrary, the modes of the distribution appear to be negligibly influenced by the gas velocity.

The analysis of experimental data on average rise velocity as a function of bubble equivalent diameter reported in Fig10.35 shows a behavior different trend than expectation, *i.e.* than that of Eqn.10.21. At smaller diameters, the average rise velocities are larger than those predicted, while at the larger diameters the experimental data are quite noisy. In the mid-range of diameters, the data trend follow correctly the square-root law expected, but velocity is somewhat smaller than that deriving form a velocity coefficient of $\phi = 0.71$, and a velocity coefficient of $\phi = 0.58$ should be adopted. These findings can be all explained if the bubbling conditions adopted for experiments are recalled. In a few word, the systems investigated ranged from poorly bubbling to highly slugging system. The more intense the bubbling regime, the strong are bubble bubble-to-bubble interactions within the bed. On this basis, it is easy to imagine that small bubbles velocities are largely influenced by interaction with larger bubbles, that tend to accelerate them toward coalescence. At the same time, it is clearly very difficult to accurately measure the velocity of large, high-interacting bubbles, because of the chaotic motion of their boundary due to coalescence phenomena, bubble splitting phenomena and deformation along their path along the bed.

The data presented can not be therefore easily compared with existing correlations developed for single bubbles or bubbles in weak bubbling conditions, but, on the contrary, must be further investigated to better explain and model the phenomena governing bubble motion and interactions.

10.8 Overall bubble velocity fields

The experimental bubbles vector plots are reported in Figs.10.6-10.8 for all experiments conduced with corundum particles. The plots are obtained by suitable time averaging of instantaneous bubble velocity maps. In accordance to the previous discussions, bubble trajectories would be slightly oriented toward the center of the bed in the lower part of the bed and then vertically directed in the upper section of the bed. Moreover, the velocity field plots confirm the evidence for the local bubble hold-up maps shown in Figs.10.6-10.8. These latter allow for the visualization of preferential bubble paths along the bed height, whereas the former relates the relevant bubble average velocities to preferential paths.

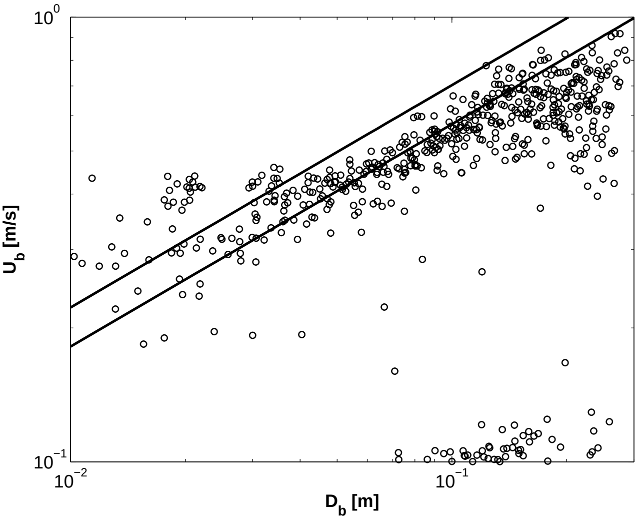

Figure 10.35: Bubble average rise velocities

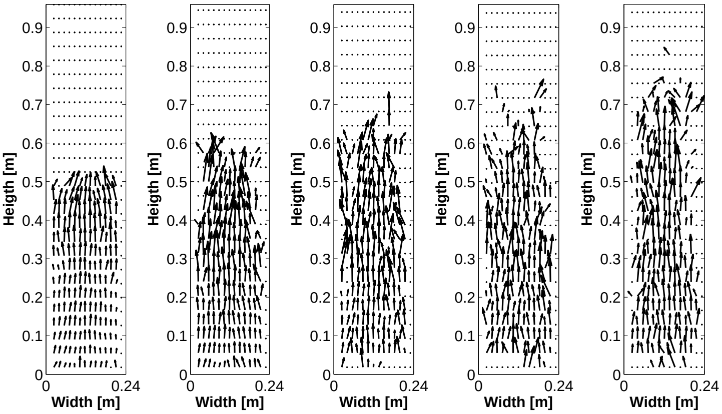

(a) 0.0 (b) 0.2 (c) 0.5 (d) 0.5 (e) 0.5

Figure 10.36: Velocity vector plots at fixed inlet gas velocity $(0.56 m/s)$ and different flotsam compositions.

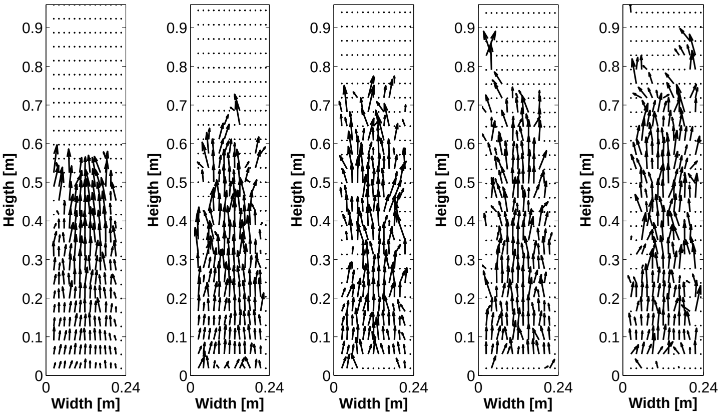

(a) 0.0 (b) 0.2 (c) 0.5 (d) 0.5 (e) 0.5

Figure 10.37: Velocity vector plots at fixed inlet gas velocity ($0.64 m/s$) and different flotsam compositions.

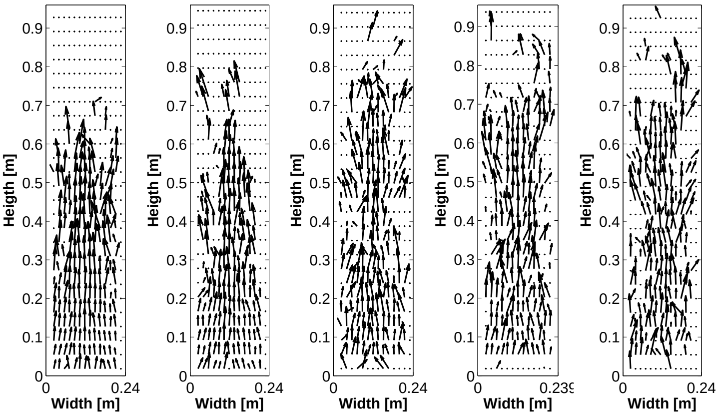

(a) 0.0 (b) 0.2 (c) 0.5 (d) 0.5 (e) 0.5

Figure 10.38: Velocity vector plots at fixed inlet gas velocity ($0.72 m/s$) and different flotsam compositions.

11 Concluding remarks

A digital image analysis technique (DIAT) was developed in this PhD work to study the hydrodynamics of a lab-scale two dimensional bubbling fluidized bed. The DIAT allows for the simultaneous measurements of the most significant bubble properties by means of a purposely in-house developed software. The statistical analysis performed on the test case here presented allows to state that the highly automated technique here developed may well be used to fully characterize the complex dynamic behavior of freely bubbling beds, highlighting its large potential. Moreover, the present image analysis technique may well be applied also to the case of CFD simulations of bubbling fluidized beds where results may be conveniently shown in terms of solid (or gas) phase distribution maps thus being a post-processing tool particularly useful for validation.

A thorough analysis of bubbling characteristics in fluidized bed has been performed, highlighting the complexity of phenomena involved. In particular, a large part of the work was devoted to the systematic analysis of bubble dynamic analysis in different operative condition, *i.e.* by widely varying the inlet gas velocity and the powder composition, this latter aspect being poorly analyzed in the pertinent literature. A novel full statistical analysis of bubble size distribution in 2D gas fluidized beds has been developed. The analysis of local bubble size distributions highlighted a characteristic bimodality that can be explained through the coalescence/splitting behavior of bubbles inside the bed, under the hypothesis of separable effects (*i.e.* the split bubbles give rise to a peak on the local BSD appreciably different from that of coalescing bubbles). The full statistical approach for the characterization bubble population (in terms of average values of large bubbles, relevant standard deviations and BSD shape) can be adopted for more in depth characterization of bubbling dynamics.

The analysis of bubbling dynamics of mixed powders has shown that most of the properties investigated can be sufficiently well explained on the basis of well accepted parameters such as the Excess gas flow, provided that some care must be taken in data analysis when high velocity fluidization is considered.

The work here presented is of course only a part of a more extended work on fluidization dynamic analysis. In particular, future developments could be aimed at the measurement of different particle-fluid systems. On the other hand, data obtained could be used for the development of more accurate or reliable models for the prediction of fluidization dynamics.

Part III

Fluidization Modeling

12 Introduction to linear stability modeling

12.1 Fundamental aspects of fluidized beds modeling

The widespread application of gas particle flow systems and fluidization in industry demands the development of reliable and accurate mathematical models, to be validated by detailed experimental data. The recent development of mathematical modeling of particulate solids behavior together with the increased computing power enables researchers to simulate the behavior of fluidized powders and to link fundamental particle properties directly to the powder behavior and predict the interaction between particles and gaseous or liquid fluids. To this regard, computational fluid dynamics (CFD) modeling provides a fundamental tool to support engineering design and research in multiphase systems. Many authors recognize that computational modeling in multiphase systems has the potential to increase process efficiency and reduce the number of scale-up steps in the design of reliable commercial plants.

Gas-fluidized bed may be seen as suspension of solid particles in a gas with high to moderate particle concentrations and so they can be regarded to as a two phase system, in which the solid phase has a distinctive discrete nature with solid particles having their own shape and size. On the other end, the gas phase can be assumed to form a physical continuum. The continuum hypothesis implies that even a very small volume of gas still remains a continuum itself, entirely filled with a large number of molecules (Batchelor, 1973). Variations in the gas properties and variables on a molecular scale can be ignored, since they average out over all length scales of interest.

In the general framework of multiphase flows, gas-particle flow has been characterized in various ways according to the different classification methods suggested in the literature. A general classification is that of (Ishii, 1975), which divides the two phase flows into three classes, according to the topology of the flow, *i.e.*: separated flows, mixed or transitional flows and dispersed flows.

- Separated flows are those in which each phase is materially connected and occupies a distinct region of the flow domain with a unique interface between the two phases. On the other end, dispersed flows are flows in which one phase, the dispersed phase, is not materially connected.
- Mixed or transitional flows are those in which the characteristics of separated and dispersed flows are simultaneously present, as in the case of vertical droplet annular flow with liquid droplets dispersed in a gas core and liquid film falling on the walls.
- Dispersed flows. These in turns include a number of typical regimes, depending on the nature of the two phase involved in the flow, *i.e.*: droplet flow with gas-liquid droplets, bubbly flow with liquid-gas bubbles and particulate flow with gas or liquid-solid particles, where the solid particles constitute the dispersed phase. According to Ishii's classification, particulate flow is the typical regime, which identifies the gas-solid flow in fluidized beds. However, other more specific regimes, have been identified in order to characterize particulate flows as well.

Flow regime classifications, as the ones aforementioned, point to the enormous phenomenological richness of multi-phase flows. The fact that the structure of multi-phase flows can take completely different forms represents one of the major difficulty for a definitive formulation of the governing equations of motion in these systems. In contrary to single phase fluid flow, where it is generally accepted that the Navier-Stokes equations constitute an accurate model of the flow phenomena involved (including turbulence, in terms of instant velocity), the physics underlying multi-phase flows are not yet completely understood.

In general it is not possible to fully predict the flow structure from a fundamental model; instead, the flow regime to be simulated must be born in mind in order to formulate an appropriate multi-phase flow model. Some models are very regime - specific, based on the particularities of each structure, while others are more general; however, *a priori* knowledge of the regime seems indispensable at present.

Multi-phase models for gas solid flows can be generally classified into three types:

1. Phenomenological models that comprise algebraic equations based on simplifying assumptions and mechanistic insight;

2. Semi-fundamental models, derived from the Navier-Stokes equations trough averaging procedures that, however, give rise to terms whose closure must be carried out empirically;
3. Fundamental models, based on the Navier-Stokes equations, that require tracking of all interfaces.

Initially, hydrodynamic studies of fluidized beds focused on experimental measurements and simple analytical models. The main design parameters were identified to be the temperature, pressure, particle density, particle sizes and size distribution, fluidizing gas flow rate, presence of additives, as well as the dimensional characteristics of the vessel, such diameter and height to diameter ratio. These parameters were cast into dimensionless terms and correlated experimentally to the quantities that determine the performance of the reactor, such as slip velocity, solid circulation rate, phase distribution and interfacial area. Due to the complexity of the phenomena underlying multi-phase flow however, experimental correlations lack wide predictive potential and remain tied to the equipment used for their determination. Models of the first type were the only option at an age when differential models were too expensive to compute; they are generally tailored for specific fluidization regimes; yet they can sometimes be combined with a CFD code or assist in estimating parameters.

In the case of bubbling fluidization, for example, one of the first attempts to formulate a coherent theory for describing the flow field surrounding a rising bubble may be traced back to the 50-60's in the two-phase theory presented by Toomey and F. (1952) and developed by Davidson and Harrison (1963). The two phase theory has been widely used to correlate important parameters of the bubbling flow regime, such as bubble size, bubble rise velocity and bed expansion from the knowledge of fundamental fluidization quantities such as the minimum fluidization velocity U_{mf} and the inlet superficial gas velocity U.

The third class of models is applicable in separated flows, or for modeling microscopic phenomena in dispersed flows; in these models, a single set of Navier-Stokes equations is used to describe a multiphase flow field. Therefore the variables exhibit a discontinuous change at the interfaces, that must in general be implemented with appropriate jump conditions. The main complexity in this kind of analysis arises from the fact that the location of the discontinuities is not known a priori, and a method for interface tracking (i.e. simulating the detailed shape of interface) is required.

Whatever the method, however, an essential prerequisite for this level of approximation is that the grid be fine enough to resolve the structure of the interface. In the case of gas-particle flows, these would require a sub-microscopic grid, which would limit the use of such models only to study microscopic flow phenomena around few particles. At present, large-scale CFD modeling of dispersed flows can only be carried out with models of the second type. By applying the fundamental principles of the conservation of mass, momentum and energy to both phases, the mathematical model describing the gas-solid dispersed flow will result in two sets of differential equations, one for each phase.

In setting-up the equations governing the gas-solid flow, one could alternatively decide whether to use coordinates fixed in space o or coordinates that move with the solid particle. These two procedures are known respectively as Eulerian and Lagrangian specifications. The alternative use of the Eulerian or the Lagrangian approaches for the solid phase has given rise to two different classes of semi-fundamentals models, namely the Eulerian-Eulerian model and Eulerian-Lagrangian model respectively.

In both models the gas-phase is modeled as a continuum adopting an Eulerian description. On this basis, the equations of motion for the gas-phase will resemble the single-phase counterpart, though they will be properly modified to account for the presence of dispersed particle-phase. In the remaining, it will make some simplifying assumptions, which limit the attention to the conservation of mass and momentum. No mass or heat transfer between the two phases is considered and therefore isothermal flow with no phase change or chemical reaction is modeled. The description of the particle phase as a fluid implies that all the fluid elements (*i.e.* the particles) have the same characteristics. The choice of a spherical shape has been made since the behavior of such spherical particles is well known experimentally and no particle size distribution has been accounted for. However the particle diameter strongly affects the value of the inter-phase drag coefficient as well as the terms in the particle phase momentum balance equation, which models the particle-particle momentum transfer, *i.e.* the solids stress tensor.

Two different approaches have been taken in early attempts to apply CFD modeling to gas-solid fluidized beds: a discrete method based on molecular dynamics (Lagrangian model); and a continuous approach based on continuum mechanics treating the two phases as interpenetrating continua (multifluid or Eulerian-Eulerian model). These two approaches have been compared by Gera et al. (1998).

In the Lagrangian model of two-phase flow, the Newtonian equations of motion for each individual particle are solved with inclusion of the effects of particle collisions and forces acting on the particles by the gas. Particle-particle collisions are modeled by the hard sphere (Gera et al., 1998), or soft sphere approach (Kobayashi and Mori, 2000). The distinct element method, DEM, is one of the trajectory models, which can calculate the particle velocity and the corresponding particle trajectory to examine interactions, such as those due to multibody collisions (Kaneko et al., 1999). The Distinct Element Method (DEM), (Cundall and Strack, 1979), allows the dynamic simulation of the solid phase motion by tracking individual particles along the system, whereas a CFD algorithm is commonly used to simulate the flow field of the continuous fluid phase. The first application reported in literature of a combined DEM-CFD model was by (Tsujii et al., 1993a). One of the most attractive feature of the DEM-CFD approach is its first principles derivation, which makes it a very powerful tool for fundamental analyses. While in the overwhelming majority of papers in the literature bubbling fluidization is simulated and analyzed, very few of them deal with homogeneous gas-fluidization and, to the author's knowledge, none of which addresses the stability prediction problem. Several studies (Hoomans et al., 1996; Xu and Yu, 1997) have employed the Eulerian-Lagrangian model to simulate freely bubbling and circulating fluidized beds, since the first work by Tsujii et al. (1993b).

General development of TFM, as presented in Enwald et al. (1996), starts from integral conservation equation of mass, momentum and energy across phase boundaries. By applying Gauss and Leibniz theorems, local instantaneous conservation equations and relevant jump conditions are obtained. The subsequent step is the averaging procedure, suitably devised in order to avoid the condition of a space point in which only one phase exists, thus eliminating the consequent difficulty in momentum transfer calculation across phase boundary. An extensive literature was produced on averaging procedures (Anderson and Jackson, 1967; Ishii, 1975; Crowe et al., 1998; Jackson, 2001; Enwald et al., 1996). Volume averaging is actually the most used in practical application, since it is possible to verify the scale separation condition.

Once averaging procedures are applied, the complete set of partial differential conservation equations is obtained (consisting of one volume fraction balance, two mass conservation equations and six momentum conservation equations to solve six velocity components, two volume fractions and pressure).

The most commonly used forms of conservation equations have been developed by Ishii (1975) and Anderson and Jackson (1967). The Ishii model was originally developed for liquid-liquid flows and then was adapted to describe solid-fluid flows (Drew, 1983; Enwald et al., 1996). Conservation equations for both phases are exactly symmetrical, and momentum equations are both Navier-Stokes alike. Conversely, the Anderson and Jackson model was directly derived for gas-solid dispersed flows. It was originally formulated by Anderson and Jackson (1967), and then revisited by Jackson alone (Jackson, 1997, 1998, 2001). The starting point is a set of local equations in the form of Navier-Stokes equations for the fluid phase and second Newton's law for particles. After averaging, a set of Partial Differential Equations (PDE) is obtained, similar to Ishii's ones but with some remarkable differences between the fluid and solid phases equations.

The solid-phase momentum equation contains an additional term to account for momentum exchange due to particle-particle collisions. The absence of the stress term of the particle phase in the particulate momentum equation has led to different models adopting different closure methods, including the kinetic theory model (Sinclair and Jackson, 1989; Gidaspow, 1994; Hrenya and Sinclair, 1997) based on the kinetic theory approach by Chapman and Cowling (1970). The interphase momentum transfer between gas and solid phases is one of the dominant forces in the gas- and solid-phase momentum balances.

The application of kinetic theory to model the motion of a dense collection of nearly elastic spherical particles is based on an analogy to the kinetic theory of dense gases. A granular temperature, θ, is defined to represent the specific kinetic energy of the velocity fluctuations or the translational fluctuation energy resulting from the particle velocity fluctuations. In granular flow, particle velocity fluctuations about the mean are assumed to result in collisions between particles being swept along together by the mean flow. The granular particle temperature equation can be expressed in terms of production of fluctuations by shear, dissipation by kinetic and collisional heat flow, dissipation due to inelastic collisions, production due to fluid turbulence or due to collisions with molecules, and dissipation due to interaction with the fluid (Gidaspow, 1994). Numerous studies have shown the capability of the kinetic theory approach for modeling bubbling fluidized beds, (Pain et al., 2001; Sinclair and Jackson, 1989; Hrenya and Sinclair, 1997; Ding and Gidaspow, 1990; Gelderbloom et al., 2003). The coefficient of restitution quantifies the elasticity of particle collisions between 1, for fully elastic collisions, and 0 for fully inelastic collisions. It was utilized by Jenkins and Savage (1983) to account for the loss of energy due to collision of particles, which is not considered in the classical kinetic theory. The energy dissipated as a result of collisions of granular inelastic particles has been calculated to obtain the ratio of the velocity fluctuations to the mean flow as a function of the coefficient of restitution (Lun et al., 1984). A decrease in the coefficient of restitution results in less elastic collisions generating more fluctuating kinetic energy (Goldschmidt et al., 2001). In dense two-phase flows, the particle interaction time may be much larger than the particle mean free flight time. Thus, the assumption that a pair of particles completes its interaction before interacting with another particle may be invalid as the solids concentration increases (Zhang and Rauenzahn, 2000).

Within the class of TFMs, Gibilaro and Foscolo developed the so-called Particle Bed Model (PBM). The PBM is originated from Wallis' theory on the stability of homogeneous fluidization (Wallis, 1969), where it is stated the need for a voidage-gradient dependent term in solid phase momentum balance to correctly predict the state of homogeneous expansion of fluidized beds. Wallis' theory, based on fluid bed characteristic wave velocities, was further developed by Foscolo and Gibilaro (Foscolo et al., 1983; Foscolo and Gibilaro, 1984; Gibilaro et al., 1985, 1988; Foscolo and Gibilaro, 1987; Foscolo et al., 1995; Gibilaro et al., 1998) who introduced the complete formulation and theoretical bases for the elastic behaviour of the fluidized beds. The PBM was eventually revisited by Gibilaro (2001).

In this model the particle phase is considered as non-viscous and the isotropic contribution to the internal stress is considered negligible, thus eliminating the need for complete stress tensor formulation. Moreover, inter-particle forces are also assumed negligible. Only fluid dynamic effects due to particle concentration gradients are considered through an elastic force contribution within the momentum balance of the solid phase. Different research groups have used the original PBM assumptions to develop new models for the description of fluidization hydrodynamics, such as Lettieri et al. (2001), Brandani and Zhang (2006). PBM based simulations have been compared with relevant experimental data (Owoyemi et al., 2005; Lettieri et al., 2006; Mazzei and Lettieri, 2006), showing promising predictivity.

In particular, Brandani and Zhang (2006) started from Foscolo and Gibilaro's PBM to derive a modified hydrodynamic model. They stated that the elastic term in the solid phase momentum balance equation, defined as an inter-phase force term (*i.e.* hydrodynamic interaction), does not disappear in overall momentum balance. Both phases are treated as continua without any statement about scale separation criteria or explicit averaging procedures. On this basis, Brandani and Zhang (2006) derived a mathematical model in which the elastic force term is included in both fluid and solid phase momentum balance equations.

As far as mathematical closure of the conservation equations is concerned, it is necessary to completely specify momentum transfer between phases (drag forces). Drag forces for dense granular phases can be computed by suitably correcting the well-established correlations developed for isolated particle, or from pressure-drop correlation derived for packed beds (Ergun, 1952; Gibilaro, 2001; Richardson and Zaki, 1954; Gibilaro et al., 1985; Wen and Yu, 1966; Rowe, 1961; Gidaspow, 1994;

Di Felice, 1994; Syamlal et al., 1993; Garside and Al-Bidouni, 1977; Li and Kuipers, 2003; Mazzei and Lettieri, 2007).

On the above grounds, the work here developed stems from original PBM (Gibilaro, 2001) and the modified formulation by Brandani and Zhang (2006), with the aim to formulate a new criterion for the prediction of the onset of bubbling fluidization. This will be accomplished through the development of a set of momentum equations including suitable elastic terms, and the coupling and the linearization of momentum equations.

13 Hydrodynamic modelling

As mentioned earlier, the starting point for the derivation of the proposed stability criterion is the formulation of suitable momentum balance equations. The approach here adopted is that of eulerian-eulerian hydrodynamic modeling (two-fluid model), in which both granular and fluid phases are considered as inter-penetrating fluids.

In particular, the derivation starts from taking into account only gravity, buoyancy and drag forces, with the solid phase defined non-viscous. A discrete momentum balance on both the fluid and the granular phase can be written in mono-dimensional fashion (*i.e.* along the vertical direction), with reference to a Δz section of the bed, in which variation of volume fraction occurs, as sketched in Fig.13.1.

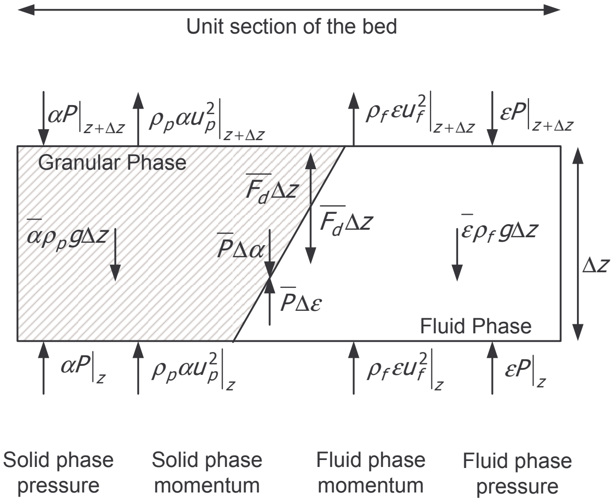

Figure 13.1: Momentum balance scheme over a finite height section of a fluidized bed.

$$
\begin{aligned}
\rho_p \frac{\partial \alpha u_p}{\partial t} = \rho_p & \left[\left(\alpha u_p^2\right)_z - \left(\alpha u_p^2\right)_{z+\Delta z} \right] + \\
& + \left[(\alpha P)_z - (\alpha P)_{z+\Delta z} \right] + \\
& - \bar{\alpha} \rho_p g \Delta z + \bar{F_D} \Delta z + \bar{P} \Delta \alpha
\end{aligned}
\tag{13.1}
$$

$$
\begin{aligned}
\rho_f \frac{\partial \epsilon u_f}{\partial t} = \rho_f & \left[\left(\epsilon u_f^2\right)_z - \left(\epsilon u_f^2\right)_{z+\Delta z} \right] + \\
& + \left[(\epsilon P)_z - (\epsilon P)_{z+\Delta z} \right] + \\
& - \bar{\epsilon} \rho_f g \Delta z - \bar{F_D} \Delta z + \bar{P} \Delta \epsilon
\end{aligned}
\tag{13.2}
$$

In this balance, time averaged properties are considered, and only spatial averaging procedure will be explicitly performed. The momentum balance for each phase, in classical eulerian-eulerian formulation, considers symmetrical forces acting on the relevant control volume: momentum ($\rho_i u_i^2$), hydrostatic pressure (P) , gravitational force ($\rho_i g$), interphase momentum exchange (drag force F_D) and hydrostatic pressure contribution at the interphase boundary. Each term is suitably multiplied by the relevant volume fraction. Notably, the forces acting on the interphase boundary are considered as acting on its center. Hydrostatic pressure field is the same for both phases. Properties which values have been considered at a suitable distance above the control volume bottom were indicated in general as $\bar{\Psi}$.

The momentum accumulation rate is intrinsically spatially averaged and therefore does not require any further average. Conversely, all terms in the form $\bar{\Psi}$ must be evaluated at $\Delta z/2$, since a linear variation of volume fraction is assumed to occur. As a consequence, the following equations can be written in a symmetrical form for both particle and fluid phases.

In the past, a number of works dealt with the modeling of interparticle forces (Rietema and Piepers, 1990; Rietema et al., 1993; Valverde et al., 2003b,a; Valverde and Castellanos, 2007) and tensional stresses due to particle attrition and flow (Enwald et al., 1996). In particular, it was shown (Jackson, 2001; Gibilaro, 2001) that the state of homogeneous fluidization, without the inclusion of suitable extra forces acting on the bed, is intrinsically unstable. Wallis (1969) demonstrated that the inclusion of an elastic force acting on the granular phase can stabilize the state of homogeneous fluidization. Rietema and Piepers (1990) reported that elastic forces can arise from the onset of a stable mechanical structure in homogeneously fluidized beds. Conversely, Gibilaro (2001) and Brandani and Zhang (2006) found that elastic forces arise from purely fluid dynamic interactions within the bed. In the present work the latter modeling approach is adopted and further developed. Of course, the need for inclusion of further terms explicitly accounting for interparticle forces will be discussed when presenting the results. With regard to tensional stresses, it must be reminded that the model to be proposed is aimed at the description of the incipient bubbling state, where granular phase motion is absent (Rietema et al., 1993; Tsinontides and Jackson, 1993; Menon and Durian, 1997).

To accomplish the scale separation, the limit of Eqns.13.1 -13.2 for Δz approaching to a finite value of 2δ must be considered. In addition to limit computation, average properties included in Eqns.13.1-13.2 have yet to be estimated. On the basis of the linear approximation considered, bed properties change linearly along z direction. Therefore, for a generic scalar quantity evaluated at the height $z + \delta$ the following equality can be written:

$$\bar{\Psi} = \Psi + \delta \frac{\Delta \Psi}{\Delta z} \tag{13.3}$$

The above expression may be adopted for each scalar quantity not yet averaged in Eqns.13.1- 13.2; dividing by Δz, the following expression is obtained for solid phase.

$$\begin{aligned} \rho_p \frac{\partial \alpha u_p}{\partial t} = \rho_p \frac{-\Delta\left(\alpha u_p^2\right)}{\Delta z} + \frac{-\Delta\left(\alpha P\right)}{\Delta z} \\ - \left[\alpha + \delta \frac{\Delta \alpha}{\Delta z}\right] \rho_p g + \left[F_D + \delta \frac{\Delta F_D}{\Delta z}\right] + \\ + \left[P + \delta \frac{\Delta P}{\Delta z}\right] \frac{\Delta \alpha}{\Delta z} \end{aligned} \tag{13.4}$$

Similar equation is obtained for fluid phase momentum balance equation.

The ratios can be now substituted with the relevant partial derivatives, being equal to first order terms inside the control volume considered:

$$\begin{aligned} \rho_p \frac{\partial \alpha u_p}{\partial t} = -\rho_p \frac{\partial(\alpha u_p^2)}{\partial z} + \left[F_D + \delta \frac{\partial F_D}{\partial z}\right] + \\ - \left[\alpha + \delta \frac{\partial \alpha}{\partial z}\right] \rho_p g - \frac{\partial(\alpha P)}{\partial z} + P \frac{\partial \alpha}{\partial z} + \delta \frac{\partial P}{\partial z} \frac{\partial \alpha}{\partial z} \end{aligned} \tag{13.5}$$

The differential form of the momentum balance equation is finally obtained by neglecting the second order terms, such as that including the product of the pressure gradient and the volume fraction gradient. By applying the same procedure to the fluid phase discretized momentum balance, the full set of momentum conservation equations can be derived. Drag force derivatives with respect to z coordinate are reported as in the following:

$$\frac{\partial F_D}{\partial z} = \frac{\partial F_D}{\partial \epsilon}\frac{\partial \epsilon}{\partial z} = \frac{\partial F_D}{\partial \alpha}\frac{\partial \alpha}{\partial z} \tag{13.6}$$

The final momentum balance equations (Eqns.13.8-13.7), relevant continuity equations (Eqns.13.9-13.10) and the volume fraction balance equation (Eqn.13.11) are reported in the following.

$$\rho_p \left(\frac{\partial \alpha u_p}{\partial t} + \frac{\partial (\alpha u_p^2)}{\partial z} \right) = F_D - \alpha \left[\rho_p g + \frac{\partial P}{\partial z} \right] + \delta \left[\frac{\partial F_D}{\partial \alpha} - \rho_p g \right] \frac{\partial \alpha}{\partial z} \tag{13.7}$$

$$\rho_f \left(\frac{\partial \epsilon u_f}{\partial t} + \frac{\partial (\epsilon u_f^2)}{\partial z} \right) = -F_D - \epsilon \left[\rho_f g + \frac{\partial P}{\partial z} \right] - \delta \left[\frac{\partial F_D}{\partial \epsilon} + \rho_f g \right] \frac{\partial \epsilon}{\partial z} \tag{13.8}$$

$$\frac{\partial \epsilon}{\partial t} + \frac{\partial \epsilon u_f}{\partial z} = 0 \tag{13.9}$$

$$\frac{\partial \alpha}{\partial t} + \frac{\partial \alpha u_p}{\partial z} = 0 \tag{13.10}$$

$$\epsilon + \alpha = 1 \tag{13.11}$$

With reference to right-hand side (R.H.S.) of momentum equation, it is worth noting that, in addition to drag, gravity and buoyancy, an extra term appears. Notably, the use of a finite length for spatial averaging, large enough to include in the control volume a piecewise linear variation in the volume fraction along the 2δ vertical distance, leads to the appearance of a term in momentum balance equations which is dependent on the δ parameter and the voidage gradient. Such term is quite similar in its expression to the extra momentum term developed by Foscolo and Gibilaro (1987) in the original PBM,accounting for the elastic behaviour of the granular phase. Moreover, it was demonstrated (Wallis, 1969) that the coefficient of the voidage gradient dependent term is proportional to the square of the shock propagation velocity u_D in the relevant phase.

The symmetrical derivation of momentum balance equations leads to the presence of an elastic term in both solid and fluid phase equations. These elastic extra terms are obviously dependent on the formulation of averaging length δ and drag force. The theoretical derivation of a closed formula for estimating δ will be discussed in the next sections.

13.1 Constitutive equations and equilibrium conditions

The trivial steady state solution of the fluidized bed equations implies an uniform expansion of the bed under given conditions of inlet gas velocity and particle properties. The homogeneously fluidization state is stable if any small voidage perturbation starting in a point of the bed will decrease its intensity along its path. Otherwise, homogeneous fluidization is an unstable condition, *i.e.* any voidage perturbation will became larger along its path through the bed. On this basis, the homogeneous fluidization state will be subsequently regarded as the equilibrium condition, for any given particle system and fluid velocity.

One of the fundamental relations for the description of homogeneously fluidized bed is the well know Richardson-Zaki expansion law (Richardson and Zaki, 1954), linking inlet gas superficial velocity U_0 with particle and fluid bed characteristics (voidage ϵ and particle settling velocity u_t):

$$U_0 = u_t \epsilon^n \tag{13.12}$$

where the exponent n was theoretically found to be bounded by the values 2.4 for inertial regime and 4.8 for viscous regime.

In this PhD work a drag force formulation based on the Richardson-Zaki expansion law (Richardson and Zaki, 1954) is adopted, as derived by Gibilaro (2001):

$$F_D = \frac{(1-\epsilon)}{\epsilon^{3.8}} \left(\rho_p - \rho_f\right) g \left(\frac{U_0 - u_p}{u_t}\right)^{4.8/n} \tag{13.13}$$

Explicit expressions for drag force and its derivative will be needed for the formulation of the stability criteria. Near-equilibrium approximations can be used to formulate simpler linear stability analysis. The use of an equilibrium formulation can correctly consider the instability phenomena arising from small perturbations of an initial equilibrium condition, nevertheless giving much simpler formulations.

The equilibrium conditions for the homogeneously fluidized bed can be written as follows:

$$\left\{\begin{array}{lcl} u_p & = & 0 \\ U_0 & = & u_t \epsilon^n. \end{array}\right. \tag{13.14}$$

Where the second equality is the Richardson-Zaki expansion law. By substituting Eqns.13.14 into Eqn.13.13, the following expressions for near-equilibrium drag force and relevant partial derivative with respect to voidage are obtained:

$$F_{D,ne} = \epsilon\left(1-\epsilon\right)\left(\rho_p-\rho_f\right) g \tag{13.15}$$

$$\frac{\partial F_{D,ne}}{\partial \epsilon} = \left(1-2\epsilon\right)\left(\rho_p-\rho_f\right) g \tag{13.16}$$

Two other drag force expressions will be considered for the purpose of comparison, both reported by Gibilaro (2001).

$$F_D = \frac{3\rho_f U^2}{4d_p}\left(0.63+\frac{4.8}{Re_p^{0.5}}\right)^2 (1-\epsilon)\epsilon^{-3.8} \tag{13.17}$$

$$F_D = \frac{\rho_f U^2}{d_p}\left(0.33+\frac{18}{Re_p}\right)(1-\epsilon)\epsilon^{-3.8} \tag{13.18}$$

The first relation (Eqn.13.17) is the expression for single particle drag force, corrected for dense bed condition (Wen and Yu, 1966), hereafter referred as DV drag. The second relation is a modified Ergun equation developed by Gibilaro et al. (1985), hereafter referred as ME drag (Eqn.13.18).

The expression for near equilibrium drag forces in both cases are obtained by inserting Eqn.13.14 respectively into Eqn.13.17 and 13.18:

$$F_{D,ne} = \frac{3\rho_f u_t^2}{4d_p}\left(0.63+\frac{4.8}{Re_t^{0.5}\epsilon^{0.5*n}}\right)^2 \frac{(1-\epsilon)}{\epsilon^{3.8-2n}} \tag{13.19}$$

$$F_{D,ne} = \frac{\rho_f u_t^2}{d_p}\left(0.33+\frac{18}{Re_t\epsilon^n}\right)\frac{(1-\epsilon)}{\epsilon^{3.8-2n}} \tag{13.20}$$

13.2 Momentum equation coupling

General two-phase coupling (Gibilaro, 2001) is achieved getting the pressure gradient from the fluid phase momentum equation (Eqn.13.8), and then substituting it in the particle phase momentum equation (Eqn.13.7).

The general form of pressure gradient can be obtained from from the fluid phase momentum equation:

$$\frac{\partial P}{\partial z} = -\rho_f \left(\frac{\partial \epsilon u_f}{\partial t} + \frac{\partial (\epsilon u_f^2)}{\partial z} \right) - \frac{F_D}{\epsilon} - \rho_f g + \frac{1}{\epsilon} \left(-\frac{\partial F_D}{\partial \epsilon} - \rho_f g \right) \delta \frac{\partial \epsilon}{\partial z} \quad (13.21)$$

This general procedure can be particularized for gas fluidization, by introducing the negligible gas density hypothesis, *i.e.* any gas-density dependent term of the fluid momentum equation is considered negligible with respect to solid-density dependent terms. This assumption is valid in the case of gas fluidization, in which gas density is about three order of magnitude smaller than solid density. The pressure gradient previously derived for general phase coupling (Eqn.13.21) can be now written as in the following:

$$\left. \frac{\partial P}{\partial z} \right|_{\rho_f = 0} = -\frac{1}{\epsilon} \left(F_D + \delta \frac{\partial F_D}{\partial \epsilon} \frac{\partial \epsilon}{\partial z} \right) \quad (13.22)$$

In this approach inertial terms depending on gas density are neglected. Conversely, the elastic force and the drag force affect the pressure gradient profile, and therefore the global hydrodynamics. Such a mathematical development where the fluid-phase elastic term is present will be hereafter referred as partial decoupling approach (PDA). This is quite different from what could be obtained applying the same procedure to the original PBM momentum equations (Gibilaro, 2001), since the elastic term does not appear in the fluid phase momentum balance equation.

Equations 13.15 and 13.16 for near-equilibrium drag force can be easily substituted into Eqn.13.22 to obtain a simple formulation of pressure gradient.

$$\left. \frac{\partial P}{\partial z} \right|_{PDA} = (1 - \epsilon)(\rho_p - \rho_f) g + \frac{(1 - 2\epsilon)(\rho_p - \rho_f) g}{\epsilon} \delta \frac{\partial \epsilon}{\partial z} \quad (13.23)$$

Starting from the PDA, a further simplification can be made by the substitution of Eqns.13.15 and 13.16 into Eqn.13.22 and neglecting the elastic term.

$$\left.\frac{\partial P}{\partial z}\right|_{TDA} = (1-\epsilon)\left(\rho_p - \rho_f\right) g \tag{13.24}$$

The resulting equations (Eqn.13.24) will be hereafter referred as total decoupling approach (TDA). Notably, the TDA will lead to the same results of the original PBM, if a suitable constant value of the δ length is adopted.

In order to derive a coupled equation to describe the behavior of small voidage perturbations traveling along the fluidized bed Eqn.13.13 and Eqn.13.11 are inserted in the R.H.S. of the solid phase momentum balance equation (Eqn.13.7):

$$\begin{aligned} \rho_p\left(\frac{\partial \alpha u_p}{\partial t} + \frac{\partial(\alpha u_p^2)}{\partial z}\right) = \\ (1-\epsilon)\left[\frac{\left(\rho_p - \rho_f\right) g}{\epsilon^{3.8}}\left(\frac{U_0 - u_p}{u_t}\right)^{4.8/n}\right] - \\ + (1-\epsilon)\left[\rho_p g + \frac{\partial P}{\partial z}\right] + \delta\left(\frac{\partial F_D}{\partial \epsilon} + \rho_p g\right)\frac{\partial \epsilon}{\partial z} \end{aligned} \tag{13.25}$$

By rearranging and putting in evidence the voidage-gradient dependent terms, the following coupled balance equation is obtained:

$$\rho_p\left(\frac{\partial \alpha u_p}{\partial t} + \frac{\partial \alpha u_p^2}{\partial z}\right) = F + \delta\left(\frac{\partial F_D}{\partial \epsilon} + \rho_p g\right)\frac{\partial \epsilon}{\partial z} \tag{13.26}$$

The net force term F includes, in its complete non-equilibrium expression, drag, pressure gradient and gravity terms.

$$F_{net} = (1-\epsilon)\left[\frac{\left(\rho_p - \rho_f\right) g}{\epsilon^{3.8}}\left(\frac{U_0 - u_p}{u_t}\right)^{4.8/n}\right] - (1-\epsilon)\left[\rho_p g + \frac{\partial P}{\partial z}\right] \tag{13.27}$$

For PDA the final coupled momentum equation is obtained by substituting the relevant expression of the pressure gradient (Eqn.13.23) in Eqn.13.27, and the relevant partial derivative of drag force (Eqn.13.16) in Eqn.13.26. By rearranging, the following is obtained:

$$\rho_p\left(\frac{\partial \alpha u_p}{\partial t} + \frac{\partial \alpha u_p^2}{\partial z}\right) = F_{PDA} + \rho_p u_B^2 \frac{\partial \epsilon}{\partial z} \tag{13.28}$$

$$F_{PDA} = (1-\epsilon)\left(\rho_p - \rho_f\right) g \left[\frac{1}{\epsilon^{3.8}} \left(\frac{U_0 - u_p}{u_t} \right)^{\frac{4.8}{n}} - \epsilon \right] \tag{13.29}$$

$$u_{D,PDA}^2 = \frac{(1-\epsilon)}{\epsilon} \delta g \tag{13.30}$$

where the dynamic velocity $u_{D,PDA}$ appears.

The same procedure can be adopted by using the TDA equations for near-equilibrium pressure gradient, *i.e.* Eqn.13.24 instead of Eqn.13.23. Eventually, equations identical to Eqns.13.28 and 13.29 are obtained, with the only difference in the formulation of the dynamic velocity (Eqn.13.30), as reported below:

$$u_{D,TDA}^2 = 2\,(1-\epsilon)\,\delta g \tag{13.31}$$

13.3 Linear Stability Criteria

As discussed in detail elsewhere (Gibilaro, 2001), the linear stability analysis is based on the decomposition of variables of the coupled momentum equation (Eqn.13.28). In particular, voidage is expressed as the sum of two terms: an equilibrium value ϵ_0 plus a deviation from equilibrium ϵ^*; particle velocity equilibrium value is assumed to be zero, so that particle velocity deviation value coincides with u_p. Under the hypothesis of near equilibrium conditions, the relevant Taylor expansion of Eqn.13.28 leads to a traveling wave equation for the ϵ^* variable. The solution of this linearized equation reveals that all voidage perturbation wave velocities in the bed are bounded by the kinematic wave velocity (long wave) and the dynamic wave velocity (short wave).

In general, the condition for the exponential decline of a voidage perturbation amplitude along the bed (necessary for stable behavior of homogeneous fluidization) is that u_D is higher than the kinematic wave velocity u_k. In form of dimensionless stability function S:

$$S = \frac{u_D - u_k}{u_k} \begin{cases} > 0 & \text{homogeneous} \\ = 0 & \text{incipient bubbling} \\ < 0 & \text{bubbling} \end{cases} \tag{13.32}$$

In this work, the kinematic wave velocity expression developed by Gibilaro (2001) is adopted:

$$u_k = n u_t \left(1 - \epsilon\right) \epsilon^{n-1} \tag{13.33}$$

13.3.1 Definition of the length parameter

Both Eqns13.30 and 13.31 needs the definition of the δ length, and therefore the height of the finite control volume. For this purpose, in mono-dimensional formulation, a control volume can be taken in which a perturbation of the flow field starts at the bottom. This perturbation needs a time interval Δt to travel through the first particle layer of height d_p, and this time interval depends on the average interstitial gas velocity. It is computed according to the equilibrium expansion law proposed by Richardson and Zaki (1954):

$$\Delta t = \frac{d_p}{u_f} = \frac{d_p}{U_0/\epsilon} = \frac{d_p}{u_t \epsilon^{n-1}} \tag{13.34}$$

During the same time interval Δt, a voidage perturbation travels through the control volume at the kinematic wave velocity, by assuming that the wave passage leads to an instantaneous change of voidage from the initial equilibrium value to the final. The kinematic wave velocity actually travels along a distance δ equal to half height of the control volume in the time interval Δt, as reported in the following expression:

$$\Delta t = \frac{\delta}{n u_t \left(1 - \epsilon\right) \epsilon^{n-1}} \tag{13.35}$$

Under these hypotheses, the full range of states involved in voidage perturbation initiation would occur within the whole control volume:

- the flow perturbation is located at the bottom of the control volume;
- the idealized kinematic wave is located at half height;
- the top is surely not affected by any perturbation, even if the front of the kinematic wave is dispersed by inertial effects.

Such definition of the control volume is certainly valid for a linear stability analysis, where the incipient bubbling state implies the equality of characteristic wave velocities, thus avoiding any perturbation to travel faster than the kinematic waves.

Eventually, by comparing Eqn.13.34 and Eqn.13.35 the time interval Δt disappears:

$$\delta = (1-\epsilon)\, n d_p \tag{13.36}$$

In mono-dimensional formulation, these assumptions lead to the definition of a control volume height variable with voidage. This is a substantial new result in fluidized bed modelling, with respect to both PBM (Gibilaro, 2001) and the Brandani and Zhang Model (Brandani and Zhang, 2006), that will be hereafter referred in the following as BZM. Remarkably it was obtained without any particular assumption but the validity of the Richardson and Zaki (1954) expansion law.

Once the averaging length is defined, Eqn.13.36 can be substituted in Eqns.13.30 and 13.31 to obtain the final expressions for u_B in the case of TDA and PDA respectively. Remarkably, the main difference of the present formulation with respect to those by Gibilaro (2001) and Brandani and Zhang (2006) lies in the expression of the dynamic velocity u_D in terms of functional dependence from the local voidage.

$$\left\{ \begin{array}{lcl} u^2_{D,TDA} & = & 2nd_pg\,(1-\epsilon)^2 \\ u^2_{D,PDA} & = & nd_pg\,(1-\epsilon)^2\,\epsilon^{-1} \\ u^2_{D,PBM} & = & 3.2d_pg\,(1-\epsilon) \\ u^2_{D,BZM} & = & d_pg\,(1-\epsilon)\,\epsilon^{-1} \end{array} \right. \tag{13.37}$$

Substituting these expressions in the stability function reported in Eqn.13.32, two fully predictive stability criteria can be obtained, *i.e.* the total decoupling (TDA) and the partial decoupling (PDA) criterion.

$$\left\{ \begin{array}{lcccl} \text{TDA} & \rightarrow & \epsilon_{mb} & = & \left(\frac{2gd_p}{nu_t^2}\right)^{\frac{0.5}{n-1}} \\ \text{PDA} & \rightarrow & \epsilon_{mb} & = & \left(\frac{gd_p}{nu_t^2}\right)^{\frac{0.5}{n-0.5}} \end{array} \right. \tag{13.38}$$

Formulation of both criteria does not include adjustable parameters, therefore leading to fully predictivity. The TDA-based criterion neglects the influence of the elastic term in the fluid phase momentum balance, thus resulting analogue to the stability criterion obtained on the basis of the PBM, with the exception derived by the use of a voidage dependent term in averaging length. This fact lead to a notably different behavior of the stability function, as will be extensively discussed in the next sections of this chapter. Conversely, the PDA-based criterion includes both new assumption of the model, *i.e.* the elasticity of the fluid phase, as in Brandani and Zhang (2006), and the use of a voidage dependent averaging length. However, in the BZM a constant averaging length equal to d_p is adopted in order to best fit literature data on minimum bubbling voidage. In the present formulation, the averaging length is theoretically derived and found to be dependent on local voidage.

14 Stability criteria validation

The two previously derived approaches will be now analyzed, *i.e.* the Total Decoupling Approach (TDA) and the Partial Decoupling Approach (PDA). The latter is the most general criterion for the case of gas fluidization, while the former is derived under the further hypothesis of negligibility of the elasticity term in the fluid phase. Both criteria are fully predictive, and they just need a closure relationship to estimate the Richardson and Zaki (1954) parameter n and the terminal settling velocity of particles, u_t. For the sake of comparison, the correlations used in this PhD work for such estimates are the same used by Gibilaro (2001):

$$Ar = \frac{g d_p^3 \rho_f \left(\rho_p - \rho_f\right)}{\mu_f^2} \tag{14.1}$$

$$n = \frac{4.8 + 0.1042 Ar^{0.57}}{1 + 0.043 Ar^{0.57}} \tag{14.2}$$

$$u_t = \frac{\mu_f}{\rho_f d_p} \left[\left(-3.809 + \left(3.809^2 + 1.832 Ar^{0.5}\right)^{0.5} \right] \right)^2 \tag{14.3}$$

The original PBM formulation leads to the following stability criterion to predict incipient bubbling voidage:

$$\frac{1.79}{n} \left(\frac{g d_p}{u_t^2} \right)^{0.5} \left(\frac{\epsilon_{mb}^{1-n}}{\left(1 - \epsilon_{mb}\right)^{0.5}} \right) = 1 \tag{14.4}$$

The stability criterion of the BZM is obtained by the substitution of δ with d_p as averaging length in the PDA formulation of the dynamic wave velocity. This leads to a quite similar dependency on voidage with respect to the original PBM stability criterion:

$$\frac{1}{n} \left(\frac{g d_p}{u_t^2} \right)^{0.5} \left(\frac{\epsilon_{mb}^{0.5-n}}{\left(1 - \epsilon_{mb}\right)^{0.5}} \right) = 1 \tag{14.5}$$

The influence of several physical parameters such as gas phase pressure (influencing mainly gas density and viscosity), temperature, particle diameter and density, strength of gravitational field will be compared with literature data. Table 14.1 summarizes the parameters and their relevant ranges here analyzed.

Parameter	Range
Temperature, $[°C]$	$25 \div 900$
Pressure, $[bar]$	$1 \div 140$
g_s/g , $[-]$	$1 \div 3$
Particle density, $[kg/m^3]$	$500 \div 2500$
Particle diameter, $[\mu m]$	$20 \div 140$

Table 14.1: Parameters tested in linear model validation.

The prediction of both PDA and TDA criteria have been validated with literature data. Moreover the predictions by the original Particle Bed Model and the model proposed by Brandani and Zhang (2006) will be also reported for the sake of a complete critical analysis. MBV predictions by means of PDA using different equations for the drag force (Eqns.13.19 and 13.20) will be reported only in a later section. Relevant stability criteria analytical expressions are not reported here.

14.1 Temperature effect

The effect of temperature is reported in Fig.14.1. In particular, in Fig.14.1(a) experimental results obtained by Rowe (1986) are shown in terms of Minimum Bubbling Voidage (MBV) of fine FCC catalyst at temperatures between $25°C$ and $500°C$. Experimental data show an increase of MBV mainly due to the increased viscosity of the gas phase. Prediction of TDA and PDA are both correct in estimating data trends, although an overestimate is evident. BZM also shows an overestimate which furthermore increases with temperature. Average overestimate by TDA and BZM is about 16%, while PDA shows an average discrepancy of 13%. For this data set, the PBM predictions are the best.

In Figs.14.1(b)-14.1(c) the experimental results by Rapagná et al. (1994) are shown for the case of a FCC catalyst at temperatures between $25°C$ and $900°C$. The predictions are correct for all models with PBM showing an optimal match for temperatures up to $200°C$. TDA and PDA slightly overestimate MBV values (5%), while PBM predictions show a slight underestimation of MBV.

Other literature data on the effect of operating temperature have been considered (Lettieri et al., 2001; Girimonte and Formisani, 2009); they will be reported in a later

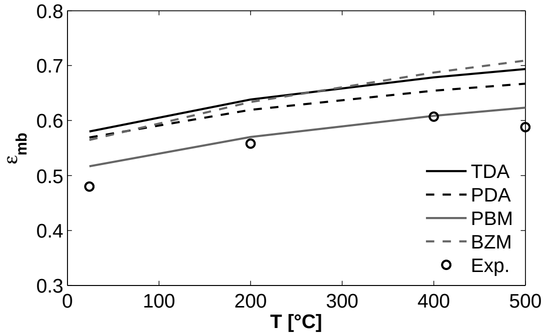

(a) MBV of FCC catalyst ($75\mu m$) fluidized by air.

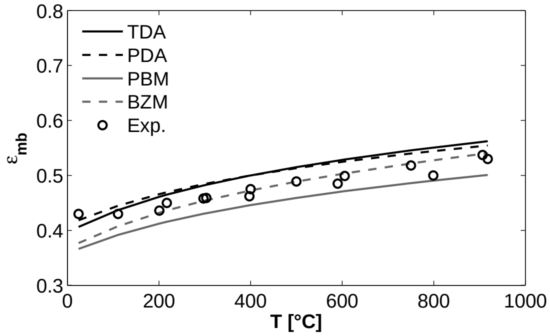

(b) MBV of FCC catalyst ($103\mu m$) fluidized by nitrogen.

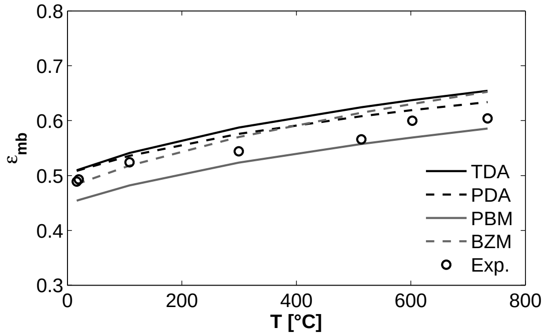

(c) MBV of FCC catalyst ($65\mu m$) fluidized by nitrogen.

Figure 14.1: Temperature Effect on MBV (Rowe, 1986; Rapagná et al., 1994).

section on overall model predictivity.

14.2 Pressure Effect

The pressure effect on MBV is shown in Fig.14.2. Pressure mainly influences the gas density value, resulting in an increase of MBV with pressure. Pressure and temperature are taken in ranges for which gas viscosity variations are negligible or second order effects. In Fig.14.2(a) and Fig.14.2(b) experimental data by Jacob and Weimer (1987) are shown (particles with $d_p = 44\,\mu m$ in the former, $d_p = 112\,\mu m$ in the latter, fluidized with syngas $H_2/CO_{vol} = 0.8$, $P = 20 \div 120\,bar$). In Fig.14.2(a) it is possible to observe that the prediction of MBV by TDA are in very good agreement with experimental data, while PDA shows an average overestimate (less than 10%) of MBV values. BZM failed to predict the transition between particulate to bubbling fluidization, because of the sensitivity of the stability function at high voidage bubbling systems. The PBM appears to be less sensitive to the numerical stability of the criterion with respect to BZM stability function, but for high MBV values this model also appears to uncorrectly predict the fluidization regime transition.

Fig.14.2(b) shows that the predictions of MBV values by PDA and TDA slightly underestimate (less than 7% for PDA, less than 4% for TDA) MBV values. BZM underestimates MBV at low pressures and overestimates MBV at high pressures, PBM systematically underestimates MBV of about 15%.

In Fig.14.2(c) the experimental results by Crowther and Whitehead (1978) are shown (carbon powder, $63\mu m$ fluidized with CF_4) with pressures ranging from 30 to $70\,bar$. The systems reported exhibit high MBV at lower pressures and absence of bubbling at higher pressures. It can be clearly observed that the TDA better predicts the behaviour of the powder at all pressures. The PDA shows similar predictions but with higher overestimates at lower pressures, while both the PBM and the BZM fail to predict the transition from homogeneous to bubbling fluidization.

Other literature data on the effect of operating pressure have been tested (Vogt et al., 2005) but they will be reported in a later section on overall model predictivity.

14.3 Gravitational field strength effect

In Fig.14.3-14.4 the data by Rietema and Mutsers (1978) on the effect of gravitational field strength are analyzed . The Authors adopted different granular materials (FCC

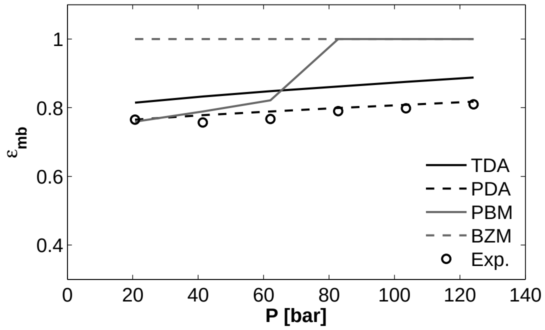

(a) MBV of carbon powder ($44\,\mu m$) fluidized by syngas.

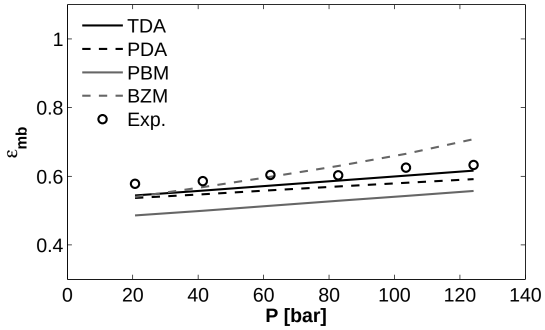

(b) MBV of carbon powder ($112\,\mu m$) fluidized by syngas.

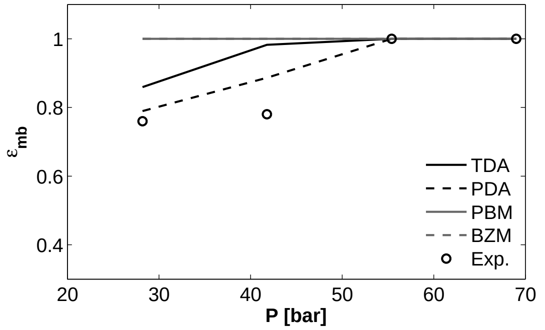

(c) MBV of carbon powder ($63\,\mu m$) fluidized by CF_4.

Figure 14.2: Pressure Effect on MBV (Jacob and Weimer, 1987; Crowther and Whitehead, 1978).

catalyst and polypropylene particles, PP) with different gases (H_2, N_2) in a centrifuge in which the gravitational field strength was varied from the normal value to three times the normal value. The experimental results show a decreasing trend in MBV, mainly due to an increased weight of particles, somewhat similar to an increase in particle density.

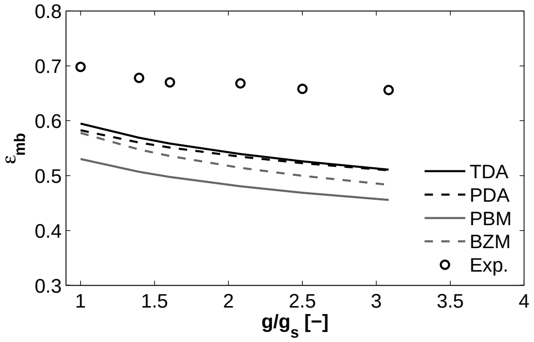

(a) Incremented gravity (Hydrogen).

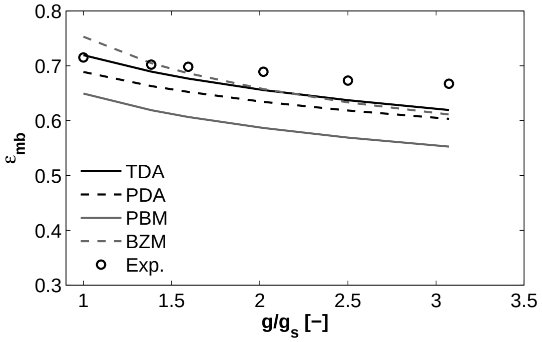

(b) Incremented gravity (Nitrogen).

Figure 14.3: Gravitational field strength effect on MBV of polypropylene particles (Rietema and Mutsers, 1978).

Figure 14.3(a), in which PP/H_2 data are reported, shows an underestimation (between 18% and 27%) of MBV values for all models, with TDA showing the minimum underestimation and the PBM the maximum underestimation. Predictions for the system PP/N_2, reported in Fig.14.3(b), show that both PDA and TDA correctly predict MBV values with slight underestimates (less than 4% for TDA, less than 7% for

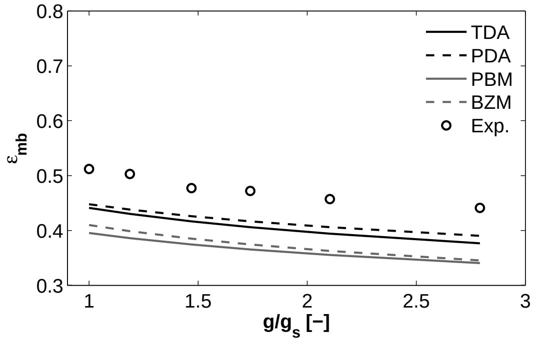

(a) Incremented gravity (Hydrogen).

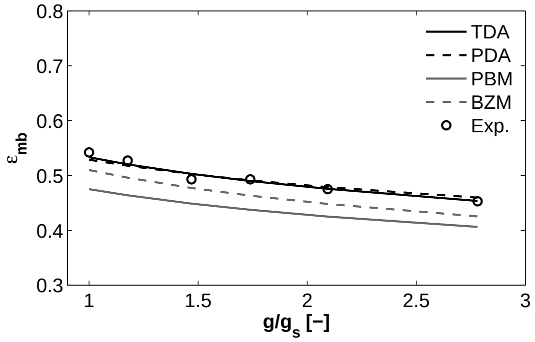

(b) Incremented gravity (Nitrogen).

Figure 14.4: Gravitational field strength effect on MBV of FCC catalyst particles (Rietema and Mutsers, 1978).

PDA), while BZM behaves differently, especially near standard gravity. Conversely PBM predictions results in the largest underestimations of the MBV. In Fig.14.4(a) the system FCC/H_2 is shown, for which all models give correct predictions, with slight underestimates in MBV values, larger for PBM and BZM (about 20%), and smaller for TDA and PDA (14%). In Fig.14.4(b) data for FCC/N_2 system are shown, for which prediction of MBV by PDA and TDA are substantially overlapped and in excellent agreement with experimental data, while PBM and BZM predictions suffer from a systematic underestimation (less than 5% and 10% respectively). It is important to point out the evidence of a systematic disagreement exhibited by all models for the cases of experiments conducted with hydrogen.

14.4 Particle density effect

Figure 14.5 shows the effect of particle density on the MBV value. Data are extrapolated from several literature works and reviewed by Gibilaro et al. (1988). They refer to cases of fluidization of various particles having the same diameter with ambient air. As expected, MBV value decreases with particle density. The PBM prediction shows the best matching for all the systems analyzed. Conversely, BZM shows acceptable agreement only at lower MBV values. This is probably due to the sensitivity of the stability criterion. TDA and PDA show an overestimate over the entire density range (less than 11% for PDA), but a qualitatively correct trend prediction is found.

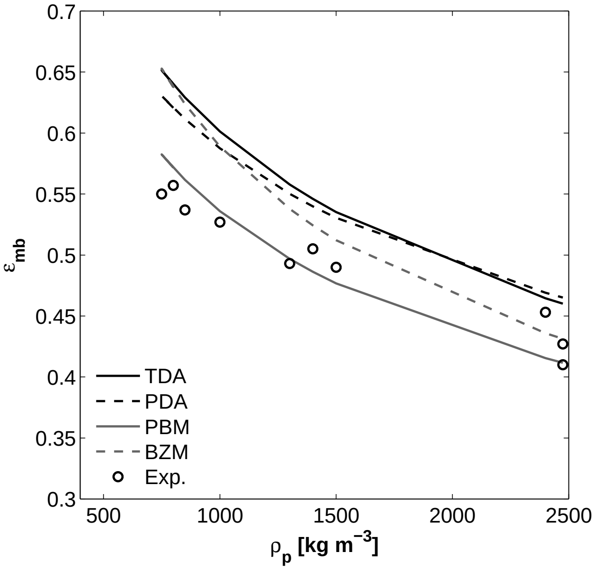

Figure 14.5: Experimental data reviewed by Gibilaro (2001) about particle density effect on MBV of different powders ($60\,\mu m$) fluidized by ambient air and model predictions.

14.5 Particle diameter effect

Figure 14.6 reports experimental data to assess the particle diameter effect (Crowther and Whitehead, 1978; De Jong and Nomden, 1974; Xie and Geldart, 1995). In particular, Fig.14.6(a) shows a system exhibiting always particulate fluidization at lower diameters and transition to bubbling fluidization at higher diameters. PBM and BZM are not able to predict such transition, while TDA and PDA show the correct trend, with fairest agreement for TDA (error less than 10%). Also for the case of the experimental data reported in Figs.14.6(b) and 14.6(c) similar considerations apply. PBM gives a good agreement only for systems with low MBV value. The BZM predictions also follow a correct trend at low MBV values. Both PBM and BZM show in fact significant levels of overestimation for systems with high MBV due to the numerical sensitivity of the linear stability criterion. Coversely, TDA predictions provide better agreement with minimum underestimate for large diameters (less than 6%) and slightly higher overestimates for small diameters.

An effort has been made to discuss the effect of particle forces. When interparticle bounding forces are higher than particle weights, a cohesive behavior of powders will result, or a homogeneous expansion of particle aggregates (Valverde et al., 2003a). For this last case, predictions of MBV result always in homogeneous fluidization. However, when the average size and density of aggregates (Valverde et al., 2003a) is taken into account, excellent agreement with experimental data is obtained, as it can be seen in Fig.14.7. Notably TDA predictions give the best agreement with experiments, while PDA predictions slightly underestimate the MBV. PBM predicts the transition to bubbling only for the largest particles, while BZM predicts always homogeneous fluidization for the smallest particle sizes, and a sudden decrease of MBV at larger particle diameters. Such results underline the crucial importance of the modeling of interparticle forces for small (or light) particles (*i.e.* for the prediction of aggregates properties), and highlights that the behavior of the resulting aggregates is fully described by the governing equations of fluid motion.

14.6 Overall predictivity

On overall, the predictions obtained by the stability criteria derived from the presented model in its mono-dimensional formulation show good agreement of predictions with relevant experimental data. As it can be seen in Fig.14.8, TDA and PDA give rise to the lowest data dispersion, especially at higher MBV values (where PBM and BZM are not able to predict the transition from homogeneous to bubbling fluidization). In particular, PDA shows the minimum data dispersion between all models.

Each model presents its own distribution of prediction residuals (*i.e.* difference between model predictions and experimental data). In particular, the mean value of percentage residual and relevant standard deviation (STD) are used to characterize the

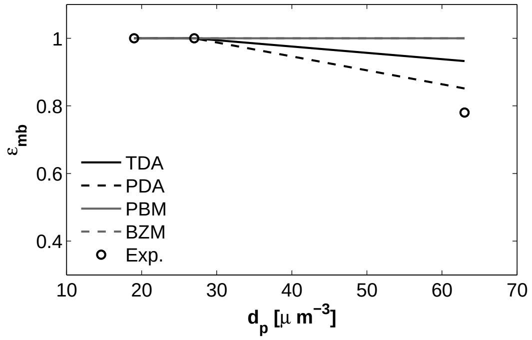

(a) MBV of carbon powder fluidized by Argon at 67 bar.

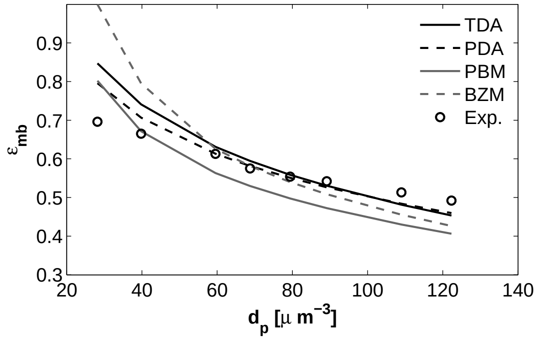

(b) MBV of alumina fluidized by air.

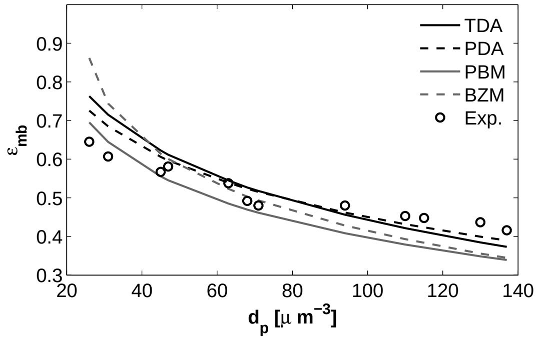

(c) MBV of FCC catalyst fluidized by air.

Figure 14.6: Particle diameter effect on MBV (Crowther and Whitehead, 1978; De Jong and Nomden, 1974; Xie and Geldart, 1995).

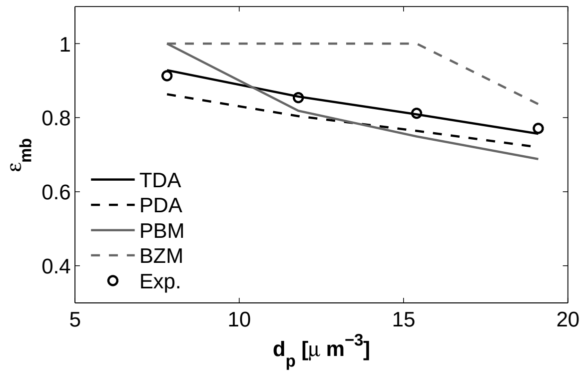

Figure 14.7: Experimental data by Valverde et al. (2003a) about particle diameter effect effect on MBV of different additivated toners fluidized by nitrogen and model predictions by using aggregates average size and density measured by the same Authors.

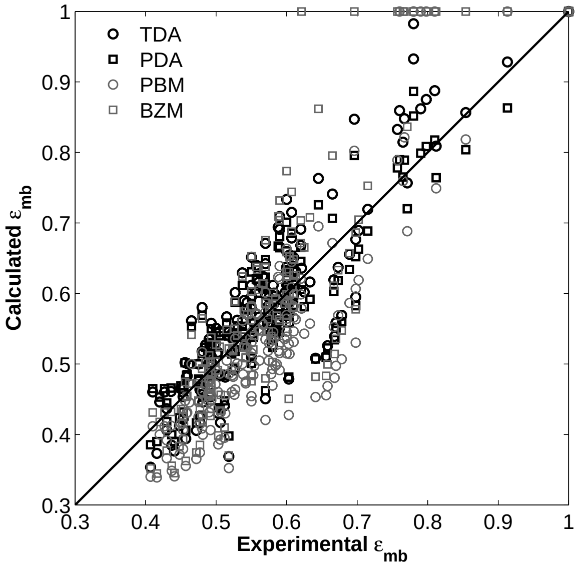

Figure 14.8: Comparison between MBV experimental values and model predictions.

residual distribution, as reported in Table 14.2. It is worth noting that mean residuals are in the range of $\pm 2\%$ with the exception of BZM, and relevant standard deviation lie in the range $\pm 15\%$. TDA and PDA show the smaller values of both mean value and standard deviations, with best results obtained by PDA.

Approach	**% Mean**	**% STD**
PDA	0.07	8.48
TDA	1.63	9.93
PBM	1.30	14.08
BZM	-6.91	11.17

Table 14.2: Model prediction evaluation.

For the sake of comparison, as an alternative to the Richardson-Zaki equation for the drag force, overall predictions obtained by means of Eqns.13.19 and 13.20 are shown in Fig.14.9. Unexpectedly, the such predictions lead to worse agreements, especially for systems exhibiting high MBV. This is due to the fact that the elastic force depends on the derivative of the drag force with respect to voidage, rather than the drag force value itself.

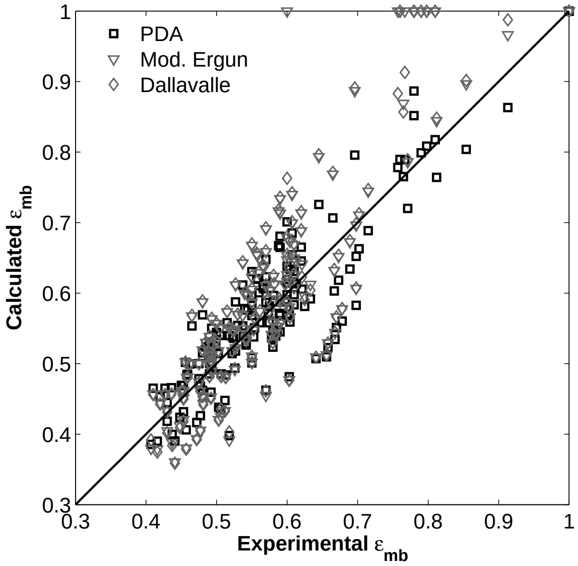

Figure 14.9: Comparison between MBV experimental values and PDA predictions when using different drag force expressions.

It is worth noting that with reference to the literature data here analyzed, both TDA and PDA correctly describe the behavior of particulate systems with MBV equal to one (*i.e.* those systems not showing a transition from homogeneous to bubbling fluidization). Conversely, PBM and BZM results in predicting values of MBV equal to one in 7 and 14 systems here examined respectively, for systems having MBV less than unity.

Using the stability criteria derived from TDA and PDA, a predicted Geldart chart for fluidization with ambient air can be obtained, as shown in Fig.14.10. The separation line between group-A and group-B powders is obtained by finding the density-diameter couples with MBV value equal to 0.40 (*i.e.* for which MBV is equal to the maximum packing voidage value), while the separation line between group-B and group-D powders is obtained by finding the density-diameter couples for which MBV value is equal 0.1, on the base of fluidization quality considerations (Gibilaro, 2001). It is evident from Fig.14.10 the sound agreement between model predictions and the well-known Geldart chart.

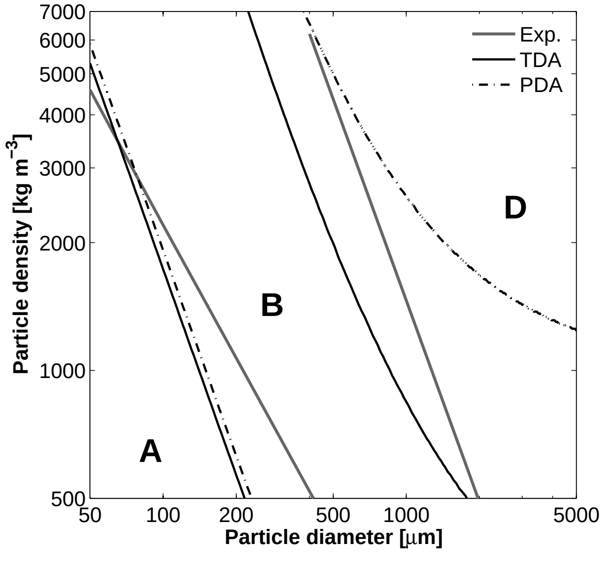

Figure 14.10: Experimental Geldart chart and predicted chart by TDA and PDA.

14.7 Comparison of alternative stability functions

All functional dependencies of the stability function for TDA, PDA, PBM and BZM were analyzed. In general the stability function for each model takes the form reported in Eqn.13.32. Each model, in particular, is characterized by its own definition of the dynamic wave velocity, leading to different functional dependencies of the stability function. In the case of PBM and BZM, a characteristic asymmetrical U-shaped stability function is obtained, as it can be easily observed in Fig.14.11, where all the stability function for a particular test case have been reported as a function of voidage ϵ. These curves exhibit a descending section at low voidage, a plateau section and a suddenly increasing asymptote at voidage values approaching to one. This is a marked difference with respect to the monotone decreasing dependence of the stability function for both TDA and PDA. Different systems show different values of the stability function, but the shape remains substantially the same.

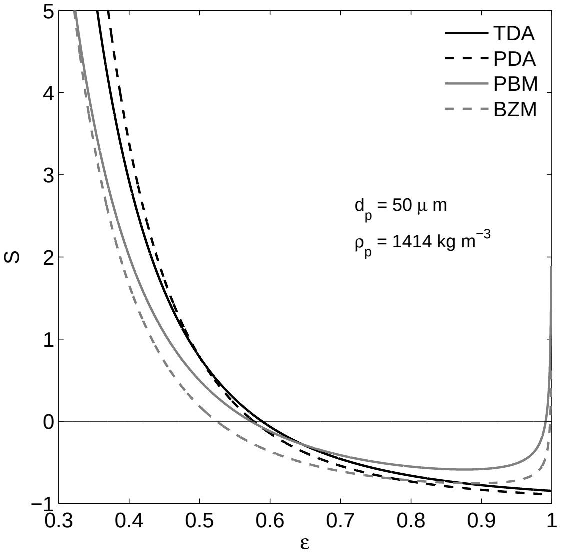

Figure 14.11: Typical stability function plot for Geldart-A powder.

The lower value of the two roots of the stability function is the ϵ value corresponding to incipient bubbling conditions. Gibilaro (2001) found that the higher value of the two roots corresponds to the bubble phase voidage value. On this ground, the newly formulated models are not able to predict this second root, because of the monotonic behavior of the relevant stability functions.

Nevertheless, the U-shaped stability functions of PBM and BZM lead to the impossibility of predicting MBV values lying on the right hand side of the minimum value of the stability function itself. This in practice cancels out the possibility of predicting MBV values higher than 0.80 for PBM and 0.85 for the BZM.

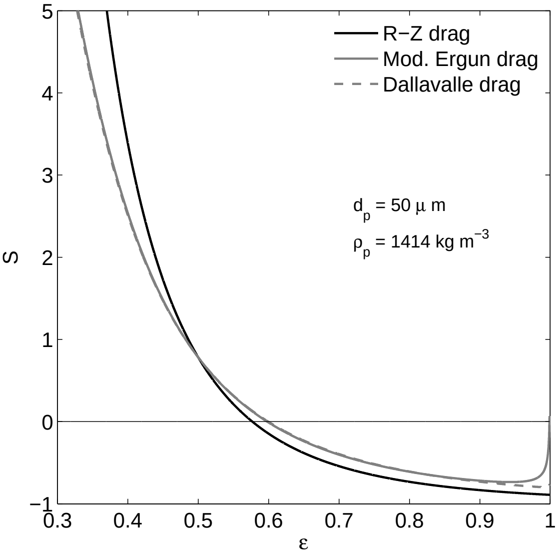

Figure 14.12: Influence of drag force correlation on TDA stability function plot for Geldart-A powder.

It is worth noting that different expressions of near-equilibrium drag force results in different dependencies on voidage, as reported in Fig.14.12. In particular, U-shaped curves result for Dallavalle and Modified Ergun drag formulation. This occurrence leads to the existence of two roots, whose physical meaning was discussed above, but negatively affects the model predictivity at high MBV values, as seen in Fig.14.9. It should be therefore emphasized the importance of selecting the Richardson-Zaki drag expression (Gibilaro, 2001), which best describes the voidage dependence of drag force for homogeneously fluidized beds.

On overall, TDA and PDA stability functions show an increased robustness for prediction of MBV with respect to PBM and BZM, thanks to the monotonic dependence on voidage of the stability function. This feature makes possible to predict MBV values over the entire range. The information from the second root of the PBM stability function can not be obtained by TDA and PDA, however both approaches have the noticeable advantage of an accurate and robust fully predictivity.

15 Concluding remarks

The developed linear stability criteria have been derived starting from the formulation of the Particle Bed Model with the aim to purposely introduce an averaging length on the basis of a theoretical analysis at incipient bubbling fluidization.

In particular, the stability criteria were obtained by introducing an alternative elastic term and a new voidage dependency on the local elastic properties in both the fluid and particle phase momentum equations. The balance equations thus obtained were suitably coupled and linearized to derive the stability criteria. Validation of the proposed model was carried out by means of a simple mono-dimensional linear stability analysis. From such analysis two different criteria to predict the onset of bubbling resulted. Predictions so far obtained on the base of the proposed stability criteria were finally compared with literature data available. On overall the agreement was found good particularly for the case of systems characterized by high values of minimum bubbling voidage, where the previously developed models were not able to make reliable predictions. This is mainly due to the characteristic monotonic dependence on voidage of the newly developed stability functions, which are markedly different from those of previous models.

Notably, the proposed model is only at a first stage of its validation. The linear stability analysis allowed for the validation only in terms of correct perturbation propagation, while future works should be aimed at the implementation in Computational Fluid Dynamic codes, in order to validate the ability of the model in predicting other fundamental fluid bed characteristics, such as those already presented in previous chapters.

Bibliography

J.C. Abanades and G.S. Grasa. Modeling the axial and lateral mixing of solids in fluidized beds. *Ind. Eng. Chem. Res.*, 40:5656–5665, 2001.

A.R. Abrahamsen and D. Geldart. Behaviour of gas-fluidised beds of fine powders part ii: Voidage of the dense phase in bubbling beds. *Powder Technol.*, 26:55, 1980.

P.K. Agarwal. Bubble charateristics in gas fluidized beds. *Chem. Eng. Res. Des.*, 63: 323–337, 1985.

S.S. Alves, C.I. Maia, and J.M.T. Vasconcelos. Experimental and modelling study of gas dispersion in a double turbine stirred tank. *Chem. Eng. Sci.*, 57:487–496, 2002a.

S.S. Alves, C.I. Maia, J.M.T. Vasconcelos, and A.J. Serralheiro. Bubble size in aerated stirred tanks. *Chem. Eng. J.*, 3990:1–9, 2002b.

T.B. Anderson and R. Jackson. A fluid mechanical description of fluidized beds. equation of motion. *Ind. Eng. Chem. Fundamentals*, 6:527–539, 1967.

D.T. Argyriou, H.L. List, and R. Shinnar. Bubble growth by coalescence in gas fluidized beds. *AIChE J.*, 17:122–130, 1971.

M.M. Aslan, C. Crofcheck, D. Tao, and M.P. Menguc. Evaluation of micro bubble size and gas-hold-up in two-phase gas-liquid columns via scattered light measurements. *J. Quant. Spectrosc. Radiat. Transfer*, 101:527–539, 2006.

M. Barigou and M. Greaves. Bubble size in the impeller region of a rushton turbine. *Chem. Eng. Res. Des.*, 70:153–160, 1992a.

M. Barigou and M. Greaves. Bubbles size distributions in a mechanically agitated gas-liquid contactor. *Chem. Eng. Sci.*, 47(8):2009–2025, 1992b.

M. Barigou and M. Greaves. Gas holdup and interfacial area distributions in a mechanically agitated gas-liquid contactor. *Chem. Eng. Res. Des.*, 74:397–405, 1996.

G.K. Batchelor. *An introduction to fluid dynamics*. Cambridge University Press, Cambridge, UK, 1973.

R.B. Bird, W.E. Stewart, and E.N. Lightfoot. *Transport Phenomena, 2nd ed.* Wiley, New York, 2002.

S. Boden, M. Bieberle, and U. Hampel. Quantitative measurement of gas hold-up distribution in a stirred chemical reactor using x-ray cone-beam computed tomography. *Chem. Eng. J.*, pages 351–362, 2008.

A. Boemer, H. Qi, and U. Renz. Verification of eulerian simulation of spontaneous bubble formation in a fluidized bed. *Chem. Eng. Sci.*, pages 1835–1846, 1998.

G.A. Bokkers, M. van Sint Annaland, and J.A.M. Kuipers. Mixing and segregation in a bidisperse gas-solid fluidized bed: a numerical and experimental study. *Powder Technol.*, 140:176–186, 2004.

A. Bombac and I. Zun. Gas filled cavity structures and local void fraction distribution in vessel with dual impeller. *Chem. Eng. Sci.*, 55:2995–3001, 2000.

A. Bombac, I. Zun, B. Filipic, and M. Zumer. Gas filled cavity structures and local void fraction distribution in aerated stirred vessels. *AIChE J.*, 43(11):2921–2931, 1997.

M. Bouaifi and M. Roustan. Bubble size and mass transfer coefficients in dual impeller agitated reactors. *Can. J. Chem. Eng.*, 76(3):390–397, 1998.

M. Bouaifi, G. Hebrard, D. Bastoul, and M. Roustan. A comparative study of gas hold-up, bubble size, interfacial area and mass transfer coefficients in stirred gas-liquid reactors and bubble columns. *Chem. Eng. Proc.*, 40:97–111, 2001.

C. Boyer, A.M. Duquenne, and G. Wild. Measuring techniques in gas-liquid and gas-liquid-solid reactors. *Chem. Eng. Sci.*, 57:3185–3215, 2002.

S. Brandani and K. Zhang. A new model for the prediction of the behaviour of fluidized beds. *Powder Technol.*, 163:80–87, 2006.

D. Broder, S. Lain, and M. Sommerfeld. Experimental studies of the hydrodynamics in a bubble column. In *Fifth German-Japanese symposium bubble columns*, number

ISBN: 3-86012-109-X 2000, pages 125–130, Medienzentrum der Bergakademie Freiberg, 2000.

A. Brucato and L. Rizzuti. Simplified modelling of radiant fields in heterogeneous photoreactors. 1. case of zero reflectance. *Ind. Eng. Chem. Res.*, 36:4740–4747, 1997a.

A. Brucato and L. Rizzuti. Simplified modelling of radiant fields in heterogeneous photoreactors. 2. limiting two-flux model for the case of reflectance greater than zero. *Ind. Eng. Chem. Res.*, 36:4748–4755, 1997b.

G.L.L. Buffon. Essai d'arithmetique morale. *Histoire Natureel*, 4A:685, 1777.

A. Busciglio, G. Vella, G. Micale, and L. Rizzuti. Analysis of the bubbling behaviour of 2d gas solid fluidized beds. part i. digital image analysis technique. *Chem. Eng. J.*, 140:398–413, 2008.

A. Busciglio, G. Vella, G. Micale, and L. Rizzuti. Experimental analysis of bubble size distributions in 2D gas fluidized beds. *Chem. Eng. Sci.*, 65(16):4782–4791, 2010.

G.R. Caicedo, J.J.P. Marquès, M.G. Ruìz, and J.G. Soler. A study on the behaviour of a 2D gas-solid fluidized bed using digital image analysis. *Chem. Eng. Process.*, 42: 9–14, 2003.

P.H. Calderbank. Physical rate processes in industrial fermentation. part 1. the interfacial area in gas-liquid contacting with mechanical agitation. *Trans. Inst. Chem. Engrs.*, 36:443–463, 1958.

J. Chaouki, F. Larachi, and M.P. Dudukovic. Noninvasive tomographic and velocimetric monitoring of multiphase flows. *Industrial and Engineering Chemistry Research*, 36:4476–4503, 1997.

S. Chapman and T.G. Cowling. *The mathematical theory of non uniform gases, ed.3rd.* Cambridge University Press, Cambridge, UK, 1970.

J. Chen, A. Kemoun, M.H. Al-Dahhan, M.P. Dudukovic, D.J. Lee, and L.S. Fan. Comparative hydrodynamics study in a bubble column using computer-automated radioactive particle tracking (carpt)/computed tomography (ct) and particle image velocimetry (piv). *Chem. Eng. Sci.*, pages 2199–2207, 1999a.

Z. Chen, L.G. Gibilaro, and P.U. Foscolo. Two-dimensional voidage waves in fluidized beds. *Ind. Eng. Chem. Res.*, 38:610–620, 1999b.

W. Cheng, Y. Murai, T. Sasaki, and F. Yamamoto. Bubble velocity measurements with a recursive cross correlation PIV technique. *Flow Meas. and Instrum.*, 16:35–46, 2005.

N. P. Cheremisinoff. Review of experimental methods for studying the hydrodynamics of gas-solid fluidized beds. *Ind. Eng. Chem. Process Des. Dev.*, 25:329–351, 1986.

K.H.K. Chung, M.J.H. Simmons, and M. Barigou. Local gas and liquid phase velocity measurement in a miniature stirred vessel using piv combined with a new image processing algorithm. *Exp. Therm. Fluid Science*, 33:743–753, 2009.

N.N. Clark and R. Turton. Chord length distribution related to bubble size distributions in multiphase flow. *Int. J. Multiphase Flow*, 14(4):413–424, 1988.

N.N. Clark, W. Liu, and R. Turton. Data interpretation techniques for inferring bubble size distribution from probe signals in fluidized systems. *Powder Technol.*, 88:179–188, 1996.

C. Crowe, M. Sommerfeld, and Y. Tsujii. *Multiphase flow with droplets and particles.* CRC Press, 1998.

M.E. Crowther and J.C. Whitehead. *Fluidisation.* Cambridge University Press, Cambridge, UK, 1978.

P.A. Cundall and O.D. Strack. A discrete numerical method for granular assemblies. *Geotechnique*, 29:47–65, 1979.

R.C. Darton, R.D. LaNauze, J.F. Davidson, and D. Harrison. Bubble growth due to coalescence in fluidized beds. *Trans. Instn. Chem. Engrs.*, 55:274–280, 1977.

J.F. Davidson and D. Harrison, editors. *Fluidised Particles*. Cambridge University Press, 1963.

J.F. Davidson and D. Harrison, editors. *Fluidization*. Accademic Press, New York USA, 1971.

J.F. Davidson, R. Clift, and D. Harrison, editors. *Fluidization (2nd Edn.)*. Academic Press, New York USA, 1985.

J.A.H. De Jong and J.F. Nomden. Homogeneous gas-solid fluidization. *Powder Technol.*, 9:91, 1974.

M.A. Delesse. Procédé méchanique pour déterminer la composition des roches. *C. R. Acad. Sci. Paris*, 25:544–545, 1847.

E. Delnoij, J. Westerweel, N.G. Deen, J.A.M. Kuipers, and W.P.M. van Swaaij. Ensemble correlation PIV applied to bubble plumes rising in a bubble column. *Chem. Eng. Sci.*, 54:5159–5171, 1999.

R. Di Felice. The voidage function for fluid particle interaction systems. *Int. Journ. of Multiphase Flow*, 20:153–159, 1994.

J. Ding and D. Gidaspow. A bubbling fluidization model using kinetic theory of granular flow. *AIChE J.*, 36:523–538, 1990.

D.A. Drew. Mathematical modelling of two phase flow. *Annu. Rev. Fluid Mech.*, 83: 261–291, 1983.

H. Enwald, E. Peirano, and A.E. Almstedt. Eulerian two phase flow theory applied to fluidization. *Int. Journal of Multiphase Flow*, 22, Supplement 1:21–66, 1996.

S. Ergun. Fluid flow through packed columns. *Chem. Eng. Progress*, 48(2):89, 1952.

H. Essadki, I. Nikov, and H. Delmas. Electrochemical probe for bubble size prediction in a bubble column. *Experimental Thermal and Fluid Science*, 14:243–250, 1997.

Z. Fan, G.T. Chen, B.C. Chen, and H. Yuan. Analysis of pressure fluctuations in 2D fluidized bed. *Powder Technol.*, 62(2):139–145, 1990.

J.J. Ford, T.J. Heindel, T.C. Jensen, and J.B. Drake. X-ray computed tomography of a gas-sparged stirred-tank reactor. *Chem. Eng. Sci.*, pages 2075–2085, 2008.

P.U. Foscolo and L.G. Gibilaro. A fully predictive criterion for the transition between particulate and aggregate fluidization. *Chem. Eng. Sci.*, 39:1667, 1984.

P.U. Foscolo and L.G. Gibilaro. Fluid dynamic stability of fluidized suspensions: the particle bed model. *Chem. Eng. Sci.*, 42:1489, 1987.

P.U. Foscolo, L.G. Gibilaro, and S.P. Waldram. A unified model for particulate expansion of fluidised beds and flow in fixed porous media. *Chem. Eng. Sci.*, 38:1251, 1983.

P.U. Foscolo, L.G. Gibilaro, and S. Rapagná. Infinitesimal and finite voidage perturbations in the compressible particle phase description of a fluidized bed. In *Developments in fluidization and fluid particle systems (J.C. Chem. Ed.)*, volume 91(308) of *AIChE Symposium Series*, page 44, 1995.

D. Funfschilling and H-Z. Li. Flow of non-newtonian fluids around bubbles: PIV measurements and birefringence visualisation. *Chem. Eng. Sci.*, 56:1137–1141, 2001.

Z. Gao, J.M. Smith, and H. Muller-Steinhagen. Void fraction distribution in sparged and boiling reactors with modern impeller configuration. *Chem. Eng. Process.*, 40: 489–497, 2001.

J. Garside and M.R. Al-Bidouni. Velocity voidage relationship for fluidization and sedimentation. *I&EC Proc. Des. Dev.*, 16:206–214, 1977.

D. Geldart. The expansion of bubbling fluidized beds. *Powder Technol.*, 1:355–368, 1967.

D. Geldart. The effect of particle size distribution on the behaviour of gas-fluidised beds. *Powder Technol.*, 6:201–215, 1972.

D. Geldart. Types of gas fluidization. *Powder Technol.*, 7:285–292, 1973.

D Geldart. *Predicting the expansion of gas fluidized beds. In: Fluidization Technology*, pages 237–244. Hemisphere, Washington DC., 1975.

D. Geldart. *Gas fluidization technology*. John Wiley, Chichester, 1986.

S.J. Gelderbloom, D. Gidaspow, and R.W. Lyczkowski. CFD simulations of bubbling/collapsing fluidized beds for three geldart groups. *AIChE J.*, 49:844–858, 2003.

D. Gera and M. Gautam. Bubble rise velocity in two-dimensional fluidized beds. *Powder Technol.*, 84:283–285, 1995.

D. Gera, M. Gautam, Y. Tsuji, T. Kawaguchi, and T. Tanaka. Computer simulation of bubbles in large-particle fluidized beds. *Powder Technol.*, 98:38–47, 1998.

L.G. Gibilaro. *Fluidization Dynamics.* Butterworth-Einemann, Oxford, UK, 2001.

L.G. Gibilaro, R. Di Felice, S.P. Waldram, and P.U. Foscolo. Generalized friction factor and drag coefficient correlations for fluid particle interaction. *Chem. Eng. Sci.*, 40:1817, 1985.

L.G. Gibilaro, R. Di Felice, and P.U. Foscolo. On the minimum bubbling voidage and the geldart classification for fluidised beds. *Powder Tech.*, 56:21–29, 1988.

L.G. Gibilaro, R. Di Felice, and P.U. Foscolo. Added mass effect in fluidized beds: application of the geurst wallis analysis of inertial coupling in two phase flow. *Chem. Eng. Sci.*, 45:259–256, 1998.

D. Gidaspow. *Multiphase flow and fluidization.* Academic Press, San Diego, 1994.

R. Girimonte and B. Formisani. The minimum bubbling velocity of fluidized beds operating at high temperature. *Powder Technol.*, 189:74–81, 2009.

M.J.V. Goldschmidt, J.A.M. Kuipers, and W.P.M. Van Swaaij. Hydrodynamic modelling of dense gas-fluidised beds using kinetic theory of granular flow: effect of coefficient of restitution on bed dynamics. *Chem. Eng. Sci.*, 56:571–578, 2001.

M.J.V. Goldschmidt, J.M. Link, S. Mellema, and J.A.M. Kuipers. Digital image analysis measurements of bed expansion and segregation dynamics in dense gas-fluidized beds. *Powder Technol.*, 138:135–159, 2003.

M. Greaves and K.A.H. Kobbacy. Measurement of bubble size distribution in turbulent gas-liquid dispersions. *Chem. Eng. Res. Des.*, 62:3–12, 1984.

F. Gruy and S. Jacquier. Thechord length distribution of a two sphere aggregate. *Comput. Mater. Sci.*, 44:218–233, 2008.

D.J. Gunn and H.H. Al-Doori. The measurement of bubble flows in fluidized beds by electrical probe. *Int. J. Multiphase Flow*, 11:535–551, 1985.

J.M. Hammersley and D.C. Handscomb, editors. *Monte Carlo Methods*. Chapman and Hall Ltd., London, 1983.

U. Hampel, H.V. Hristov, A. Bieberle, and C. Zippe. Application of high resolution gamma ray tomography to the measurement of gas hold-up in a stirred chemical reactor. *Flow Meas. Instrum.*, 18:184–190, 2007.

N. Harnby, M.F. Edwards, and A.W. Nienow. *Mixing in the process industries, second edition*. Butterworth-Heinemann, Oxford, 1992.

I.T.M. Hassan and C.W. Robinson. Mass-transfer-effective bubble coalescence frequency and specific interfacial area in a mechanically agitated gas-liquid contactor. *Chem. Eng. Sci*, 35:1277–1289, 1980.

G. Hebrard, M. Bouaifi, D. Bastoul, and M. Roustan. A comparative study of gas hold-up, bubble size, interfacial area and mass transfer coefficients in stirred gas-liquid reactors and bubble column. *Chem. Eng. Process.*, 40(2):97–111, 2001.

J.R. Hernandez-Aguilar, R.G. Coleman, C.O. Gomez, and J.A. Finch. A comparison between capillary and imaging techniques for sizing bubbles in flotation systems. *Miner. Eng.*, 17:53–61, 2004.

R.A. Herringe and M.R. Davis. Structural development of gas-liquid mixture flows. *J. Fluid Mechs.*, 73(1):97–123, 1976.

E.F. Hobbel, R. Davies, F.W. Rennie, T. Allen, L.E. Butler, E.R. Waters, J.T. Smith, and Sylvester R.W. Modern methods of on-line size analysis for particulate process streams. *Part. Part. Syst. Charact.*, 8:29–34, 1991.

B.P.B. Hoomans, J.A.M. Kuipers, W.J. Briels, and W.P.M. Van Swaaij. Discrete particle simulation of bubble and slug formation in a two dimensional gas fluidized bed: a hard sphere approach. *Chem. Eng. Sci.*, 51:99–118, 1996.

M. Horio and A. Nonaka. A generalized bubble diameter correlation for gas-solid fluidized beds. *AIChE J.*, 33:1865–1872, 1987.

D. Horn, G. Montante, F. Magelli, and A. Paglianti. Bubble size distribution and turbulent two-phase flow in aerated stirred vessel. In *Proceedings of the 6th International Conference on Multiphase Flow, ICMF*, Leipzig, Germany, July 9-13, 2007.

C.M. Hrenya and J.L. Sinclair. Effects of particle-phase turbulence in gas-solid flows. *AIChE J.*, 43:853–869, 1997.

B. Hu, A.W. Pacek, E.H. Stitt, and A.W. Nienow. Bubble sizes in agitated air-alcohol systems with and without particles: Turbulent and transitional flow. *Chem. Eng. Sci.*, 60:6371–6377, 2005.

B. Hu, P. Angeli, O.K. Matar, C.J. Lawrence, and G.F. Hewitt. Evaluation of drop size distribution from chord length measurements. *AIChE J.*, 52(3):931, 2006a.

B. Hu, A.W. Nienow, E.H. Stitt, and A.W. Pacek. Bubble sizes in agitated solvent/reactant mixtures used in heterogeneous catalytic hydrogenation of 2-butyne-1,4-diol. *Chem. Eng. Sci.*, 61:6765–6774, 2006b.

A.S. Hull, Z. Chen, J.W. Fritz, and P.K. Agarwal. Influence of horizontal tube tanks on the behaviour of bubbling fluidized beds. 1. bubble hydrodynamics. *Powder Technol.*, 103:230–242, 1999.

I. Hulme and A. Kantzas. Determination of bubble diameter and axial velocity for a polyethylene fluidized bed using x-ray fluoroscopy. *Powder Technol.*, 147:20–33, 2004.

P.J.G. Huttenhuis, J.A.M. Kuipers, and W.P.M. Van Swaaij. The effect of gas-phase density on bubble formation at a single prifice in a two-dimensional gas-fluidized bed. *Chem. Eng. Sci.*, 51(24):5273–5288, 1996.

V. Ilchenko, R. Maurus, and T. Sattelmayer. Processing and analysis of holographic images for the bubbles characterization in an aerated stirred tank. *Proc. Eurotherm*, 71:137–144, 2002.

M. Ishii. *Thermo-fluid dynamic theory of multiphase flow*. Eyrolles, Paris, France., 1975.

R. Jackson. Locally averaged equations of motion for a mixture of identical spherical particles and a newtonian fluid. *Chem. Eng. Sci.*, 52:2457–2469, 1997.

R. Jackson. Erratum. *Chem. Eng. Sci.*, 53:1955, 1998.

R. Jackson. *The dynamic of fluidised particles.* Cambridge University Press, New York, USA., 2001.

K.V. Jacob and A.W. Weimer. High pressure particulate expansion and minimum bubbling of fine carbon powder. *AIChE J.*, 33:567, 1987.

J. T. Jenkins and S. B. Savage. A theory for the rapid flow of identical, smooth, nearly elastic, spherical particles. *J. Fluid Mech.*, 130:187–202, 1983.

F. Johnsson, S. Andersson, and B. Leckner. Expansion of a freely bubbling fluidized bed. *Powder Technol.*, 68(2):117–123, 1991.

J.B. Joshi. Computational flow modelling and design of bubble column reactors. *Chem. Eng. Sci.*, 56:5893–5933, 2001.

N. Kail, W. Marquardt, and H. Briesen. Estimation of particle size distributions from focused beam reflectance measurements based on an optical model. *Chem. Eng. Sci.*, 64:984–1000, 2009.

M. Kamiwano, M. Kaminoyama, K. Nishi, and D. Shirota. The measurement of bubble diameter distributions and liquid side mass transfer coefficients in a gas-liquid agitated vessel using a real time, high speed image processing system. *Chem. Eng. Comm.*, 190:1096–1114, 2003.

Y. Kaneko, T. Shiojima, and M. Horio. A new method for gray-level picture thresholding using the entropy of the histogram. *Chem. Eng. Sci.*, 54:5809–5821, 1999.

J.N. Kapur, P.K. Sahoo, and A.K. Wong. A new method for gray-level picture thresholding using the entropy of the histogram. *Comput. Graphics Image Process.*, 29: 273–285, 1985.

W.T. Kawecki, T. Reith, J.W. van Heuven, and W.J. Beek. Bubble size distribution in the impeller region of a stirred vessel. *Chem. Eng. Sci.*, 22:1519–1523, 1967.

A.R. Khopkar, A.R. Rammohan, V.V. Ranade, and M.P. Dudukovi. Gas-liquid flow generated by a rushton turbine in stirred vessel: Carpt/ct measurements and cfd simulations. *Chem. Eng. Sci.*, 60:2215–2229, 2005.

R. Kobayashi, N.and Yamazaki and S. Mori. A study on the behaviour of bubbles and solids in bubbling fluidized beds. *Powder Technol.*, 113:327–344, 2000.

D. Kunii and O. Levenspiel, editors. *Fluidization Engineering*. Butterworth-Heinemann, 1991.

M. Kwauk and J. Li. Fluidization regimes. *Powder Technol.*, 87:193–202, 1996.

M. Laakkonen, M. Honkanen, P. Saarenrinn, and J. Aittamaa. Local bubble size distributions, gas-liquid interfacial areas and gas holdups in a stirred vessel with particle image velocimetry. *Chem. Eng. J.*, 109:37–47, 2005a.

M. Laakkonen, P. Moilanen, and J. Aittamaa. Local bubble size distributions in agitated vessels. *Chem. Eng. J.*, 106:133–143, 2005b.

M. Laakkonen, P. Moilanen, T. Miettinen, K. Saari, M. Monkanen, P. Saarenrinne, and J. Aittamaa. Local bubble size distribution in agitated stirred vessel - comparison of three experimental techniques. *Chem. Eng. Res. Des.*, 83:50–58, 2005c.

P.A. Langston, A.S. Burbridge, T.F. Jones, and M.J.H. Simmons. Particle and droplet size analysis from chord measurements using bayes' theorem. *Powder Technol.*, 116:33–42, 2001.

J.A. Laverman, I. Roghair, and M. Van Sint Annaland. Investigation into the hydrodynamics of gas-solid fluidized beds using particle image velocimetry coupled with digital image analysis. *Can. J. Chem. Eng.*, 86(3):523–535, 2008.

J.C. Lee and D.L. Meyrick. Gas-liquid interfacial area in salt solutions in an agitated tank. *Trans. I. Chem. E.*, 48:T37, 1970.

P. Lettieri, S. Brandani, J.G. Yates, and D. Newton. A generalization of the foscolo and gibilaro particle-bed model to predict the fluid bed stability of some fresh fcc catalysts at elevated temperatures. *Chem. Eng. Sci.*, 56:5401–5412, 2001.

P. Lettieri, R. Di Felice, P. Pacciani, and P. Owoyemi. CFD modelling of liquid fluidized beds in slugging mode. *Powder Technol.*, 167:94–103, 2006.

J. Li and J.A.M. Kuipers. Gas particle interactions in dense gas fluidised beds. *Chem. Eng. Sci.*, 58:711–718, 2003.

M. Li and D. Wilkinson. Determination of non-spherical particle size distribution from chord length measuremens. part i: theoretical analysis. *Chem. Eng. Sci.*, 60: 3251–3265, 2005.

M. Li, D. Wilkinson, and Patchingolla. Determination of non-spherical particle size distribution from chord length measuremens. part ii: experimental validation. *Chem. Eng. Sci.*, 60:4992–5003, 2005.

C.N. Lim, M.A. Gilbertson, and A.J.L. Harrison. Bubble distribution and behaviour in bubbling fluidized beds. *Chem. Eng. Sci.*, 62:56–69, 2007.

C.N. Lim, M.A. Gilbertson, and A.J.L. Harrison. Characterisation and control of bubbling behaviour in gas-solid fluidised beds. *Control Engineering Practice*, 17: 67–79, 2009.

K.S. Lim and P.K. Agarwal. Conversion of pierced lengths measured at a probe to bubble size measures: an assessment of the geometrical probability approach and bubble shape models. *Powder Technol.*, 63:205–219, 1990.

K.S. Lim, P.K. Agarwal, and B.K. O'Neill. Mixing of homogeneous solids in bubbling fluidized beds: Theoretical modelling and experimental investigation using digital image analysis. *Chem. Eng. Sci.*, 48(12):2251–2265, 1993.

V. Linek, T. Moucha, and J. Sinkule. Gas-liquid mass transfer in vessel stirred with multiple impellers - i. gas liquid mass transfer characteristics in individual stages. *Chem. Eng. Sci.*, 51(12):3203–3212, 1996.

W. Liu and N.N. Clark. Relationship between distributions of chord lengths and distribution of bubble sizes including their statistical parameters. *Int. J. Multiphase flow*, 21(6):1073–1089, 1995.

W. Liu, N.N. Clark, and A.I. Karamavruc. General method for the tranfromation of chord length data to a local bubble size distribution. *AIChE J.*, 42(10):2713, 1996.

W. Liu, N.N. Clark, and A.I. Karamavruc. Relationship between distributions bubble size distribution and chord length distribution in heterogeneously bubbling systems. *Chem. Eng. Sci.*, 53(6):1267–1276, 1998.

W.-M. Lo and S.-J. Ju. Local gas hold-up, mean liquid velocity and turbulence in an aerated stirred tank using hot-film anemometry. *Chem. Eng. J.*, 35:9–17, 1987.

C.K.K. Lun, S.B. Savage, D.J. Jefferey, and N. Chepurniy. Kinetic theories for granular flow: inelastic particles in couette flow and slightly inelastic particles in a general flow field. *J. Fluid Mech.*, 140:223, 1984.

V. Machon, A.W. Pacek, and A.W. Nienow. Bubble sizes in electrolyte and alcohol solutions in a turbulent stirred vessel. *Chem. Eng. Res. Des.*, 75A:339–348, 1997.

A. Mandal, G. Kundu, and D. Mukherjee. A comparative study of gas hold-up, bubble size distribution and interfacial area in a downflow bubble column. *Trans IChemE, part A, Chem. Eng. Res. Des.*, 83(A4):423–428, 2005.

C.A. Mandarim De Lacerda. Stereological tools in biomedical research. *An. Acad. Bras. Cienc.*, 75(4):469–486, 2003.

G. Marrucci and L. Nicodemo. Coalescence of gas bubbles in acqueous solutions of inorganic electrolytes. *Chem. Eng. Sci.*, 22:1257–1265, 1967.

L. Mazzei and P. Lettieri. A numerical algorithm for the analysis of the bubble dynamics in two-dimensional fluidized beds simulated by means of cfd multiphase-flow codes. *Int. J. Chem. Reactor Eng.*, 4:1–20, 2006.

L. Mazzei and P. Lettieri. A drag force closure for uniformly dispersed fluidized suspensions. *Chem. Eng. Sci.*, 62:6129–6142, 2007.

S.L. McKee, R.A. Williams, and A. Boxman. Development of solid liquid mixing models using tomographic techniques. *Chem. Eng. J.*, 56:101–107, 1995.

N. Menon and D.J. Durian. Particle motions in a gas-fluidized bed of sand. *Phys. Rev. Lett.*, 79:3407–3410, 1997.

K. Mohanty, D. Das, and M.N. Biswas. Mass tranfer characteristics of a novel multi-stage external loop airlift reactor. *Chem. Eng. J.*, 133:257–264, 2007.

G. Montante, F. Magelli, and A. Paglianti. Experimental analysis and computational modelling of gas-liquid stirred vessels. *IChemE*, 85(A5):647–653, 2007.

G. Montante, D. Horn, and A. Paglianti. Gas-liquid flow and bubble size distribution in stirred tanks. *Chem. Eng. Sci.*, 63:2107–2118, 2008.

S. Mori and C.Y. Wen. Estimation of bubble diameter in gaseous fluidized beds. *AIChE J.*, 21:109–115, 1975.

S. Morooka, K. Tajima, and T. Miyauchi. Behavior of gas bubble in fluid beds. *Int. Chem. Eng.*, 12:168–174, 1972.

R.F. Mudde, H.B.M. Schulte, and H.E.A. van der Akker. Analysis of a bubbling 2-d gas-fluidized bed using image processing. *Powder Technol.*, 81:149–159, 1994.

M.A. Northrup, T.S. Kulp, S.M. Angel, and G.F. Pinder. Direct measurement of interstitial velocity field variations in a porous medium using fluorescent particle image velocimetry. *Chem. Eng. Sci.*, 48:13–21, 1993.

O. Owoyemi, P. Lettieri, and R. Plac. Experimental validation of eulerian-eulerian simulations of rutile industrial powders. *Ind. Eng. Chem. Res.*, 44:9996–10004, 2005.

A. Pintus S. Paglianti. An impedance probe for the measurement of liquid hold-up and mixing time in two-three phase stirred tank reactor. *Exp. Fluids*, 31:417–427, 2001.

C.C. Pain, S. Mansoorzadeh, and C.R.E. de Oliveira. A study of bubbling and slugging fluidised bed s using the two-fluid granular temperature model. *Int. J. Multiphase Flow,*, 27:527–551, 2001.

D. Pallares and Johnsson F. A novel technique for particle tracking in cold 2-dimensional fluidized beds. simulating fuel dispersion. *Chem. Eng. Sci.*, 61:2710–2720, 2006.

R. Parthasarathy and N. Ahmed. Bubble size distribution in a gas sparged vessel agitated by a rushton turbine. *Ind. Eng. Chem. Res.*, 33:703–711, 1994.

E.L. Paul, V.A. Atiemo-Obeng, and S.M. Kresta. *Handbook of industrial mixing*. Wiley interscience, Hoboken, New Jersey, 2004.

O. E. Potter, editor. *Mixing. In Fluidization; Davidson, J. F.and Harrison, D. Eds.* Accademic Press, New York USA, 1971.

S. Rapagná, P.U. Foscolo, and L.G. Gibilaro. The influence of temperature on the quality of gas fluidization. *Int. J. Multiphase Flow*, 20(2):305–313, 1994.

J.F. Richardson and W.N. Zaki. Sedimentation and fluidization: part i. *Trans. Inst. Chem. Eng.*, 32:35, 1954.

K. Rietema and S.M.P. Mutsers. The effect of gravity upon the stability of a homogeneously fluidized bed, investigated in a centrifugal field. *Fluidization, Cambridge University Press*, 1978.

K. Rietema and H.W. Piepers. The effect of interparticle forces on the stability of gas-fluidized beds-i. experimental evidence. *Chem. Eng. Sci.*, 45(6):1627–1639, 1990.

K. Rietema, E.J.E Cottaar, and H.W. Piepers. The effects of interparticle forces on the stability of gas-fluidized beds-ii. theoretical derivation of bed elasticity on the basis of van der waals forces between powder particles. *Chem. Eng. Sci.*, 48(9): 1687–1697, 1993.

L. Rizzuti and P.L. Yue. The measurement of light transmission through an irradiated fluidised bed. *Chem. Eng. Sci.*, 38(8):1241–1249, 1983.

P.N. Rowe. Drag forces in a hydraulic model of a fluidised bed, part ii. *Trans. Inst. Chem. Eng.*, 39:175, 1961.

P.N. Rowe. Drag forces in a hydraulic model of a fluidised bed, part ii. In *AIChE Annual Meeting*, number 58 in f, Miami Beach, 1986.

P.N. Rowe and D.J. Everett. Fluidised bed bubbles viewed by X-rays part II: The transition from two to three dimensions of undisturbed bubbles. *Trans. Instn. Chem. Engrs.*, 50:49–54, 1972.

P.N. Rowe and B. Partridge. An X-ray study of bubbles in fluidized beds. *Trans. Instn. Chem. Engrs.*, 43:157–175, 1965.

P.N. Rowe and C. Yacono. The distribution of bubble size in gas fluidized beds. *Trans. Instn. Chem. Engrs.*, 53:59–60, 1975.

P.N. Rowe and C.X.R. Yacono. The bubbling behaviour of fine powders when fluidised. *Chem. Eng. Sci.*, 31:1179–1192, 1976.

A. Ruf, J. Worlitschek, and M. Mazzotti. Modeling and experimental analysis of psd measurements through fbrm. *Part. Part. Syst. Char.*, 17:167–179, 2000.

J.C. Russ and R.T. Dehoff. *Practical Stereology, 2nd ed.* Plenum Press, New York, NY, 1999.

L. Shen and M. Zhang. Effect of particle size on solids mixing in bubbling fluidized beds. *Powder Technol.*, 97:170–177, 1998.

L. Shen and X. Zhang, M.and Yiqian. Solids mixing in fiuidized beds. *Powder Technol.*, 84:207–212, 1995.

L. Shen, F. Johnsson, and B. Leckner. Digital image analysis of hydrodynamics two-dimensional bubbling fluidized beds. *Chem. Eng. Sci.*, 52:2607–2617, 2004.

M.J.H. Simmons, P.A. Langston, and A.S. Burbridge. Particle and drop size analysis from chord distribution. *Powder Technol.*, 102:75–83, 1999.

J.L. Sinclair and R. Jackson. Gas-particle flow in a vertical pipe with particle-particle interactions. *AIChE J.*, 35:1473–1486, 1989.

M Sommerfeld and D. Broder. Analysis of hydrodynamics and microstructure in a bubble column by planar shadow image velocimetry. *I&EC*, 48(1):330–340, 2009.

P. Sridhar and O.E. Potter. Interfacial areas in gas-liquid stirred vessels. *Chem. Eng. Sci.*, 35(3):683–695, 1980.

P Stroeven and J. Hu. Review paper - stereology: historical perspective and applicability to concrete technology. *Materials and Structures*, 39:127–135, 2006.

M. Syamlal, W. Rogers, and T.J. O'Brien. Mfix documentation theory guide. Technical note DOE/METC-94/1004, U.S. Department of Energy, Office of fossil Energy., 1993.

K. Takahashi and A.W. Nienow. Bubble size and coalescence rates in an aerated vessel agitated by a rushton turbine. *J. Chem. Eng. Japan*, 26(5):536–542, 1993.

K. Takahashi, W.J. McManamey, and A.W. Nienow. Bubble size distribution in impeller region in gas sparged vessel agitated by a rushton turbine. *J. Chem. Eng. Japan*, 25(4):427–432, 1992.

K. Takenaka and K. Takahashi. Local gas hold-up and gas recirculation rate in an aerated vessel equipped with a rushton turbine impeller. *J. Chem. Eng. Japan*, 29: 799–804, 1996.

R. D. Toomey and Johnstone H. F. Gaseous fluidazion of solid particles. *Chem. Eng. Prog.*, 48:220, 1952.

D. Toye, M. Crine, and P. Marchot. Imaging of liquid distribution in reactive distillation packings with a new high energy x-ray tomography. *Meas. Sci. Technol.*, 16: 2213–2220, 2005.

S.C. Tsinontides and R. Jackson. The mechanics of gas fluidized beds with an interval of stable fluidization. *J. of Fluid Mechanism*, 255:237–274, 1993.

Y. Tsujii, T. Kawaguchi, and T. Tanaka. Discrete particle simulation of two dimensional fluidised bed. *Powder Technol.*, 77:79–87, 1993a.

Y. Tsujii, T. Kawaguchi, and T. Tanaka. Discrete particle simulation of two dimensional fluidised bed. *Powder Technol.*, 77:79–87, 1993b.

J.A.and Glicksman L.R. Valenzuela. Gas flow distribution in a bubbling fluidized bed. *Powder Technol.*, 44(2):103–113, 1985.

J.M. Valverde and A. Castellanos. Types of gas fluidization of cohesive granular materials. *Phys. Rev. E: Stat. Phys., Plasmas, Fluids*, 75:031306, 2007.

J.M. Valverde, A. Castellanos, P. Mills, and M.A.S. Quintanilla. Effects of particle size and interparticle force on the fluidization behaviour of gas fluidized beds. *Phys. Rev. E: Stat. Phys., Plasmas, Fluids*, 67:051305, 2003a.

J.M. Valverde, M.A.S. Quintanilla, A. Castellanos, and P. Mills. Experimental study on the dynamics of gas fluidized beds. *Phys. Rev. E: Stat. Phys., Plasmas, Fluids,*, 67:016303, 2003b.

J.J. van Deemter, editor. *Mixing. In Fluidization (2nd Edn.), Davidson, J.F. and Clift, R. and Harrison, D., Eds.* Academic Press, New York USA, 1985.

C.E.J. van Lare, H.W. Piepers, J.N. Schoonderbeek, and D. Thoenes. Investigation on bubble characteristics in a gas fluidized bed. *Chem. Eng. Sci.*, 52:829–841, 1997.

C. Vogt, R. Schreiber, G. Brunner, and J. Werther. Fluid dynamics of the supercrititical fluidized beds. *Powder Tech.*, 158:102–114, 2005.

G.B. Wallis. *One dimensional two-phase flow.* McGraw Hill, 1969.

M. Wang, A. Dorward, D. Vlaev, and R. Mann. Measurements of gas-liquid mixing in a stirred vessel using electrical resistance tomography (ert). *Chem. Eng. J.*, 77: 93–98, 2000.

X.S. Wang, V. Palero, J. Soria, and M.J. Rhodes. Laser-based planar imaging of nano-particle fluidization: Part i - determination of aggregate size and shape. *Chem. Eng. Sci.*, 61:5476–5486, 2006.

C.Y. Wen and Y.H. Yu. Mechanics of fluidization. *Chem. Eng. Progress Symp. Series*, 62:100, 1966.

J. Werther. Bubbles in gas fluidized beds - part i. *Trans. Instn. Chem. Engrs.*, 52:149, 1974a.

J. Werther. Bubbles in gas fluidized beds - part ii. *Trans. Instn. Chem. Engrs.*, 52:160, 1974b.

J. Werther and O. Molerus. The local structure of gas fluidized beds-i. a statistically based measuring system. *Int. J. of Multiphase Flow*, 1:103–122, 1973a.

J. Werther and O. Molerus. The local structure of gas fluidized beds-ii. the spatial distribution of bubbles. *Int. J. of Multiphase Flow*, 1:123–138, 1973b.

R.A. Williams, R. Mann, F.J. Dickin, O.M. Ilyas, P. Ying, and R.B. Edwards. Application of electrical impedence tomography to mixing in stirred vessels. *AIChE Symp. Ser.*, 293:8–15, 1993.

I.N.S. Winaya and T.and Yamada D. Shimizu. A new method to evaluate horizontal solid dispersion in a bubbling fluidized bed. *Powder Technol.*, 178:173–178, 2007.

R.H.S. Winterton and J.S. Munaweera. Bubble size in two phase gas-liquid bubbly flow in ducts. *Chem. Eng. Process.*, 40:437–447, 2001.

J. Worlitschek, T. Hocker, and M. Mazzotti. Restoration of psd from chord length distribution data using the method of projection onto convex sets. *Part. Part. Syst. Charact.*, 22:81–98, 2005.

E.J.W. Wynn. Relationship between particle-size and chord-length distributions in focused beam reflectance measurement: stability of direct inversion and weighting. *Powder Technol.*, 133:125–133, 2003.

A.M. Xavier, D.A. Lewis, and J.F. Davidson. The expansion of bubbling fluidised beds. *Trans. IChemE*, 56:274, 1978.

H.Y. Xie and D. Geldart. Fluidization of fcc powders in the bubble free regime: effect of types of gases and temperature. *Powder Technol.*, 82:269–277, 1995.

B.H. Xu and A.B. Yu. Numerical simulation of the gas-solid flow in a fluidized bed by combining discrete particle method with computational fluid dynamics. *Chem. Eng. Sci.*, 52(16):2785–2809, 1997.

W.-C. Yang. *Handbook of fluidization and fluid particle systems.* Marcel Dekker (Hemisphere), New York (NY), 2003.

J.G. Yates and S.J.R. Simons. Experimental methods in fluidization research. *Int. J. Multiphase Flow*, 20(1):297–330, 1994.

J.G. Yates, d.D.J. Cheesman, and Y.A. Sergeev. Experimental observations of voidage distribution around bubbles in a fluidized bed. *Chem. Eng Sci.*, 49:1885–1895, 1994.

P.L. Yue, L. Rizzuti, and V. Augugliaro. Bubble phase voidage and dense phase voidage in thin two dimensional fluidized bed. *Chem. Eng Sci.*, 41(1):171–177, 1986.

D.Z. Zhang and R. M. Rauenzahn. Stress relaxation in dense and slow granular flows. *J. Rheol.*, 44:1019–1041, 2000.

C. Zhu, Q. Yu, R.N. Dave, and R. Pfeiffer. Gas fluidization characteristics of nanoparticle agglomerates. *AIChE J.*, 51(2):426–439, 2005.